2010

Cell Compatible Electrospun Poly(vinyl alcohol) Fibers for Tissue Regeneration

Kenneth K.H. Wong

Cell Compatible Electrospun Poly(vinyl alcohol) Fibers for Tissue Regeneration

(Spine title: Cell Compatible Electrospun Poly(vinyl alcohol) Fibers)

(Thesis format: Monograph)

by

Kenneth K.H. Wong

Graduate Program in Medical Biophysics

A thesis submitted in partial fulfillment
of the requirements for the degree of
Doctor of Philosophy

The School of Graduate and Postdoctoral Studies
The University of Western Ontario
London, Ontario, Canada

THE UNIVERSITY OF WESTERN ONTARIO
SCHOOL OF GRADUATE AND POSTDOCTORAL STUDIES
CERTIFICATE OF EXAMINATION

Joint-Supervisor

Dr. Wankei Wan

Dr. Martin Zinke-Allmang

Supervisory Committee

Dr. Silvia Mittler

Dr. Amin Rizkalla

Examiners

Dr. Andrew Hrymak

Dr. Lyudmila Goncharova

Dr. Silvia Mittler

Dr. Frank Ko

The thesis by

Kenneth K.H. Wong

entitled:

Cell Compatible Electrospun Poly(vinyl alcohol) Fibers for Tissue Regeneration

is accepted in partial fulfillment of the
requirements for the degree of
Doctor of Philosophy

Date_____

Chair of the Thesis Examination Board

Abstract

Poly(vinyl alcohol) (PVA) is a well known biocompatible synthetic polymer. PVA is not cell compatible due to its high hydrophilicity. As prepared by electrospinning in the form of nanofibers, it is unstable in aqueous environments including cell culture media. For tissue regeneration applications, this study demonstrates the use of PVA scaffold utilizing electrospun nanofibers with aqueous stability and cell compatibility toward creating biomaterial-tissue hybrid based medical devices. Two different approaches: heat treatment and ion beam treatment were developed to improve aqueous stability and promote cell compatibility for PVA fibers. Using a thermal annealing method at elevated temperatures, the fibers became stable in water. This observation correlated closely to the change in the crystallinity of PVA. Elastic moduli of individual fibers were determined using a multi-points bending approach by atomic force microscopy. Elastic moduli of as-spun PVA fibers were determined to be a function of fiber diameter and humidity. Significant changes in the elastic modulus of the modified PVA fibers were also observed. To improve the cell compatibility, low energy N^+ and He^+ ion beams were used to introduce amine and carbonyl functional groups. Cell compatibility was assessed *in vitro* using primary human skin fibroblasts (hsF). Confocal microscopy confirmed the adhesion and proliferation of hsF on both the random and aligned PVA fibers after the ion beam treatment, while cells failed to adhere to the untreated fibers. Cell morphology was observed to align and elongate along the fiber axis on aligned PVA fibers. After 10 days of proliferation, cells were found to form confluent layers and even multiple layers on the N^+ treated fibers. Cell proliferation depends on ion species, ion dose and fiber alignment. With the two post-processing treatments, PVA fibrous scaffold showed the potential to become biomaterial-tissue hybrid based medical devices for tissue regeneration applications.

Keywords: Electrospun Polymer Fiber; Poly(vinyl alcohol); Ion Implantation; Thermal Annealing; Surface Morphology; Nanomechanical Measurement; Elastic Modulus; Aqueous Stability; Fibroblast; Cell Compatibility

Co-Authorship

Chapter 1 & 2: Kenneth Wong – author; Wankei Wan and Martin Zinke-Allmang – guidance and chapter revision

Chapter 2: Kenneth Wong – author; Wankei Wan and Martin Zinke-Allmang – guidance and chapter revision

Chapter 3: Kenneth Wong – author, experimental design; Wankei Wan, Martin Zinke-Allmang – experimental design, guidance and chapter revision

Chapter 4: Kenneth Wong – author, data collection and analysis; Jeffery L. Hutter – provided the computer codes for AFM cantilever's spring constant calibration, AFM force-volume data analysis and single fiber elastic modulus determination; Yan Wu and David O'Gorman – provided the human skin fibroblasts for cell studies; Wankei Wan and Martin Zinke-Allmang – guidance and chapter revision

Chapter 5, 6 & 7: Kenneth Wong – author; Wankei Wan and Martin Zinke-Allmang – guidance and chapter revision

Acknowledgements

I would like to sincere gratitude to the following people:

My wife and parents for their love and support.

Dr. Wankei Wan for his guidance and inspiration to my academic and personal development.

Dr. Martin Zinke-Allmang for his guidance, encouragement and support over the years.

Dr. Jeffery L. Hutter for his supervision on the AFM studies of this thesis work.

Donna Padavan, Jack Hendriks, Dr. Todd Simpson, Dr David O'Gorman and Yan Wu for their help and support.

Table of Contents

Certificate of Examination ii

Abstract iii

Co-Authorship iv

Acknowledgements v

Table of Contents vi

List of Abbreviations x

List of Figures xi

List of Tables xix

Chapter 1 Introduction 1

Chapter 2 Background and Literature Review

2.1 Electrospinning 6

2.1.1 Design of the Fiber Collector 7

2.1.2 Functional Fiber Structures 9

2.1.3 Production Rates of Electrospun Fibers 11

2.1.4 Materials for Electrospinning 12

2.1.2 Poly(vinyl alcohol) 13

2.2 Mechanical Testing Technique 14

2.3 Polymer Post-Processing Modifications 20

2.3.1 Surface Modification 20

2.3.2 Ion Beam Modification on Polymer 21

2.3.2.1 Simulation of Ion Implantation in Polymers 21

2.3.2.2 Ion Beam Surface Modification on Physical Properties 23

2.3.2.3 Ion Beam Surface Modification for Bio/Cell-Compatibility 24
2.3.3 Bulk Modification 24
2.3.4 Post-Processing Modification of PVA 25
2.4 Use of Electrospun Fibrous Scaffolds in Biomedical Application 25
2.4.1 Cell – Substrate Interaction 26
2.4.2 Medical Devices Based on Electrospun Fibrous Scaffolds 27
Chapter 3 Materials and Methods
3.1 Poly(vinyl alcohol) 28
3.2 Electrospinning Process 28
3.3 Thermal Annealing 29
3.4 Ion Beam Implantation 30
3.5 Cell Culture 34
3.6 Atomic Force Microscopy 36
3.6.1 Sample Preparation for Mechanical Testing 36
3.6.2 Applying Clamped Beam Model using AFM 37
3.6.3 Thermal Noise Cantilever Calibration 41
3.6.4 Mechanical Measurement and Elastic Modulus Determination 41
3.7 Characterization Techniques
3.7.1 Differential Scanning Calorimetry 45
3.7.2 Confocal Laser Scanning Microscopy 45
3.7.3 Infrared Spectroscopy 47
3.7.4 Proliferation Assay 48
3.7.5 Scanning Electron Microscopy 50
3.7.6 X-ray Photoelectron Spectroscopy 51

3.7.7 X-ray Diffraction 53

Chapter 4 Results 56

4.1 Fabrication of PVA Fibers Using Electrospinning Technique 57

4.1.1 Effect of PVA Concentration on Fiber Diameter 59

4.1.2 Effect of Electric Potential on Fiber Diameter 61

4.1.3 Effect of Working Distance on Fiber Diameter 62

4.2 Mechanical Properties of Electrospun PVA Nanofibers 63

4.2.1 Role of Fiber Diameter on Mechanical Properties 66

4.2.2 Role of Ambient Humidity on Mechanical Properties 69

4.3 Improve Aqueous Stability and Mechanical Properties of PVA Fibers Using Thermal Annealing 70

4.3.1 Effect of Annealing on the Aqueous Stability of Fibers - Temperature 71

4.3.2 Effect of Annealing on the Aqueous Stability of Fibers - Time 77

4.3.3 Effect of Annealing on Mechanical Properties 79

4.3.4 Effect of Annealing on Crystallinity 81

4.3.5 Crystallinity and Mass of Annealed Fibers after Water Immersion 84

4.3.6 Effect of Annealing on Melting Temperature 85

4.4 Physical and Chemical Properties of Ion Beam Treated PVA Fibers

4.4.1 Ion Beam Treatment 87

4.4.2 Effect of Ion Implantation on Fiber Diameters 88

4.4.3 Mechanical Properties of N^+ Treated PVA Fibers 91

4.4.4 Effect of N^+ Ion Dosage on Mechanical Properties 92

4.4.5 Mechanical Properties of He^+ Treated PVA Fibers 94

4.4.6 Effect of Ion Implantation on Chemical Structure 95

4.5 Cell Compatibility of Electrospun PVA Fibrous Scaffolds

4.5.1 Modifying PVA Fibers for *In Vitro* Cell Compatibility Evaluation 100

4.5.2 Human Skin Fibroblasts Culture on Modified PVA Fibers 106

4.5.3 Effect of Ion Implantation on Cell Morphology 109

4.5.4 Effect of Fiber Orientation on Cell Morphology 112

4.5.5 Cell Counting on Modified PVA Fibers 115

Chapter 5 Discussion 124

5.1 Preparation of PVA Fibers by Electrospinning 125

5.2 Mechanical properties of PVA Fibers 129

5.3 Stability of Electrospun PVA Fibers in Aqueous Media 137

5.4 Ion Beam Modification of Electrospun PVA Fibers for Cell Compatibility

5.4.1 Ion Beam Modification 140

5.4.2 Cell Compatibility of Ion Beam Treated Electrospun PVA Fibers 144

Chapter 6 Conclusions

6.1 Conclusions 150

6.2 Future Work 152

References 154

Appendices

Appendix A: Derivation of Equations – Clamped Beam Model 177

Appendix B: Copyright Waivers 183

Curriculum Vitae 185

List of Abbreviations

α–MEM	alpha-Minimum Essential Media
AFM	Atomic Force Microscopy
Alexa 488	Alexa Fluor 488 Phalloidin
ANOVA	Analysis of Variance
BSA	Bovine Serum Albumin
CLSM	Confocal Laser Scanning Microscopy
DAPI	4',6-diamidino-2-phenylindole
DSC	Differential Scanning Calorimetry
ELISA	Enzyme-Linked Immunosorbent Assay
FBS	Fetal Bovine Serum
FTIR	Fourier Transforms Infrared Spectroscopy
He^+	Helium ion
hsF	Human Skin Fibroblasts
IR	Infrared Spectroscopy
N^+	Nitrogen ion
PBS	Phosphate Buffered Saline
PVA	Poly(vinyl alcohol)
SD	Standard Deviation
SE	Standard Error
SEM	Scanning Electron Microscopy
SIMS	Secondary Ion Mass Spectroscopy
Ta	Tantalum
TEM	Transmission Electron Microscopy
WST	Water-Soluble Tetrazolium Salt
XPS	X-ray Photoelectron Spectroscopy
XRD	X-ray Diffraction

List of Figures

Figure 2.1 (a) Schematic drawing of an electrospinning setup, (b) the process of electrospinning at the tip of a needle 7

Figure 2.2 Stationary electrospinning collectors based on (a) two parallel, (b) four and (c) six electrodes for fabricating uniaxially aligned fibers (Adapted from [47]) 8

Figure 2.3 Rotating electrospinning collector based on (a) mandrel, (b) disk and (c) wire-framed drum for fabricating aligned fibers (Adapted from [86-89]) 9

Figure 2.4 Schematic drawing of the polymer solution feeding setup for (a) solid fibers, (b) composite fibers and (c) coaxial electrospinning. 10

Figure 2.5 Different multi-nozzle designs for multiple jets electrospinning (Adapted from [116, 121, 122, 124, 125]). 12

Figure 2.6 Various single nanofiber mechanical characterization techniques based on (a) tensile test, (b) resonance excitation and (c) bending test. (Adapted from [183-185]) 15

Figure 3.1 Chemical structure of PVA 28

Figure 3.2 The electrospinning setup with (a) a stationary collector and (b) a rotating collector 29

Figure 3.3 Schematic plan view of the Tandetron Accelerator Laboratory at The University of Western Ontario [275]. The sample holder is placed inside the implantation chamber (where the yellow circle is indicating) for implantation 30

Figure 3.4 Schematic cross-sectional view of the sample holder with Ta foil 31

Figure 3.6 a) Histograms of the nitrogen (with incident energy 1.7 MeV) and helium (with incident energy 520 keV) and helium ion energy transmitted through the Ta foil as simulated by SRIM. (b) The matching ion doping depth profiles (SRIM) in the sample with the gray circles illustrating 5 layers of fibers 33

Figure 3.6 Experimental ToF-SIMS and theoretical SRIM depth profile of N^+ implanted into a silicon wafer through a 1.0 μm thick Ta foil 33

Figure 3.7 Image of a 96 wells plate loaded with 5 mm diameter PVA fibrous scaffolds for *in-vitro* test 35

Figure 3.8 Optical image (reflective dark field) of electrospun PVA fibers collected on a TEM grid. The circles indicate suspended fibers suitable for mechanical testing 37

Figure 3.9 Schematic sketch of fiber with a suspended length of L clamped to a substrate while a vertical force F is applied at a distance a from one end of the fiber by an AFM tip 38

Figure 3.10 AFM trace and retrace contact mode images. We note that the centre of the suspended portion bends toward the tip scanning direction, but the supported portions remain anchored on the substrate 39

Figure 3.11 Schematic drawing of a fiber that underwent tensile deformation 40

Figure 3.12 SEM image of a representative example for AFM mechanical testing of a PVA fiber suspended across a corner of a TEM grid hole 42

Figure 3.13 Approach force spectra obtained on the bare grid (hollow triangles) and near-center of a suspended fiber (solid circles). The shallower slope for the suspended fiber allows its mechanical strength to be measured 43

Figure 3.14 A topographical image from the AFM force-volume measurement with 92 data points chosen along the fiber. 44

Figure 3.15 Plot of the slopes of force spectra (hollow circles) as a function of position a along a suspended fiber of length L = 3.7 μm. The best fit using the clamped beam model is shown as a solid curve 44

Figure 3.16 Six different vibrational modes for a hydrocarbon molecule 48

Figure 3.17 CLSM image of hsF nuclei for cell counting to determine the rate of proliferation on an ion beam treated PVA fiber scaffold 49

Figure 3.18 XRD spectrum of as-spun PVA fibers fitted with Pearson VII function 54

Figure 4.0 A flow-chart illustrating the outline of this chapter 57

Figure 4.1 (a–c) SEM images of PVA fibers produced from 8.5, 9.5 and 10.5 wt% solutions, respectively 60

Figure 4.2 Histograms of the fiber diameters along with best-fit normal distribution obtained from the three solutions at 22 kV applied voltage and 15 cm tip-to-collector distance. (the data are fitted with Gaussian distribution function) 61

Figure 4.3 (a) Histograms of the fiber diameter along with best-fit normal distribution obtained from a solution with 9.5 wt% of PVA at 15cm with 20, 22, 24 and 26 kV. (b) Histograms of the fiber diameter along with best-fit normal distribution obtained from a solution with 9.5 wt% of PVA using 24 kV at 10, 15 and 20 cm 63

Figure 4.4 SEM images of a fiber (a) before and (b) after the AFM nanomechanical measurement. The fiber remained well anchored and its position was unchanged 66

Figure 4.5 (a) Plot of elastic modulus vs. diameter of 73 PVA fibers. (b) Plot of the average elastic modulus in 3 diameter ranges 68

Figure 4.6 SEM images of as-spun PVA fibers after immersed in DI water for 1 minute (area affected at the left side) 71

Figure 4.7 SEM images of PVA fibers with 4 hours of 85 °C annealing treatment after (a) annealing, (b) immersed in DI water for 1 day, (c) immersed in DI water for 10 days, and (d) immersed in DI water for 30 days 73

Figure 4.8 SEM images of PVA fibers with 4 hours of 110 °C annealing treatment after (a) annealing, (b) immersed in DI water for 1 day, (c) immersed in DI water for 10 days, and (d) immersed in DI water for 30 days 74

Figure 4.9 SEM images of PVA fibers with 4 hours of 135 °C annealing treatment after (a) annealing, (b) immersed in DI water for 1 day, (c) immersed in DI water for 10 days, and (d) immersed in DI water for 30 days 75

Figure 4.10 SEM images of PVA fibers with 4 hours of 160 °C annealing treatment after (a) annealing, (b) immersed in DI water for 1 day, (c) immersed in DI water for 10 days, and (d) immersed in DI water for 30 days 76

Figure 4.11 Fiber diameters after 4 hours of annealing at 4 different temperatures; at 5 different stages during the stability test in DI water. (The error bars are SD) 76

Figure 4.12 SEM images of PVA fibers with (a) 8 hours of 110 °C (b) 30 minutes of 135 °C, and (c) 1 hour of 135 °C treatment after immersed in DI water for 10 days 78

Figure 4.13 High resolution SEM image of the sample shown in Figure 4.12b 78

Figure 4.14 XRD spectra (in the range between $2\theta = 16° - 32°$) of PVA as-spun fibers, and fibers after 4 hours of 85°C annealing, 4 hours of 110 °C annealing, 4 hours of 135 °C annealing and 4 hours of 160 °C annealing (arbitrary scale on intensity and offset for clarity) 81

Figure 4.15 FTIR spectra (in the range between 975 and 1550 cm^{-1}) of PVA solution, as-spun fibers, and fibers after 4 hours of 85°C annealing, 4 hours of 135°C annealing and 4 hours of 185°C annealing (arbitrary scale on absorbance intensity and offset for clarity). The schematic of determining the ratio *a*/*b* is also shown 83

Figure 4.16 DSC heating curves (in the range between 200 and 245 °C) of as-spun PVA fibers and fibers annealed at four different temperatures. (arbitrary scale on heat flow and offset for clarity) 87

Figure 4.17 Histograms of the fiber diameter along with best-fit normal distributions before and after N^+ and He^+ treatment 88

Figure 4.18 (a) SEM image of the original PVA fibrous scaffold prior to N^+ treatment. (b) SEM image of the PVA fibrous scaffold after treated with 1.2×10^{16} N^+/cm^2 89

Figure 4.19 High resolution SEM image of the PVA fibers after treated with 1.2×10^{16} N^+/cm^2 90

Figure 4.20 (a) SEM image of the original PVA fibrous scaffold prior to He^+ treatment. (b) SEM image of the PVA fibrous scaffold after treated with 1.2×10^{16} He^+/cm^2 90

Figure 4.21 The mean elastic modulus (solid line) and diameter (dashed line) of 10 fibers each measured after three steps of nitrogen ion dose implanted. (The error bars are standard errors) 94

Figure 4.22 The mean elastic modulus (solid line) and diameter (dashed line) of 17 fibers before and after helium ion treatment. (The error bars are standard errors) 95

Figure 4.23 High resolution XPS spectra for C_{1s} (left column), O_{1s} (middle column) and N_{1s} (right column), measure for untreated (top row), 1.6×10^{16} ions/cm^2 of N^+ treated (middle row) and 1.6×10^{16} ions/cm^2 of He^+ (bottom row) PVA fibers. The peaks are interpreted on terms of contributions from various chemical groups (lettered peaks), as defined in Table 4.12 97

Figure 4.24 SEM image of the boundary area of the original (left side) and treated fibers (right side) after 10 minutes of soaking in DI water 99

Figure 4.25 (a) SEM image of a control sample consisted of randomly orientated fibers (b) SEM image of aligned fibers 100

Figure 4.26 FTIR spectra of as-spun PVA fibers and the fibers after 4 hours of 135°C annealing (arbitrary scale on absorbance intensity and offset for clarity). The peaks are labeled numerically for various chemical groups, as defined in Table 4.13 101

Figure 4.27 XPS survey spectra of as-spun, as-annealed, N^+ treated and He^+ treated PVA fibrous scaffold 103

Figure 4.28 HR XPS C_{1s} of as-spun, as-annealed, high dose N^+ treated, low dose N^+ treated and He^+ treated PVA fibrous scaffold. (The corresponding functional groups associated with each peak are listed in Table 4.12) 104

Figure 4.29 HR XPS O_{1s} of as-spun, as-annealed, highest dose N^+ treated, lowest dose N^+ treated and He^+ treated PVA fibrous scaffold. (The corresponding functional groups associated with each peak are listed in Table 4.12) 105

Figure 4.30 HR XPS N_{1s} of high dose N^+ treated PVA fibrous scaffold. (The corresponding functional groups associated with each peak are listed in Table 4.12) 106

Figure 4.31 (a) SEM image and (b) CLSM image of hsF on a sample C after 72 hours of culture 108

Figure 4.32 CLSM image of hsF on a sample N4 after 72 hours of culture 109

Figure 4.33 (a) Low and (b) high magnification SEM images of hsF on a sample N4 after 72 hours of culture 110

Figure 4.34 (a) Low and (b) high magnification SEM images of hsF on a sample N1 after 72 hours of culture 111

Figure 4.35 (a) Low and (b) high magnification SEM images of hsF on a sample He3 after 72 hours of culture. (c) High resolution SEM image of the extended filopodia in the lower part of the hsF shown in (b) 112

Figure 4.36 CLSM image of hsF on a sample N3A after 72 hours of culture. (The arrow indicates the oriented direction of the fibers) 113

Figure 4.37 (a) Low and (b) high magnification SEM images of hsF on a sample N3A after 72 hours of culture 114

Figure 4.38 (a) Low and (b) high magnification SEM images of a hsF migrated and attached to the second layer of fibers on a sample N3A 114

Figure 4.39 Average hsF number on the four different N^+ treated randomly oriented fibrous scaffolds after 3 stages of culture 115

Figure 4.40 SEM image of all ion beam treated PVA fibrous scaffolds after 1, 4 and days of hsF culture. (All have the same scale bar of 100 μm) 117

Figure 4.41 Proliferation rate of hsF on the N^+ treated aligned and He^+ treated randomly oriented fibrous scaffolds. (Sample C, N3 and N4 are showed for comparison) 119

Figure 4.42 CLSM images of sample (a) N3, (b) N4 and (c) N3A after 1 day of culture 121

Figure 4.43 CLSM images of sample (a) N3, (b) N4 and (c) N3A after 4 days of culture 122

Figure 4.44 CLSM images of sample (a) N3, (b) N4 and (c) N3A after 10 day of culture 123

Figure 5.1 SEM images of a fiber (a) before and (b) after the AFM imaging. The red dotted lines indicated the fiber becomes loosen after the AFM measurement 132

Figure 5.2 Plot of the slopes of force spectra (hollow circles) as a function of position *a* along the suspended fiber shown in Figure 5.1 133

Figure 5.3 XPS survey spectra of 2.4×10^{16} ions/cm^2 N^+ treated PVA fibrous scaffold 144

Figure 5.4 SEM image of hsF on a sample N4 after 72 hours of culture. It shows the well extended filopodia toward the fibers and the other hsF. 145

Figure 5.5 CLSM image of hsF on a sample N4 after 72 hours of culture. It shows multiple hsF grew on top of each other and form multiple layers. 147

List of Tables

Table 2.1	List of tensile testing approaches for various types of nanofibers	16
Table 2.2	List of indentation approaches for various types of nanofibers	17
Table 2.3	List of resonance excitation methods for various types of nanofibers	18
Table 2.4	List of AFM-based bending test approaches for various types of nanofibers	19
Table 2.5	Stopping values of different cores and bonds in the unit of $eV/10^{15}$ atoms/cm^2 for proton at 125 keV [232]	23
Table 4.1	Three groups of electrospinning parameters	58
Table 4.2	The dimensions of five individual PVA fibers and the respective AFM (force-volume mode) operating parameters	65
Table 4.3	The nanomechanical measurement results of the individual fibers	65
Table 4.4	One-way ANOVA results of the three diameter groups	68
Table 4.5	The dimensions and elastic modulus of ten PVA fibers at RH of 9 % and 32 %	70
Table 4.6	The dimensional and elastic modulus changes of individual fibers before and after 4 hours of 135 °C annealing	80
Table 4.7	The results of XRD characterization of the as-spun PVA fibers and the fibers after 4 hours of four different annealing temperatures	82
Table 4.8	Effect of annealing treatment on the crystallinity of electrospun PVA fibers	84
Table 4.9	The crystallinity and mass loss of annealed PVA fibers after immersed in DI water for 1 day	85
Table 4.10	The melting transition peak of the as-spun PVA fibers and annealed fibers	86

Table 4.11 The dimensional and elastic modulus changes of individual fibers before and after 8.0×10^{15} ions/cm^2 of N^+ treatment 92

Table 4.12 List of different chemical functional groups represented by the peaks labeled in XPS spectra at the corresponding binding energy shown in Figure 4.23 and 4.28–4.30 [309] 98

Table 4.13 List of different chemical functional groups represented by the peaks labeled in FTIR spectra at the corresponding wavenumber shown in Figure 4.26 [310] 102

Table 4.14 List of seven differently treated PVA fibrous scaffolds 103

Table 4.15 One-way ANOVA test results of all samples at (a) day 1, (b) day 4 and (c) day 10 (✓ = significantly different and × = insignificantly different) 118

Chapter 1 Introduction

Poly(vinyl alcohol) (PVA) is a well known Food and Drug Administration approved biocompatible polymer [1, 2] with good thermal stability and chemical resistance. It has been successfully used for medical devices in the form of hydrogel for artificial heart valves [3] and load-bearing cartilage [4]. For tissue regeneration applications, PVA is seldom considered as the material of choice to fabricate scaffold. Because of its high hydrophilicity, PVA inhibits cell adhesion, viability and growth [5]. There have been continuing efforts to impart cell compatibility to PVA using different approaches, such as surface functionalization [5-11], blending [8, 12-19], forming composites [20] and surface coating [21] with different bioactive macromolecules. For some targeted tissue regeneration applications such as skin [22], ear drum [23], vascular [14], bladder [24] nerve [25] and bone [26], a scaffold with cell compatibility is required.

The currently accepted dogma in tissue regeneration is that the scaffold should be biodegradable and ideally, it should degrade without non-toxic byproducts and at a rate similar to tissue formation. PVA is not degradable in a physiological environment, and has a limited use in the research community for tissue regeneration applications [27]. There have been some recent efforts to make degradable PVA via chemical functionalization [28]. However, Cahn et al. [29] reported the benefit of using a non-degradable, cell-compatible scaffold (e.g. polyester fiber mesh) in a rather unique skin re-construction application. When compared with a degradable counterpart, it provided better long-term results in term of stabilizing the interface as well as transferring the mechanical stress between tissue and device. This study also showed that there was no significant difference in foreign body response and tissue regeneration. Therefore, Cascone et al. [30] proposed a concept of creating biomaterial-tissue hybrid based medical devices based on non-degradable, cell-compatible PVA scaffold. This concept has been applied to cartilage [1, 31, 32], cornea [33, 34], as well as vascular [14] regenerations.

Three-dimensional (3D) nanofibrous scaffolds, consist of fibers with diameters less than 500 nm [35] that are fabricated by the electrospinning technique, have many of the desired properties and much potential in tissue regeneration/tissue repair applications.

Compared to microporous and microfibrous scaffolds [36], nanofibrous scaffolds are considered to be more suitable for tissue regeneration applications because they (1) mimic the fibrous structure of the native extracellular matrix (ECM), (2) provide a high surface area to volume ratio for cell adhesion, as well as (3) display high porosity and pore-interconnectivity to allow cell migration into the scaffold [37] and the flow of nutrients and fluids into and metabolites out of the scaffold.

Electrospinning [38] is a simple but versatile technique capable of producing 3D non-woven fibrous scaffolds consisting of nanometer (< 500 nm) sized fibers made from a wide variety of synthetic and natural polymers [39] including proteins and polysaccharides [40] for applications such as protective clothing [41], membranes [42], wound dressings [43], drug delivery systems [44] and scaffold for tissue regeneration [45]. Electrospun nanofibrous scaffolds are particularly distinguished due to their high surface area to volume ratio and interconnected porous network. Electrospinning has become the method of choice in fabricating scaffolds for tissue regeneration applications [36, 46]. In addition, fibrous scaffolds can be electrospun with controlled alignment to closely mimic the organized structure of the extracellular matrix (ECM) [47, 48].

PVA is a hydrophilic polymer, and it readily dissolves in water. Indeed, water can be used as a solvent to prepare a PVA solution for electrospinning to fabricate nanofibers. To maintain the nanofiber geometry for biomedical applications in aqueous and cell culture media environments, they have to be stabilized. PVA can be chemically cross-linked using glutaraldehyde [49, 50], radiation [51, 52], or physically crosslinked by freezing/thawing processes [53] to achieve good aqueous stability for medical device applications such as artificial meniscus [1], heart valves [3] and wound dressings [54]. For electrospun PVA nanofibers, glutaraldehyde vapor [15, 16] and methanol [55, 56] have been shown to be suitable post-processing agents for their aqueous stability, but the morphological features of the electrospun fibrous scaffolds are largely lost. In addition, their chemical properties are altered due to the crosslinking reactions. Water stable PVA hydrogels have been prepared by a thermal cycling process. Control of their stability and mechanical properties has been attributed to an increase in the polymer crystallinity [57-59] as a function of the number of thermal cycles. For macroscopic PVA samples, thermal annealing has been reported to increase the degree of crystallinity without

changing its chemical structure [60, 61]. We hypothesize that annealing will lead to an increase in crystallinity of electrospun PVA fibers. This should then result in an increase in their aqueous stability and a concurrent improvement in the fiber mechanical properties.

Ion implantation is a well-established technique in the materials processing industry, largely because of its controllability, homogeneity, high "dopant" purity and reproducibility. In this process, specific ionic species are electrostatically accelerated to high speeds and incorporated directly into the superficial layers of a sample. Shallow layers can be implanted with high doping gradients, allowing near-surface intrinsic modification while preserving the structure and characteristic of the bulk material. Choosing implantation parameters such as ion species, energy, current and dose allows us to selectively modify tribological [62], chemical [63] and physical properties [64] of the material surface. For temperature-sensitive polymers, the ability to control these treatment parameters becomes more critical as excessive energy deposition could cause permanent damage [65, 66]. Broad-energy (non-monochromatic) ion beam implantation is often used because it provides a wider range of ion doping depths, thus distributing energy over a greater depth range and minimizing thermal damage [67]. This approach is commonly used for improving surface mechanical properties of bulk polymer materials (e.g., for surface hardening [68-70]). For a tissue regeneration scaffold, the ability to tailor its stiffness to mimic the natural environment can induce cell adhesion [71, 72]. On the other hand, the characteristics of the surface chemistry of a scaffold will mediate the adsorption of biologic molecules (e.g. cell adhesion proteins [73]) that regulate cell activities, such as adhesion, migration and proliferation. For instance, implantation of helium ions results in drastic alteration of the cell adhesion properties on polypropylene and polytetrafluoroethlyene [74]. Incorporating nitrogen via nitrogen ion implantation near the surface of certain synthetic polymer scaffolds can form specific nitrogen-containing functional groups (e.g. amine or amide) that enhance the attachment of proteins and cells [75, 76]. Therefore, ion beam treatment is a convenient method to tailor both the mechanical and chemical properties of polymer surfaces for specific applications. Of particular interest is the potential ability to alter the cell adhesion properties of PVA fibrous scaffold by implantation of specific ion species, nitrogen and helium. The ability

to modify the mechanical properties of PVA fibers using ion beam treatment is also examined.

This thesis aims at developing a stabilized, cell compatible PVA-based fibrous scaffold for tissue regeneration/tissue repair applications (e.g. skin and tympanic membrane).

There are five primary objectives:

(1) To fabricate PVA fibrous scaffolds consisting of random or aligned nanometer size fibers via electrospinning;

(2) To stabilize scaffolds in an aqueous environment using thermal annealing while preserving the fibrous morphology;

(3) To modify the surface chemical properties of the scaffold under controlled conditions using N^+ and He^+ ion beam implantation;

(4) To characterize the effect of the thermal annealing and ion beam modification in terms of aqueous stability, mechanical properties and chemical properties of the fibers; and

(5) To evaluate the *in-vitro* cell compatibility of the modified PVA scaffold for tissue regeneration applications.

This thesis is organized in the following way. Chapter 2 is a literature review which provides the background on the major components of this thesis: electrospinning, nano-mechanical measurements, post-processing modifications and cell compatibility of PVA nanofibers. Implications of the results for biomedical applications of PVA nanofibers will also be reviewed. Chapter 3 describes the principles and experimental details of the techniques used in this thesis for the fabrication, modification and characterization of the PVA fibers. The procedure for *in vitro* cell compatibility tests will also be included. In Chapter 4, results of the work performed to achieve the objectives of this thesis are presented. These include: optimizing the electrospinning process parameters for fabricating PVA fibers of < 500 nm diameters; the role of fiber diameter and humidity on the mechanical properties of as-spun PVA fibers; the use of a thermal

annealing to improve aqueous stability and enhance mechanical properties of the PVA fibers; the change in crystallinity of the fibers as a function of annealing condition as determined by Fourier transform infrared spectroscopy (FTIR) and X-ray diffraction (XRD); mechanical properties of individual PVA fibers prior to, and following, annealing as determined by an atomic force microscopy (AFM) multi-point bending test; N^+ and He^+ ion beam treatment to modify the mechanical and chemical properties of PVA fibers and their single fiber mechanical properties by AFM; characterization of the ion beam modified fibers using X-ray Photoelectron Spectroscopy (XPS). Finally, results of the study on the response of primary human skin fibroblasts *in-vitro* on the modified PVA fiber scaffold in terms of the biological parameters including cellular attachment, morphology and proliferation as a function of implanted ion species and ion dosage will be presented. A comparison of the effect of fiber orientation on the fibroblasts attachment and orientation is also included. Chapter 5 is a discussion of the results presented in Chapter 4 and their implication and relevance in terms of possible biomedical applications. In the final chapter, Chapter 6, we summarize the work done, identify the main results and present the conclusions. Suggestions for future work will also be included.

Chapter 2 Background and Literature Review

2.1 Electrospinning

In 1934, Formhals invented the electrospinning process [38, 77, 78]. The original experimental setup was developed strictly for production of polymer filaments using electrostatic force. It has since been modified to spin fibers from many kinds of synthetic [79] and natural polymers including proteins [40] and polysaccharides [80, 81]. A standard electrospinning setup consists of a high voltage power supply, a syringe with a metallic needle, a syringe pump, and a metal (or any electrically conductive material) collector, as illustrated in Figure 2.1a. A polymer solution is made by either dissolving one polymer or two polymers [16, 82] in a solvent. The solution is loaded into the syringe and fed through the needle at a controlled flow rate using the syringe pump. At the tip of the needle, the polymer fluid is held by its own surface tension. The polymer fluid passes through several steps before it solidifies while it travels in air and forms fibers on the collector as illustrated in Figure 2.1b; 1) The electric field induces a charge on the surface of the polymer fluid, this forms a repulsive force in direction opposite to the action of the surface tension [83]. 2) There is a threshold value for the electric field to create the repulsive force to overcome cohesion. Below the threshold, the hemispherical surface of the fluid at the tip of the capillary tube elongates to form a conical shape known as the Taylor cone [84]. Above the threshold, a jet of charged polymer fluid is ejected from the tip of the Taylor cone. An electric potential above the threshold value applied to the system changes the diameter of this 'true' tip is one of the process parameters (e.g., tip-to-collector distance and solution feeding rate) to define the size of the polymer fibers. 3) The solvent evaporates when the polymer fluid jet travels through air, the jet undergoes a whipping process [85], and produces a charged polymer fiber, which grounds and lays itself randomly on the collector surface. All fibers and fibrous mats/scaffolds used in this thesis are produced by the electrospinning technique.

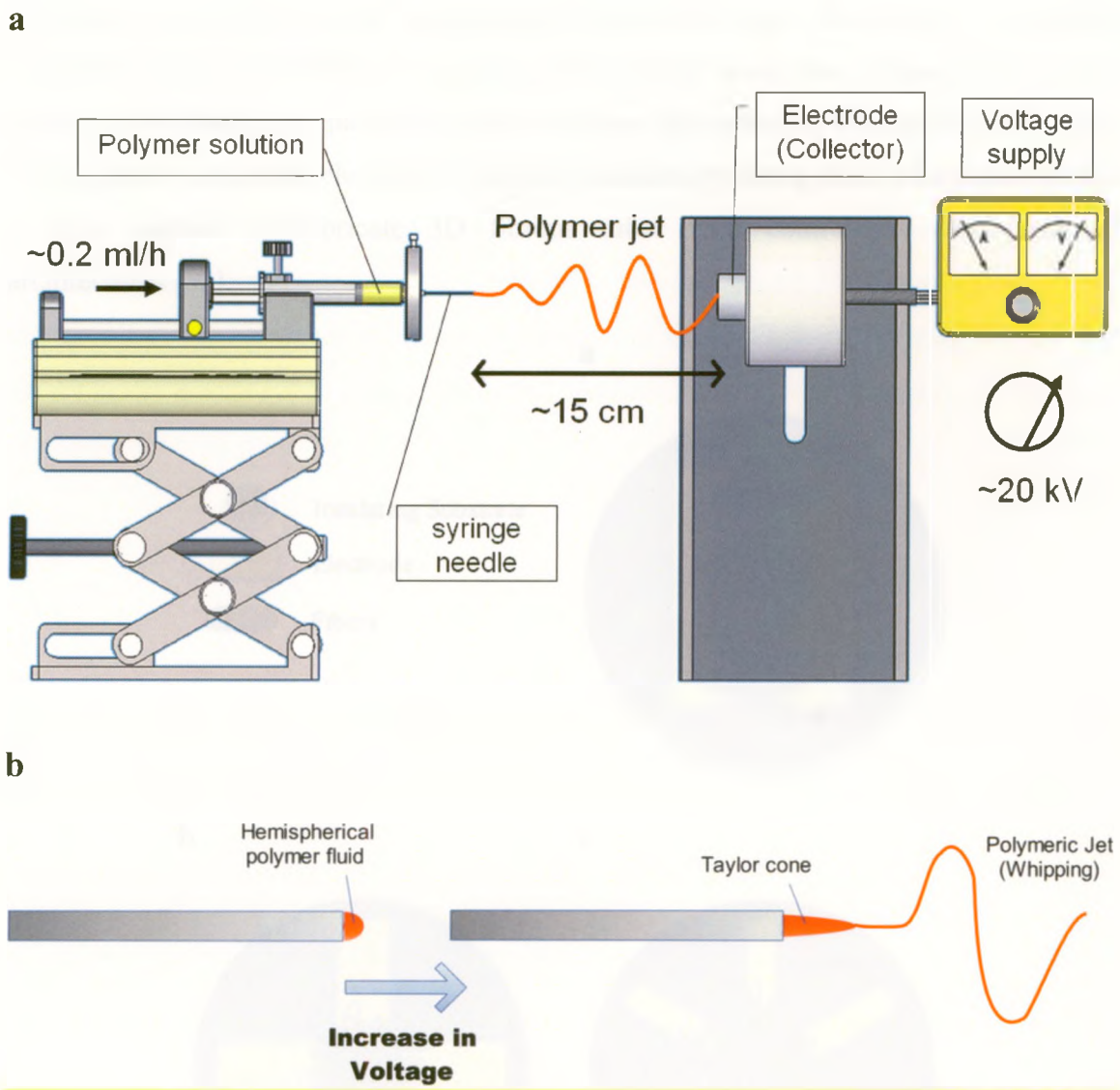

Figure 2.1. (a) Schematic drawing of an electrospinning setup, (b) the process of electrospinning at the tip of a needle.

2.1.1 Design of the Fiber Collector

Generally, a simple stationary collector can only collect electrospun fibers in random orientation. To collect and organize fibers into a fibrous mat with controllable architecture, a number of different approaches are being used by various research groups. Li et al. [47] demonstrated the use of a stationary collector with two parallel conductive strips (electrodes) separated by a void gap. As shown in Figure 2.2a, this method collects

and aligns the fibers into an uniaxial array across the gap. Multi-layers of complex hierarchically aligned fiber mats are also achieved by using four (Figure 2.2b) or six (Figure 2.2c) electrodes, patterned with alternating grounding of the electrodes in pairs. This concept of multiple electrodes is further extended by Zhang et al., who demonstrated a static method to fabricate 3D fibrous tubes with controllable fiber-patterned architectures [48].

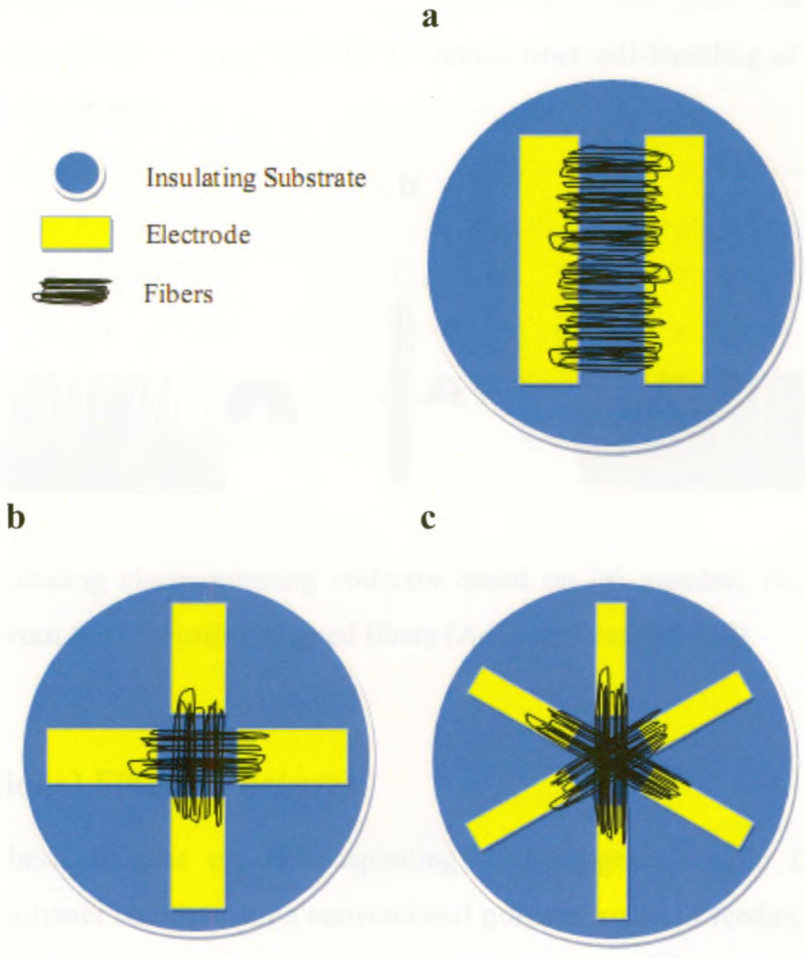

Figure 2.2. Stationary electrospinning collectors based on (a) two parallel, (b) four and (c) six electrodes for fabricating uniaxially aligned fibers (Adapted from [47]).

Instead of using an electrode configuration to control fiber orientation, some basic mechanical approaches are based on a rotating mandrel [86, 87], disk [88] or wire-framed drum [89]. These yield 3D fibrous scaffolds, as shown in Figure 2.3a to c,

respectively. Since this mechanism is based on rolling the continuous fibers together to form a tube, the fiber orientation depends on the rotating speed of the collector. Perfect fiber alignment is rarely achieved due to the instabilities of the polymer jet [85] and the velocity mismatch between the whipping jet and the rotating collector. Alternatively, a fibrous scaffold consisting of aligned continuous fiber yarns (instead of continuous fibers to obtain greater control in fiber alignment) was demonstrated by Wang et al. [90]. Their self-bundling electrospinning method collects continuous fiber yarns using a grounded needle tip in front of the rotating collector to induce fiber self-bundling at the beginning of electrospinning process.

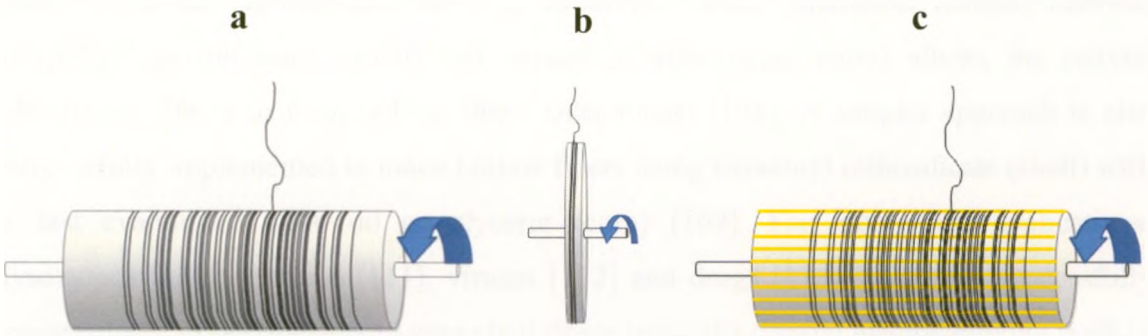

Figure 2.3. Rotating electrospinning collector based on (a) mandrel, (b) disk and (c) wire-framed drum for fabricating aligned fibers (Adapted from [86-89]).

2.1.2 Functional Fiber Structures

This thesis focuses on electrospinning of homogenous solid fibers from a homogenous polymer solution and a conventional polymer solution feeding setup (single syringe/needle), as illustrated in Figure 2.4a. In order to specify the functionality and increase the efficiency of the fibers, a number of different approaches are being implemented by various research groups to fabricate fibers with different structures such as composite fibers, porous fibers, hollow fibers (tubes) and core-shell coaxial fibers using electrospinning. To enhance the mechanical properties of the fiber, bacterial cellulose fibril [91] or carbon nanotubes [56, 92-98] are blended into the polymer solution, as illustrated in Figure 2.4b, to reinforce the polymer matrix. Alternatively, the composite fibers can be filled with metal nanoparticles for wound dressings [99, 100] and

sensors [101, 102]. Some research groups showed that the surface area of the electrospun solid fibers can be increased using a thermally induced phase separation method [103] or a selective dissolution technique [104] to form highly porous fibers. To obtain more complex structures like core-shell coaxial fibers or hollow fibers, some changes in the polymer solution feeding setup are required. Figure 2.4c shows a schematic drawing of a spinneret for coaxial extrusion of two fluids, which is used for coaxial electrospinning [105-107]. For applications such as sensor array, membrane for selective separation and catalysis, hollow fibers are more effective than solid fibers. The spinneret consists of concentric inner and outer tubes where two immiscible fluids are introduced at different rates. Li et al. showed that using a controlled phase separation method between poly(vinyl pyrroli-done) (shell) and tetraethyl orthosilicate (core) allows the coaxial electrospun fibers to form hollow fibers (nanotubes) [108]. A simpler approach is also successfully implemented to make hollow fibers using tetraethyl orthosilicate (shell) with a fast evaporated olive oil or glycerin (core) [109]. For biomedical applications, lysozymes [110], proteins [111], viruses [112] and drugs [113] have been successfully encapsulated in polymer-based core-shell fibers using the coaxial electrospinning method for controlled release. Jayasinghe et al. extend this method to fabricate biologically viable 3D scaffolds by encapsulating living aorta smooth muscle cells in poly(dimethyl siloxane) [114, 115].

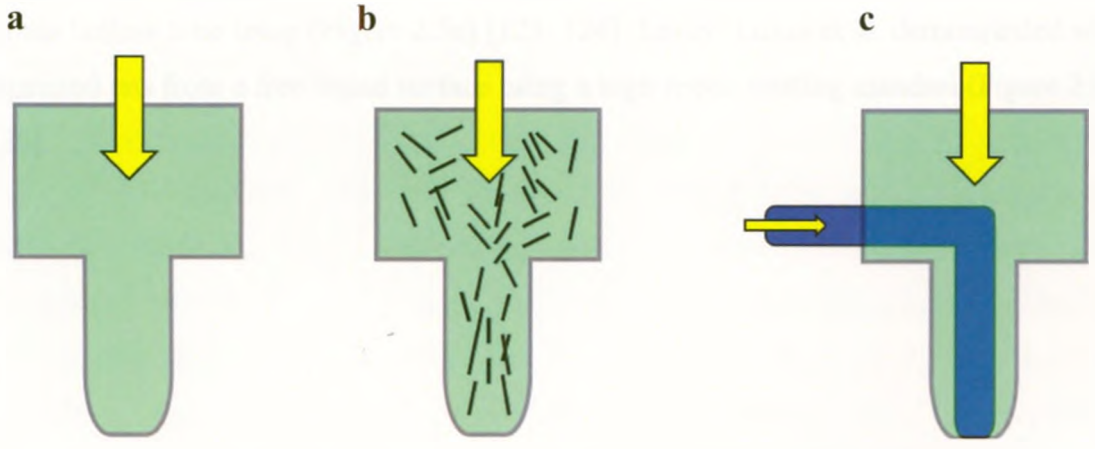

Figure 2.4. Schematic drawing of the polymer solution feeding setup for (a) solid fibers, (b) composite fibers and (c) coaxial electrospinning.

2.1.3 Production Rates of Electrospun Fibers

It is well established that the fiber production rates are very low for the conventional single syringe/needle electrospinning setup (Figure 2.5a). The solution feed rate through the single nozzle setup is typically limited to between 0.1 to 1.0 mL/h. Thus, the amount of fiber mat fabricated per hour cannot be adequate for mass production and commercialization. Therefore, various research groups actively pursue alternative designs to increase the number of nozzles in order to increase the fiber production rate. By packing multiple nozzles in an array, as shown in Figure 2.5b, the fiber production rate can be increased several times. But theoretical studies and experimental observations [116-120] show that the separation distance between the nozzles has a significant effect on the Coulombic interaction and the subsequent spinning path of individual charged jets. There is a minimum inter-nozzle distance in order to obtain fiber mats with reasonable uniformity in fiber diameter and morphology. Different varieties of multi-nozzle system have been successfully tested to increase fiber production rates in electrospinning. Xin et al. demonstrated a needleless electrospinning approach using a cone-shape nozzle made from a copper wire coil (Figure 2.5c) [121]. Liu et al. applied air bubbles from the bottom of the polymer solution reservoir to induce bubble cones on the surface of polymer solution, each cone acts as the equivalent to the Taylor cone from a nozzle in traditional electrospinning (Figure 2.5d) [122]. Reneker et al. obtained multiple jets based on a porous hollow tube setup (Figure 2.5e) [123, 124]. Lastly, Lukas et al. demonstrated self-organized jets from a free liquid surface using a high speed rotating mandrel (Figure 2.5f) [125].

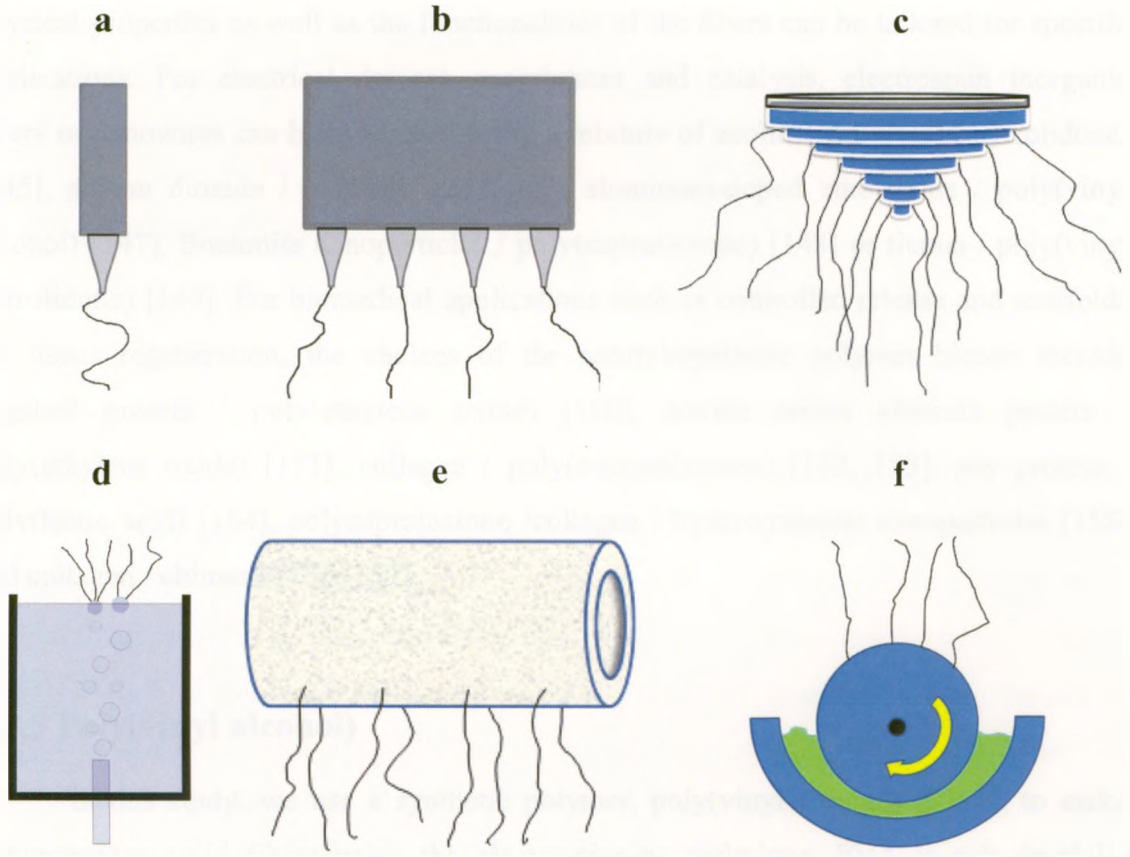

Figure 2.5. Different multi-nozzle designs for multiple jets electrospinning (Adapted from [116, 121, 122, 124, 125]).

2.1.4 Materials for Electrospinning

Electrospinning is a versatile technique, capable of producing fiber mats from a wide range of synthetic polymers. These include poly(*L*-lactic acid) [126], poly(*D,L*-lactic-*co*-glycolic acid) [127, 128], polystyrene [129], polyurethane [43, 130, 131] and polyamide (nylon) [132, 133]. Natural polymers, both proteins and polysaccharides, can also be electrospun. Examples include type I collagen from calf skin [40, 134], type I and type III collagen from human placenta [135], chitosan [80, 136, 137], hyaluronic acid [138, 139], elastin [40], gelatin [40, 140], human tropoelastin [40], dragline silk protein from *N.clavipes* spiders [141] and silk protein from silk fibroin [142-144]. Some research groups favor producing electrospun fibers from a blend of natural/synthetic polymers, or a mixture of inorganic materials/synthetic polymers. As a result, the chemical and

physical properties as well as the functionalities of the fibers can be tailored for specific applications. For electrical devices, membranes and catalysis, electrospun inorganic fibers or nanowires can be fabricated using a mixture of zeolite / poly(vinyl pyrrolidone) [145], silicon dioxide / pluronic 123 [146], aluminum-doped zinc oxide / poly(vinyl alcohol) [147], Boehmite nanoparticles / poly(caprolactone) [148] or titania / poly(vinyl pyrrolidone) [149]. For biomedical applications such as controlled release and scaffolds for tissue regeneration, the choices of the natural/synthetic polymer blends include eggshell protein / poly(ethylene oxide) [150], bovine serum albumin protein / poly(ethylene oxide) [151], collagen / poly(ε-caprolactone) [152, 153], soy protein / poly(lactic acid) [154], polycaprolactone /collagen / hydroxyapatite nanoparticles [155] and collagen / chitosan [156, 157].

2.1.5 Poly(vinyl alcohol)

In this study, we use a synthetic polymer, poly(vinyl alcohol) (PVA), to make homogeneous solid fibers using the electrospinning technique. PVA is a hydrophilic polymer, and can be dissolved in water or other polar solvents such as dimethylsulfoxide and N-methyl-2-pyrrolidone to prepare solutions for electrospinning [158]. PVA has good thermal stability, chemical resistance and biocompatibility [2]. PVA is a non-degradable polymer and has been demonstrated to have long term stability and biocompatibility in physiological environments [1, 159]. Medical devices such as artificial meniscus [1], heart valves [3], cartilage [32, 160] and wound dressings [54] have been successfully manufactured based on PVA. The highly hydrophilic nature of PVA is known to inhibit cell adhesion [5]. Thus PVA is seldom considered as a prime candidate to use where cell population at the surface is necessary such as scaffolds for tissue regeneration. Various research groups have been focusing on improving cell adhesion and the cell on PVA in the form of film, crosslinked hydrogel or nanofiber. These include surface phosphorylation [6]; surface functionalizing using fibronectin [5, 7] or cell-adhesive peptides RGD [8-11]; blending with chitosan [8, 12-14], lipase [15], gelatin [16, 17], starch [18], or carboxymethyl chitin [19]; forming composites with porcine small intestinal submucosa [20]; and surface coating using hydroxyapatite [21],

in order to exploit its favorable biocompatibility characteristics and extend its use in cell contacting applications.

2.2 Mechanical Testing Technique

Polymer fibers have been used for a wide range of applications such as membranes [42], wound dressings [43], scaffolds for tissue regeneration [45] and protective clothing [41]. The overall mechanical properties of these devices are as a function of the mechanical properties of the individual fiber making up the device as well as fiber orientation [152, 161], connectivity between fibers [162, 163] and fiber density [164, 165]. During the service lifetime of a device, the mechanical stress exerted on the device may result in permanent deformation or failure. A conventional uniaxial tensile testing system is the most frequently used technique to characterize the mechanical properties of a device [94, 130, 166-169]. This method provides accurate measurement of the mechanical performance of the device. However, mechanical properties information of single fiber provides essential fundamental information for researchers and engineers to tailor the mechanical properties of a device for a particular application [161, 170, 171]. Furthermore, nano-sized materials differ in the size dependence of their mechanical properties compared to bulk materials [134, 172-175]. In most cases, this size dependent effect is nonlinear and depends on molecular structure. Although the elastic modulus of a bulk material is generally regarded as a constant, many polymers, when shaped into the form of fibers with diameter in the range of < 500 nm, exhibit size dependence with values exceeding the bulk values significantly. These values increase rapidly as the fiber diameter decreases to the nanometer range [176].

There is no suitable commercial mechanical testing system available to perform mechanical measurements on a single fiber with the diameter in nanometer range. The pertinent challenges are: (1) preparation/manipulation of the nanofiber, (2) observation, and (3) sensitivity/resolution of the instrument. Various mechanical characterization techniques based on tensile test, bending test, indention and resonance excitation have been developed to overcome these challenges.

Yu et al. [177], Tan et al. [178, 179] and Zussman et al. [172] showed that the nanoNewton force detection sensitivity of the atomic force microscope and nanoindenter are suitable for performing a tensile test on single nanofibers. One end of a nanofiber is attached tightly to the tip of a cantilever while the other one is fixed onto a substrate, as illustrated in Figure 2.6a. The tensile testing process is driven by moving either the cantilever or the sample stage and the force is measured via the deflection of the cantilever. A full stress-strain curve (including elastic region, plastic region and ultimate tensile strength) of the nanofiber can be obtained. More complex micro-devices such as a nano-stressing stage [180, 181] or a micro-electromechanical system [182] were also developed specifically for single nanofiber tensile testing. Table 2.1 provides a list of different tensile testing methods for various types of nanofibers.

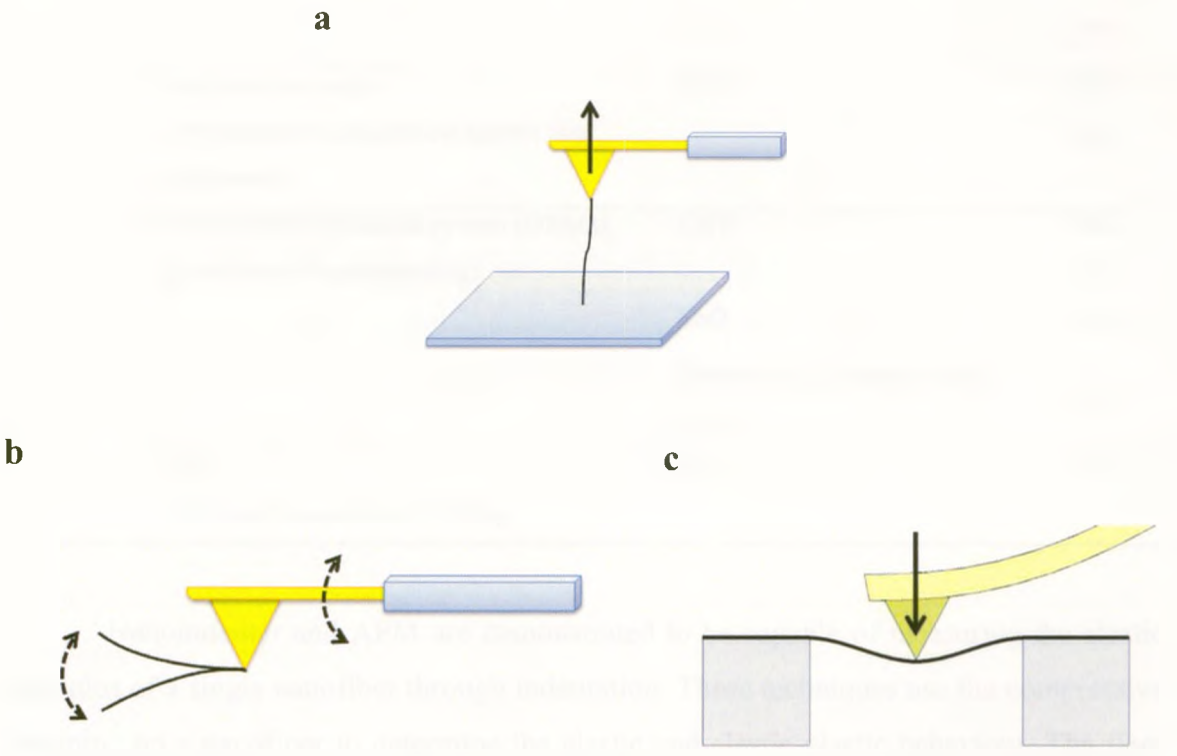

Figure 2.6. Various single nanofiber mechanical characterization techniques based on (a) tensile test, (b) resonance excitation and (c) bending test (Adapted from [183-185]).

Table 2.1. List of tensile testing approaches for various types of nanofibers.

Method	Instruments and technique	Materials	Refs
Tensile test	Nanoindenter (fiber attached to nanoindenter tip)	poly (L-lactic-co-glycolicacid) fiber	[178]
	AFM (fiber attached to AFM tip)	Electrospun Nylon	[186]
		Electrospun Polyacrylonitrile	[172]
		Single Molecules of Type I Collagen	[187]
		Collagen Fibrils	[184]
		Electrospun polyethyleneoxide fiber	[179]
		CNT	[177]
	Nano-stressing stage (fiber attached to and pulled against two cantilevers)	CNT	[180, 181]
	Micro-electromechanical system (MEMS) (in situ unaxial tensile testing)	CNT	[188, 189]
		ZnO	[190]
		Electrospun polyacrylonitrite fiber	[182]
	TEM (electrical induced tensile testing)	CNT	[191]

Nanoindenter and AFM are demonstrated to be capable of measuring the elastic modulus of a single nanofiber through indentation. These techniques use the compressive straining on a nanofiber to determine the elastic and elastic-plastic behaviour. The fiber can be tested by simply lying on a hard and flat substrate with sufficient adhesion in between. For soft polymer nanofibers, Tan et al. [192] summarized a number of issues including the hardness of the underlying substrate, the shape of the probing tip, the fiber surface roughness, the surface curvature of the fiber, the probing direction of the tip and the adhesion force between the fiber and the tip needed to be resolved in order to obtain a

reliable mechanical measurement. Table 2.2 provides a list of nanoindentation-based methods various types of nanofibers.

Table 2.2. List of indentation approaches for various types of nanofibers.

Method	Instruments and technique	Materials	Refs
Nanoindentation	Commercial nanoindenter	Human bone tissue	[193]
	Elastic indention using AFM	Poly(L-lactic acid) fiber	[192]
	AFM-based nanoindentation system (elastic–plastic indention)	Silver nanowire	[194]
		Electrospun polyacrylonitrile/CNT fiber	[195]
		Electrospun *B.mori* silk/poly(ethylene eoxide) fiber	[196]

Resonance response of a nanofiber is another approach developed to determine the elastic modulus. Ding et al. [183] attached one end of a (short) nanofiber to the tip of an AFM cantilever and induced resonance deflection using electrical and mechanical excitation, as illustrated in Figure 2.6b. The resonantly deflected contours of the cantilevered nanofiber at the fundamental frequency and higher harmonics were used to obtain the value of elastic modulus. Cuenot et al. [197, 198] used a similar approach based on the measurement of resonance frequencies of AFM cantilevers in contact with a suspended nanofiber to determine its elastic modulus. This approach can be applied to a nanofiber that is suspended on a grating or porous membrane and requires a minimum sample preparation and manipulation. Table 2.3 shows a list of various resonance excitation approaches for various types of nanofibers.

Table 2.3. List of resonance excitation methods for various types of nanofibers.

Method	Instruments and technique	Materials	Refs
Resonance frequency	AFM cantilever (electrical & mechanical excitation through cantilever)	Boron nanowire	[183]
	TEM (electric-field-induced resonance method)	ZnO nanowire	[199]
	AFM (frequency-dependent viscoelasticity)	Electrospun PVA fiber	[200]
	Micro-fabricated tuning fork (resonance frequency across the two prongs)	Nitrocellulose/toluene sulfonamide formaldehyde resin fiber	[201]
	AFM (resonant contact)	Polypyrrole fiber	[197]
		Silver, lead nanowire	[198]
	TEM (electrically induced deflection / mechanical resonances)	CNT	[202]

Salvetat et al. [203] first demonstrated the use of AFM to conduct bending test on a suspended nanofiber. Figure 2.6c shows a nanofiber suspended over a hole or groove with two ends fixed on a substrate as described by the clamped-beam model [204]. A force applied by an AFM tip mechanically bends the nanofiber and the elastic modulus can be determined from the deflection of the nanofiber. Most of the bending tests conducted in the literature are three-point bending tests which use the nanometer spatial resolution of AFM to locate and perform a bending measurement at the center of the suspended section of the nanofiber. A multi-point bending test based on the same AFM approach was introduced later by Guhados et al. [205] to allow them to confirm the validity of the boundary condition of the clamped-beam model from the collected data and eliminate the need to verify the position along the nanofiber at which the force is applied. All the mechanical tests conducted in this thesis are based on this multi-point

bending test. However, more complex variations of the AFM-based bending test have been developed in the literature; Table 2.4 shows a list of different approaches for various types of nanofibers.

Table 2.4. List of AFM-based bending test approaches for various types of nanofibers.

Method	Instruments and technique	Materials	Refs
Bending test	AFM three-point bending	titanium dioxide fiber	[206]
		Electrospun poly (L-lactic acid) fiber	[207]
		Polypyrrole nanotube	[208]
		SiO_2 nanobeam	[209]
		Si nanobeam	[210-212]
		Poly(2-acrylamido-2-methyl-1-propanesulfonicacid) fiber	[173]
		Cupric oxide nanowire	[213]
		Gold nanowire	[214]
		Electrospun collagen Type I fibers	[134]
		Electrospun Nylon/SiO_2 composite fiber	[175]
		Cellulose fibril	[215-217]
		CNT	[203, 218]
		Poly(3,4-ethylenedioxythiophene) fiber	[219]
	AFM-multi-point bending test on silicon grating	Bacterial cellulose fiber	[205]
		CNT	[220]
		Electrospun Poly(vinyl alcohol)/CNT composite fiber	[95]
	AFM (Lateral displacement of free-end of fiber)	Polyacrylonitrile fiber	[221]
	Buckling of fiber using AFM	SiC nanorod, CNT	[222]
		WS_2 nanotube	[223]

2.3 Polymer Post-Processing Modifications

Materials used in any application have to fulfill property requirements in the specific application environment. Post-processing modifications offer a simple, but effective approach to tailor or optimize some specific physical, chemical and other functional properties of existing materials to fulfill these requirements. Depending on the needs, modification can be effected either in the bulk or on the surface of the material. Post-processing modifications are for example known to be very useful in controlling wear and corrosion resistance, surface roughness, wettability, protein adsorption and cell attachment of metals for orthopedic implants [224-229]. This is also applicable to polymers. In comparison to synthesizing a new polymer, post-processing modifications can significantly fast-track the research and development time to introduce a new and improved polymer product.

2.3.1 Surface Modification

Appropriate surface modifications can be used to generate functional properties on polymeric material surfaces for specific applications. Numerous methods of surface treatment are available [230] including chemical treatment, chemical or physical vapor deposition and sol-gel coating. Ion implantation using a linear accelerator or pulse machines, which can introduce any kind of dopant into any solid material, is a well-established technique in the materials post-processing industry, largely because of its controllability and reproducibility. Ion Implantation can be selectively applied to defined areas and depth of the outermost layers of a sample without affecting the bulk properties. There is virtually no boundary between the modified surface layer and the bulk substrate, thus preventing the surface layer to delaminate from the substrate. However, main drawbacks of this technique are relatively high cost and narrow doping range. Broad-energy (non-monochromatic) ion beam implantation is often used because, relative to monochromatic beam, it provides a wider range of ion doping depths, thus distributing energy over a greater depth range and minimizing thermal damage [67]. In this thesis, we developed a method to convert a monochromatic energy ion beam to a

non-monochromatic one using a metal foil for the purpose of modifying the electrospun fibers with diameter of ~150 nm.

2.3.2 Ion Beam Modification on Polymer

There are two major interactions between the energetic ions and the material during implantation: ionization as target electrons are removed (collisions via electronic stopping) and recoil of target atoms (collision via nuclear stopping). Both these effects occur as the ions penetrate the material and slow down. For polymers, the recoil process leads to chain scission, lowers the average molecular weight [62]. On the other hand, the ionization process leads to the formation of free radicals that allow the chains to crosslink and thereby increase the molecular weight [62]. Depending on the structure of a polymer chain, both processes coexist but usually one dominating over the other [231]. Eventually, the ions reach the end of the implantation path and are stopped; ion-induced chemical modifications at this doping site depend on the reactivity of the ion.

Choosing implantation parameters such as ion species, energy, beam current, dose and incident angle allows us to selectively modify the structure, composition and tribological [62], chemical [63] and physical properties [64] of the surface of a polymeric material. For temperature-sensitive (and also insulating) polymers, the ability to control these implantation parameters becomes very critical as excessive ion/energy deposition near the surface can cause permanent radiation damages to the materials [65, 66], which are undesirable modifications.

2.3.2.1 Simulation of Ion Implantation in Polymers

Stopping and Range of Ions in Matter (SRIM 2008) is a computer simulation software package that includes a program called TRIM (the Transport of Ions in Matter) [232]. It uses a Monte Carlo approach to calculate the stopping and range of ions (up to 2GeV/amu) based on literature data on ion-atom collisions in a broad range of materials. TRIM can handle a complex target material, for example one that includes up to eight layers with different compositions. Based on the composition of the material, it calculates

collision events associated with the ion energy loss. This includes ionization, recoil of target nuclei, sputtering, and target damage.

Ions lose energy and have their direction deflected as they penetrate a material, either through the collision with target nuclei or electrostatic interaction with target electrons. The calculation takes into account one atom or electron interaction at a time; no interference between subsequent collision events is considered. Stopping cross-sections for each element are known allowing us to calculate the total stopping cross section for a compound material using the following equation [233];

$$e_{A+B+.....} = (e_A c_A) + (e_B c_B) + ... \quad [1]$$

e_x is the stopping cross section for each target element and c_x is the concentration of each target element. This formula, known as Bragg's Rule, was first introduced by Bragg and Kleeman in 1905. This rule is a simple estimation with reasonable accuracy and requires the least amount of information. Measured stopping cross sections in a compound usually deviate by less than 20% from Bragg's rule. Bragg's rule becomes inaccurate when we consider the differences between elemental materials and their compounds, as electron orbiting states and excitation alter the amount of energy loss to the same atom in different bonding states. Therefore, corrections are required in the calculations to account for bonding states along the polymer chain to achieve sufficient precision of the ion penetration profile.

For these corrections in compound, ion implantation with known chemical composition and structure, we use the "Core and Bond" approach. By adding the stopping power due to the atomic 'cores' (in superposition) and the bonding electrons, the correction predicts the total stopping power in a compound [234]. First, Bragg's rule is applied to calculate the total core stopping power for each individual atom in the compound. Then the necessary correction is made for the stopping power based on the chemical bonds in the compound. For example, for hydrocarbons the C–C and C=C structures have different bonding energy. This causes the stopping power of a carbon atom in a C=C bond to be more than two times that of a carbon atom in single-bond state. Table 2.5 shows the stopping values of different cores and bonds for common organic polymers. SRIM uses this approach to correct the error made in Bragg's rule to improve

the stopping power of chemical compounds. Especially, any compounds containing the common elements H, C, N, O, F, S and Cl require the correction for the "Core and Bond" effect because these light atoms contribute a large bonding effect to the total stopping power.

Table 2.5. Stopping values of different cores and bonds in the unit of $eV/10^{15}$ atoms/cm^2 for proton at 125 keV [232].

Core	H = 0	C = 6.15	N = 5.86	O = 5.45			
Bond	H-C = 7.22	H-N = 8.24	C-C = 3.94	C-N = 5.08	C-O = 6.17	C=O = 13.93	N-O = 15.80

2.3.2.2 Ion Beam Surface Modification on Physical Properties

For membrane applications, Guenther et al. [63] demonstrated that by introducing chemical modifications via boron ion implantation into polyimide and polyethersulfone matrices, the moisture uptake behavior of both polymer membranes can be controlled, leading to improved filtering efficiency. Similarly, two separate studies demonstrated that by implanting nitrogen or oxygen ion species, the water contact angle of polyethylene can be decreased [235] and increased [236], respectively. Moreover, tribological properties such as the friction coefficient and surface roughness of polyethylene can be modified using helium, argon [64] and nitrogen ion implantation [237]. In the previous section it was already pointed out that the ion-induced crosslinking process can transform two-dimensional linear chains into three-dimensional interconnected networks, thereby changing the mechanical properties of the polymer matrix. This is very useful for polyethylene [70] and polycarbonate [68] as their mechanical properties were successfully optimized for particular mechanical applications using ion implantation.

2.3.2.3 Ion Beam Surface Modification for Bio/Cell-Compatibility

Ion-induced chemical transformations of a polymer surface have a strong influence on protein adsorption and cell adhesion, as demonstrated by Girard-Lauriault et al. [76]. Articular/epiphyseal cartilage cells, growth plate chondrocytes and human macrophages can adhere, spread and proliferate on nitrogen ion treated polyethylene films. Kusakabe et al. [74] showed a similar improvement of endothelial cell adhesion on polytetrafluoroethylene films after neon ion implantation. On the other hand, fluorine ion implantation can be used to reduce cell attachment on polymethylmethacrylate intraocular lens to reduce the long-term failure rate for ophthalmic implants [238]. Besides synthetic polymers, ion implantation has also been used to successfully modify the surface of collagen films to control platelet adhesion and plasma protein adsorption [239]. Several ion-induced mechanisms were proposed to explain these changes of bio-/cell-compatibility of the polymers; surface wettability is frequently suggested as one of the major factors [240-242]. Jagielski et al. [243] provided a list of different ion beam surface implantations on various types of polymeric materials for the control of bio-/cell-compatibility.

2.3.3 Bulk Modification

Among the post-processing modification approaches, thermal annealing is a widely used bulk modification technique for polymers. Ma et al. [244] demonstrated that annealing polysulphone electrospun fiber membranes can increase the crystallinity of the polymer matrix and subsequently increase their mechanical strengths. No significant chemical structural change is reported for the annealing treatment. Similar mechanical property improvements are also observed on poly(L-lactic acid) [245] and poly(ε-caprolactone) [246] fiber mats. Chemical treatment using crosslinking agents such as glutaraldehyde or glyoxal, is another widely used bulk modification technique for polymers [134, 247, 248]. This method modifies the chemical structure to increase the stiffness as well as improve the aqueous stability. But in the case of electrospun fibers mats, the morphological features are largely lost after the treatment.

2.3.4 Post-Processing Modification of PVA

For PVA, the majority of previous reports have focused on modifying its properties employing bulk modification techniques such as annealing and chemical treatments. Its high solubility in water requires the use of radiation [51, 52], chemical agents [49, 50] or freezing-thawing processes [53, 57, 59] to crosslink the polymer chains to impart stability for biomedical applications. Peppas et al. [249] combined electron beam irradiation and annealing to crosslink and crystallize PVA films for mechanical property improvement. In the case of electrospun fibers, Taepaiboon et al. [250] and Wang et al. [15] chemically crosslinked the fiber mats using glutaraldehyde or glyoxal vapor for drug controlled release applications. Kenawy et al. [251] and Yao et al. [55] showed that the aqueous stability of the fibers can be improved by immersing the samples in methanol for up to 1 day. Although, these two approaches have been used to successfully stabilize the fiber mat in aqueous environments, the resultant mats are not suitable for most applications as the fibrous morphology was largely lost during the process. In this study, we will demonstrate some approaches to improve the aqueous stability of PVA fibers without sacrificing the fibrous morphology. Moreover, no previous report was found that examined the possibility of applying ion beam surface modification on electrospun PVA fibers to improve mechanical properties and cell compatibility. This will be the focus of the current study.

2.4 Use of Electrospun Fibrous Scaffolds in Biomedical Applications

When a surface wound is inflicted, the normal body response initiates a series of complex events that include acute inflammation, the formation of granulation tissue, and eventually scar formation [252] to heal the wound. An internal wound created when a medical device is implanted into the body, different response known as the foreign body reaction is triggered which is a function of the chemical, physical and topographical properties as well as the size and shape of the device. This *in-vivo* response may persist for the lifetime of the device and is best assessed as biocompatibility of the device material [1, 159]. For a biocompatible but inert device, our body induces an avascular, collagenous fibrous tissue to produce a fibrous capsule which is typically 50 – 200 μm

thick [253] to insulate the body from the device. This results in minimum degree of integration of the device with the body. For a scaffold used in tissue regeneration, this is clearly undesirable. A scaffold should not induce fibrous capsule formation; it should possess the correct structure, geometry, mechanical properties and compatible with the cell type that is present in the tissue that is being regenerated. Electrospun PVA fibrous scaffold that are thermally annealed can possibly provide the structure, geometry and mechanical properties which mimic that of the extracellular matrix of most soft tissues. The additional criterion of cell compatibility still has to be assessed.

2.4.1 Cell – Substrate Interaction

In this study, primary human skin fibroblasts were used to *in-vitro* assess the cell compatibility of electrospun PVA fibers before and after post-processing modifications. Fibroblasts are migratory and can secrets collagen, fibronectin and growth factors [254]. They are capable of sensing mechanical tension and morphology in the surrounding tissue or the substrate using their filopodia and responding to other cells during migration [255]. The extension of filopodia from the leading edge of fibroblasts is an important indication of cell migration. Fibroblasts join other support cells, chondrocytes, osteoblasts, myofibroblasts and adipocytes, to provide the essential structure of a tissue [256].

For in-vitro studies, a 3D environment is considered to be more realistic than a 2D environment (e.g. cover slips) to mimic the in-vivo condition for cell experiments [257]. Fibroblasts are reported to have a flattened, lamellar morphology and minimum migratory ability on a highly rigid, 2D planar environment [258]. On the other hand, they adopt a bipolar elongated morphology and are able to migrate actively using the extension of filopodia on 3D extracellular matrix [254]. Previous results showed that the degree of tension [259-261], topography [262-266] and stiffness [72, 267-269] of the substrate are important in cellular morphology, signaling and proliferation. For a 3D fiber scaffold, which is stressed to the bottom of a culture dish (e.g. not floating in the culture media) and cell-compatible material such as collagen [266, 270-275], the fibroblasts adopt a biopolar or stellate morphology [259, 260] and undergo proliferation.

Although, *in-vitro* tests are not equal to *in-vivo* tests, *in-vitro* is simpler and generally accepted as a first order approximation in testing for toxicity or compatibility of a material, requiring fewer procedural steps, protocols, guidelines and standards to follow. The *in-vitro* cell culture tests study cell death, cell adhesion, cell morphology, cell proliferation and biosynthetic activity in a more controlled environment than *in-vivo* tests; and may provide useful information on the degree of integration at the interface between a scaffold and the living tissue.

2.4.2 Medical Devices Based on Electrospun Fibrous Scaffolds

Electrospun fibrous mats are particularly attractive for medical applications due to their high surface area and interconnected porous network. Electrospinning has become the method of choice in fabricating 3D scaffolds for tissue regeneration. In addition, the fibrous structure can be electrospun with controlled alignment to mimic the natural extra cellular matrix [47, 48]. To regenerate blood vessels, Xu et al. [45] proposed the use of aligned poly(*L*-lactide-*co*-caprolactone) copolymer fibrous scaffolds and demonstrated the concept using human coronary artery smooth muscle cells. Similarly, Soffer et al. [143] used a natural polymer, *bombyx mori* silk fibroin, to produce fibrous vascular grafts via electrospinning. The grafts showed mechanical characteristics that were well matched to those of the native vessels and supported the culture of human aortic endothelial cells and coronary smooth muscle cells. Electrospun fibrous scaffolds based on synthetic polymers, natural polymers or synthetic / natural blends, have also been successfully studied for regenerating cartilage [276], bone [277-280], bladder [24, 129], skin [54, 128, 142] and neural tissue [25, 153].

Lee et al. [276] showed that the fibroblasts were sensitive, in term of alignment, elongated direction and collagen synthesis, to the fiber alignment and the mechanical strain. These similar fiber alignment effects were also observed in human smooth muscle cells [45, 129] and human Schwann cells [153, 281]. In this study, we will investigate the behavior of fibroblasts in terms of their attachment, morphology and proliferation on both random and aligned PVA fibrous scaffolds to assess their potential for medical device applications.

Chapter 3: Materials and Methods

3.1 Poly(vinyl alcohol)

The material investigated in this thesis is poly(vinyl alcohol) (PVA). PVA is produced by a two step chemical reaction: 1. Polymerization of vinyl acetate monomers into polyvinyl acetate. 2. Hydrolysis of polyvinyl acetate. PVA was purchased from Sigma–Aldrich in powder form with a molecular weight of 89,000 – 98,000 g/mol and 99+ % hydrolyzed. The chemical composition of PVA is $(C_2H_4O)_n$ and its chemical structure is shown in Figure 3.1.

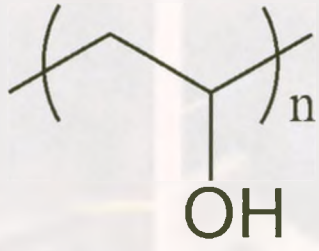

Figure 3.1. Chemical structure of PVA.

3.2 Electrospinning Process

PVA solutions were prepared by dissolving 8.5 – 12 wt% of PVA powder in a solvent consisting of 70 – 90 % de-ionized (DI) water and 30 – 10 % ethanol at 90°C with magnetic stirring for 1 hour. Ethanol is used to lower solution viscosity and increase solvent evaporation rate. The solution was cooled down to room temperature prior to electrospinning. The range of process parameters used in this study were a negative polarity electric field of 10 – 25 kV (Glassman High Voltage Inc.), a working distance between the tip of the syringe needle and the collector of 15 – 25 cm and a solution feed rate of 0.18 – 0.30 mL/h using a syringe pump. (Kd Scientific Inc.).

To collect individual, isolated electrospun fibers for AFM mechanical testing, a transmission electron microscopy (TEM) grid (Structure Probe, Inc.) with a 7.5 μm × 7.5 μm square mesh was used on a silicon substrate and mounted at the center of the collector. For all other studies, non-woven PVA fibers were collected on aluminum foils or silicon wafers.

Randomly orientated fibers were collected using a custom designed stationary collector as shown in Figure 3.2a. To collect fibers with the fibers highly aligned parallel to each other, another custom designed step motor driven rotating collector was used as shown in Figure 3.2b. All aligned-fibrous scaffolds produced in this work were collected with the step motor operated at 32 V and the collector rotating at ~ 6.4 m/s.

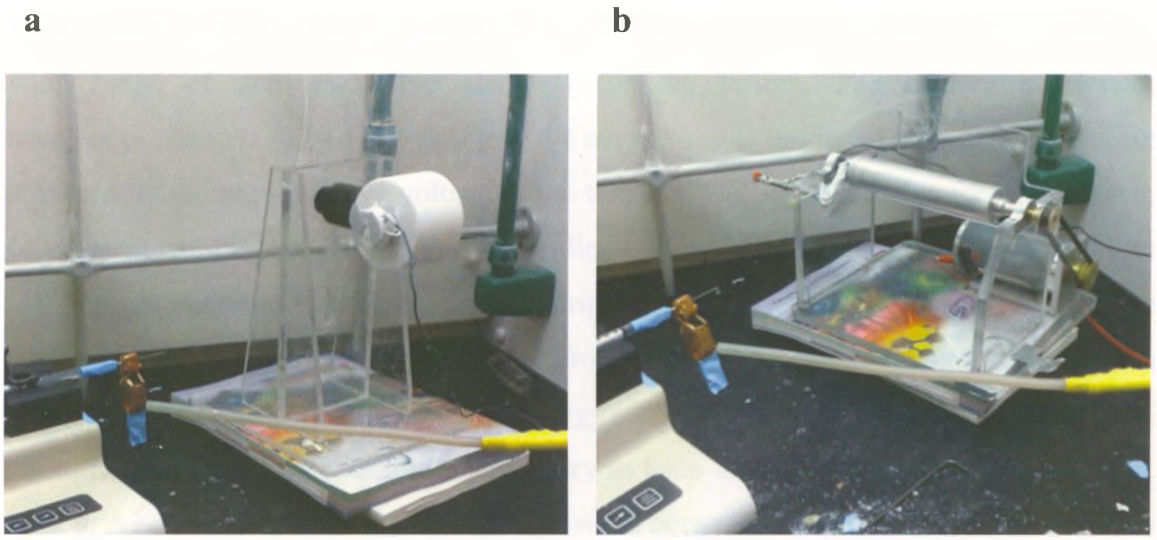

Figure 3.2. The electrospinning setup with (a) a stationary collector and (b) a rotating collector.

3.3 Thermal Annealing

The PVA fibers were annealed in a vacuum oven (10 torr) at six different annealing temperatures: 85, 110, 135, 160, 185 and 210°C. This temperature range is between the glass transition temperature and melting temperature of as-spun PVA fibers determined from DSC (Section 3.7.1 and 4.3.6). The annealing time used was between 30 minutes and 8 hours. The samples remained in the vacuum for an additional 2 hours to cool down before unloading from the oven.

The annealed PVA fibers were immersed in DI water for 1, 10 and 30 days at room temperature. For scanning electron microscopy characterization, the wet samples were immersed into isopropyl alcohol for 5 minutes and then dried in a vacuum (10 torr).

3.4 Ion Beam Implantation

Nitrogen ion (N^+) and helium ion (He^+) beams were generated using the General Ionex 1.7 MV tandetron accelerator at The University of Western Ontario (Figure 3.3). A tandem accelerator provides ion beams capable for both materials analysis and modification. There are two ion sources (duoplasmatron for He^- from He gas and sputter sources for N^- from graphite–boron nitride, shown at the right) capable of generating a wide range of non-radioactive elements for the beams. The tandem accelerator accelerates the ions in two stages. First, the negative ions produced from the sources are attracted by the high positive voltage at the terminal halfway down the accelerator tank. In the terminal, they pass a short section called the stripping canal; the negative ions lose two or more electrons in collisions with a stripping gas (N_2). Then at the second stage, the now positive ions are accelerated away from positive terminal voltage. This tandem effect is very effective to generate high-energy ion beams with energies up to a few MeV. An ultra high vacuum beam line is necessary to keep the beam line free of residual gas. This prevents beam intensity reducing collisions between the ions and the molecules, or the formation of a contamination layer on the sample during the implantation.

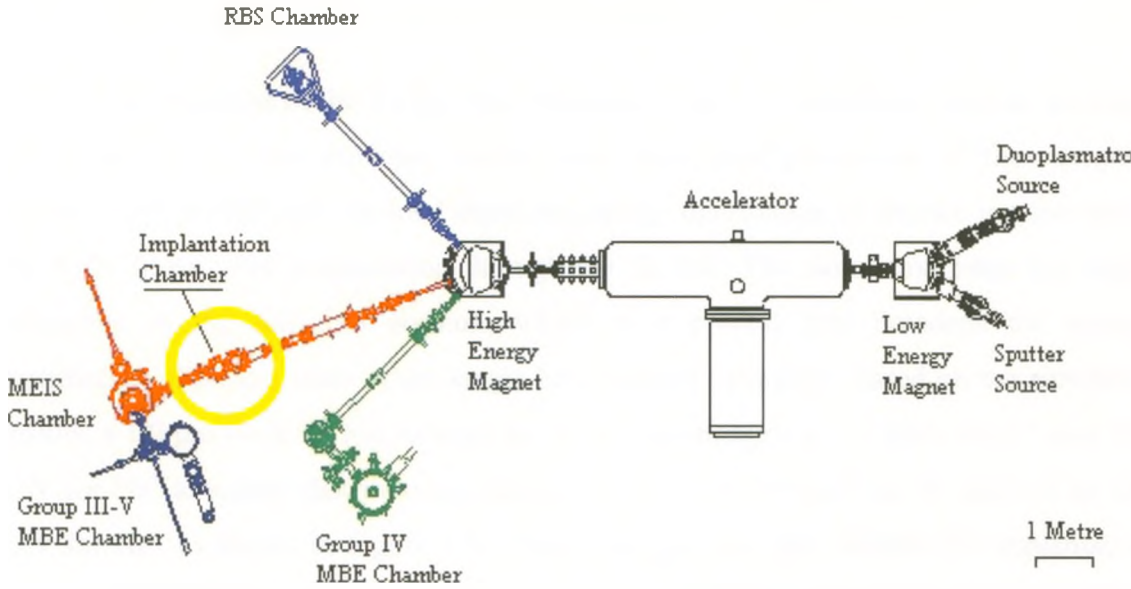

Figure 3.3. Schematic plan view of the Tandetron Accelerator Laboratory at The University of Western Ontario [282]. The sample holder is placed inside the implantation chamber (where the circle indicates) for implantation.

The sample holder arrangement is shown in Figure 3.4. PVA fiber sample was mounted with a 1.0 μm thick tantalum (Ta) foil (Ta, 99.9% purity, Goodfellow Cambridge Ltd.) that was included to slow down the ion beam 2 mm in front of the sample. Ion beam implantation was performed at room temperature in ultra-high vacuum (~10^{-8} torr). The energies of N^+ and He^+ beam from the accelerator were 1.7 MeV and 520 keV, respectively. The beam currents were kept below 300 nA.

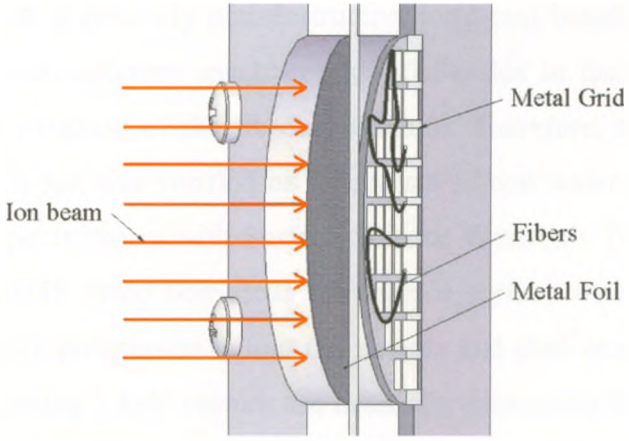

Figure 3.4. Schematic cross-sectional view of the sample holder with Ta foil.

The thickness of the Ta foil was determined with the simulation software package SRIM-2008 [232] that provides, in our case, theoretical projections of the energies, doping depth profiles and the total deposited energy distribution of the two ion species in the PVA fibers after transmission through the Ta foil. The simulation takes ion beam straggling in the foil into account, which is a process that broadens the energy distribution of an ion beam when single ions interact randomly. Based on the simulated results, a 1.0 μm thick Ta foil reduces the initial ion energies of 1.7 MeV for N^+ and 520 keV for He^+ to energy distributions ranging from > 0 to 300 keV for N^+ and > 0 to 100 keV for He^+ ,as shown in Figure 3.5a. These energies are then suitable for implantation into the PVA fibers as they provide us with nearly identical doping depth profiles, ranging from the surface to about 900 nm depth. Figure 3.5b shows the simulated ion implantation depth profiles as histograms with 40 nm bins. The gray circles depict fibers of average diameter 120 nm, and correlate to the ion doping distribution along the axis of

the 5 outmost layers of the fibers. The calculated fractions of the N^+ and He^+ beams that penetrate the foil and are implanted into the fibers (the total doping yield) are 48% and 53%, respectively. However, all ion implantation doses (in ions/cm^2) reported in this work are incident doses to the Ta foil. Accordingly, the total amount of energy deposited into the sample is then calculated as 3.2 times higher for N^+. The thickness of the Ta foil was also confirmed using scanning electron microscope.

The doping depth profile in PVA fiber is difficult to verify experimentally. For example, we cannot use a generally non-destructive ion beam based analysis techniques such as Rutherford backscattering spectroscopy (RBS), due to the decomposability of PVA and the porous structure of the fibrous structure. Therefore, the ion transmission process through the Ta foil was verified on a separate silicon wafer using time-of-flight secondary ion mass spectrometry with Surface Science Western's ToF-SIMS IV system (ION-TOF^{TM}). The SIMS setup bombards the sample surface with a primary 25 keV gallium ion beam to dig progressively into the sample and then analyzes the secondary ions ejected by a sputtering 1 keV cesium ion beam. By measuring the mass/charge ratio of the secondary ions and their time of flight between sample and detector, a depth profile of the elemental composition of the outer layers of the sample is obtained. The total sputtered depth of the silicon wafer was subsequently to the SIMS measurement determined using a Dektak surface profilemeter. Figure 3.6 shows the theoretical (N^+) and experimental (Si+N) depth profiles in silicon (Si) with 1.7 MeV N^+ implanted through the Ta foil. The Si SIMS profile is also shown as a baseline reference. The experimental nitrogen doping depth profiles determined by SIMS shows good agreement with the SRIM simulated profile.

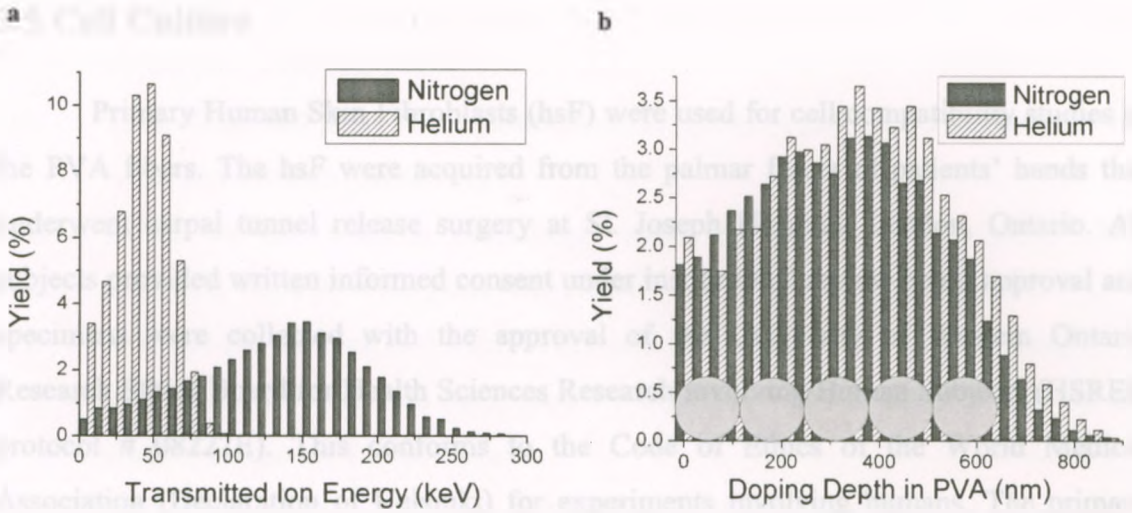

Figure 3.5. (a) Histograms of the nitrogen (with incident energy 1.7 MeV) and helium (with incident energy 520 keV) ion energy transmitted through the Ta foil as simulated by SRIM. (b) The matching ion doping depth profiles (SRIM) in the sample with the gray circles illustrating 5 layers of fibers.

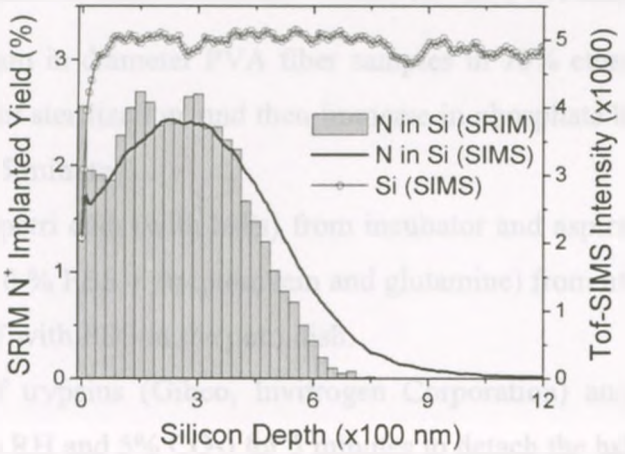

Figure 3.6. Experimental ToF-SIMS and theoretical SRIM depth profile of N^+ implanted into a silicon wafer through a 1.0 μm thick Ta foil.

3.5 Cell Culture

Primary Human Skin Fibroblasts (hsF) were used for cell compatibility studies of the PVA fibers. The hsF were acquired from the palmar fascia of patients' hands that underwent carpal tunnel release surgery at St. Joseph Hospital, London, Ontario. All subjects provided written informed consent under institutional review board approval and specimens were collected with the approval of the University of Western Ontario Research Ethics Board for Health Sciences Research involving Human Subjects (HSREB protocol # 08222E). This conforms to the Code of Ethics of the World Medical Association (Declaration of Helsinki) for experiments involving humans. The primary cultures obtained by Dr. Yan Wu from the clinical specimen were maintained [283] in alpha-minimum essential media (α–MEM) (Gibco, Invitrogen Corporation) with 10% fetal bovine serum (FBS) (Clontech Laboratories, Palo Alto, CA) and antibiotics (Penicillin G + streptomycin sulfate, Gibco, Invitrogen Corporation) until use. All fibroblasts used were passaged less than seven times.

The following procedure is used to seed and culture hsF on PVA samples:

1. Immerse 5 mm in diameter PVA fiber samples in 70% ethanol + 30% water for 30 minutes for sterilization, and then immerse in phosphate buffered saline (PBS) for another 15 minutes.
2. Remove the petri dish (with hsFs) from incubator and aspirate the growth media (α–MEM + 10 % FBS + streptomycin and glutamine) from hsF.
3. Wash the hsF with PBS in the petri dish.
4. Add 3mL of trypsins (Gibco, Invitrogen Corporation) and leave in incubator (37°C, >95% RH and 5% CO_2) for 5 minutes to detach the hsF from the dish.
5. Add 1mL of growth media to deactivate the trypsin.
6. Move solution containing hsF to centrifuge tube and centrifuge (1200 rpm) for 4 minutes.
7. Aspirate the growth media as much as possible without touching the hsF pellicle, and add exactly 1 mL of growth media.
8. Break the pellicle by pipetting the medium up/down until a uniform solution is acquired.

9. Take 20 μL of the growth media/hsF solution and 20 μL of PBS with 0.4% of trypan blue stain into a tube.
10. Take 10 μL and place in the hemocytometer [284] (a grid with 5 squares) for hsF count and average cell density
11. Dilute the hsF solution accordingly using the growth media, place ~3000 cells/well into a 96 wells plate (BD Falon™ non-treated polystyrene).
12. Add an equal amount of 0.1 mL of hsF and media into each well containing 5 mm in diameter PVA sample (as Figure 3.7 shown). , this is equivalent to the cell seeding density of 15,000 cells/cm^2.
13. Place the samples in a 5% CO_2 incubator at 37 °C for culturing.
14. Exchange with fresh culture media every 3 days.

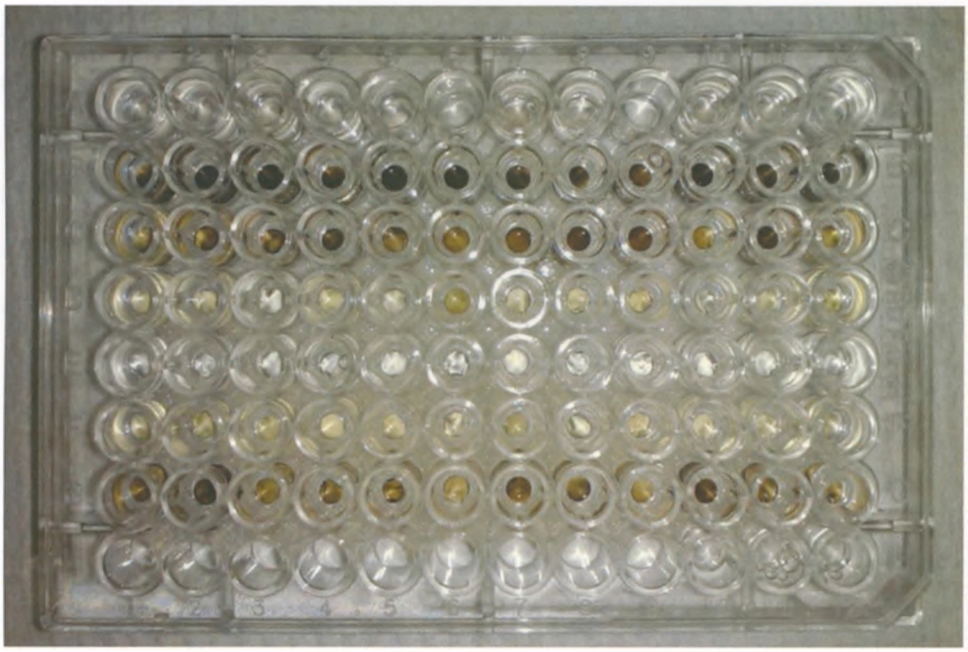

Figure 3.7. Image of a 96-wells plate loaded with 5 mm diameter PVA fibrous scaffolds for *in-vitro* test.

3.6 Atomic Force Microscopy

A multimode atomic force microscope (AFM) with a Nanoscope IIIa controller (Veeco Instruments) was used in this study. High resolution topographical height information of a sample was acquired through contact mode and the elasticity was obtained using the force-volume mode. The AFM consists of a cantilever with a sharp tip that is used to scan the sample surface. Depending on the application, the interactions between the tip and the sample surface include van der Waals forces, capillary forces, chemical bonding, and electrostatic forces. These interactions lead to an initial deflection of the cantilever according to Hooke's law. To monitor the upward and downward movements of the tip, the deflection profile of the cantilever is obtained from a laser beam reflecting off the cantilever and into a photodetector. This approach offers good sensitivity, capable of detecting atomic scaled features. The photodetector monitors the laser beam movement vertically and horizontally. As the tip traces across a sample with features causing it to move upward and downward, the reflection of the laser beam shifts between the upper and lower component of the photodetector, creating voltage differences which are electronically converted into height information. Lateral movements of the beam are used to monitor frictional phenomena on the surface.

3.6.1 Sample Preparation for Mechanical Testing

Mechanical testing of individual PVA fibers was performed in the AFM force-volume mode at room temperature and equilibrium humidity except for the relative humidity which was done under a controlled humidity environment of 32%, and 9% in nitrogen. Force spectroscopy measures force-distance curves, which result from the deflection of the cantilever that is sensed as a function of piezoelectric displacement, as the tip extends toward and retracts from the surface. The slope of the force-distance curve is correlated to the elasticity of the sample. The data is usually acquired along with topographic images, which allow us to compare height and mechanical properties.

Prior to AFM mechanical testing, an optical microscope (Zeiss Axioskop2 Mat Microscope) was used in the dark-field mode to capture 200x magnification images of the mesh areas near the edge of the TEM grid. Figure 3.8 shows an optical image used to identify the precise location of individual fibers and served as a map for the subsequent AFM and SEM measurements before and after various post-processing treatments.

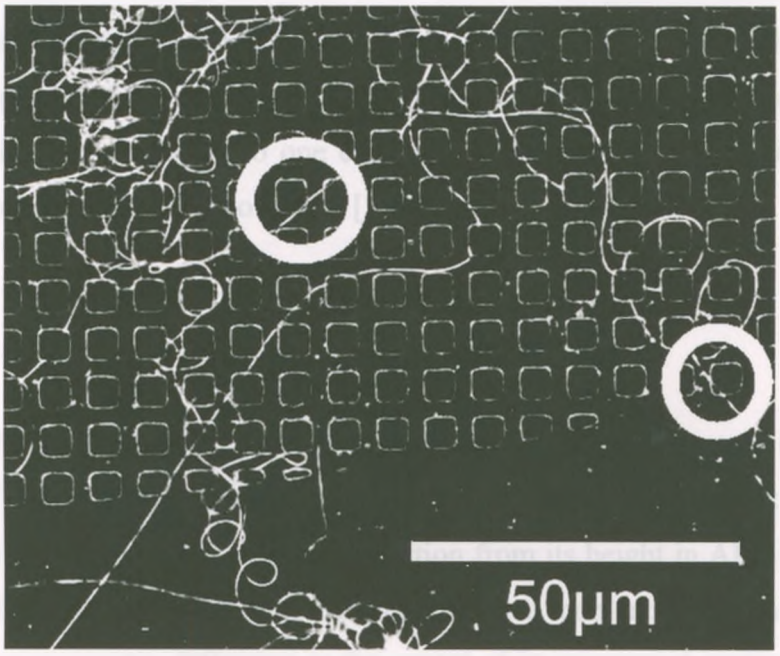

Figure 3.8. Optical image (reflective dark field) of electrospun PVA fibers collected on a TEM grid. The circles indicate suspended fibers suitable for mechanical testing.

3.6.2 Applying Clamped Beam Model to the AFM Data

For a fiber with a suspended length of L clamped to a substrate while a vertical force F is applied at a distance a from one end of the fiber by an AFM tip, as illustrated in Figure 3.9. We use the clamped beam model, which is derived from the Euler-Bernoulli beam theory [204], to analyze the experimental data and determine its elastic modulus. This model is valid when certain boundary conditions are met: the two supported ends of the suspended fiber must remain firmly attached to the substrate with no displacement and rotation throughout the force-volume measurements. Figure 3.10

shows AFM trace and retrace contact mode images of a fiber with suspended length of 8.0 μm. By acquiring a contact-mode image before and after measurements in the force volume mode, the position of the fiber can be verified its ends as properly anchored, which in turn satisfies the boundary condition. The AFM technique measures the deflection of a fiber at the point where the cantilever applies its force. We define this point by the distance to one anchor point of the fiber, *a*. The point of measurement can be any point along the suspended portion as the cantilever scans across the fiber. If we assume a suspended fiber of length *L* and subjected to an AFM tip load *F*, which is applied at a distance *a* relative to one end, then the deflection $\delta(a)$ of the fiber due to tensile deformation is expected to follow [285]:

$$\delta(a) = \frac{F}{3EI}\left[\frac{a(L-a)}{L}\right]^3 \tag{1}$$

where *E* is Young's modulus of the fiber and *I* is its area moment of inertia. (A full derivation of clamped beam model equation is presented in Appendix A) The fiber diameter *D* is measured on the suspended portion from its height in AFM images and its width in SEM images, allowing us to calculate the area moment of inertia as $I = \pi D^4/64$. The fiber has a maximum deflection at the center of its suspended portion, where $\delta(a = L/2) = FL^3/192EI$.

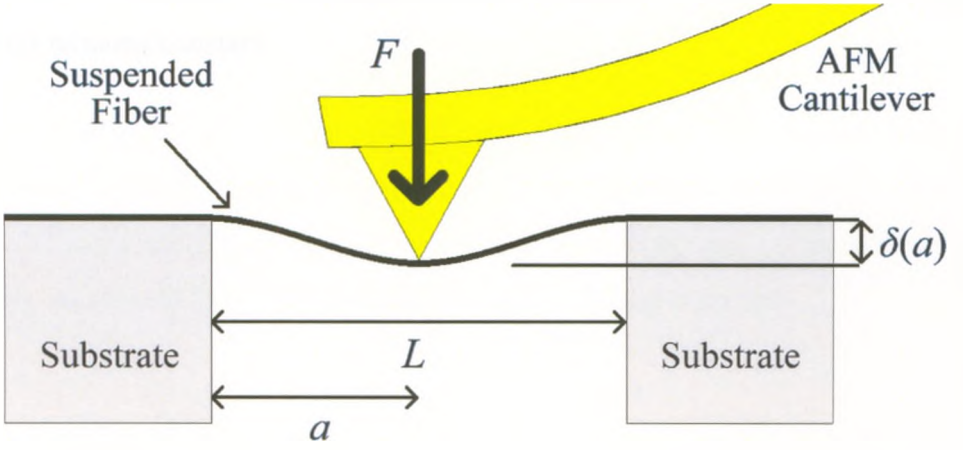

Figure 3.9. Schematic sketch of fiber with a suspended length of *L* clamped to a substrate while a vertical force *F* is applied at a distance *a* from one end of the fiber by an AFM tip.

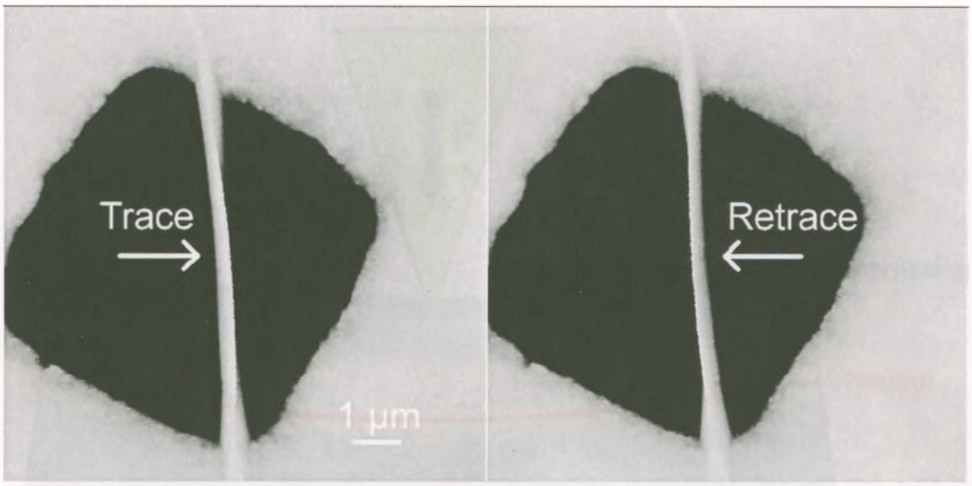

Figure 3.10. AFM trace and retrace contact mode images. We note that the centre of the suspended portion bends toward the tip scanning direction, but the supported portions remain anchored on the substrate.

The clamped beam model we used for PVA fibers is exclusively based on tensile deformation. During bending, the fiber deforms in both tension and compression, as illustrated in Figure 3.11. The inside portion of the fiber, where the force is applied, will undergo compression and shorten, while the outside portion experiences tension and stretch to a greater length. The degree of shortening and stretching is equal at the same but opposite distance from the neutral axis. The neutral axis is the boundary line inside the fiber where no tension or compression force is presented. Therefore, the length of the neutral axis remains constant.

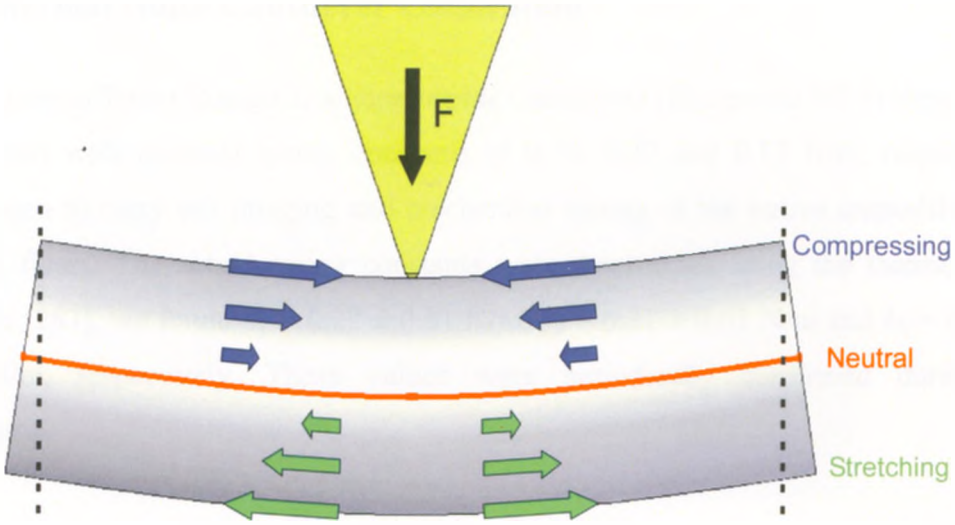

Figure 3.11. Schematic drawing of a fiber that underwent tensile deformation.

The force curve varies with the vertical sample displacement Δz, which in turn is equal to the sum of the cantilever deflection Δy and the fiber deflection $\delta(a)$ at the contact point. The force applied by the AFM cantilever is given by $F = k\Delta y$, where k is the spring constant of the cantilever. The slope of the position along a suspended fiber is predicted (Appendix A) as:

$$\frac{dy}{dz} = \left[1 + \frac{k}{3EI}\left(\frac{a(L-a)}{L} \right)^3 \right]^{-1} \qquad (2)$$

The only unknown variable on the right side of Eq. (2) is Young's modulus of the fiber. E is determined by fitting this equation to the (normalized) slopes measured as a function of position (a) along the fiber using the Igor Pro software package (Wavemetrics) built-in Levenberg-Marquardt [286] non-linear least-squares fitting algorithm.

3.6.3 Thermal Noise Cantilever Calibration

Three different triangular silicon nitride cantilevers (Sharpened NP Probes, Veeco Instruments) with nominal spring constants of 0.58, 0.32 and 0.12 N/m, respectively, were chosen to carry out imaging and mechanical testing of the native unmodified and modified fibers. The actual spring constants were determined using the thermal noise technique [287], we found $k_1 = 0.27 \pm 0.01$ N/m, $k_2 = 0.21 \pm 0.01$ N/m and $k_3 = 0.097 \pm 0.002$ N/m, respectively. These values were periodically confirmed during the experiments.

3.6.4 Mechanical Measurement and Elastic Modulus Determination

Mechanical testing is performed in the AFM force-volume mode, as described previously [205]. A force (F) is applied to the sample as the sample is moved upward against the AFM tip (stopping at a pre-set trigger threshold). The resulting force spectrum (i.e., the recorded deflection of the AFM cantilever (Δy) as a function of the sample's vertical displacement (Δz)) is acquired for positions in an array of 64 x 64 pixels (spanning square regions of width 3.5 – 6.0 μm). Another topographical image of 64 x 64 pixel resolution is acquired simultaneously by recording the piezo height required to achieve the trigger threshold. The vertical ramp size and trigger threshold were set for the two cantilevers between 300 – 600 nm and 50 – 200 nm, respectively.

A representative example for AFM mechanical testing of a PVA fiber is shown in the SEM image of Figure 3.12. All fibers were studied in the same orientation as shown in Figure 3.12, i.e., aligned at approximately 45° to the scanning direction of the AFM tip. The diameter D of the fiber was determined from a SEM image on the suspended portion of the fiber. We averaged the diameter of 10 locations along the fiber axis. For the fiber shown, the average diameter was 114 ± 4 nm with the standard derivation due the diameter irregularity of the electrospun fiber.

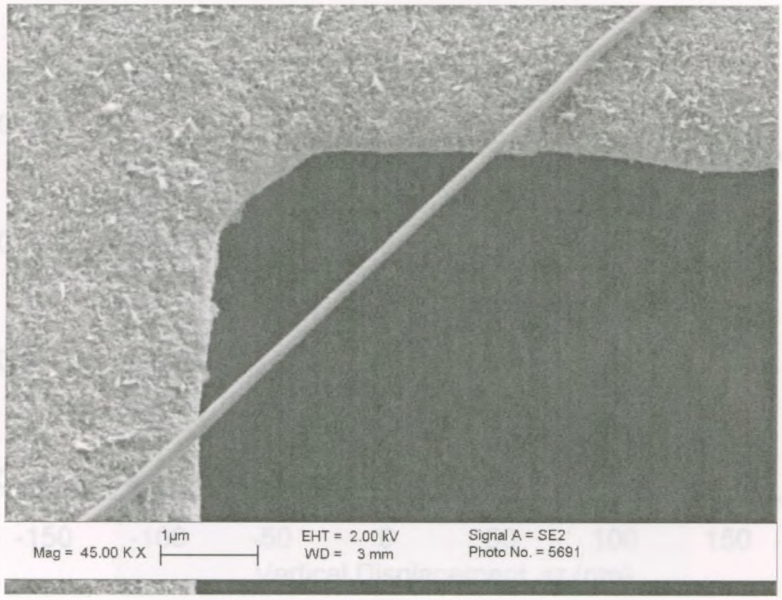

Figure 3.12. SEM image of a representative example for AFM mechanical testing of a PVA fiber suspended across a corner of a TEM grid hole.

Data was extracted from the force-volume images and analyzed using the Igor Pro software package (Wavemetrics) with a custom analysis routine. Slopes of the individual force spectra can be divided in two groups, as illustrated in Figure 3.13. The majority of data are obtained on the rigid surface of the TEM grid, for which the cantilever deflection is expected to equal the sample displacement (i.e., $\Delta z = \Delta y$) after contact is made; this is also valid for data obtained on the portions of the fiber supported by the rigid TEM grid, because compressive deformation of the fiber due to the maximum force applied by the AFM tip is expected to be less than one third of a nanometer. The theoretical slope of the force curve for all such positions is then $dy/dz = 1$, which can be used to calibrate the sensitivity of the cantilever deflection signal Δy as follows. A histogram of the slopes is plotted, and the deflection signals are normalized to the mean value of the peak corresponding to the majority of the data in the histogram. Then data obtained on the suspended portion of a fiber display a linear curve with $\Delta z = \Delta y + \delta$, with $\Delta z > \Delta y$ after contact because of the fiber deformation δ. The force curve in the contact regime thus displays a slope $dy/dz < 1$. Therefore, the deflection of the fiber can be measured by comparing the difference between the approach force curve obtained on the bare TEM grid (or supported portions of a fiber) to those obtained on the suspended fiber.

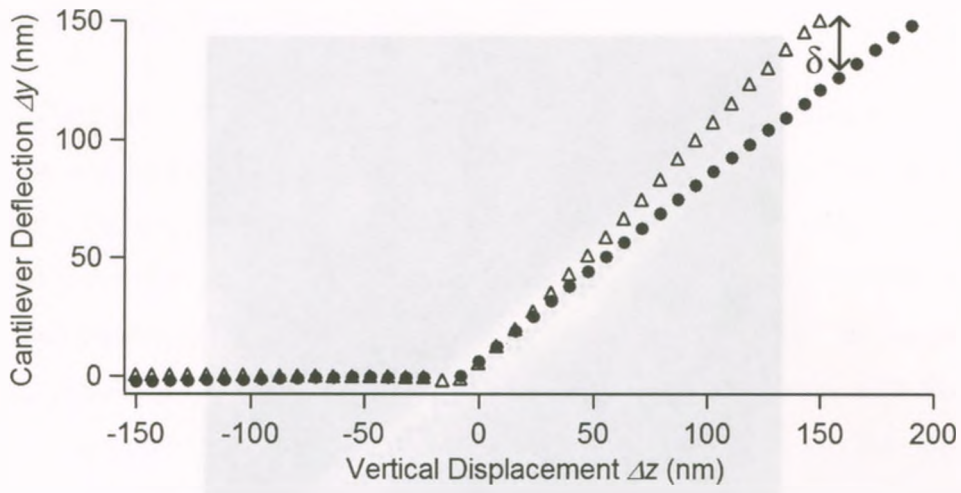

Figure 3.13. Approach force spectra obtained on the bare grid (hollow triangles) and near-center of a suspended fiber (solid circles). The shallower slope for the suspended fiber allows its mechanical strength to be measured.

The elastic modulus was determined from fits to the data of typically more than 60 force spectra chosen from suspended and supported sections along the fiber in a given force-volume image. To select the data points, a topographic image was used to identify the midline of the fiber, as illustrated in Figure 3.14 with 92 data points (this image shows the same fiber as Figure 3.12). Generally 2 points were selected close to the midline along every row of pixels crossing the suspended portion of the fiber. Only 1 point was selected on the supported portion, as these points do not enter into the curve-fit and are only used to validate the calibration of the deflection sensitivity. Note that for positions at a significant offset from the midline of the supported portion, the applied force is no longer perpendicular to the surface due to the curvature of the fiber. Force spectra taken under these circumstances are distorted depending on which side of the fiber the tip probed.

The slopes of the chosen force spectra and the relative fiber deflections were plotted as a function of position *a* from one end of the fiber in Figure 3.15. The solid line in the figure is a fit to Eq. (2). The agreement between experimental data and the derived

curve for the clamped beam model provides confidence that the experimental AFM multi-point mechanical test data validates the model.

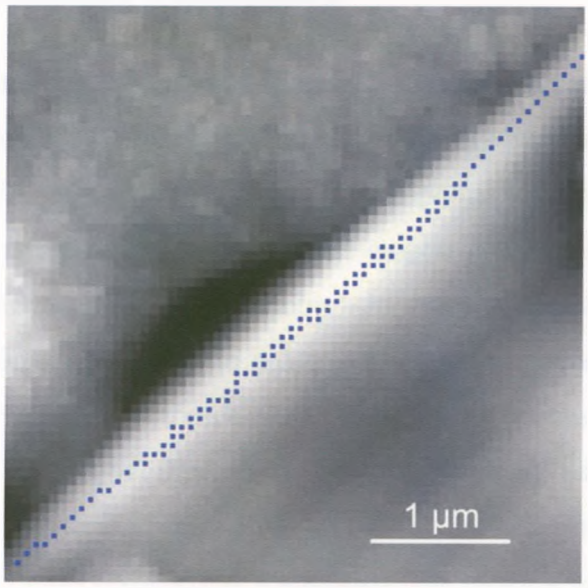

Figure 3.14. A topographical image from the AFM force-volume measurement with 92 data points chosen along the fiber.

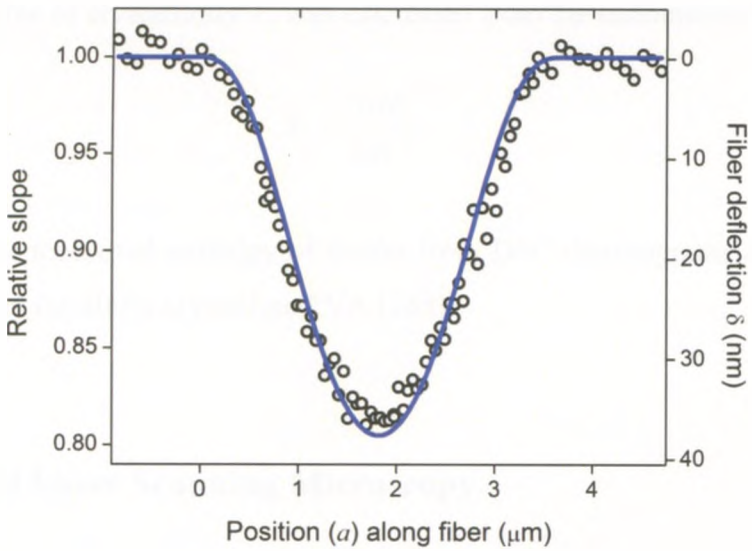

Figure 3.15. Plot of the slopes of force spectra (hollow circles) as a function of position a along a suspended fiber of length $L = 3.7$ μm. The best fit using the clamped beam model is shown as a solid curve.

3.7 Characterization Techniques

3.7.1 Differential Scanning Calorimetry

Differential scanning calorimetry (DSC) is a common technique to study the thermal properties of a polymer. In the instrument, there are two pans that are heated by two separate heaters. To perform a measurement, one pan is loaded with the sample and the second pan which is the reference pan, is left empty. A computer is programmed to heat the two pans at the same rate (°C / minute). In order to heat the sample pan at the same rate, extra heat flow is required to achieve the same temperature as a function of time when compared to the reference pan. Thermal properties of the sample are determined from the differential heat flow between the two pans as a function of temperature. Typical properties measured by DSC include melting (endothermic transition) and crystallization (exothermic transition). The melting temperature of as-spun PVA fibers was determined using DSC (Perkin Elmar Pyris 1) between 50°C and 250°C at a heating rate of 10°C per minute. The DSC thermograms were analyzed using Thermal Analysis Instrument Control and Data Analysis Software V. 3.01 Rev. A (Perkin Elmer). The degree of crystallinity X_c was calculated from the endothermic area from:

$$X_c = \frac{\Delta H_f}{\Delta H^o_f} \qquad [3]$$

Where ΔH_f is the measured enthalpy of fusion from DSC thermograms and ΔH^O_f is the enthalpy of fusion for 100% crystalline PVA [288].

3.7.2 Confocal Laser Scanning Microscopy

Confocal laser scanning microscope (CLSM) can obtain a high resolution 2D fluorescent image slices of biological objects labeled with fluorescent markers by using point illumination to scan the specimen one point at a time and a pinhole to detect the

light emitted from the focal plane. By reconstructing a series of 2D image slices at different focal planes, CLSM is particularly useful for 3D visualization.

To image the hsF with a CLSM, fluorescent markers are used to label specific molecules (protein or nucleic acid) of the hsF, so that those molecules with the markers are excited and emit photons at a lower energy for detection. For hsF, Alexa Fluor 488 Phalloidin (Alexa 488) (M_W=1320, absorption max = 495nm, emission max = 519, Invitrogen) was used to stain the F-actin (fluoresced in green) and 4',6-diamidino-2-phenylindole (DAPI) (M_W=350, absorption max = 358 nm, emission max = 461, Molecular Probes) to stain for the cell nucleus (fluoresced in blue).

The fluorescence images of hsF were obtained using a Zeiss LSM 510 multichannel point scanning confocal microscope (Carl Zeiss MicroImaging Inc.). An argon-ion laser with excitation line of 488 nm and a diode laser with excitation line of 405 nm were the sources used to excite Alexa 488 and DAPI, respectively.

To apply the two fluorescent labels (staining) to the hsF in contact with the PVA samples for confocal microscopic imaging, the following procedure was used:

1. Aspirate the growth media (from the wells with PVA fiber samples + hsF after *n* days of culturing) and wash twice with PBS on a shaker for 5 min.
2. Fix the hsF by storing them in 4 wt% of paraformaldehyde (reagent grade, $(CH_2O)_n$, Fisher Scientific) in PBS (0.1 mL/well) for 45 minutes.
3. Wash the samples twice with PBS (10 minutes each).
4. Wash the samples twice with 0.1wt% Triton X-100 (Sigma) in PBS to permeabilize the hsF membranes for fluorescent stain.
5. Wash twice with 0.1wt% Tween®20 (M_W=1228, Calbiochem) in PBS.
6. Wash the samples using PBS solution with 3 wt% bovine serum albumin (BSA) (Fraction V, purity > 96%, Bioshop) + 0.1 wt% Tween + 5 wt% slim milk powder (30 minutes each).
7. Add 0.125 wt% of Alexa 488 into PBS solution with Tween, BSA and slim milk powder, use this to wash the samples for 20 minutes under aluminum foil.
8. Wash 3 times with Tween + PBS (10 minutes each).

9. Wash the samples twice using PBS solution with Tween + BSA + slim milk powder (10 minutes each).
10. Add 0.1 wt% of DAPI into PBS solution with Tween, BSA and slim milk powder, use this to wash the samples for 20 minutes under aluminum foil.
11. Wash 4 times with Tween + PBS (10 minutes each)
12. Mount the wet samples with 1 drop of mounting media (Dako Cytomation, Fluorescent Mounting Medium) on microscope glass slide and seal with a 1μm thick cover glass prior to confocal imaging.

3.7.3 Infrared Spectroscopy

Infrared (IR) spectroscopy can be used to identify functional groups in organic compounds, based on the unique rotations and vibrations at discrete energy levels of a molecule. Incident IR radiation can only be absorbed at the energy levels of the oscillating molecular groups, which is associated with changes in the dipole moment. In order to have rotational and vibrational modes to be IR active, the molecule must be asymmetric with changes in dipole moment, such as water and carbon dioxide molecules. A symmetric O_2 or N_2 molecule has no dipole moment, so it is IR inactive.

The simple hydrocarbon (CH_2) group can vibrate in six different ways: symmetrical and anti-symmetrical stretching, scissoring, rocking, wagging and twisting, as illustrated in Figure 3.16. Stretching a bond length requires higher energy than changing the bond angle; thus all six vibrational modes will be IR active at different frequencies. Each type of vibration within the molecule has its own unique infrared absorption cross-section (this is also true for the molecule itself), i.e., not all vibration modes have equally strong peaks in the spectrum.

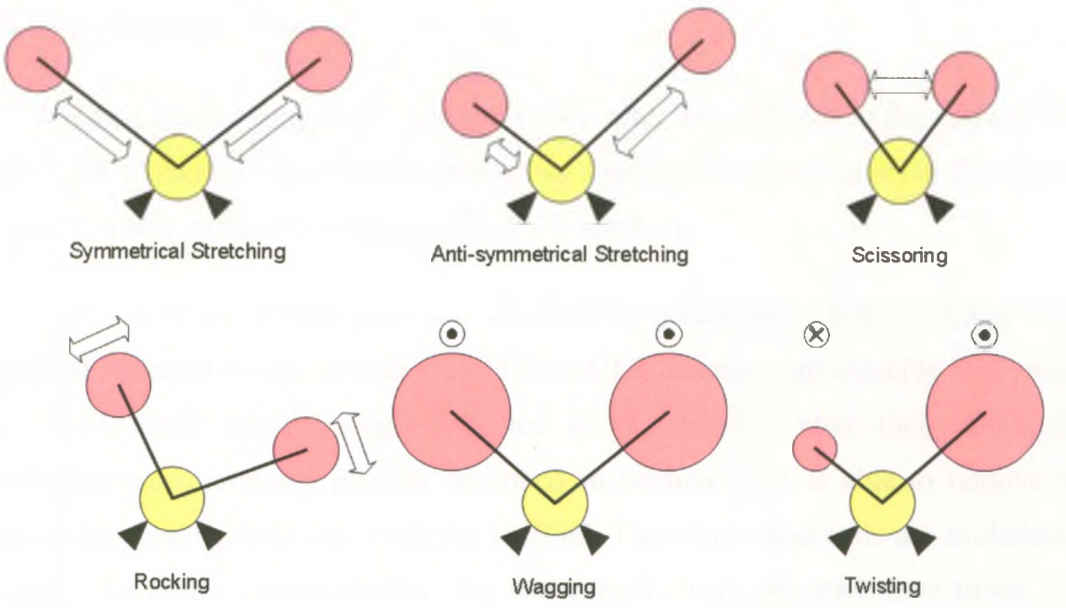

Figure 3.16. Six different vibrational modes for a hydrocarbon molecule.

IR spectra can also be used to qualitatively detect the existence of crystalline regions of polymeric materials. Some bands, which are associated with specific vibrational modes of the molecules in the polymer chain, can be sensitive to inter-molecular and intra-molecular order. For PVA, the intensity of the 1141 cm^{-1} band, which is associated with the symmetric C—C stretching mode, has been shown to be sensitive to the degree of the crystallinity [61, 289]. On the other hand, the intensity and shape of the 1425 cm^{-1} band, characteristic of —CH_2— bonds and the 1093 cm^{-1} band, characteristic of —CO— bonds, remain unchanged as a function of crystallinity.

Attenuated total reflectance - Fourier transform infrared spectroscopy (ATR FTIR) was used to qualitatively verify the increase in the degree of crystallinity of the PVA sample upon heat treatment. In the present experiments, we used an FTIR spectrometer (Bruker Vector 22; Milton, ON) with a horizontal attenuated total reflectance attachment and a diamond crystal. The chamber was continuously purged with dry air to minimize water vapor and carbon dioxide interference. A background spectrum was collected prior to that of the PVA fiber samples.

3.7.4 Proliferation Assay

To examine the long term response of hsF after they adhered to the surface of to modified PVA fibers *in vitro*, we conducted two approaches to determine the hsF growth rate after 1, 4 and 10 days of culture on the PVA scaffolds.

The rate of hsF proliferation was analyzed by performing a hsF cell count based on the DAPI-stained nuclei on each sample from CLSM images, an example is shown in Figure 3.17. Cells are no longer attached to the scaffold after their death; the washing/fluorescent staining process described in Section 3.7.2 is able to remove the detached and floating dead cell from the scaffold. Therefore, dead cells are excluded in the image. To assess reproducibility, the experiments were repeated three times with different electrospun/modified batches of fiber scaffolds. Six images were captured at six different regions of each sample with a total culturing area of 3.62 mm^2. The number of hsF was counted using the image processing program, ImageJ (National Institutes of Health).

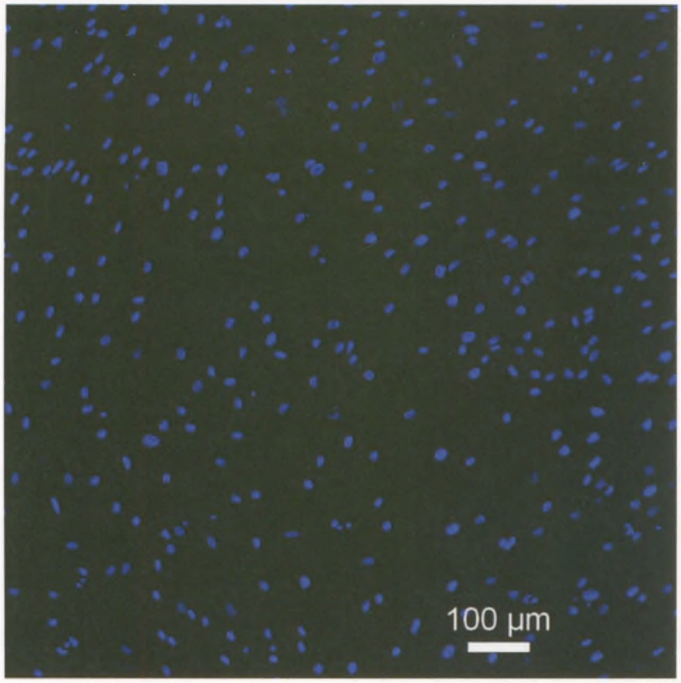

Figure 3.17. CLSM image of hsF nuclei after 4 days of culture for cell counting to determine the rate of proliferation on an ion beam treated PVA fiber scaffold.

3.7.5 Scanning Electron Microscopy

The Scanning Electron Microscope (SEM) is primarily used to study surface morphology. Higher magnification and depth resolution are achieved by shorter wavelength of the incident particles. To obtain high resolution, electron energies in the range of 1 keV to 30 keV are normally used to achieve ~5nm resolution.

As the primary e^- beam probes along the material surface, the interaction between the beam and the specimen causes a range of characteristic phenomena, such as elastic scattering (backscattered electron) or inelastic scattering (secondary electron, electron beam and orbiting (or weakly bonded) electron interaction, ejection of the new electrons). These phenomena allow us to obtain different information of the specimen. To do topographical imaging, only secondary e^- formed in multiple inelastic scattering processes with kinetic energies lower than 50 eV are used. After secondary e^- are detected in their current as a function of the probe position, the microscope image consists of a plot of the current against the probe position on the surface. The yield of secondary e^- is independent of the atomic number; i.e., every element is displayed on the image with equal intensity. Several other processes may change the intensity in a micrograph, but the major variations are from surface topography. Because of the very small primary e^- beam spot (1~10 nm for field-emission SEM), SEM images can have large depth of field, which allows us to observe more features at slightly different depth of focus at the same time and increases the sharpness of the image. Overall, the SEM image is a direct image of the real surface structures (assuming an ideally conductive surface).

The dimension and morphology of the fibers for all studies, including AFM mechanical measurements, were determined from SEM topological images, which were obtained with a Leo 1530 or Leo 1540XB (LEO Electron Microscopy Ltd) at 1 – 2 kV. ImageJ was used to analyze the SEM images to determine the dimension of the fibers. No conductive coating was applied to most of the samples except fibroblasts cultured samples.

For fibroblasts cultured samples, we first washed the samples twice with PBS for 10 minutes each to remove growth media and any unattached hsF. They were then fixed using 4 wt% paraformaldehyde in PBS for 2 hours. Subsequently, the samples were dehydrated in an ascending series of graded ethyl alcohols (70, 80, 90 and 100%) for 15 minutes each. The drying process for the samples was completed with a critical point dryer (EMS-850, Electron Microscopy Science). Prior to the SEM observation, a Denton Desk II was used to sputter-coat (15 mA for 100 seconds) the sample with a conductive gold–palladium layer.

3.7.6 X-ray Photoelectron Spectroscopy

X-ray photoelectron spectroscopy (XPS) is a highly sensitive surface analysis technique to determine the elemental composition, chemical stoichiometry, chemical state and electronic state of the elements that exist at a sample surface. XPS uses low energy X-ray photons to penetrate the surface and excite the core electron of each individual atom in the sample. The excited electron experiences inelastic or elastic collision on its way out through the surface. The kinetic energy of an electron that escaped from the surface is equal to the difference between the incident photon's energy ($h\nu$) and the binding energy of the electron in the atom (including a correction for the work function of the electron energy analyzer). The kinetic energy of electrons released at greater depth is further reduced by inelastic collision events that occur along the escape path for the electron, limiting the analysis to electrons of maximum kinetic energy. This is the reason that the analysis depth of XPS is limited to 1 – 10 nm from the surface.

Two different resolutions of spectra are generally collected with the XPS technique. First, a survey spectrum scans and reveals the elemental composition of the surface. The number of electron is independent on the chemical state, each electron detected at a particular kinetic energy represents one specific element present at the sample surface; the number of electrons can be used to quantify each element. XPS is not able to detect hydrogen because it has "no" binding electron. The high-resolution spectrum with no more than 15 eV energy range at each element found in the survey

spectrum can also be collected for detailed chemical bonding characterization. Every orbiting electron in an atom is sensitive to the chemical environment of the atom; the binding energy shift is dependent on the chemical state and the molecular structure. The hydrocarbon bond in C_{1s} (Carbon 1s core-level state) spectrum has a 285.0 eV binding energy and is often used as a reference energy number. A shift occurs if a carbon atom binds with different atoms or in a different chemical state. For example; C–N → 286.0 eV, C–O–C → 286.5 eV and C=O → 288.0 eV. This shift occurs similarily for all other elements, thus a detailed peak analysis can be used to calculate the respective ratio of occurrence of different chemical groups. Unfortunately some binding energy shifts for similar molecular structures are very close, for example: C–O and C–N are at 286.5 and 286.0 eV, respectively. No practical method in XPS exists to precisely distinguish the two signals in cases like this. Other analysis techniques, e.g. FTIR, are needed to identify the presence of these two chemical functionalities.

The XPS system from Kratos Axis Ultra with a 210 W Al-K_α monochromatic source was used to analyze chemical modifications resulting from the ion beam treatment of the fibers. It features a magnetic immersion lens and a charge neutralization system with a Spherical Mirror Analyzer. Any electrically non-conductive sample can be analyzed using the charge neutralization system. The Spherical Mirror Analyzer uses a full range of pass energies to give chemical state and elemental imaging. The combination of the magnetic lens and selected area apertures is capable to provide an exceptionally small X-ray beam spot (< 15 μm) Using the advanced zoom optics gives a clear view for the identification of any microscopic features on the sample surface. For this study, the pass energy of the survey scan was 160 eV and the high-resolution scan was 20 eV. The program CasaXPS (Casa Software Ltd.) was used to construct and curve-fit multiple peaks for the data envelop that appeared in the core-level energy spectra based on the CasaXPS built-in Marquardt-Levenberg [290] optimization algorithm.

3.7.7 X–ray Diffraction

X–ray diffraction (XRD) is used to determine the inter-atomic spacing of the repetitive atomic structures in a crystalline or semi-crystalline solid. The X–ray diffraction pattern is produced by constructive interference of scattered X–rays from a crystalline structure. By using Bragg's Law in the form: $\lambda = 2d \sin\theta$, the distance between similar atomic planes, d, can be determined by the angle of diffraction, θ.

XRD spectra were collected using a Rigaku – Rotaflex RU–200BH diffractometer with a Co-K_α radiation (wavelength λ = 1.79 Å) source operating at 30 kV and 44 mA. The 2θ spectra were scanned from 16.0° to 32.0° with a 0.1° step size. The diffraction peaks were analyzed by fitting Pearson VII function [291] as:

$$y = y_o \left[1 + \frac{4(2^{1/m} - 1)}{w^2} (x - x_c)^2 \right]^{-m} \qquad [4]$$

where m is the shape factor with the value set at 1, w is the full width at half maximum (FWHM) and x_c is the center of the peak. Figure 3.18 shows an XRD spectrum of as-spun PVA fibers. The shown X-ray peak at 2θ = 22.8° corresponds to a d-spacing of 4.5 Å. The FWHM of the peak was determined from the fit and has a value of 3.46°.

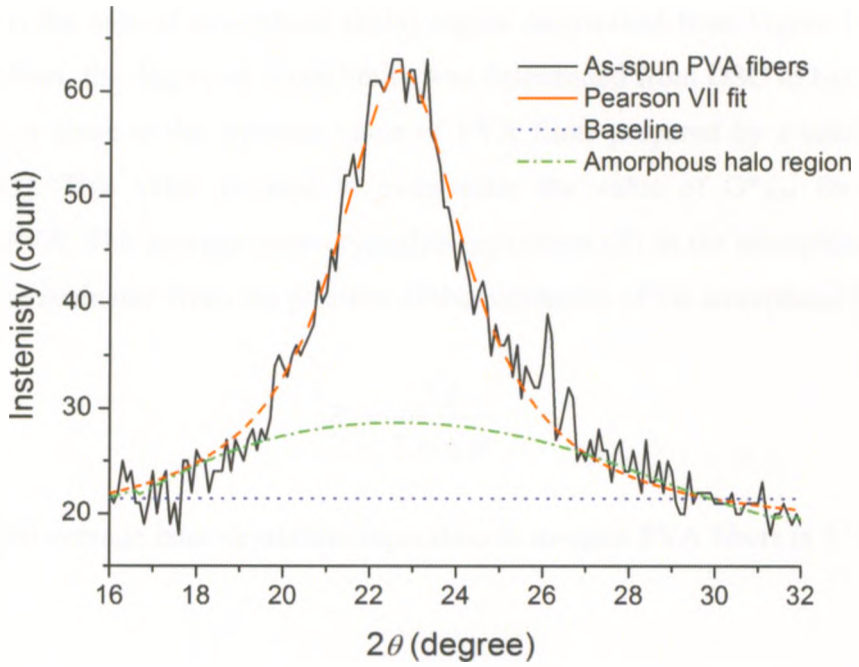

Figure 3.18. XRD spectrum of as-spun PVA fibers fitted with Pearson VII function.

The average crystallite size (P) was estimated by using Scherrer's equation [292]:

$$P = \frac{k\lambda}{(w\cos\theta)} \qquad [5]$$

where w is again FWHM in radians, θ is the Bragg's angle, and k = 1 (or 0.9) is a constant and related to several aspects including the shape of the crystal and the Miller index of the reflecting crystallographic planes and crystallite shape. The calculated crystallite size of the as-spun PVA fibers is 3.5 ± 0.1 Å.

The X-ray diffraction pattern of PVA shows crystalline peaks, which are superimposed on an amorphous halo as shown in Figure 3.18. The degree of crystallinity (X_c) was determined from the ratios of the areas under the crystalline peaks and the respective halos using the method of Hermans and Weidinger [293, 294]:

$$X_c(\%) = 1 - \frac{O_{AM}}{O^*_{AM}} \qquad [6]$$

where O_{AM} is the area of amorphous (halo) region determined from Figure 3.18. For as-spun PVA fibers, the degree of crystallinity was determined from DSC to have a value of 57%, which is close to the reported value of PVA films prepared by a solution casting method [295]. This value is used to extrapolate the value of O^*_{AM} for the totally amorphous PVA. The average inter-crystallite separation (R) in the amorphous region of the fibers was evaluated from the position of the maximum of the amorphous halo [296]:

$$R = \frac{5\lambda}{8\sin\theta} \qquad [7]$$

The calculated average inter-crystallite separation in as-spun PVA fibers is 5.7 Å.

Chapter 4: Results

This chapter starts with a fundamental study on the production of PVA fibers using the electrospinning technique (Section 4.1). The effects of three electrospinning parameters: applied voltage, polymer solution concentration and tip-to-collector distance on fiber diameter and fiber morphology are investigated. Subsequently, mechanical properties of individual PVA fibers are measured using AFM (Section 4.2). Elastic moduli of as-spun PVA fibers as a function of fiber diameter and ambient humidity are determined.

PVA fibers, as spun, are not stable in an aqueous environment including cell culture media. Moreover, PVA, being very hydrophilic, does not have good cell adhesion properties. In order to consider the use of these fibers in biomedical applications, these issues have to be overcome.

For stability in an aqueous solutions and cell culture media, an annealing treatment above room temperature is used (Section 4.3).

To promote cell compatibility, the surface of the fibers is modified by a low energy, broad spectrum nitrogen or helium ion beam. This treatment has the added advantage of also rendering the ion implanted fibers stable in water (Section 4.4). In-vitro cell compatibility of the annealed and ion implanted PVA fibers is assessed using primary human skin fibroblasts (hsF) as a function of ion species, ion dosage and fiber orientation on cell attachment, cell morphology and cell proliferation (Section 4.5).

Figure 4.0 is a flow-chart illustrating the outline of this chapter.

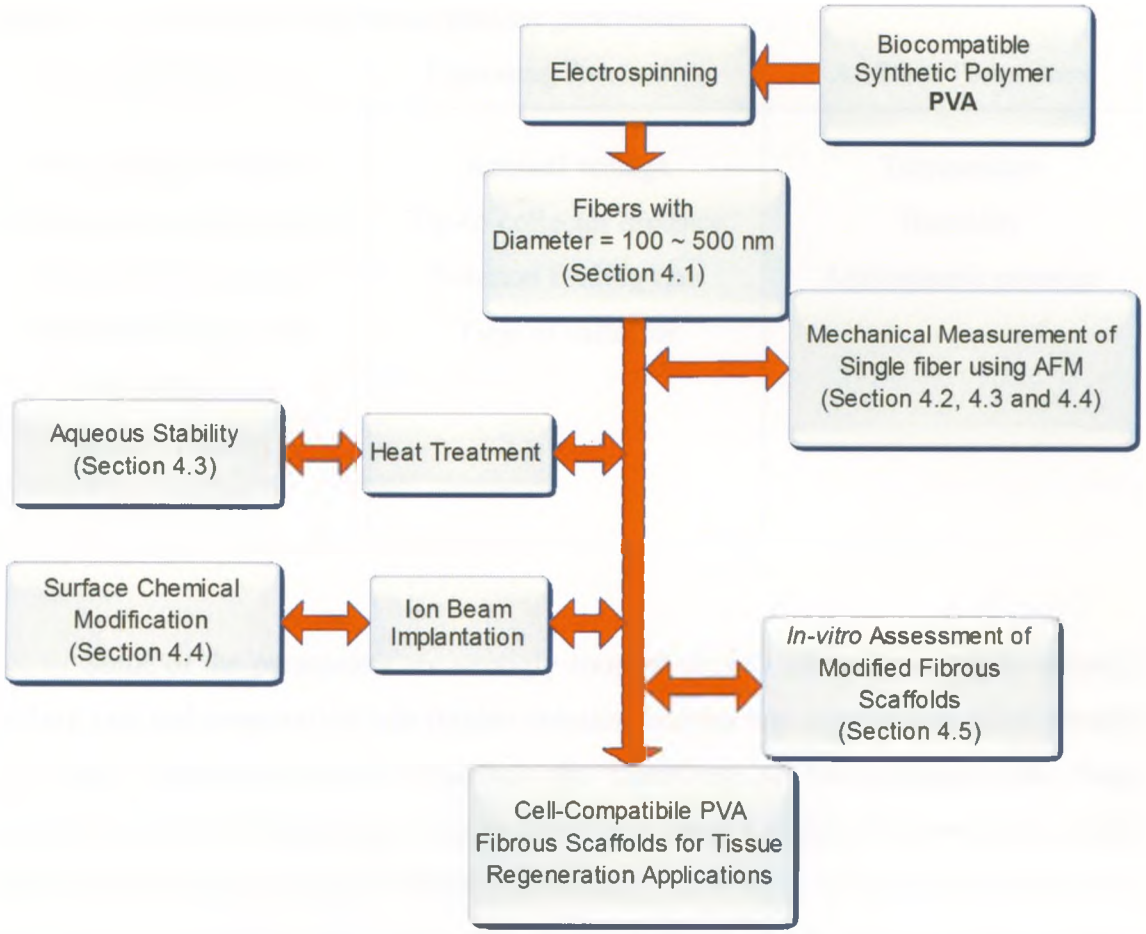

Figure. 4.0. A flow-chart illustrating the outline of this chapter.

4.1 Fabrication of PVA Fibers Using Electrospinning Technique

Fiber production based on the electrospinning technique depends on a wide range of parameters. None of these parameters can be neglected as they all critically affect fiber formation, final fiber diameters and morphology. In Table 4.1, we divide these parameters into three groups as they are related to the solution, the electrospinning process and the ambient environment.

Table 4.1. Three groups of electrospinning parameters.

Solution Parameters	Operating Parameters	Ambient Parameters
Viscosity of solution	Applied voltage	Temperature
Polymer molecular weight	Tip-to-collector distance	Humidity
Polymer concentration	Solution feeding rate	Atmospheric pressure
Electrical conductivity	Type of collector	
Evaporation rate		
Surface tension		
Temperature		

Some of the parameters are strongly coupled to each other, for example, solution feeding rate and evaporation rate (higher solution feeding rate is necessary for a solution with high evaporation rate to maintain the continuity of the polymeric jet). Such parameters and coupling effects can be examined using a design of experiments (DoE) within the context of response surface methodology [297, 298]. Among the parameters in Table 4.1, we simplify our study and focus on three parameters: polymer solution concentration, voltage and tip-to-collector distance. These were chosen because they are the most accessible, controllable and reproducible parameters as we are interested in polymer fibers of a particular diameter range (100 to 500 nm).

As Figure 3.2a and b showed, our electrospinning setup is located inside a fume hood, i.e., we cannot separate our system from the laboratory environment. The impact of ambient temperature, humidity and air pressure on the evaporation rate of the DI water / ethanol solvent system and the equilibrium humidity in the polymer jet can affect the fiber formation and final diameter, which we therefore must keep in mind at every stage of this study. We addressed these issues by adjusting the polymer concentration, voltage and tip-to-collector distance to offset the effect of the ambient parameters to obtain smooth fibers with a relatively narrow diameter range.

4.1.1 Effect of PVA Concentration on Fiber Diameter

The concentration and molecular weight of the polymer in the solution play a significant role in the resulting fiber diameter and the adverse bead formation in electrospinning. Higher polymer concentration and molecular weight increase the degree of polymer chain entanglement in the solution [299], which allows the electrically charged polymer jet to carry more polymer chains to form larger diameter fibers. If the entanglement is below a certain limit and not uniform in the solution, beads are formed along with smaller diameter fibers. On the other hand, if the concentration of the polymer is above a certain limit, the high cohesiveness in the solution due to the polymer chain entanglements may prevent the formation of a Taylor cone at the tip and subsequent fiber formation.

We first varied the PVA concentration in the 80 % DI water and 20 % ethanol solvent system to optimize the fibers diameter and morphology under a constant applied voltage and tip-to-collector distance for our electrospinning setup. The applied voltage and tip-to-collector distance for all solutions were set at 22kV and 15 cm, respectively. Figure 4.1(a–c) show the SEM images of the PVA fibers obtained from solutions with 8.5, 9.5 and 10.5 wt % of PVA, respectively. The fibers are smooth and free of beads. The average fiber diameter was determined from 400 fibers randomly imaged (SEM) from 5 samples for each concentration. The solution with 8.5 wt% of PVA produced fibers with an average diameter of 280 nm with a standard deviation (SD) of 100 nm. This concentration turned out to be the lower limit to produce smooth, bead-free fibers while using this set of process parameters. When we increase the concentration of PVA by 1 wt% to 9.5 wt%, we increase the fiber diameter to an average value of 330 ± 100 nm. The highest concentration of PVA we use in this study is 10.5 wt%. It produces fibers with the largest average diameter, with a value of 490 ± 110 nm. The distributions of the fiber diameters for the three solutions are shown in Figure 4.2. Note that the differences between these distributions are statistically significant ($p < 0.05$).

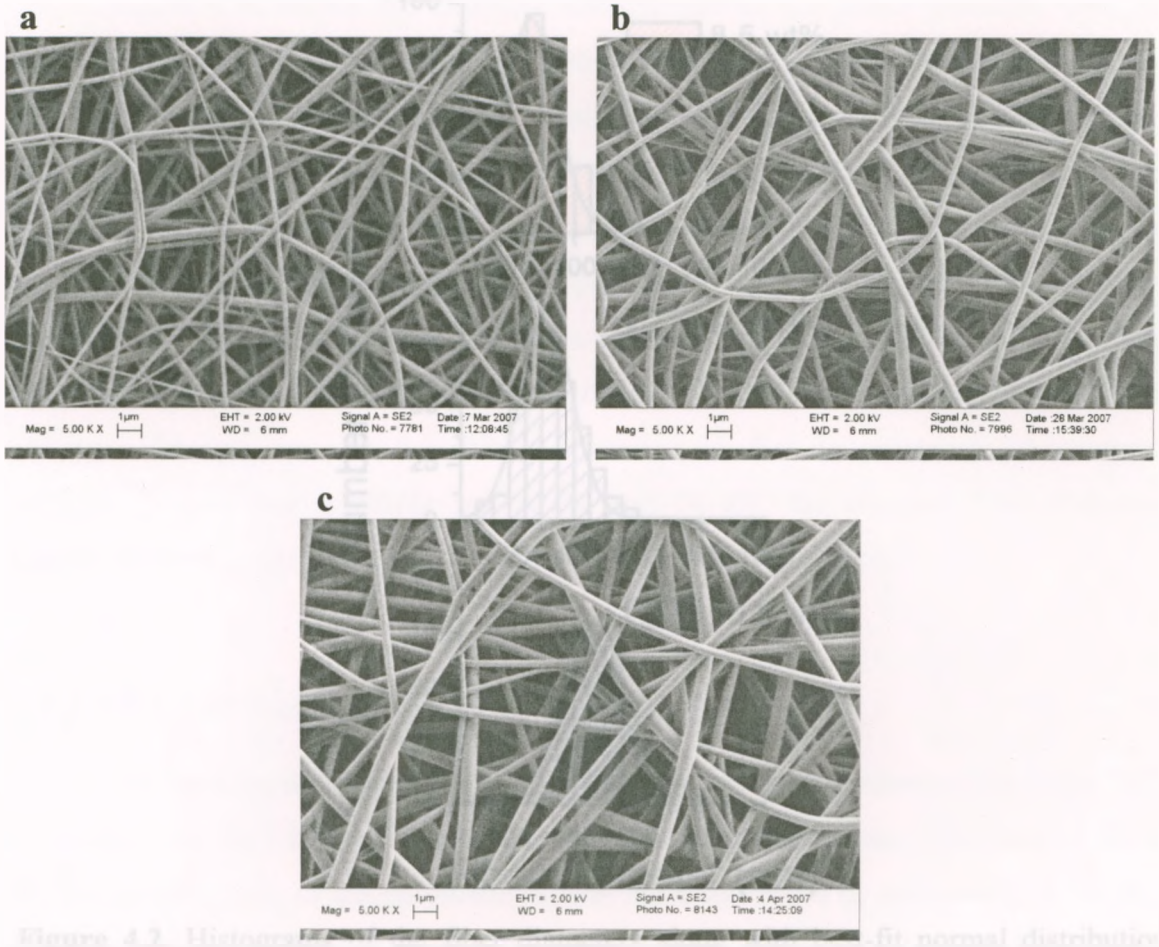

Figure 4.1. (a–c) SEM images of PVA fibers fabricated from 8.5, 9.5 and 10.5 wt% solutions, respectively.

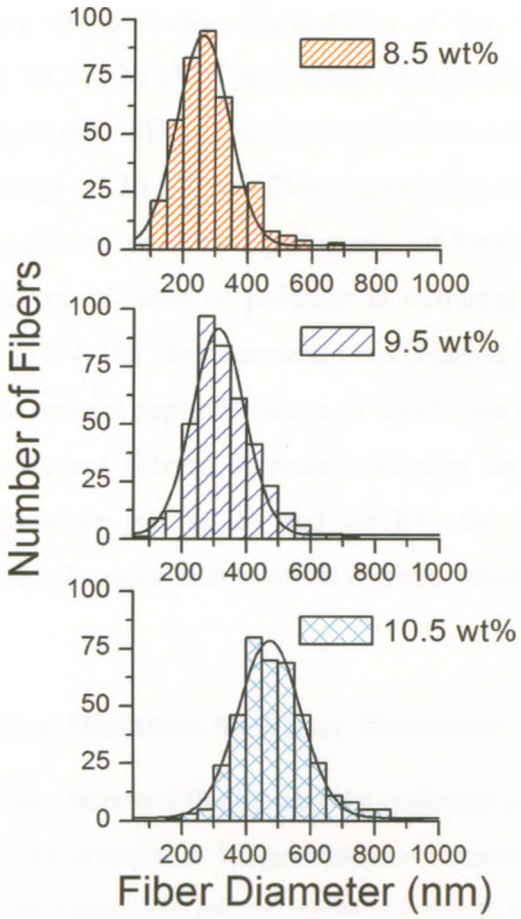

Figure 4.2. Histograms of the fiber diameters along with best-fit normal distribution obtained from the three solutions at 22 kV applied voltage and 15 cm tip-to-collector distance. (The data are fitted with Gaussian distribution function)

4.1.2 Effect of Electric Potential on Fiber Diameter

The polymer solution with 9.5 wt% of PVA was electrospun using potentials in the range of 20 to 26 kV applied voltage with a constant tip-to-collector distance of 15 cm to produce smooth bead-free fibers. Higher applied voltages were not feasible because they increase the mass of polymer extracted from the Taylor cone. The polymeric solution in the Taylor cone then becomes electrically over-charged and subsequently splits into multiple jets [300]. With multiple jets, the resulting fibers are usually less uniform in diameter.

Figure 4.3a shows the diameter distributions of the fibers produced with an applied voltage of 20, 22, 24 and 26 kV. The average fiber diameter was determined from 400 fibers randomly imaged with SEM from 5 samples obtained at each applied voltage. At the lowest applied voltage of 20 kV, the fiber diameter is 280 ± 90 nm. For voltages below 20 kV we were unable to produce a polymeric jet from the Talyor cone. As the applied voltage increased, more mass of polymer is extracted and providing a larger polymeric jet. At 22 and 24 kV, the fiber diameters increased to 330 ± 100 and 390 ± 130 nm, respectively. With the highest applied voltage of 26 kV, the fiber diameter was 410 ± 130 nm. Although, we were not able to determine whether the polymeric jet remained coherent or split into multiple jets at 24 and 26 kV, the obtained fiber diameter distribution was significantly broader than at lower applied voltages.

4.1.3 Effect of Working Distance on Fiber Diameter

The working distance between the tip and the collector determines the flight time of the fiber for the whipping process. A longer distance extends the flight time to allow for greater stretching of the polymeric jet and more solvent to be evaporated. A smaller fiber diameter is expected at increased working distance. Figure 4.3b shows the effect of the working distance on the fiber diameter. A solution with 9.5 wt% of PVA was used to produce fibers at 24 kV; three different working distances were set at 10, 15 and 20 cm. The smallest fiber diameter of 290 ± 80 nm was obtained from the working distance at 20 cm. If the applied voltage is set constant, an increase in the distance decreases the electric field gradient. 20 cm was the longest possible distance to successfully obtain fiber formation at 24 kV. The fiber diameter distribution increased to 390 ± 130 nm and 380 ± 110 nm as the distance was shortened to 15 and 10 cm, respectively. The results at 15 cm and 10 cm were not significantly different ($p > 0.05$).

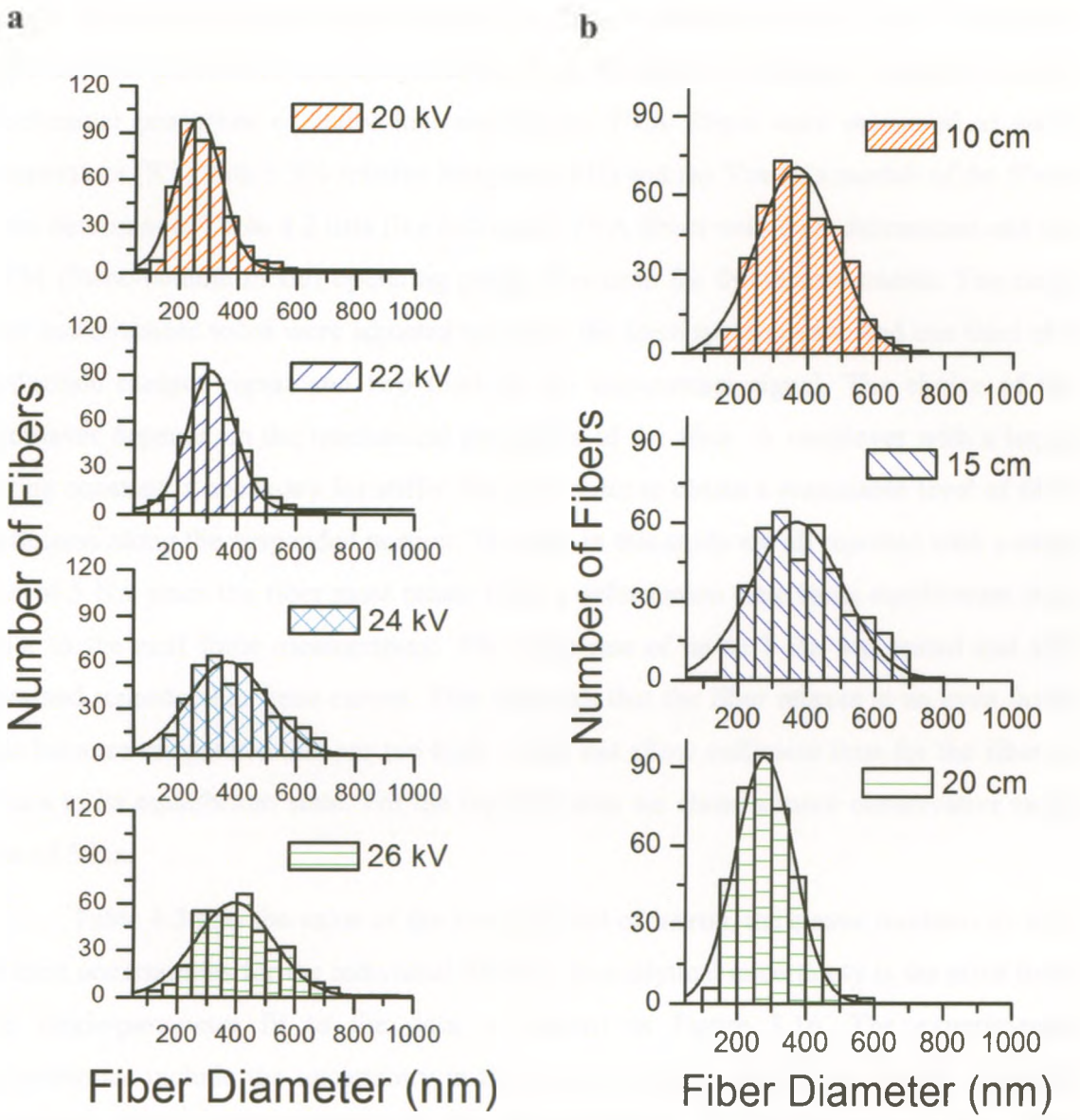

Figure 4.3. (a) Histograms of the fiber diameter along with best-fit normal distribution obtained from a solution with 9.5 wt% of PVA at 15cm tip-to-collector distance with potential difference of 20, 22, 24 and 26 kV. (b) Histograms of the fiber diameter along with best-fit normal distribution obtained from a solution with 9.5 wt% of PVA using 24 kV potential difference at 10, 15 and 20 cm tip-to-collector distance.

4.2 Mechanical Properties of Electrospun PVA Nanofibers

In order to mimic the mechanical properties of a native extra cellular matrix, understanding the material properties of the individual fibers in a scaffold is essential for

optimizing the scaffold design in term of fiber orientation [152, 161]. Using the experimental procedures and analytical methods described in Chapter 3, section 3.6, the mechanical properties of individual electrospun PVA fibers were measured at room temperature (RT) with ≤ 9% relative humidity (RH) and the Young's moduli of the fibers were determined. Table 4.2 lists five individual PVA fibers with their dimensions and the AFM (force-volume mode) operating parameters used for the measurements. The ramp size and threshold value were adjusted such that the force spectrum showed one third of a deflection contact signal and two third of the non-contact signal. The choice of the cantilever depends on the mechanical properties of the fiber. A cantilever with a larger spring constant is necessary for stiffer fibers in order to obtain a reasonable level of fiber deflection along the suspended portion. The data in this study are all reported with a ramp rate of 5 Hz, since the fiber must return from a deformation state to its equilibrium state prior to the next force measurement. The ramp rate of up to 7 Hz was tested and still obtained reproducible force curves. This indicates that the fiber relaxes at an even faster rate because ramp rates that are too high would not allow sufficient time for the fiber to return to its equilibrium state. For the reported data we chose a more conservative ramp rate of 5 Hz.

Table 4.3 lists the value of the area moment of inertia, the elastic modulus as well as their uncertainties for the individual fibers. The analytical uncertainty is the error from the single-parameter fit to the data, as shown in Figure 3.16. The experimental uncertainties include the uncertainty in the spring constant calibration and the standard deviation of the measurements on the fiber diameter. The combination of the two uncertainties is reported throughout this study.

Note that none of fibers tested in this study possess an anisotropic core-shell structure as the AFM force-volume data show good agreement with the clamped beam model, which is based exclusively on tensile deformation [185]. Good reproducibility and consistency of these results were found by further repeating the measurements on randomly selected fibers.

Table 4.2. The dimensions of five individual PVA fibers and the respective AFM (force-volume mode) operating parameters.

Fiber #	L (μm)	D (nm)	I (m^4)	Scan size (μm)	Scan rate (Hz)	Cantilever spring's constant (N/m)
1	7.9	249 ± 5	$(1.9 \pm 0.2)\times10^{-28}$	7.5		
2	8.1	255 ± 7	$(2.1 \pm 0.2)\times10^{-28}$	8.25		
3	7.9	258 ± 6	$(2.2 \pm 0.2)\times10^{-28}$	7.5	5	0.27 ± 0.01
4	7.5	215 ± 4	$(1.06 \pm 0.07)\times10^{-28}$	7		
5	8.0	246 ± 5	$(1.8 \pm 0.2)\times10^{-28}$	8		

Table 4.3. The nanomechanical measurement results of the individual fibers.

Fiber #	± Analytical uncertainty (GPa)	± Experimental uncertainties (GPa)	Elastic Modulus (GPa)
1	0.1	0.3	2.7 ± 0.3
2	0.2	0.6	5.1 ± 0.8
3	0.2	0.4	4.0 ± 0.5
4	0.2	0.3	3.7 ± 0.5
5	0.1	0.3	3.2 ± 0.4

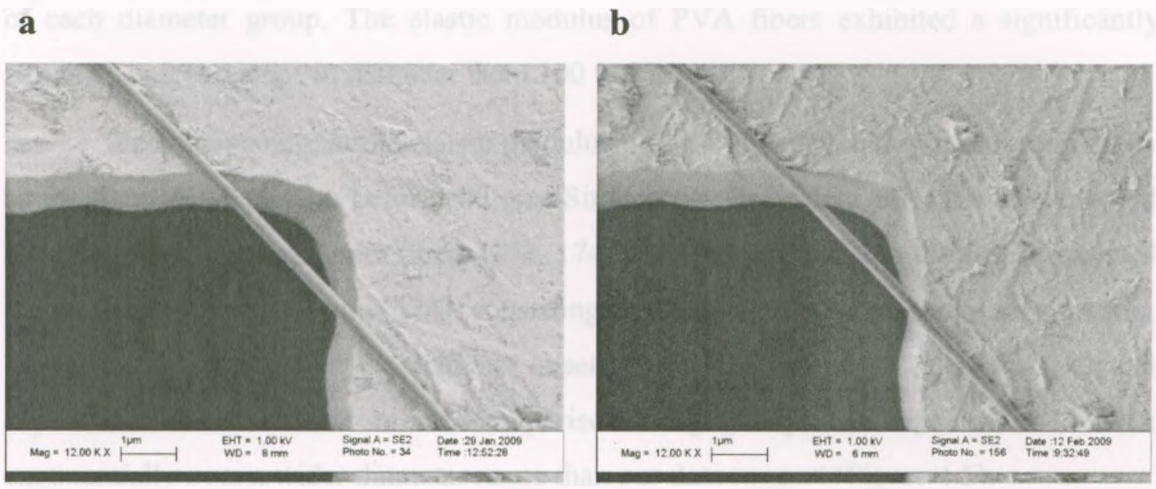

Figure 4.4. SEM images of a fiber (a) before and (b) after the AFM nanomechanical measurement. The fiber remained well anchored and its position was unchanged.

SEM images (Figure 4.4) were taken of the fiber (a) prior to and (b) after the AFM nanomechanical measurement. By comparing the two images, we ensured that the AFM measurement did not relocate the fiber, and the suspended length remained unchanged.

4.2.1 Role of Fiber Diameter on Mechanical Properties

Figure 4.5a shows the elastic moduli of a total of 73 PVA fibers with diameters ranging from 106 to 370 nm. The average elastic modulus of all PVA fibers with an average diameter of 200 ± 80 nm was estimated to be 16 ± 11 GPa. The elastic moduli of PVA fibers exhibited a significant size-dependence, increasing from 1.5 to 40 GPa as the diameter decreases from 370 to 106 nm. Most of these values of the elastic modulus were significantly higher than the PVA bulk modulus of 1.7 GPa [301]. The data set was divided into three groups based on the diameter of the fibers (100 – 200, 200 – 300 and 300 – 375 nm) and plotted against the average elastic modulus (±SD) of each group. These data are shown in Figure 4.5b. A statistical test, One-way ANOVA, was used and confirmed that the results are significantly different from each other. Table 4.4 lists the one-way ANOVA results, the average elastic modulus E_{avg} and the number of fibers (n)

of each diameter group. The elastic modulus of PVA fibers exhibited a significantly strong size-dependence in diameter from 100 to 375 nm.

We anticipated that the elastic modulus of PVA fibers would increase continually as the diameter decreases below 100 nm. Similar size-dependent effects were observed for other electrospun polymer fibers [173, 174] and were attributed to the size increase of the supramolecular structure [174], consisting of aligned domains of the polymer chains. These results showed that the diameter onset of this size-dependent effect was polymer dependent. Elastic moduli in the comparison study [174] were reported to increase exponentially over a wider diameter range than our data suggest (Figure 4.5).

a

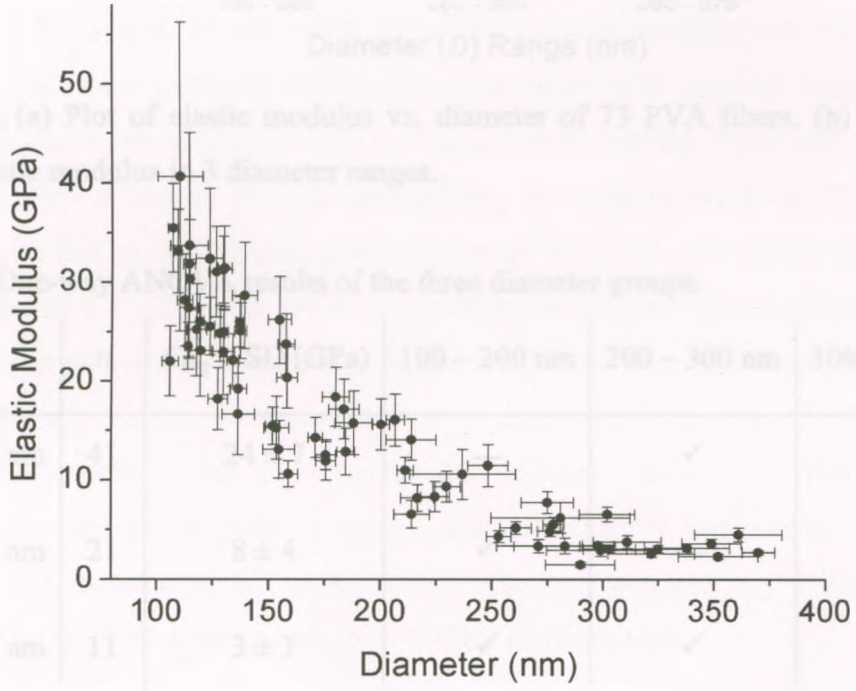

b

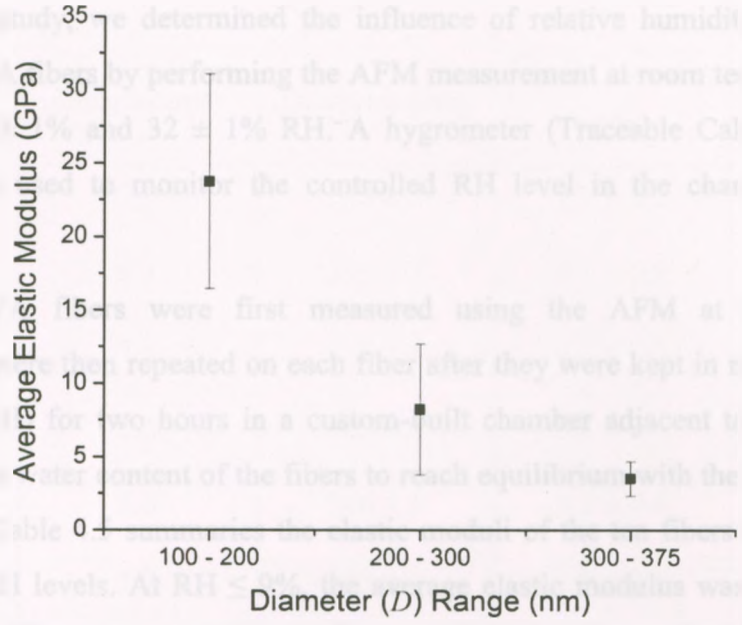

Figure 4.5. (a) Plot of elastic modulus vs. diameter of 73 PVA fibers. (b) Plot of the average elastic modulus in 3 diameter ranges.

Table 4.4. One-way ANOVA results of the three diameter groups.

	n	E_{avg} ± SD (GPa)	100 – 200 nm	200 – 300 nm	300 – 375 nm
100 – 200 nm	41	24 ± 7	---	✓	✓
200 – 300 nm	21	8 ± 4	✓	---	✓
300 – 375 nm	11	3 ± 1	✓	✓	---

4.2.2 Role of Ambient Humidity on Mechanical Properties

In this study, we determined the influence of relative humidity on the elastic modulus of PVA fibers by performing the AFM measurement at room temperature and at humidity of 9 ± 1% and 32 ± 1% RH. A hygrometer (Traceable Calibration Control Company) was used to monitor the controlled RH level in the chamber during the measurement.

Ten PVA fibers were first measured using the AFM at 32% RH. The measurements were then repeated on each fiber after they were kept in nitrogen (N_2) gas ambient (9% RH) for two hours in a custom-built chamber adjacent to the AFM unit. This ensures the water content of the fibers to reach equilibrium with the N2 gas ambient environment. Table 4.5 summaries the elastic moduli of the ten fibers measured at the two different RH levels. At RH $\leq$ 9%, the average elastic modulus was 3.9 ± 0.7 GPa. Since the PVA fibers were not chemically cross-linked with covalent bonds, the non-bonded inter-chain interactions include hydrogen bonds; van der Waals and electrostatic interactions play a crucial role in determining the mechanical properties of PVA. Increasing the RH to 32% significantly (one-way ANOVA, $p < 0.05$) decreased the average value to 2.8 ± 0.8 GPa. PVA is a hydrophilic polymer, and readily dissolves in DI water. At high relative humidity, a larger number of water molecules between the hydrophilic PVA chains weakened the inter-chain interactions [302] and thereby increased the intermolecular freedom for the polymeric molecules. This induced a plasticization effect in the polymer matrix and consequently weakens the mechanical properties. The increase in this plasticization effect of moisture in the PVA fibers is responsible for the 40% average reduction in their elastic moduli.

Table 4.5. The dimensions and elastic modulus of ten PVA fibers at RH of 9 % and 32 %.

Fiber #	Length (μm)	Diameter (nm)	RH at 9%	RH at 32%
			Elastic modulus (GPa)	Elastic modulus (GPa)
1	7.9	249 ± 5	2.7 ± 0.3	2.1 ± 0.3
2	8.1	255 ± 7	5.1 ± 0.8	4.0 ± 0.6
3	7.9	258 ± 6	4.0 ± 0.5	2.0 ± 0.3
4	7.5	215 ± 4	3.7 ± 0.5	3.2 ± 0.4
5	8.0	246 ± 5	3.2 ± 0.4	2.2 ± 0.3
6	5.7	213 ± 4	3.9 ± 0.5	1.9 ± 0.3
7	7.8	206 ± 8	3.4 ± 0.7	2.7 ± 0.6
8	6.5	201 ± 3	4.2 ± 0.4	2.6 ± 0.3
9	8.6	212 ± 3	4.4 ± 0.4	3.7 ± 0.4
10	7.0	202 ± 7	4.1 ± 0.8	3.4 ± 0.6
Mean ± *SD*		230 ± 20	3.9 ± 0.7	2.8 ± 0.8

4.3 Improve Aqueous Stability and Mechanical Properties of PVA Fibers Using Thermal Annealing

Figure 4.6 shows an SEM image of as-spun PVA fibers displaying very poor stability in DI water. As the left side of the image shows, the fiber structure has completely disappeared and a film with no porosity was formed after immersed in de-ionized (DI) water for 1 minute. Although PVA is biocompatible, it readily dissolves in water. It must be stabilized to realize its potential in biomedical applications in nanofiber form. In this study, a thermal annealing approach is used to improve the aqueous stability of electrospun PVA fibers.

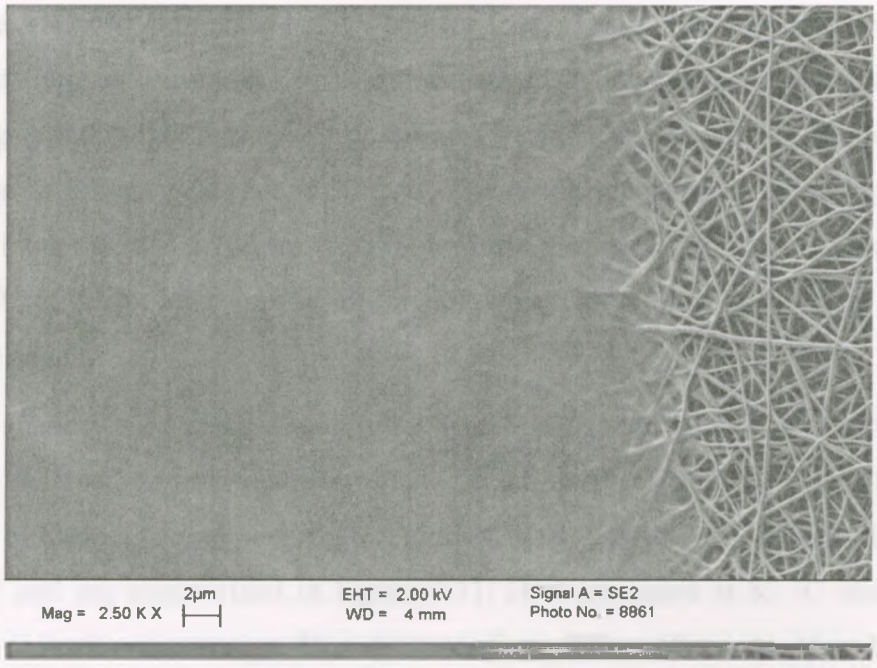

Figure 4.6. SEM images of as-spun PVA fibers after immersed in DI water for 1 minute (area affected at the left side).

4.3.1 Effect of Annealing on the Aqueous Stability of Fibers – Temperature

To investigate the enhancement of aqueous stability of PVA fibers by annealing, four samples with average fiber diameter in the range of 244 to 270 nm were heat treated separately at 85, 110, 135 and 160 °C for 4 hours each. SEM images of these fibers after heat treatment are shown in Figure 4.7a – 4.10a, respectively. In all cases, the fibers showed no significant morphological and size (diameter) changes after treatment. These samples were then immersed in DI water for 1 day and re-examined with SEM. The results are shown in Figure 4.7b – 4.10b. The sample treated at 85 °C and shown in Figure 4.7b was partially dissolved, leading to a reduction in fiber diameter and porosity of the fibrous structures. Annealing at 110 °C also resulted in partial dissolution, however, in this case the aqueous instability led to fusion of some of the fibers into bundles. As a result, they are no longer cylindrical and a slight reduction in the average diameter was observed (Figure 4.8b). The porosity of the woven structure was also reduced. Fig. 4.9b and 4.10b show the SEM images of the samples treated at 135 and 160

°C, respectively, after immersed in DI water for 1 day. The morphology and average fiber diameter of these two samples remained unchanged, indicating good aqueous stability. To investigate the longer term stability, all heat treated samples were re-immersed in DI water for an additional 10 days and 30 days. The results are summarized in Figure 4.7c – 4.10c and Figure 4.7d – 4.10d, respectively. These results are similar to those shown in Figure 4.7b – 4.10b after immersion in DI water for 1 day, indicating no further dissolution beyond day 1.

To quantify the aqueous stability of these fibers under the four different annealing conditions, the average fiber diameters (250 randomly selected fibers from 3 samples in each case) of samples corresponding to Figure 4.7a–d, 4.8a–d, 4.9a–d and 4.10a–d were determined and are summarized in Figure 4.11. Heat treatment at 85 °C allowed for a significant reduction in average fiber diameter from 270 ± 60 nm to 46 ± 14 nm (the uncertainties are SD) after 1 day immersion in DI water, but then remained unchanged after 10 days and 30 days. Treatment at 110°C led to a lower degree of fiber size reduction after 1 day in DI water. The average fiber diameter decreased by 34 % to 190 ± 50 nm. However the average fiber diameter increased from 190 to 220 nm after immersed in DI water for 10 days. This increase is due to the bundling of some of individual fibers as shown in Figure 4.8c. Thereafter, the fiber diameter remained unchanged for up to 30 days in DI water. Contrast to these results, fibers treated at 135°C and 160°C were stable from day 1 to day 30 in DI water. Both the morphology and average fiber diameter remained unchanged. These 30 days stability test results provide sufficient confidence to allow for extrapolation of stability of these annealed fibers to significantly longer time point.

The increase in aqueous stability of electrospun PVA fibers can either be a result of chemical, physical or a combination of these changes since it has been established that thermal annealing of bulk PVA does not result in chemical change (except various degree of carbonization) but in a change in the degree of crystallinity [60, 61]. The most likely explanation of our observation is an increase in fiber crystallinity, although the morphology of the PVA fibers is significantly different from that of bulk PVA. For a given treatment time, there is a threshold temperature above which these fibers become stable in an aqueous solution. This is an important requirement for biomedical and other

applications in an aqueous environment. For a heat treatment time of 4 hours, the minimum temperature to obtain stable PVA fibers is ~135 °C.

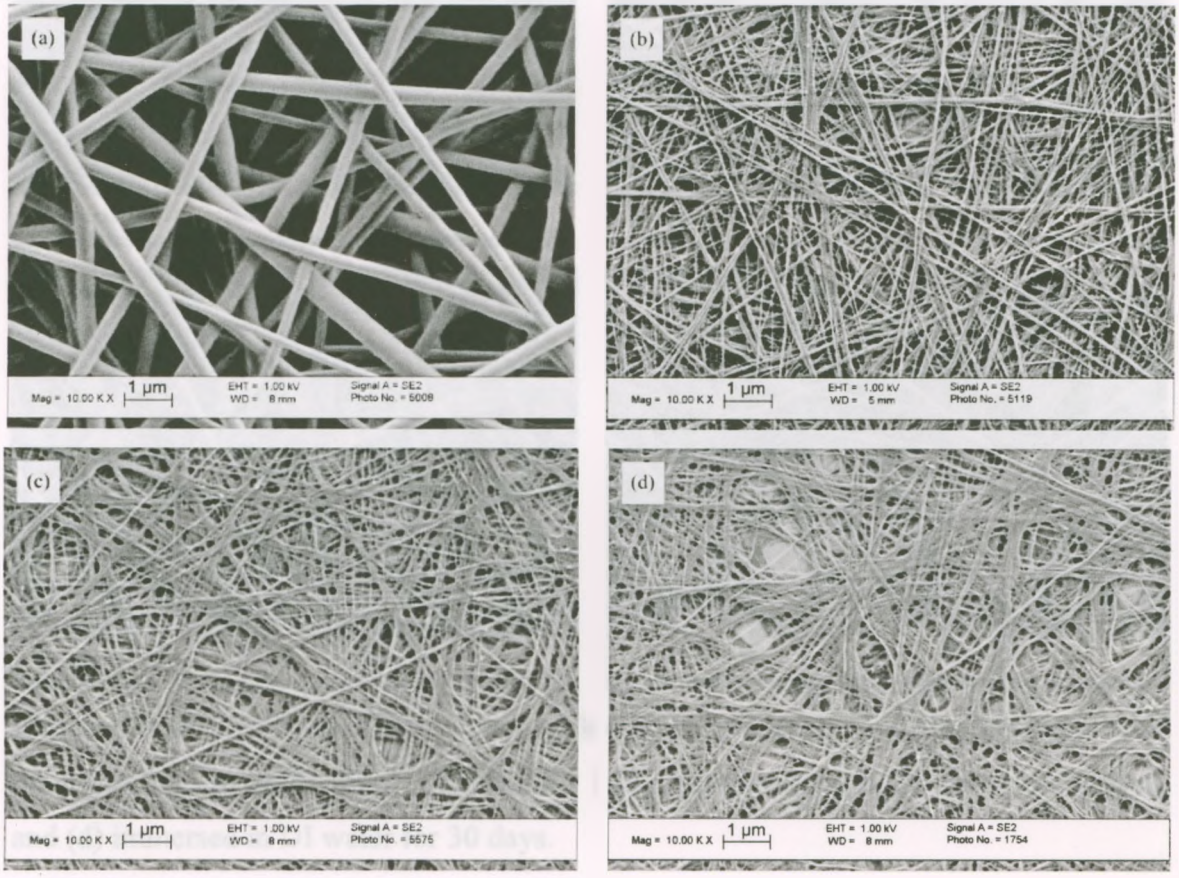

Figure 4.7. SEM images of PVA fibers with 4 hours of 85 °C annealing treatment after (a) annealing, (b) immersed in DI water for 1 day, (c) immersed in DI water for 10 days, and (d) immersed in DI water for 30 days.

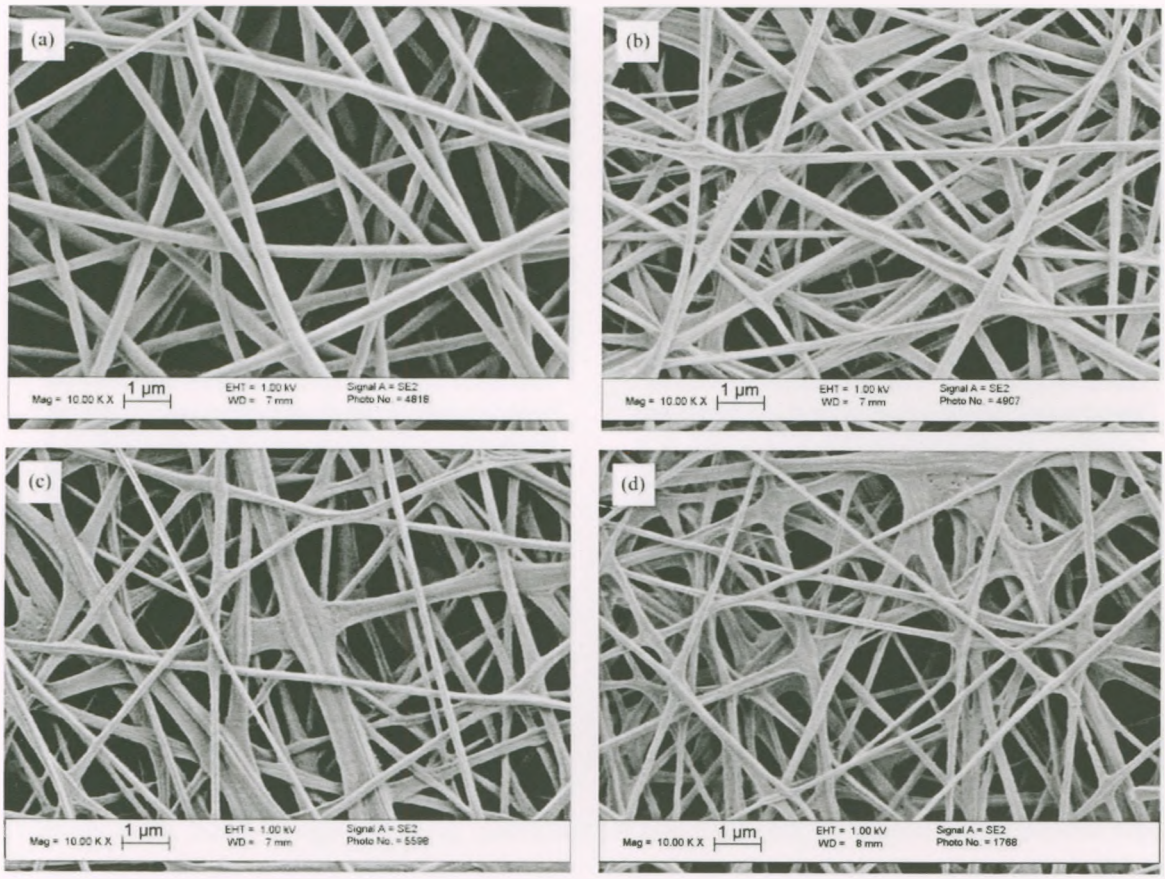

Figure 4.8. SEM images of PVA fibers with 4 hours of 110 °C annealing treatment after (a) annealing, (b) immersed in DI water for 1 day, (c) immersed in DI water for 10 days, and (d) immersed in DI water for 30 days.

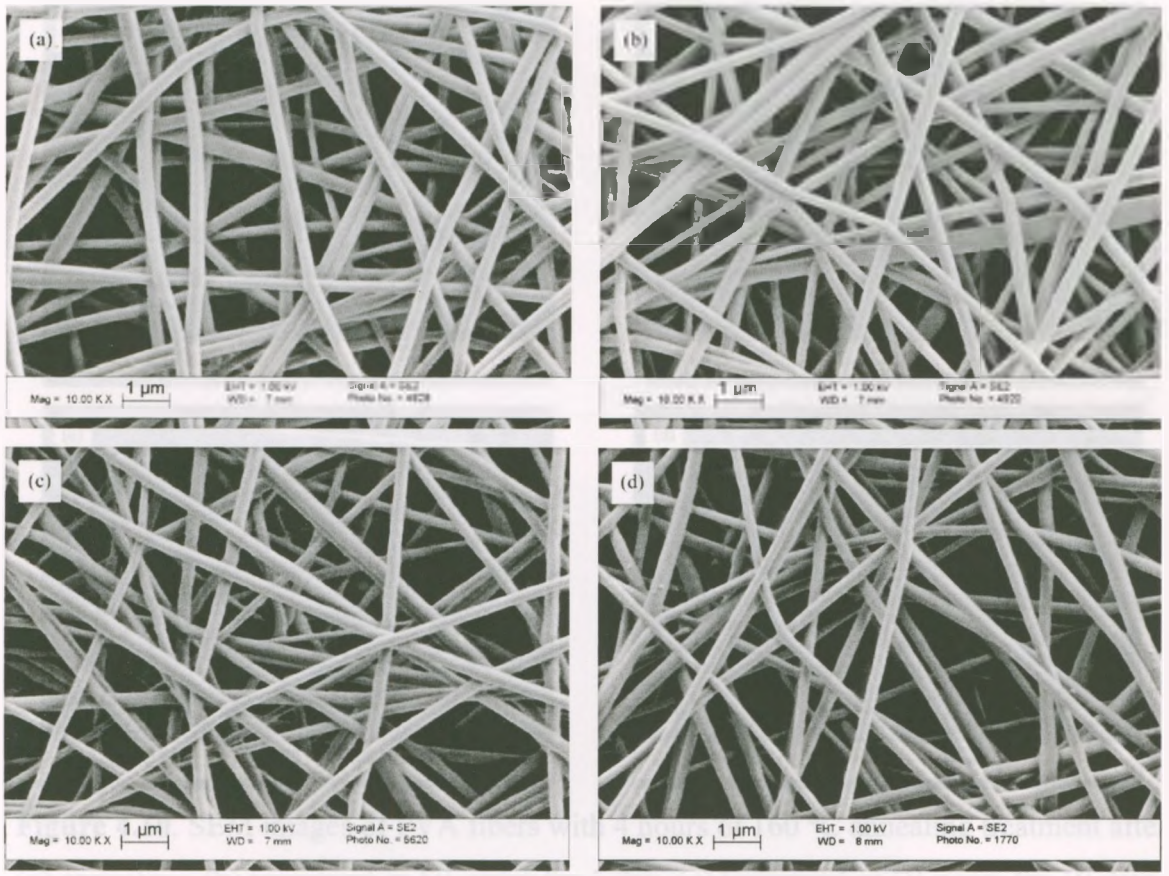

Figure 4.9. SEM images of PVA fibers with 4 hours of 135 °C annealing treatment after (a) annealing, (b) immersed in DI water for 1 day, (c) immersed in DI water for 10 days, and (d) immersed in DI water for 30 days.

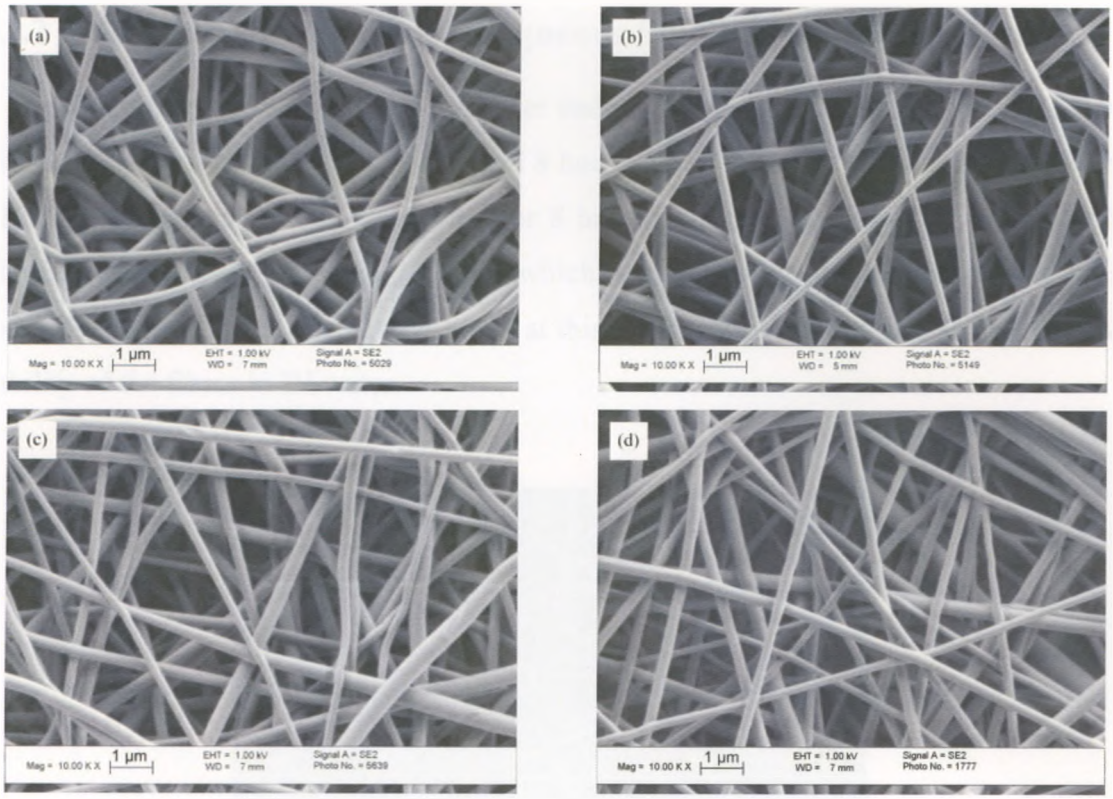

Figure 4.10. SEM images of PVA fibers with 4 hours of 160 °C annealing treatment after (a) annealing, (b) immersed in DI water for 1 day, (c) immersed in DI water for 10 days, and (d) immersed in DI water for 30 days.

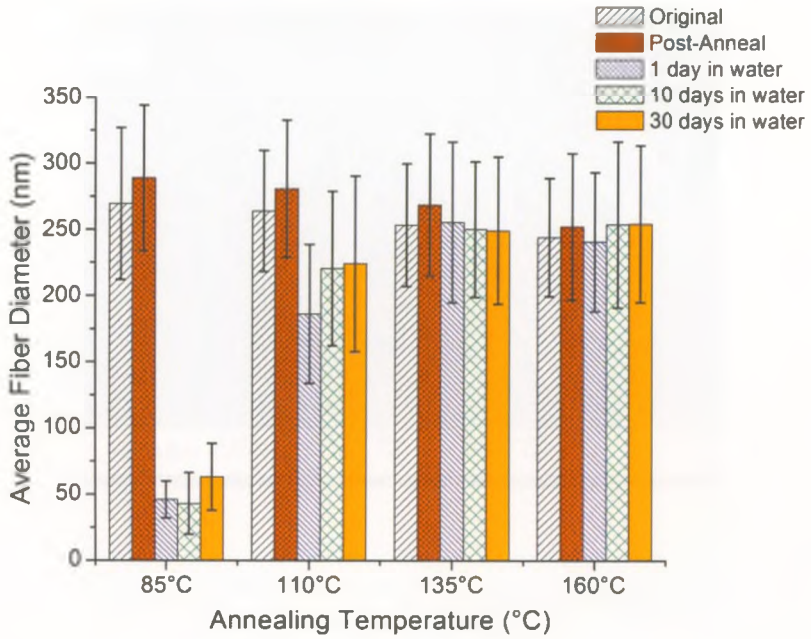

Figure 4.11. Fiber diameters after 4 hours of annealing at 4 different temperatures; at 5 different stages during the stability test in DI water. (The error bars are SD)

4.3.2 Effect of Annealing on the Aqueous Stability of Fibers – Time

The effect of annealing time on fiber stability was investigated at 110 and 135 °C with time varying between 30 minutes and 8 hours. The results are summarized in Figure 4.12. The morphology of fibers treated for 8 hours at 110 °C is shown in Figure 4.12a after immersed in DI water for 10 days, which is a treatment very similar to that for 4 hours (Figure 4.8c), i.e., the extra 4 hours at this temperature did not further improve the stability of the fibers in DI water.

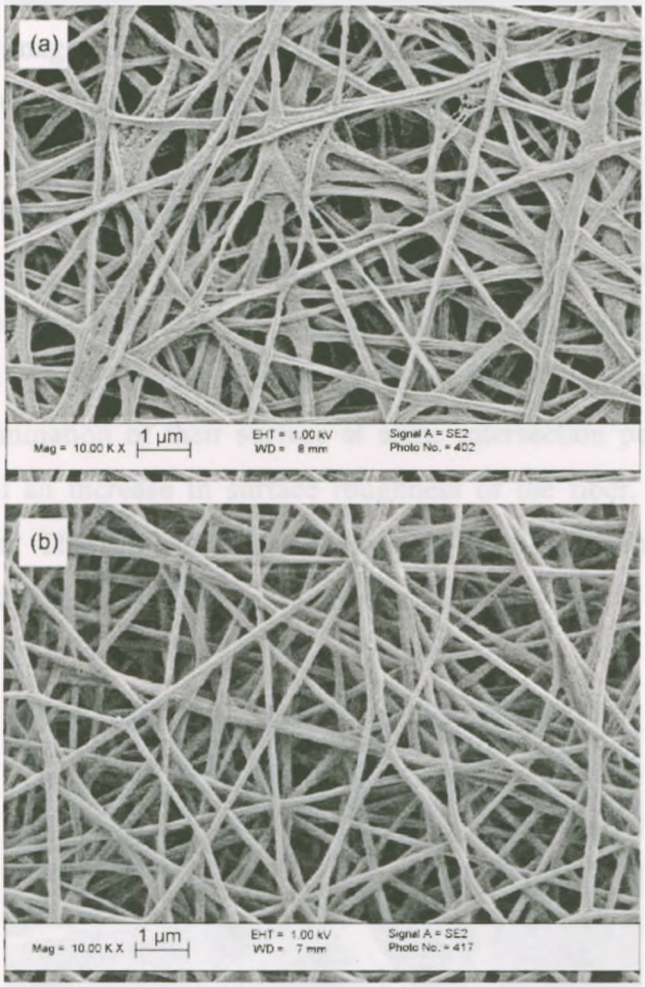

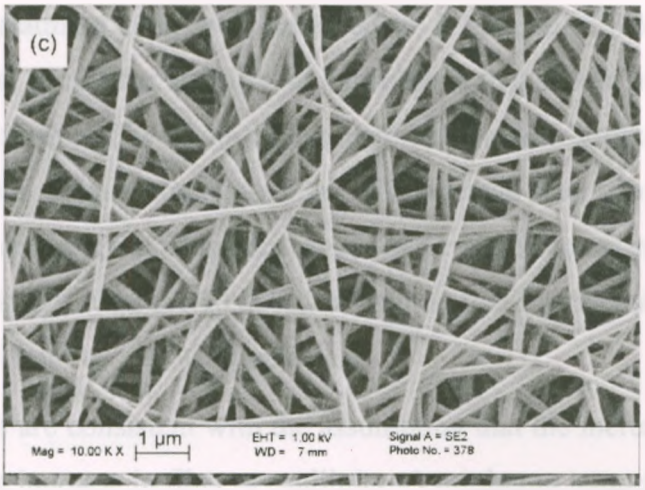

Figure 4.12. SEM images of PVA fibers with (a) 8 hours of 110 °C (b) 30 minutes of 135 °C, and (c) 1 hour of 135 °C treatment after immersed in DI water for 10 days.

The results for heat treatment at 135 °C for 30 minutes and 1 hour are shown in Figure 4.12b and 4.12c, respectively. From Figure 4.12b, it can be seen that even for a short treatment time, the fiber stability was significantly improved and the cylindrical shape of the fibers was largely retained, but some of the fibers stuck together to form bundles. Close examination of their surface at some intersection points (e.g. in Figure 4.13) also indicated an increase in surface roughness of the fiber, which is a sign of selective dissolution. This indicates that 30 minutes heat treatment at 135 °C is not sufficient to establish reliable stability of the fibers.

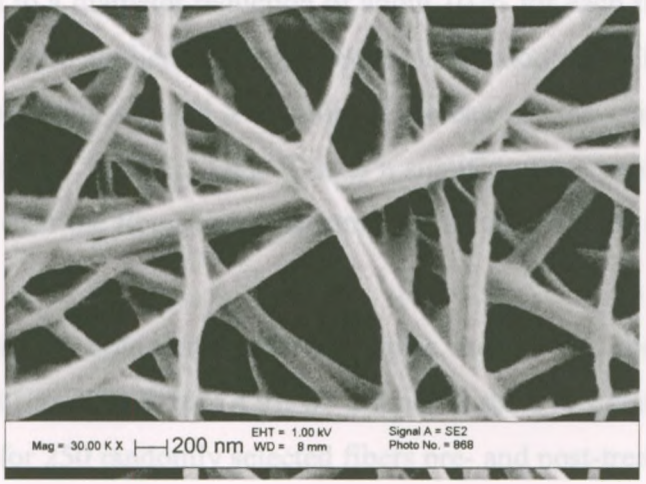

Figure 4.13. High resolution SEM image of the sample shown in Figure 4.12b.

When the treatment time was increased to 1 hour, the SEM results shown in Figure 4.12c indicate good fiber stability, comparable to that shown in Figure 4.8c after 4 hours of 13 5°C annealing. The fibers maintained their smooth surface, similar to that of the as-spun fibers, and did not bundle together. The average fiber diameter also exhibited no change over the entire series of experiments (180 ± 30 nm for as-treated and 175 ± 30 nm after immersed in DI water for 10 days), indicating that for fiber stability in DI water, a heat treatment of 1 hour at 135 °C is sufficient.

These results are consistent with the assumption that the increase in fiber stability is associated with an increase in fiber crystallinity. A minimum temperature is required to allow polymer chain mobility within the fiber, which is a prerequisite for the creation of sufficient crystallinity. On the other hand, once this temperature is reached, the time required to achieve stability is only a function of the polymer chain mobility.

4.3.3 Effect of Annealing on Mechanical Properties

The change in mechanical properties associated with increased nanofiber stability in DI water by heat treatment was also investigated. 16 fibers with diameters ranging from 150 to 250 nm were analyzed using the AFM based bending test before thermal treatment. This yielded a mean elastic modulus of 4.4 ± 1.4 GPa (the uncertainties are SD). These fibers were then annealed for 4 hours at 135 °C. During annealing the fiber diameter range decreased significantly to 135 – 230 nm (one-way ANOVA, $p < 0.05$) which corresponded to a diameter reduction of about 10 % for each fiber. A bending test using the AFM was again applied to determine the elastic modulus of these 16 fibers after heat treatment. The results showed a significant increase in the elastic modulus of all fibers to a mean value of 7.6 ± 2.3 GPa. This is a significant increase of 80 % (one-way ANOVA, $p < 0.05$) over the fibers before treatment. The summarized results are provided in Table 4.6.

It is interesting to note that for fiber samples used in the fiber stability study (4 hours at 135 °C and shown in Figure 4.9), we did not observe any statistically significant change in diameter for 250 randomly selected fibers pre- and post-treatment (Figure 4.11). Although the same fiber samples were used for these measurements, the regions selected

within the sample were not the same pre- and post-treatment. The random variation in fiber size led to similar average diameters (250 ± 50 nm vs. 270 ± 50 nm). On the other hand, for the fibers used to determine the elastic modulus, the diameter of each of the 16 fibers was measured and compared both before and after the treatment. This allowed us to measure the heat treatment effect on the diameter of each fiber individually.

Table 4.6. The dimensional and elastic modulus changes of individual fibers before and after 4 hours of 135 °C annealing.

	Pre-annealing			Post-annealing		
Fiber #	Length (μm)	Diameter (nm)	Elastic modulus (GPa)	Length (μm)	Diameter (nm)	Elastic modulus (GPa)
1	3.6	252 ± 7	2.7 ± 0.6	3.6	232 ± 7	4.1 ± 0.7
2	3.4	183 ± 3	4.5 ± 0.6	3.2	164 ± 4	6.3 ± 0.6
3	4.5	199 ± 4	4.1 ± 0.6	4.5	182 ± 3	7.9 ± 0.9
4	3.7	207 ± 5	2.7 ± 0.3	3.7	179 ± 3	7.3 ± 0.9
5	3.5	181 ± 3	6.1 ± 0.8	3.5	161 ± 3	8.6 ± 1.1
6	3.3	191 ± 2	5.7 ± 0.7	3.2	178 ± 2	8.4 ± 1.0
7	3.8	238 ± 5	2.6 ± 0.3	3.9	217 ± 3	5.8 ± 0.9
8	4.7	153 ± 2	6.3 ± 0.7	4.6	135 ± 3	8.5 ± 0.9
9	4.2	242 ± 3	4.0 ± 0.4	4.2	220 ± 3	6.2 ± 0.7
10	3.9	200 ± 5	5.1 ± 0.7	3.9	185 ± 3	6.8 ± 1.1
11	3.9	223 ± 3	4.6 ± 0.6	3.8	199 ± 3	8.8 ± 1.2
12	4.4	172 ± 4	3.5 ± 0.5	4.4	147 ± 3	6.0 ± 0.8
13	3.6	205 ± 4	6.7 ± 0.8	3.5	190 ± 4	13.8 ± 2.0
14	5.0	217 ± 4	5.5 ± 0.7	5.0	189 ± 5	9.0 ± 1.3
15	4.4	225 ± 3	2.6 ± 0.3	4.3	206 ± 3	5.0 ± 0.6
16	4.8	213 ± 5	4.1 ± 0.6	4.7	190 ± 4	9.6 ± 1.5
Mean ± *SD*		210 ± 30	4.4 ± 1.4		190 ± 30	7.6 ± 2.3

4.3.4 Effect of Annealing on Crystallinity

Figure 4.14 shows XRD spectra of as-spun PVA fibers and the fibers treated with the four different annealing conditions. The peak at $2\theta = 22.8°$ shows a gradual decrease in the FWHM as the annealing temperature increases. This is an indication of an increase in the crystallite size in the PVA matrix as a function of annealing temperature. From Equation 4 described in Chapter 3, section 3.7.7, we determine that the crystallite size of as-spun PVA fibers increases from 3.5 to 5.2 nm after annealing for 4 hours at 85 °C, and increases to 6.9 nm as the annealing temperature is elevated to 160 °C. The degree of crystallinity (X_c) (Equation 5 in Chapter 3, section 3.7.7) of the fibers is 62 ± 1 % after annealing for 4 hours at 85°C. The value of X_c increases as the annealing temperature is increased and reaches a value of 81 ± 1 % at an annealing temperature of 160 °C. The summarized results are provided in Table 4.7.

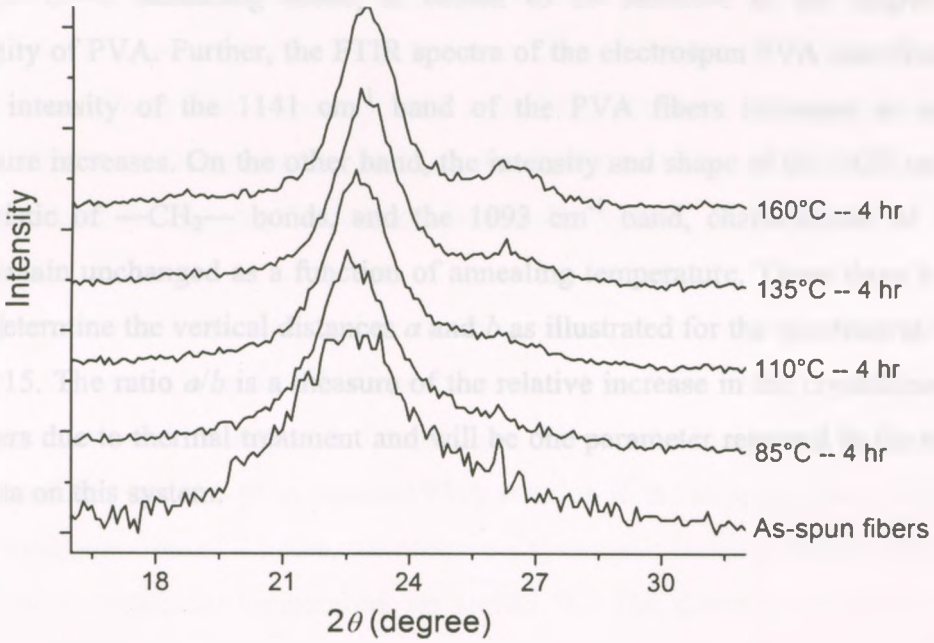

Figure 4.14. XRD spectra (in the range between $2\theta = 16° - 32°$) of PVA as-spun fibers, and fibers after 4 hours of 85°C annealing, 4 hours of 110 °C annealing, 4 hours of 135 °C annealing and 4 hours of 160 °C annealing (arbitrary scale on intensity and offset for clarity).

Table 4.7. The results of XRD characterization of the as-spun PVA fibers and the fibers after 4 hours of four different annealing temperatures.

	d – spacing (Å)	Crystallite size (nm)	Inter-crystallite separation (Å)	X_c (%) (n=3)
As-spun fibers	4.6	3.5 ± 0.1	5.7	57 ± 3
85 °C -- 4 hr	4.5	5.2 ± 0.1	5.7	62 ± 1
110 °C -- 4 hr	4.5	6.2 ± 0.1	5.7	68 ± 4
135 °C -- 4 hr	4.5	6.6 ± 0.1	5.6	74 ± 2
160 °C -- 4 hr	4.5	6.9 ± 0.1	5.6	81 ± 1

The effect of thermal treatment on the crystallinity of PVA is further quantified using an infrared spectroscopic method as outlined by Kennedy et al. [60] and Peppas [61]. In Figure 4.15, the intensity of the 1141 cm^{-1} band, which is associated with the symmetric C—C stretching mode, is shown to be sensitive to the degree of the crystallinity of PVA. Further, the FTIR spectra of the electrospun PVA nanofibers show that the intensity of the 1141 cm^{-1} band of the PVA fibers increases as annealing temperature increases. On the other hand, the intensity and shape of the 1425 cm^{-1} band, characteristic of —CH_2— bonds, and the 1093 cm^{-1} band, characteristic of —CO— bonds, remain unchanged as a function of annealing temperature. These three bands are used to determine the vertical distances a and b as illustrated for the spectrum at 85 °C in Figure 4.15. The ratio a/b is a measure of the relative increase in the crystallinity of the PVA fibers due to thermal treatment and will be one parameter reported in the summary of our data on this system.

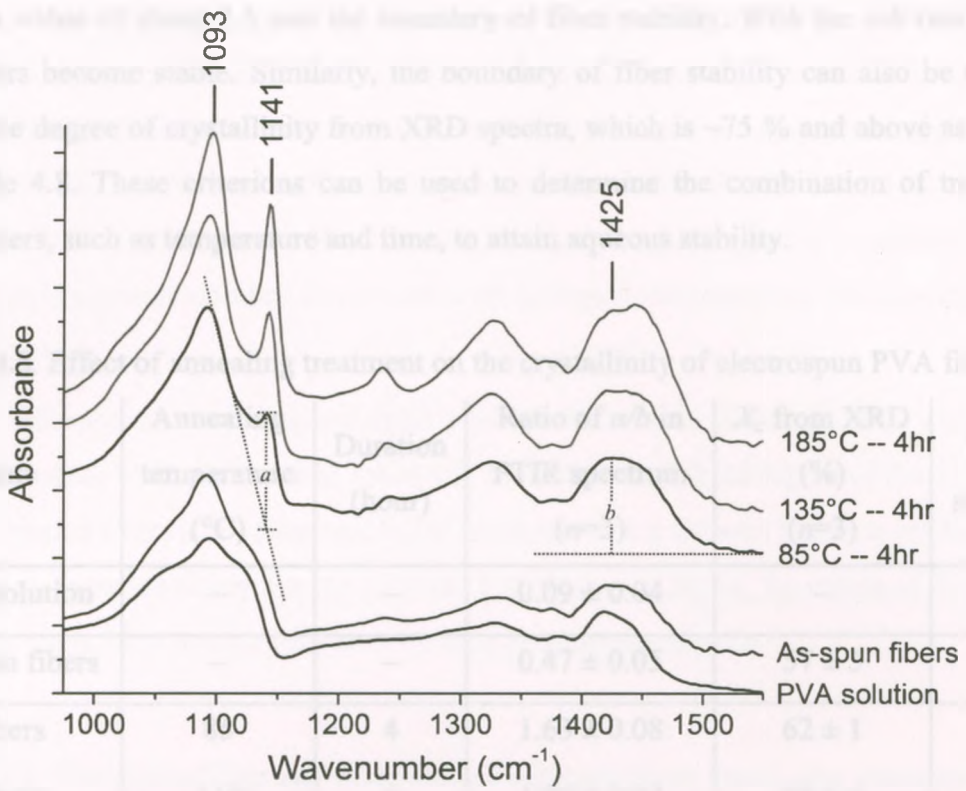

Figure 4.15. FTIR spectra (in the range between 975 and 1550 cm^{-1}) of PVA solution, as-spun fibers, and fibers after 4 hours of 85°C annealing, 4 hours of 135°C annealing and 4 hours of 185°C annealing (arbitrary scale on absorbance intensity and offset for clarity). The schematic of determining the ratio *a*/*b* is also shown.

Table 4.8 summarizes our data on this system. It includes the X_c in the XRD spectra and the ratio *a*/*b* in the FTIR spectra obtained for PVA fiber samples (n=3) after thermal treatment under the specified conditions. The results show the expected increase in the crystallinity of PVA from aqueous PVA solution to the as-spun fibers. Further, at a constant treatment time of 4 hours, we observe a systematic increase in fiber crystallinity with increasing treatment temperature up to 185 °C. The decrease of the *a*/*b* ratio at 210 °C is mostly likely due to proximity to the melting transition temperature of PVA as determined by DSC (Chapter 3, section 3.7.1). At a constant annealing temperature of 110 °C, an increase in duration from 4 to 8 hours led to a significant increase in crystallinity. On the other hand, at 135 °C, there is no change in crystallinity between 1 and 4 hours of annealing. Based on these results, a criterion for aqueous stability of electrospun PVA nanofiber by thermal annealing can be formulated in terms of the *a*/*b*

ratio. A value of about 2.5 sets the boundary of fiber stability. With the *a/b* ratio ≥ 2.5, the fibers become stable. Similarly, the boundary of fiber stability can also be defined using the degree of crystallinity from XRD spectra, which is ~75 % and above as shown in Table 4.8. These criterions can be used to determine the combination of treatment parameters, such as temperature and time, to attain aqueous stability.

Table 4.8. Effect of annealing treatment on the crystallinity of electrospun PVA fibers.

State	Annealing temperature (°C)	Duration (hour)	Ratio of *a/b* in FTIR spectrum (*n*=3)	X_c from XRD (%) (*n*=3)	Fiber stability
PVA solution	–	–	0.09 ± 0.04	–	–
As-spun fibers	–	–	0.47 ± 0.05	57 ± 3	no
Fibers	85	4	1.63 ± 0.08	62 ± 1	no
Fibers	110	4	1.86 ± 0.02	68 ± 4	no
Fibers	110	8	2.16 ± 0.08	–	no
Fibers	135	0.5	2.16 ± 0.10	–	no
Fibers	135	1	2.49 ± 0.02	–	yes
Fibers	135	4	2.46 ± 0.09	74 ± 2	yes
Fibers	135	8	2.73 ± 0.11	–	yes
Fibers	160	4	2.89 ± 0.10	81 ± 1	yes
Fibers	185	4	3.10 ± 0.08	–	yes
Fibers	210	4	2.88 ± 0.05	–	yes

4.3.5 Crystallinity and Mass of Annealed Fibers after Water Immersion

The annealing treatment increases the crystallinity, thus improving the aqueous stability of the PVA fibers as a function of annealing temperature. For the low annealing temperatures, 4 hours at 85 or 110 °C, the increases in crystallinity were not sufficient to

allow the fiber become fully stable in an aqueous environment, as we observed a significant decrease in fiber diameter after the annealed fibers were immersed in DI water (section 4.3.1). Therefore, the mass losses related to the dissolved amorphous region of fibers at 85 and 110 °C treated fibers were measured at value of 67 % and 50 %, respectively. For the 135 and 160 °C treated fibers, the higher degree of crystallinity caused good aqueous stability, associated with no significant mass loss after the exposure to DI water.

XRD spectra were obtained again after the fibers were immersed in DI water for 1 day. The values of X_c are listed in Table 4.9. Since the amorphous region of the 85 and 110 °C treated fibers were dissolved in DI water, the fibers showed higher crystallinity then the as-annealed fibers. For the 135 and 160 °C treated fibers, the values of X_c after DI water immersion remain very close to their pre-immersed state.

Table 4.9. The crystallinity and mass loss of annealed PVA fibers after immersed in DI water for 1 day.

	Crystallite size (nm)	X_c (%) (n=3)	Mass Loss (%)
85 °C -- 4 hr	4.2 ± 0.1	71 ± 2	67
110 °C -- 4 hr	4.5 ± 0.1	72 ± 1	50
135 °C -- 4 hr	4.6 ± 0.1	75 ± 1	0
160 °C -- 4 hr	6.4 ± 0.2	83 ± 1	0

4.3.6 Effect of Annealing on Melting Temperature

In Section 4.3.4 we determined that the crystallinity of the PVA fibers increases as the annealing temperature increases. Therefore, the corresponding shift of the melting temperature is expected to be a function of annealing temperature. In Figure 4.16, five heating DSC curves for as-spun PVA fibers as well as the fibers annealed at four different temperatures are shown. From the top of the endothermic peak, we determined the peak of the melting transition of each PVA sample by first derivative; the results are

listed in Table 4.10. The melting transition peak of as-spun PVA fibers is found to be 227.7 °C, which is very close to the melting point of PVA reported in the literature [303]. After 4 hours of 85 °C annealing, the peak is shifted to 230.3 °C. The 110 °C sample shows two distinctive peaks during the endothermic transition, which correspond to 227.5 and 232.5 °C. The lower peak of the 110 °C sample is equal to the as-spun fibers and the higher one is identical to the 135 and 160 °C samples. The two results at 110 °C indicate an onset of a transition stage, which can be correlated to two forms of crystalline structure [304]. While some region of the 110 °C annealed fibers are soluble like as-spun fiber, and the rest are stable like the 135 and 160 °C samples for up to 30 day in DI water.

Table 4.10. The melting transition peak of the as-spun PVA fibers and annealed fibers.

	Melting Transition T_m (°C)
As-spun fibers	227.7
85°C -- 4 hr	230.3
110°C -- 4 hr	227.5, 232.5
135°C -- 4 hr	232.5
160°C -- 4 hr	232.5

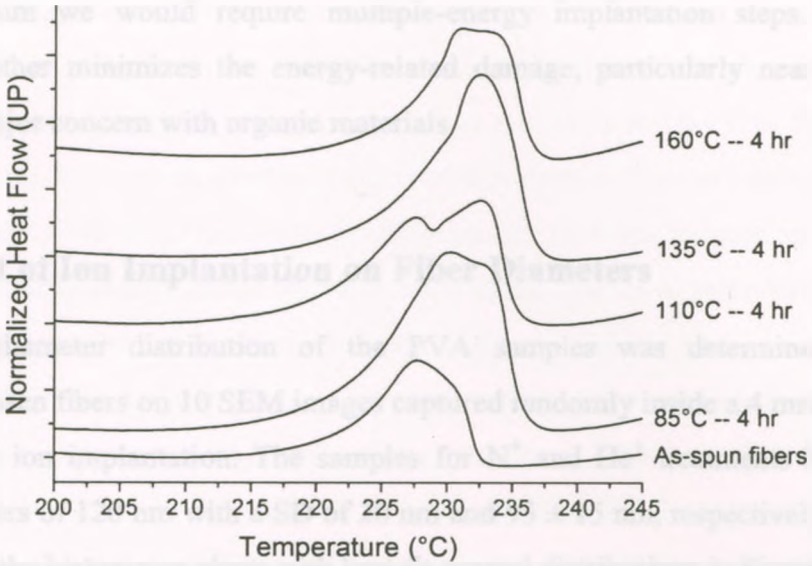

Figure 4.16. DSC heating curves (in the range between 200 and 245 °C) of as-spun PVA fibers and fibers annealed at four different temperatures. (arbitrary scale on heat flow and offset for clarity)

4.4 Physical and Chemical Properties of Ion Beam Treated PVA Fibers

4.4.1 Ion Beam Treatment

The purpose of this part of the study is to demonstrate the potential of an ion beam treatment to selectively induce intrinsic modifications to the mechanical and chemical properties of electrospun PVA fibers. Of particular interest is our ability to implant specific ion species, nitrogen [75, 76] or helium [74], both of which have an effect on cell adhesion properties.

We converted a high-energy mono-energetic ion beam, generated from a conventional ion implanter, into a low, poly-energetic beam using a Ta foil as an energy diffuser. The energy of the beam is reduced and its distribution is broadened through the collision/straggling process of the ions with the Ta atoms in the foil, providing for a widened implantation zone [305], which in our case covers the range from the surface to 900 nm depth in PVA (theoretical SRIM value). To achieve the same result with a mono-

energetic beam we would require multiple-energy implantation steps. The energy widening further minimizes the energy-related damage, particularly near the surface, which is a major concern with organic materials.

4.4.2 Effect of Ion Implantation on Fiber Diameters

The diameter distribution of the PVA samples was determined from 400 randomly chosen fibers on 10 SEM images captured randomly inside a 4 mm^2 area before and after the ion implantation. The samples for N^+ and He^+ treatments had as-grown mean diameters of 120 nm with a SD of 20 nm and 95 ± 15 nm, respectively. The results are shown in the histograms along with best-fit normal distributions in Figure 4.17.

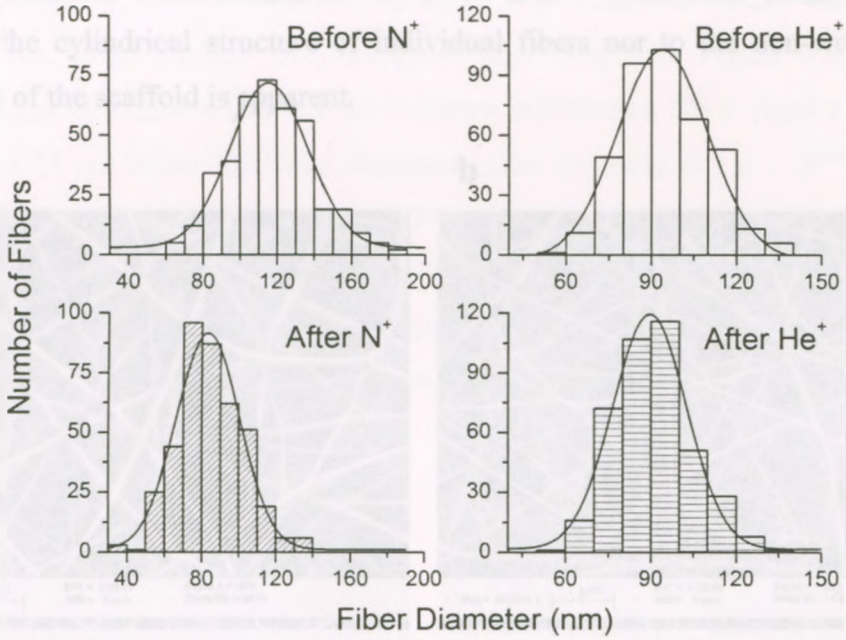

Figure 4.17. Histograms of the fiber diameter along with best-fit normal distributions before and after N^+ and He^+ treatment.

Figure 4.18a shows a SEM topological image of the PVA non-woven fibers with a diameter of 120 ± 20 nm before N^+ treatment. Figure 4.18b shows a corresponding image after exposure to 1.2×10^{16} N^+/cm^2. Visual comparison between these figures indicates that the fiber diameter is reduced after ion beam treatment, which also alters the porosity and the surface area to volume ratio of the scaffold, while the bulk porosity

remains unchanged due to a relatively shallow (~900 nm in PVA) ion implantation range. The histogram of fiber diameters before and after N^+ treatment is shown in Figure 4.17. The data confirm a significant reduction (one-way ANOVA; $p < 0.05$) in fiber diameters by 27 % to 85 ± 20 nm, with a reduced diameter distribution from an original range of 60 – 180 nm to 40 – 140 nm. This can be attributed to an ion beam induced annealing effect [306] as the kinetic energy of the ions deposited in the fiber is to some extent converted to thermal energy. During the chain scission and cross-linking processes, this thermal energy may allow the polymer chains to become mobile and re-arrange their orientations to minimize free space present in the original structure. Therefore, this effect on fiber diameter is expected to be increased as a function of the N^+ dosage and beam current until excessive thermal degradation of the polymer occurs. Fiber damage was assessed with high resolution SEM images of the fibers after N^+ treatment (Figure 4.19). No damage to the cylindrical structure of individual fibers nor to the non-woven surface morphology of the scaffold is apparent.

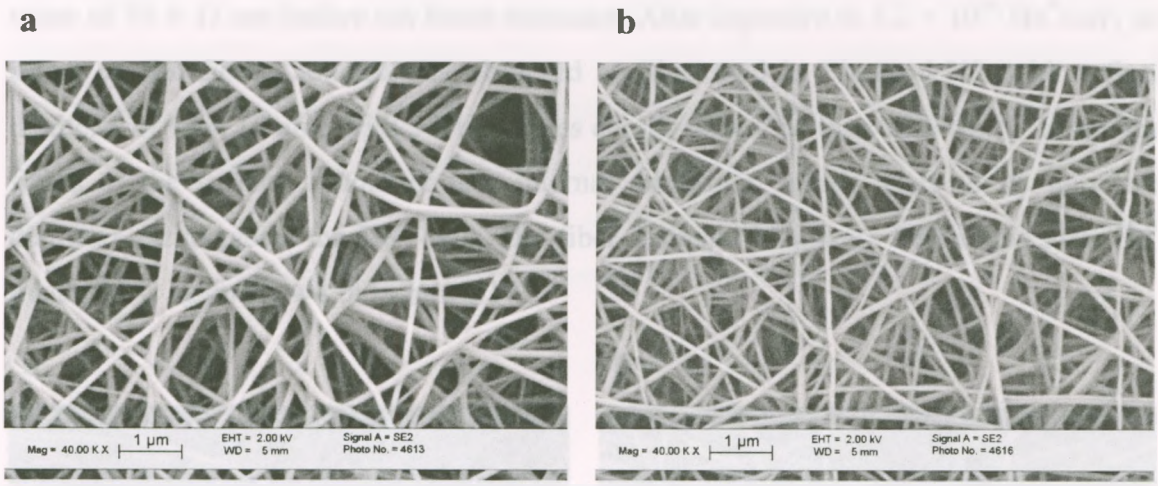

Figure 4.18. (a) SEM image of the original PVA fibrous scaffold prior to N^+ treatment. (b) SEM image of the PVA fibrous scaffold after treated with 1.2×10^{16} N^+/cm^2.

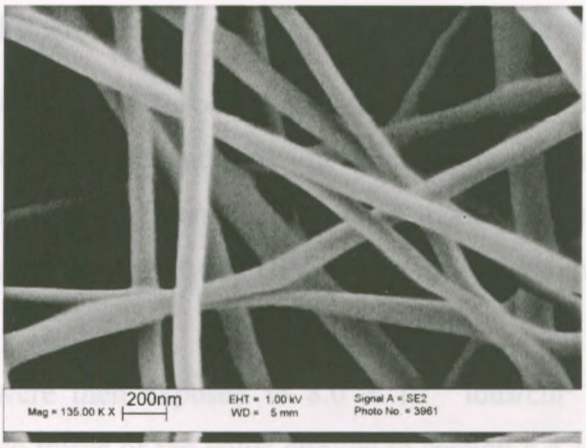

Figure 4.19. High resolution SEM image of the PVA fibers after treated with 1.2×10^{16} N^+/cm^2.

Concurrently, a PVA fibrous scaffold was analyzed before and after He^+ treatment. The initial surface morphology of this sample in Figure 4.20a is nearly identical to that in Figure 4.18a, but the diameter distribution has a slightly lower mean value of 95 ± 15 nm before ion beam exposure. After exposure to 1.2×10^{16} He^+/cm^2, no effect on the fiber diameter was observed as illustrated in Figure 4.20b with a final diameter of 90 ± 15 nm. With 3.2 times less energy deposited than with the N^+ beam, the fibers at the surface encounter less internal annealing, which leads to no noticable diameter shrinkage in the He^+ case. The fiber diameter histogram before and after He^+ treatment is again shown in Figure 4.17.

a **b**

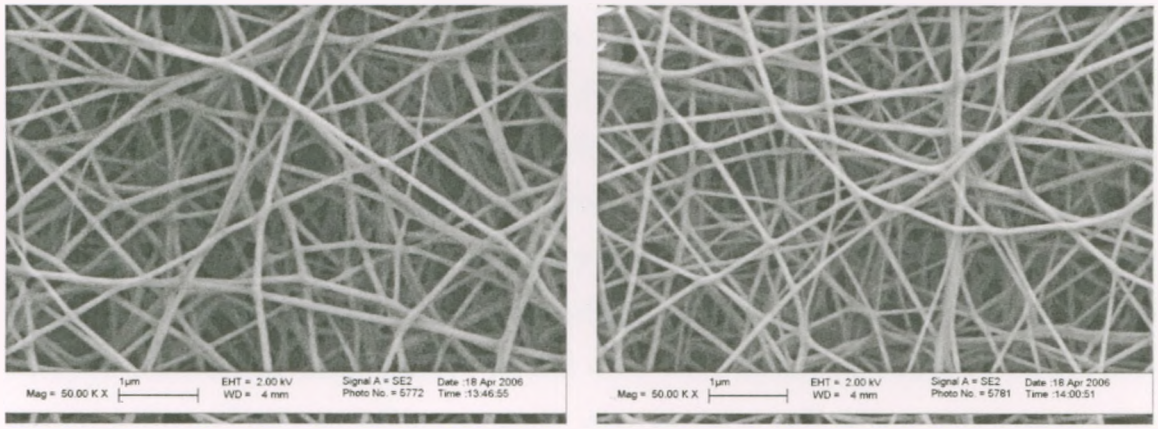

Figure 4.20. (a) SEM image of the original PVA fibrous scaffold prior to He^+ treatment. (b) SEM image of the PVA fibrous scaffold after treated with 1.2×10^{16} He^+/cm^2.

4.4.3 Mechanical Properties of N^+ Treated PVA Fibers

We used the same AFM force-volume mode protocol as before to measure the fibers at the same locations before and after ion beam treatment to determine its effect on the elastic moduli of individual fibers. The Young's moduli of ten pre-implanted fibers showed an original mean value of 30 ± 5 GPa, where the uncertainty is the SD for all ten fibers.

Those fibers were then exposed to 8.0×10^{15} ions/cm² of N^+. Note that we lowered the dose to two thirds of the value applied in section 4.4.1 to the non-wovens to reduce the decrease in fiber diameter. This was necessary to maintain a large enough diameter for the AFM measurements using the same settings with the previously used cantilever.

The result for 8.0×10^{15} N^+/cm² treatment shows a significant increase in elastic modulus for all ten fibers, with the average increase from 30 ± 5 GPa to 39 ± 5 GPa (one-way ANOVA, $p < 0.05$). The mean diameter significantly decreased (one-way ANOVA, $p < 0.05$) from 122 to 108 nm with a SD of ± 8 nm. Table 4.11 summarizes the results of our mechanical testing, including the average fiber diameter of the ten fibers. It is important to note in this context that based on our AFM contact mode images the shrinkage of the diameter did not affect the clamping condition of the fibers on the TEM grid. This was always confirmed after the mechanical measurements.

Table 4.11. The dimensional and elastic modulus changes of individual fibers before and after 8.0×10^{15} ions/cm² of N^+ treatment.

	Original PVA Fibers			After 8×10^{15} N^+/cm^2		
Fiber #	Length (μm)	Diameter (nm)	Elastic modulus (GPa)	Length (μm)	Diameter (nm)	Elastic modulus (GPa)
1	3.1	119 ± 2	26 ± 2	3.1	107 ± 3	34 ± 3
2	3.7	120 ± 5	23 ± 4	3.7	107 ± 5	31 ± 5
3	3.9	130 ± 5	23 ± 3	3.9	119 ± 4	40 ± 6
4	4	110 ± 10	41 ± 15	4	95 ± 8	47 ± 15
5	4.1	109 ± 2	33 ± 2	4.1	98 ± 1	41 ± 2
6	3.7	130 ± 2	25 ± 1	3.7	119 ± 3	40 ± 4
7	3.4	130 ± 3	31 ± 3	3.4	113 ± 3	36 ± 4
8	3.8	130 ± 2	31 ± 2	3.8	116 ± 3	44 ± 5
9	3.4	126 ± 4	31 ± 4	3.4	112 ± 1	38 ± 2
10	3.7	114 ± 3	32 ± 3	3.7	101 ± 2	36 ± 3
Mean ± *SD*		121 ± 8	30 ± 5		108 ± 8	39 ± 5

4.4.4 Effect of N^+ Ion Dosage on Mechanical Properties

In section 4.4.3, we observed a 30% increase in the elastic modulus of the PVA fibers after 8.0×10^{15} N^+/cm^2 implantation. For organic polymers, there is an upper limit of dosage for ion implantation above which the polymers become overdosed and carbonized (increase in the relative carbon concentration) [307]. It produces an amorphous carbon network [308] and reduce the stiffness of the polymer fibers. In order to determine the upper limit of N^+ dosage which the PVA fibers can sustain before their stiffness declines, the fibers used in section 4.4.3 were further exposed to a second dose step of 8.0×10^{15} N^+/cm^2 of (accumulated dose of 1.6×10^{16} N^+/cm^2). The mechanical measurements show two distinct groups of results, indicative of an onset of a transition

stage. For eight of the ten fibers, we observed a further 10 % increase of the elastic modulus to 43 ± 5 GPa (excluding the results of the other two). The remaining two fibers experienced a ~36 % drop from their original values. These two fibers maintained the same diameter as measured after the first treatment. If we combine the results of all ten fibers we find the same value as after the first treatment with a mean elastic modulus of 39 ± 11 GPa and a mean diameter of 110 ± 8 nm, the higher uncertainties in the elastic modulus due to the two deviating fibers. The modifications in elastic modulus and diameter were both significantly different (one-way ANOVA; $p < 0.05$) from the original values, but insignificantly different (one-way ANOVA; $p > 0.05$) from the values of the first treatment. Figure 4.21 summarizes the mechanical testing results as well as the mean diameter of the ten fibers before and after three steps of N^+ treatment.

As seen in Figure 4.21, a last 8.0×10^{15} N^+/cm^2 dose of treatment (accumulated dose of 2.4×10^{16} N^+/cm^2) results in overdosing of the polymer with significant carbonization. All ten fibers showed weakening to a mean elastic modulus of 18 ± 7 GPa, which represents a significant drop (one-way ANOVA; $p < 0.05$) of 54 % and 40 % from the first two treatments and the initial mean value, respectively. The higher number of amorphous carbon domain introduced by carbonization also increases the mean diameter of the ten fibers to a value of 122 ± 9 nm, which matches the original value.

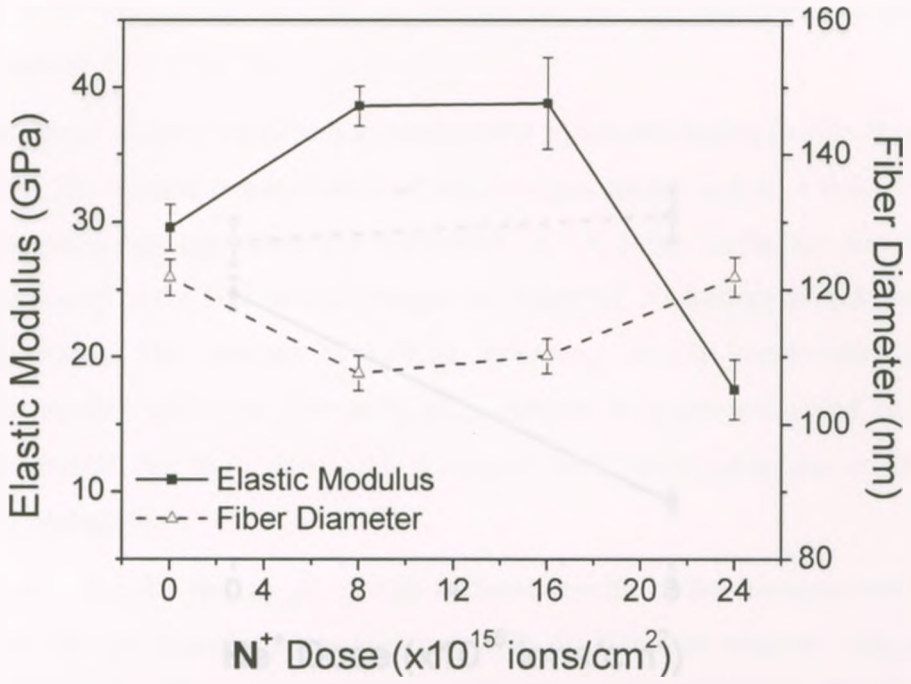

Figure 4.21. The mean elastic modulus (solid line) and diameter (dashed line) of 10 fibers each measured after three steps of nitrogen ion dose implanted. The lines are a guide to the eyes only. (The error bars are standard errors)

4.4.5 Mechanical Properties of He^+ Treated PVA Fibers

With 3.2 times less energy deposited to the polymer matrix than N^+ implantation, the treatment using chemically inert He^+ is expected to induce different mechanical properties of the PVA fibers. 17 PVA fibers deposited on a single TEM grid were treated with a single dose of 8.0×10^{15} He^+/cm^2. Figure 4.22 shows the results of the 17 fibers before and after this treatment. Their elastic moduli were reduced so drastically that an AFM cantilever of smaller spring constant (0.097 N/m) was required to obtain reliable force spectra after the treatment. The elastic modulus of the 17 fibers before the treatment had a mean value of 24 ± 5 GPa with a mean diameter of 130 ± 15 nm. After the He^+ treatment, the elastic modulus dropped dramatically (one-way ANOVA; $P < 0.05$) by about 63 % to 9 ± 3 GPa while the diameter remained at 135 ± 20 nm.

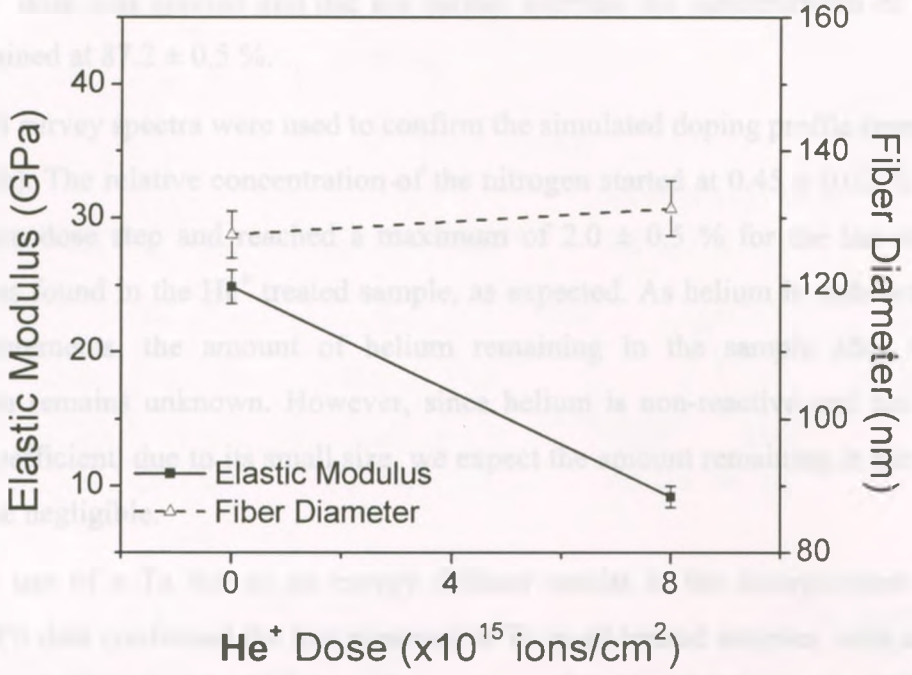

Figure 4.22. The mean elastic modulus (solid line) and diameter (dashed line) of 17 fibers before and after helium ion treatment. The lines are a guide to the eyes only. (The error bars are standard errors)

4.4.6 Effect of Ion Implantation on Chemical Structure

The chemical composition of the PVA fibrous scaffold was analyzed using XPS. Initially the fibers show the chemical composition of standard PVA [309] with 71 ± 1 % (atomic percentage) carbon and 29 ± 1 % oxygen in the survey spectrum that excludes hydrogen. This baseline allows us to follow the degree of carbonization (increase in the C concentration and decrease in H and O concentration in PVA) induced by the broad-energy ion beam surface treatment as a function of ion dose. The first dose of 8.0×10^{15} N^+/cm^2 increased the fraction of carbon to 79.3 ± 0.2 % and decreased oxygen to 20.0 ± 0.3 % (the rest are belong to N and Ta). The carbonization effect continued for the second 8.0×10^{15} ions/cm² dose step and finally reached 87.2 ± 0.5 % of carbon with 10.3 ± 0.1 % of oxygen after the third (last) 8.0×10^{15} N^+/cm^2 of dose step. On the other hand, despite He^+ transferring a lower amount of energy, the carbonization effect induced by the first dose of 8.0×10^{15} He^+/cm^2 matches that for the third N^+ dose with relative concentration of 86.7 ± 0.5 % and 13.3 ± 0.1 % of carbon and oxygen, respectively. A

second He^+ dose was applied and did not further increase the concentration of carbon, which remained at 87.2 ± 0.5 %.

XPS survey spectra were used to confirm the simulated doping profile from SRIM (Figure 3.5b). The relative concentration of the nitrogen started at 0.45 ± 0.02 % for the first nitrogen dose step and reached a maximum of 2.0 ± 0.5 % for the last step. No nitrogen was found in the He^+ treated sample, as expected. As helium is undetectable in XPS measurements, the amount of helium remaining in the sample after the ion implantation remains unknown. However, since helium is non-reactive and has a high diffusion coefficient, due to its small size, we expect the amount remaining in the treated sample to be negligible.

The use of a Ta foil as an energy diffuser results in the incorporation of this element. XPS data confirmed the low presence of Ta in all treated samples, with amounts ranging from 0.15 % for the He^+ treated samples to 0.3 % – 0.7 % for the N^+ treated samples.

To elucidate the modification of the chemical structure caused by ion implantation, high resolution (HR) XPS spectra of C_{1s}, O_{1s} and N_{1s} were obtained. Figure 4.23 shows the HR XPS spectra of C_{1s} (1st Column), O_{1s} (2nd Column) and N_{1s} (3rd Column) for the original PVA fibers (top row), as well as the N^+ (middle row) and He^+ (bottom row) implanted samples. The binding energy of each peak was used to determine the corresponding chemical functional groups present in the sample. Every peak was labeled alphabetically as shown in Figure 4.23. Table 4.12 provides the list of functional groups consistent with each peak position and the corresponding binding energy. The C_{1s} and O_{1s} spectra for the untreated PVA fibers matched standard PVA in the database [309]. The curve-fitted peak A (C–C) and B in the C_{1s} spectrum have atomic distribution of 53.4 ± 0.6 % and 46.6 ± 0.6 %, respectively. In this case, the functional group C–OH (alcohol) was the only possibility to explain peak B, as well as the peak E (100 %) in the O_{1s} spectrum.

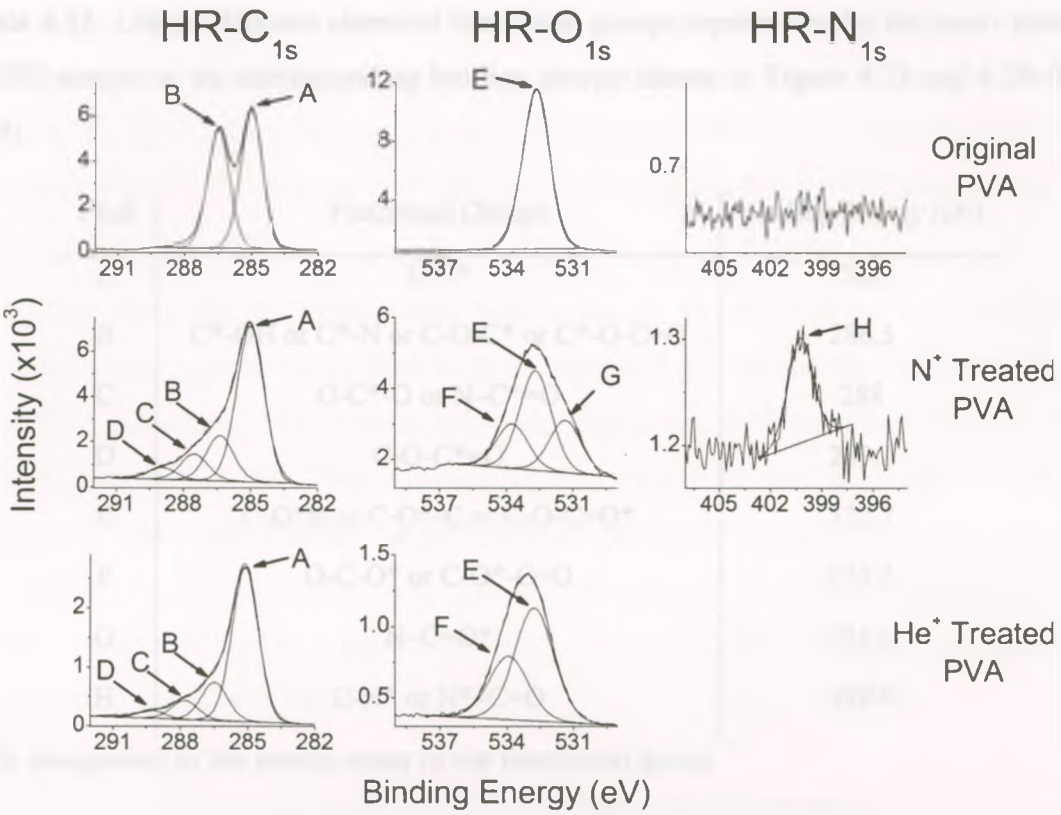

Figure 4.23. High resolution XPS spectra for C_{1s} (left column), O_{1s} (middle column) and N_{1s} (right column), measure for untreated (top row), 1.6×10^{16} ions/cm² of N^+ treated (middle row) and 1.6×10^{16} ions/cm² of He^+ (bottom row) PVA fibers. The peaks are interpreted on terms of contributions from various chemical groups (lettered peaks), as defined in Table 4.12.

After N^+ treatment, the most obvious change was a new peak H (100 %) that occurred in the N_{1s} spectrum. This confirmed that implantation of reactive ions results in chemical reactions. New functional groups include a reaction product with carbon in PVA to form C–N (amine) or N–C=O (amide) bonds. In the O_{1s} spectrum, two new peaks (F and G) occurred after the N^+ implantation. Peak G, with a binding energy of 399.9 eV, corresponds to an N–C=O (amide) group. Combining the results with the N_{1s} spectrum allows us to confirm the formation of an amide group via N^+ implantation. Furthermore, the percentage of peak G in the O_{1s} spectrum increased with N^+ dose, starting from 21 ± 2 % for the first dose, increasing to 31 ± 1 % after the second step, and reaching 35.8 ± 0.2 % for the last step. This shows that a strong correlation between the relative concentration and the dose of N^+ implanted in the sample exists.

Table 4.12. List of different chemical functional groups represented by the peaks labeled in XPS spectra at the corresponding binding energy shown in Figure 4.23 and 4.28–4.30 [309].

Peak	Functional Groups	Binding Energy (eV)
A	C-C*	285
B	C*-OH or C*-N or C-O-C* or C*-O-C=O	286.5
C	O-C*-O or N–C*=O	288
D	C-O-C*=O	289.1
E	C-O*H or C-O*-C or C-O-C=O*	532.7
F	O-C-O* or C-O*-C=O	533.5
G	N–C=O*	531.5
H	C-N* or N*–C=O	399.9

* is designated to the source atom in the functional group

C_{1s} spectra evolved almost identically for N^+ and He^+ treatment with two new peaks (C and D) supplementing the two original peaks (A and B), as shown in Figure 4.23. Since peak C has the same binding energy as the carbon in the amide group, the designation of peak C in the N^+ implanted sample appeared obvious. However, the observation of the same peak C for the He^+ implantation proved this peak is not exclusive to an amide group. In fact, peak C can also be due to the oxygen-containing hydrocarbon group O–C–O. This observation explains the trend of the percentage of peak C, which started at 11.1 ± 0.2 % after the first N^+ dose and decreased to 4.2 ± 0.1 % with the last dose. As the O_{1s} spectrum shows, the number of amide groups indeed increased steadily with the N^+ dose, but the overall number of oxygen atoms dropped as the dose is increased. As more and more oxygen atoms are recoiled, the implantation process changed from creating O–C–O groups to eliminating them. Peak C has a percentage of 8.7 ± 0.1 % after the first He^+ dose, and then remains at 10 ± 0.1 % after the second dose.

The new peak D, with a binding energy at the high-end of the C_{1s} data envelope, belongs to carbon in the carbonyl part of the C–O–C=O (carboxyl) group, for which the

other carbon contributes to peak B. Peak D shows a trend similar to that of peak C: beginning at 5.5 ± 0.2 % after the first dose of N^+, it drops to 3.0 ± 0.1 % with the third dose. For the He^+ treated sample, the carboxyl group is also created at a slightly lower percentage of 3.6 ± 0.1 % from the first dose, and remains at 4.6 ± 0.1 % after the second dose.

Generally, the ion implantation process recoils hydrogen atoms at a rate higher than carbon and oxygen atoms from both the hydroxyl groups and the carbon backbone of the PVA molecules. We know that C–O–C groups can be formed between two PVA chains as a cross-link [62]. This is especially relevant to PVA as it belongs to a category of polymers favoring cross-linking [231] during the implantation process. We were not able to confirm this conclusion with our XPS data because the C-O-C binding energy overlaps with other peaks. A similar situation occurred for the C-N (amine) group with signals mixed in peaks H and B.

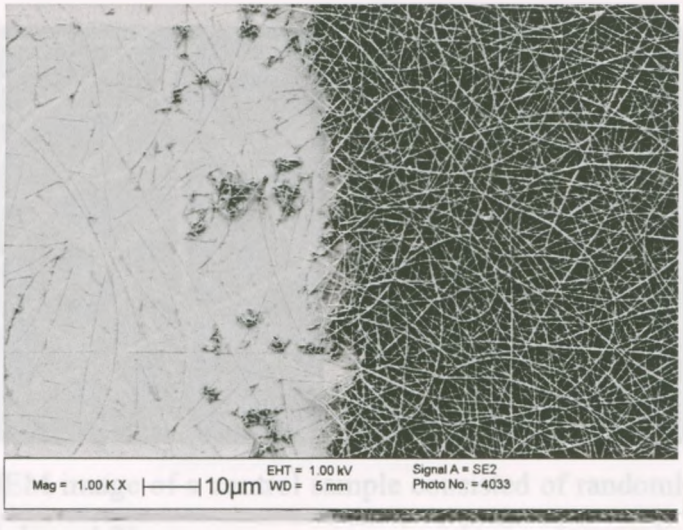

Figure 4.24. SEM image of the boundary area of the original (left side) and treated fibers (right side) after 10 minutes of soaking in DI water.

To confirm the introduction of cross-linking by the N^+ treatment, we conducted a solubility test on the PVA fibers pre- and post-treatment with 1.2×10^{16} ions/cm^2 of N^+. Figure 4.24 shows an SEM image of the boundary area of the original (left side) and N^+ treated fibers (right side) after 10 minutes of soaking in DI water. All the original fibers

on the left side dissolved. It can be seen that the untreated fibers produced from an aqueous solution is stabilized by cross-linking and are stable against dissolution when exposed to DI water.

4.5 Cell Compatibility of Electrospun PVA Fibrous Scaffolds

4.5.1 Modifying PVA Fibers for *In Vitro* Cell Compatibility Evaluation

In vitro tests based on primary human skin fibroblasts (hsF) were conducted to determine the cell compatibility of the modified random and aligned PVA fibers, as shown in Figure 4.25(a) and (b) respectively. The as-spun PVA fibers were not stable in an aqueous environment including cell culture media, stabilization through thermal annealing for four hours at 135°C was applied, as outlined in section 4.3. The fibers demonstrated the stability in DI water for up to 30 days.

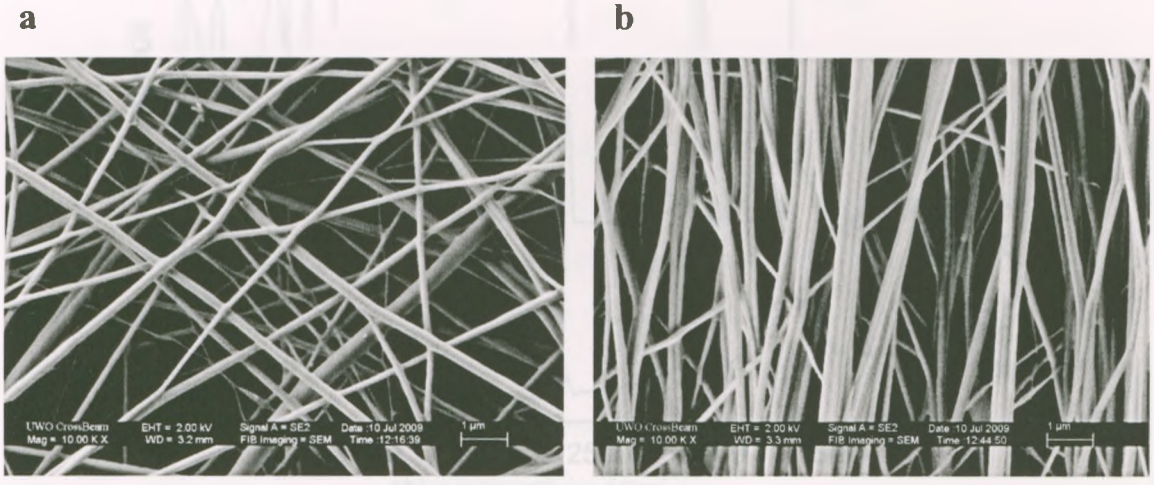

Figure 4.25. (a) SEM image of a control sample consisted of randomly orientated fibers (b) SEM image of aligned fibers.

Figure 4.26 shows FTIR spectra of the PVA fibers before and after the thermal annealing. Table 4.13 provides the list of functional groups associated with each peak and their wavenumbers [310]. The comparison shows that the only change is the increase in the intensity of the peak at wavenumber 2300 cm^{-1} (associated with O–C–O) after the thermal annealing. Easy-to-eliminate hydroxyl (–OH) groups along the PVA chain

produce H–O–H, C–O, O–C–O and C–O–C during thermal degradation [311]. From the XPS survey spectra shown in Figure 4.27, the ratio of oxygen and carbon content remained the same at 28:73 before and after the annealing. The introduction of C–O–C bonds is confirmed in the peak B of HR XPS C_{1s} spectra shown in Figure 4.28, as the C–C and C–OH bonds are transformed into C–O–C bonds, the intensity of peak A is decreased below that of peak B after annealing [61, 312]. Otherwise, the annealed PVA fibers have a similar chemical composition as the as-spun PVA fibers, but are stable in an aqueous environment; they were used as the control sample in the *in vitro* cell compatibility test.

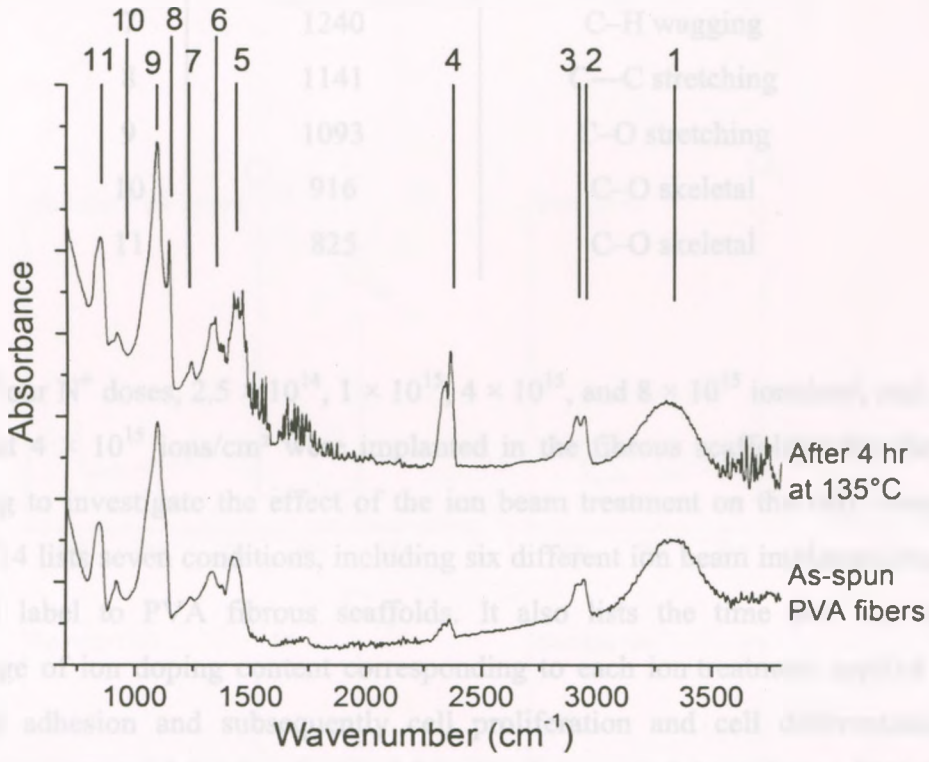

Figure 4.26. FTIR spectra of as-spun PVA fibers and the fibers after 4 hours of 135°C annealing (arbitrary scale on absorbance intensity and offset for clarity). The peaks are labeled numerically for various chemical groups, as defined in Table 4.13

Table 4.13. List of different chemical functional groups represented by the peaks labeled in FTIR spectra at the corresponding wavenumber shown in Figure 4.26 [310].

Peak #	Peak Position (cm^{-1})	Assignment
1	3300	O–H stretching
2	2950	C–H stretching (symmetric)
3	2900	C–H stretching
4	2300	O–C–O stretching
5	1425	CH_2 bending
6	1330	CH_2 wagging
7	1240	C–H wagging
8	1141	C—C stretching
9	1093	C–O stretching
10	916	C–O skeletal
11	825	C–O skeletal

Four N^+ doses, 2.5×10^{14}, 1×10^{15}, 4×10^{15}, and 8×10^{15} ions/cm², and one dose of He^+ at 4×10^{15} ions/cm² were implanted in the fibrous scaffolds after the thermal annealing to investigate the effect of the ion beam treatment on the cell compatibility. Table 4.14 lists seven conditions, including six different ion beam implantations, with an assigned label to PVA fibrous scaffolds. It also lists the time and the theoretical percentage of ion doping content corresponding to each ion treatment applied to PVA. The cell adhesion and subsequently cell proliferation and cell differentiation on a polymer are governed by the chemical functional groups of the polymer [73]. The XPS survey spectra (Figure 4.27) show that N^+ and He^+ treatments induced carbonization effects to PVA. The carbonization effect increases as the N^+ dose increases. XPS was only able to detect nitrogen in the samples implanted with the highest dose of N^+ (8×10^{15} ions/cm²), because the other three treatments with lower N^+ dose were having the total nitrogen content below 0.1 %. Table 4.14 lists the theoretical percentage of nitrogen content corresponding to each N^+ treatment in PVA.

Table 4.14. List of seven differently treated PVA fibrous scaffolds.

Sample	Condition	Ion Treatment Time	Theoretical ion doping content in PVA
C	4 hr at 135°C annealed PVA fibers (control)	0	0
N1	2.5×10^{14} N^+/cm^2 treated, annealed random fibers	~8 min	0.002 %
N2	1×10^{15} N^+/cm^2 treated, annealed random fibers	~32 min	0.01%
N3	4×10^{15} N^+/cm^2 treated, annealed random fibers	~2.1 hr	0.04%
N4	8×10^{15} N^+/cm^2 treated, annealed random fibers	~4.3 hr	0.1%
N3A	4×10^{15} N^+/cm^2 treated, annealed aligned fibers	~2.1 hr	0.04%
He3	4×10^{15} He^+/cm^2 treated, annealed random fibers	~2.1 hr	0.04%

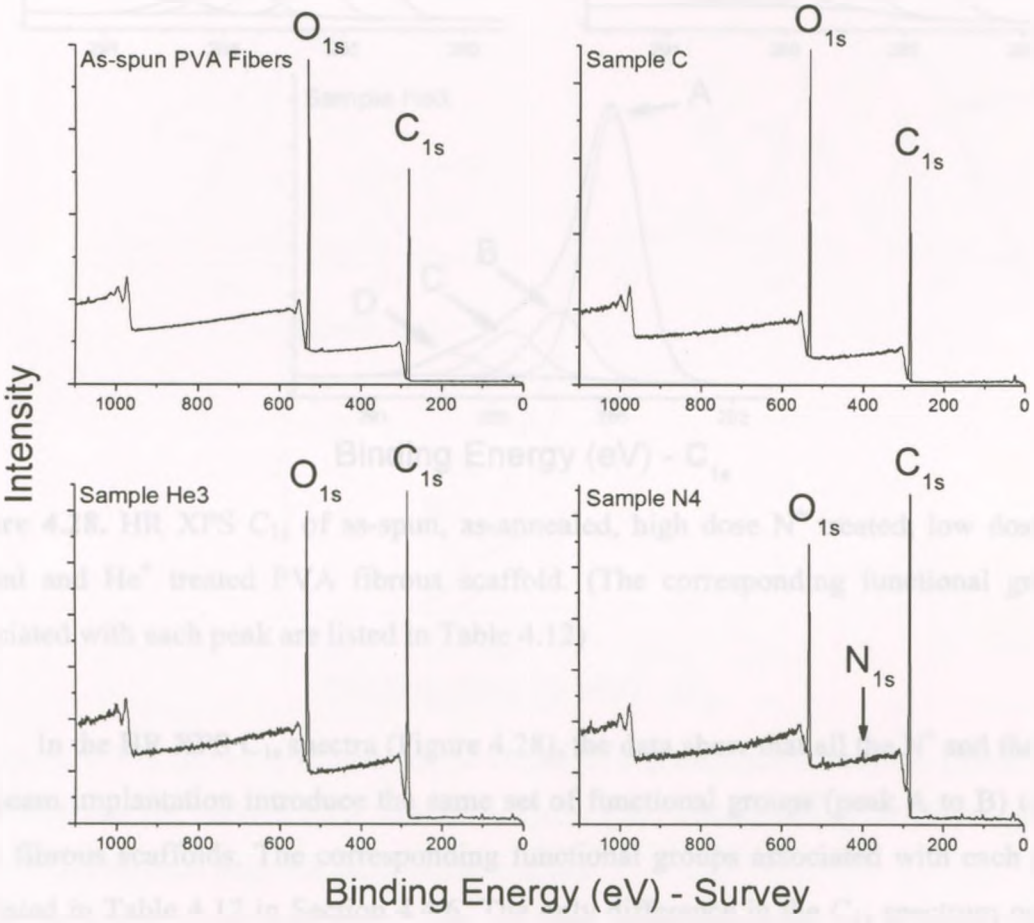

Figure 4.27. XPS survey spectra of as-spun, as-annealed, N^+ treated and He^+ treated PVA fibrous scaffold.

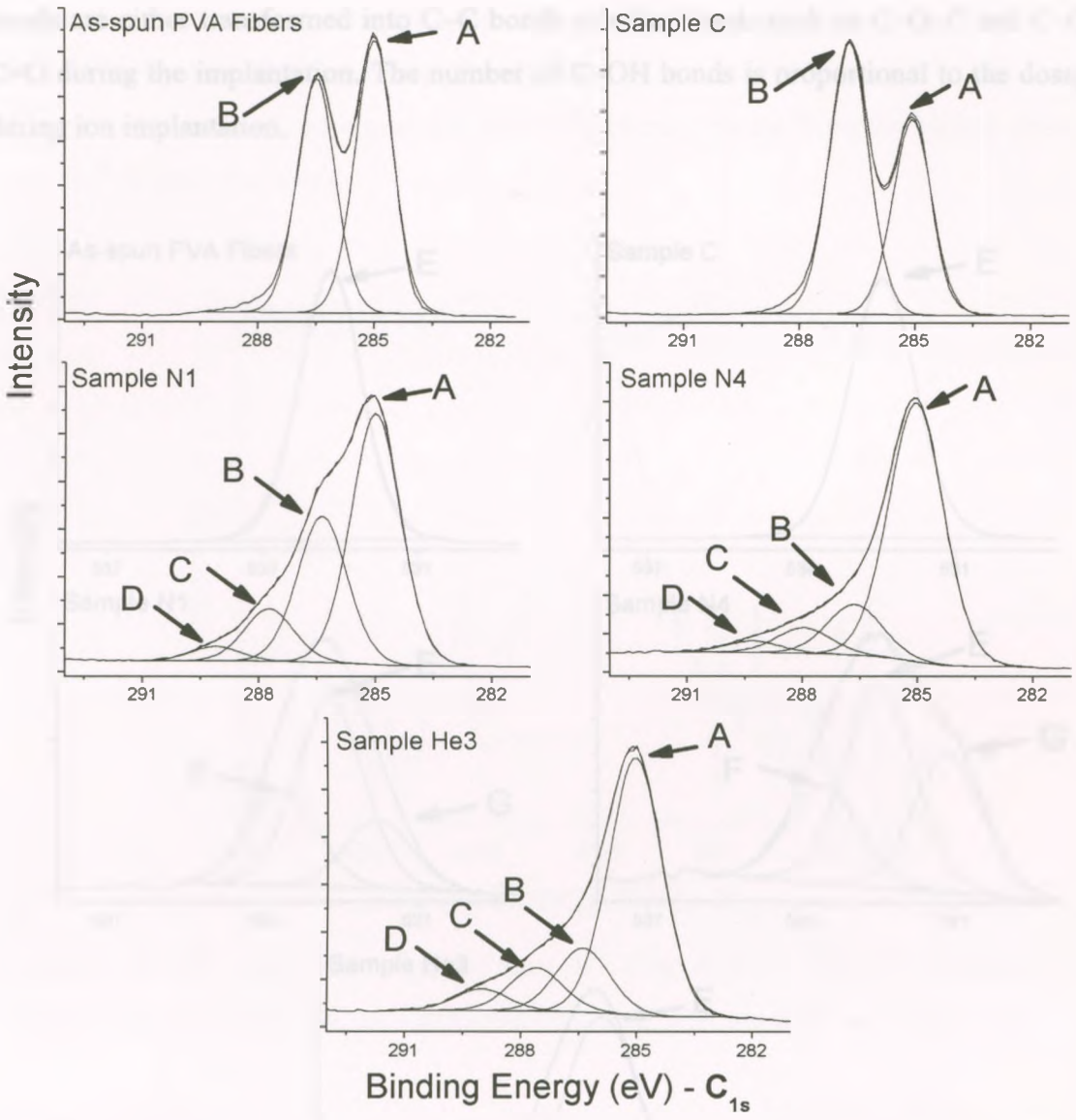

Figure 4.28. HR XPS C_{1s} of as-spun, as-annealed, high dose N^+ treated, low dose N^+ treated and He^+ treated PVA fibrous scaffold. (The corresponding functional groups associated with each peak are listed in Table 4.12)

In the HR XPS C_{1s} spectra (Figure 4.28), the data show that all the N^+ and the He^+ ion beam implantation introduce the same set of functional groups (peak A to B) to the PVA fibrous scaffolds. The corresponding functional groups associated with each peak are listed in Table 4.12 in Section 4.4.6. The only difference in the C_{1s} spectrum occurs for peak B when comparing the high dose and the low dose N^+ treated samples: the peak intensity decreases as the dose of N^+ implantation increases. This means that C–OH

bonds are either transformed into C–C bonds or other bonds such as C–O–C and C–O–C=O during the implantation. The number of C–OH bonds is proportional to the dosage during ion implantation.

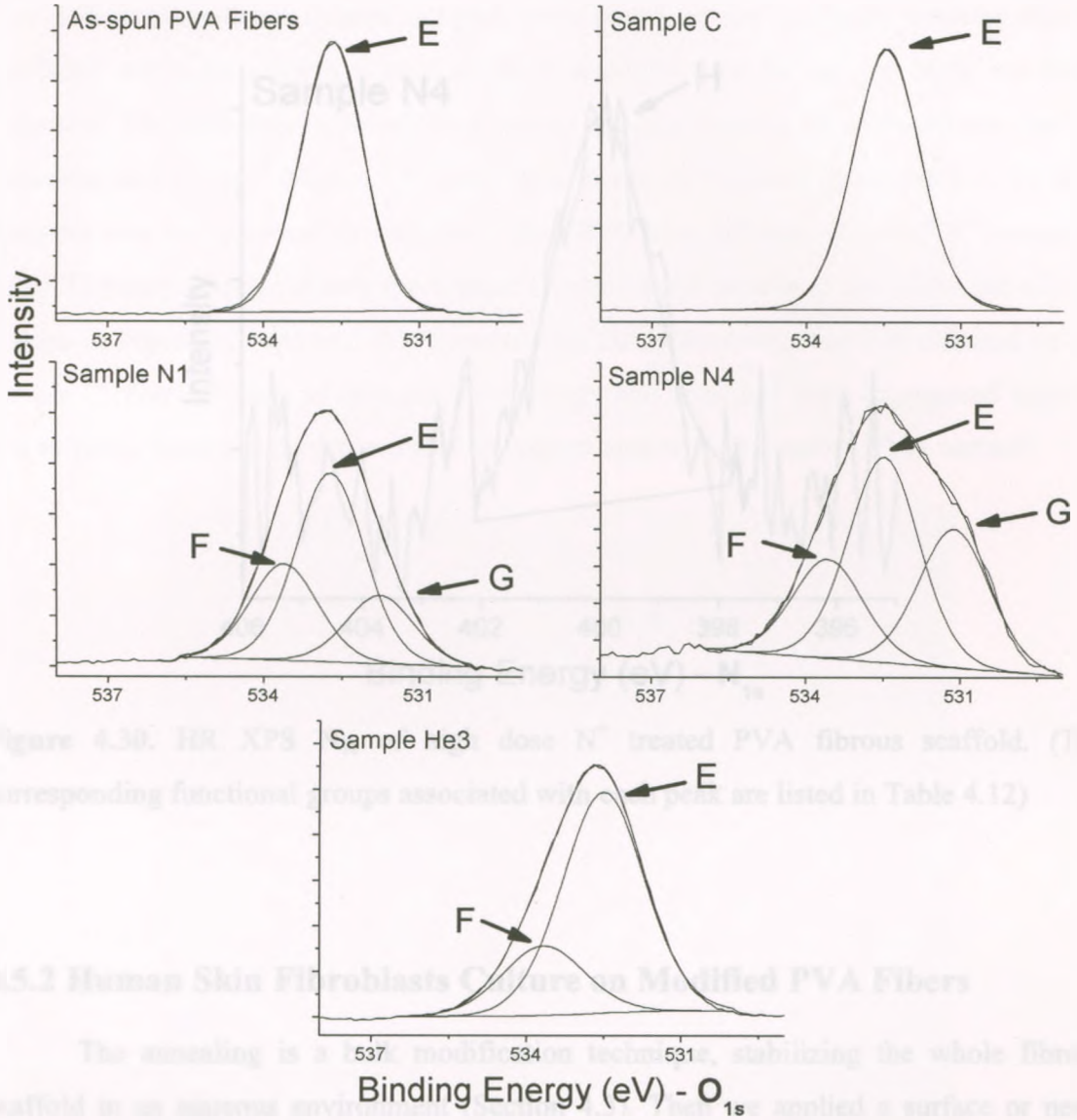

Figure 4.29. HR XPS O_{1s} of as-spun, as-annealed, highest dose N^+ treated, lowest dose N^+ treated and He^+ treated PVA fibrous scaffold. (The corresponding functional groups associated with each peak are listed in Table 4.12)

In the HR XPS O_{1s} spectra (Figure 4.29), the changes in the chemical structure noted for both the N^+ and the He^+ implantation are almost identical to the XPS results

discussed in Section 4.4.6. The intensity of the amide group associated peak G increases as the N^+ dose increases. In contrast, the HR XPS N_{1s} spectrum (Figure 4.30) only detects nitrogen and the associated amine and amide functional groups from the highest dose of 8.0×10^{15} N^+/cm^2 treatment.

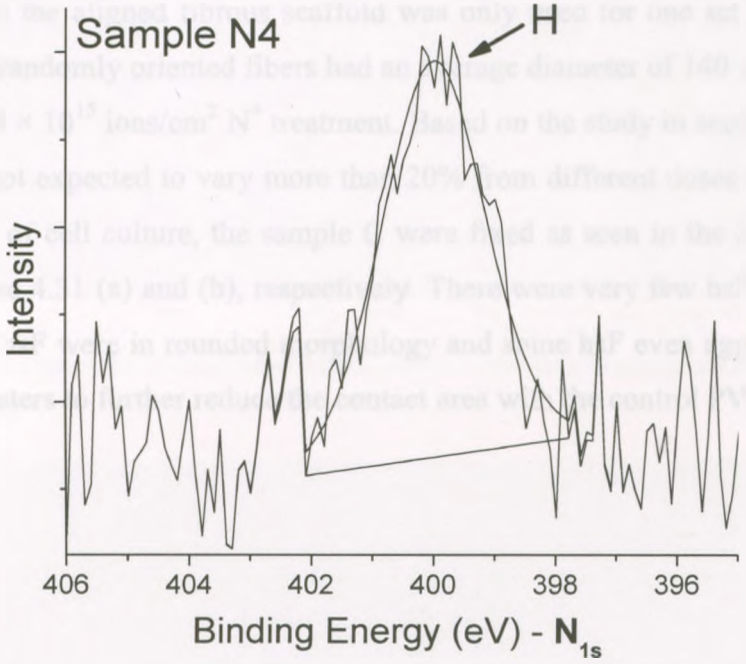

Figure 4.30. HR XPS N_{1s} of high dose N^+ treated PVA fibrous scaffold. (The corresponding functional groups associated with each peak are listed in Table 4.12)

4.5.2 Human Skin Fibroblasts Culture on Modified PVA Fibers

The annealing is a bulk modification technique, stabilizing the whole fibrous scaffold in an aqueous environment (Section 4.3). Then we applied a surface or near-surface modification to the fibrous scaffold using the ion beam treatment with 4 different doses of N^+ in a range of 2.5×10^{14} to 8×10^{15} ions/cm^2 and He^+ in 4×10^{15} ions/cm^2, as described in Section 4.4. Although, the ion beam treatment also stabilizes the fibers in the aqueous environment (section 4.4.5), the affected layer is superficial, limited to ~1 μm due to the ion implantation depth. Therefore, a combination of both post-processing

modifications is necessary for the PVA scaffolds to have aqueous stability for cell adhesion and proliferation.

Two fiber orientations, one random and one aligned, were used in the *in vitro* test as illustrated in Figure 4.25 (a) and (b), respectively. The control samples as well as the five different ion beam treated samples were based on the randomly oriented fibrous scaffolds, while the aligned fibrous scaffold was only used for one set of N^+ ion beam treatment. The randomly oriented fibers had an average diameter of 140 ± 40 nm after the annealing and 4×10^{15} ions/cm^2 N^+ treatment. Based on the study in section 4.4, the fiber diameter was not expected to vary more than 20% from different doses of N^+ treatment. After 72 hours of cell culture, the sample C were fixed as seen in the SEM and CLSM images in Figure 4.31 (a) and (b), respectively. There were very few hsF attached on the sample C. The hsF were in rounded morphology and some hsF even aggregated together and formed clusters to further reduce the contact area with the control PVA surface.

a

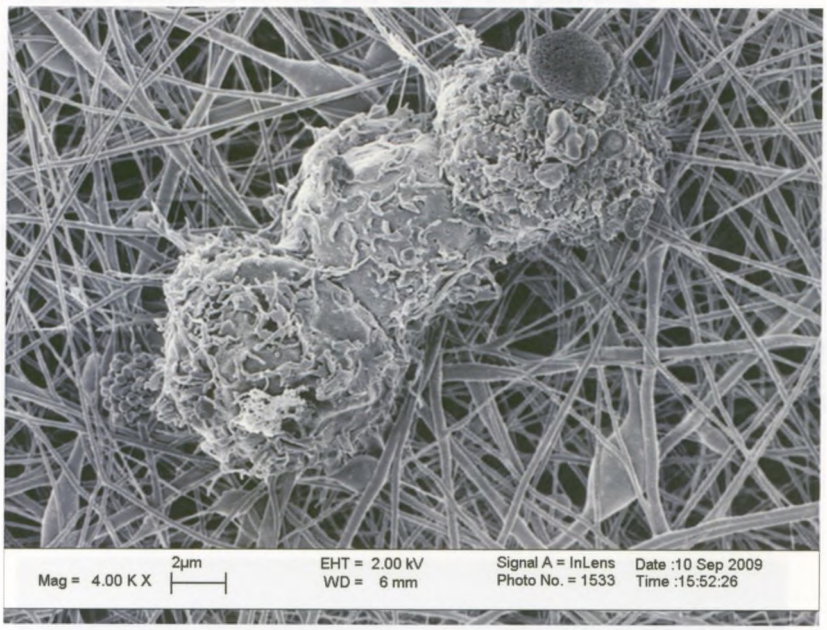

b

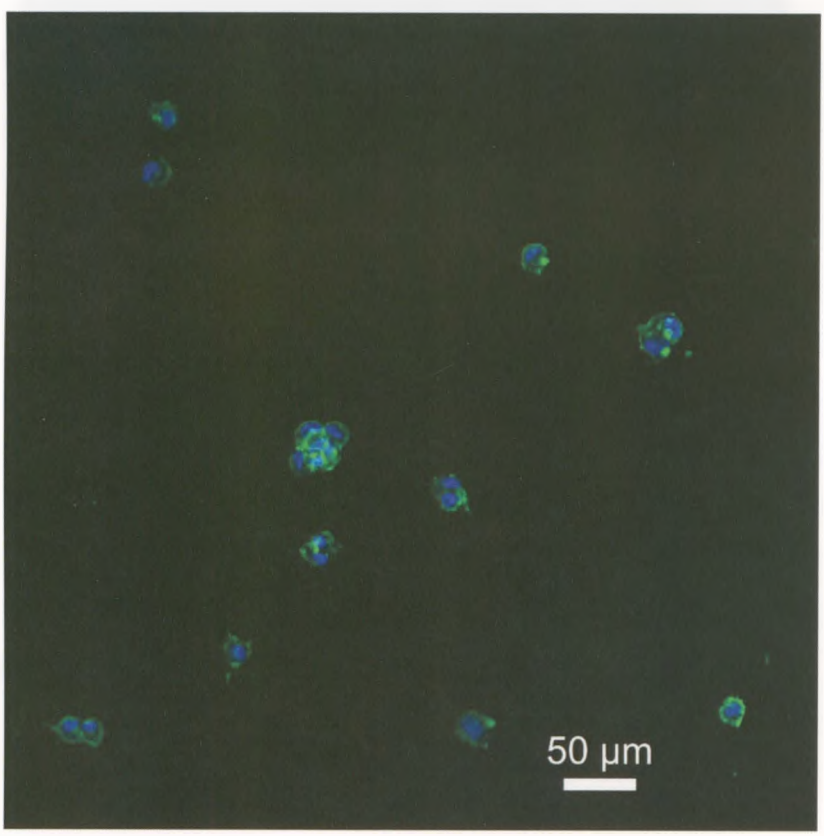

Figure 4.31. (a) SEM image and (b) CLSM image of hsF on a sample C after 72 hours of culture.

4.5.3 Effect of Ion Implantation on Cell Morphology

The CLSM image in Figure 4.32 shows the hsF on the sample N4 after 72 hours of culture. The hsF were spread out individually in random orientation with actin-aggregated stress fibers clearly visible and stretching out, which was a clear indication of good adhesion to the fibers. Figure 4.33 shows an SEM image of the same sample. The low magnification image (Figure 4.33a) displays a similar result of the hsF attachment and morphology, as shown with the CLSM image in Figure 4.32. The high magnification SEM image (Figure 4.33b) highlights one end of an hsF with lamellipodia and filopodia extending outward at different directions.

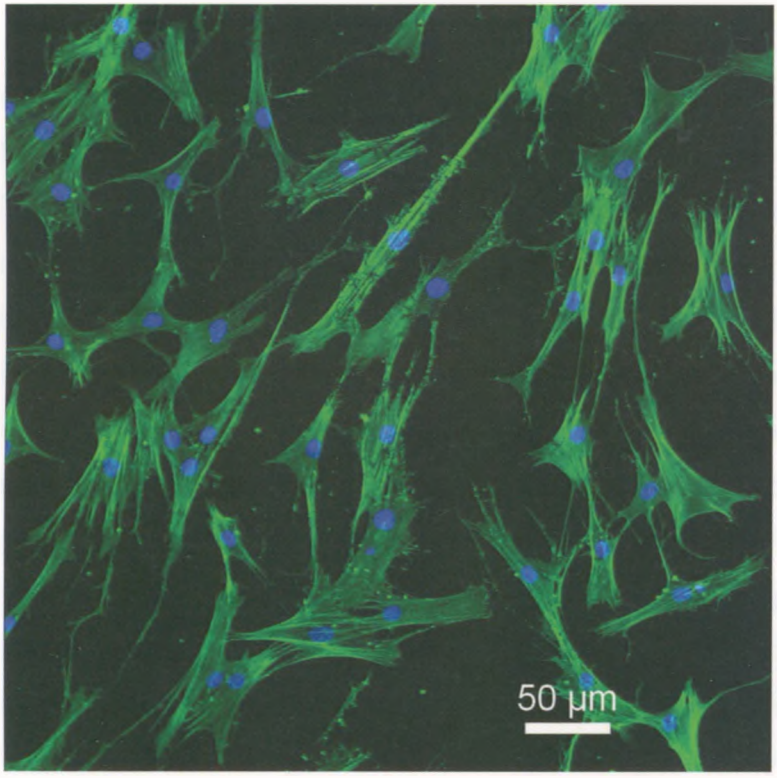

Figure 4.32. CLSM image of hsF on a sample N4 after 72 hours of culture.

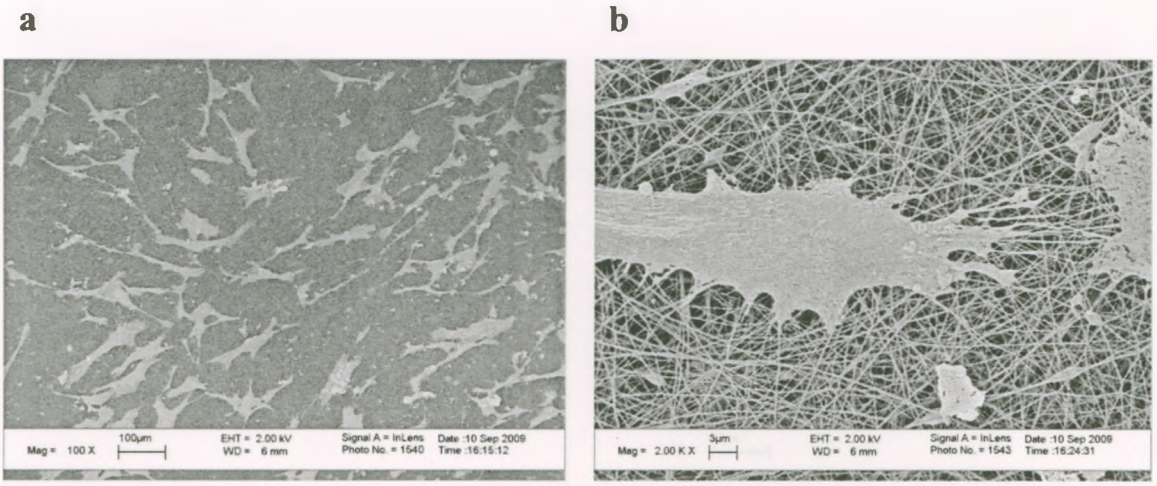

Figure 4.33. (a) Low and (b) high magnification SEM images of hsF on a sample N4 after 72 hours of culture.

After observing the successful hsF adhesion and spreading on the sample N4, N^+ treatments with lower dose of 4×10^{15} and 1×10^{15} ions/cm^2 were applied to study the effect of the N^+ dosage on the hsF. The stellar / bipolar morphology of attached hsF after 72 hours of culture on the samples N3 and N2 (the images of different time stage are shown in Figure 4.40) were similar to the result of the sample N4. The lowest N^+ dose applied to the scaffold in this study is 2.5×10^{14} ions/cm^2, which is 32 times less than the dose applied to the sample N4. The 72 hours of hsF culture result on the sample N1 is shown in Figure 4.34 and demonstrates no significant difference in terms of hsF adhesion and morphology when compared to the other results from the three samples with higher dosages. Similar hsF spreading and the extension of lamellipodia and filopodia are again observed on the sample N1. In summary, the number of nitrogen ion dose does not play a significant role in terms of the hsF adhesion, morphology and spreading. The actual number of hsF attached and the hsF growth rate over a period up to 10 days are discussed in a later section.

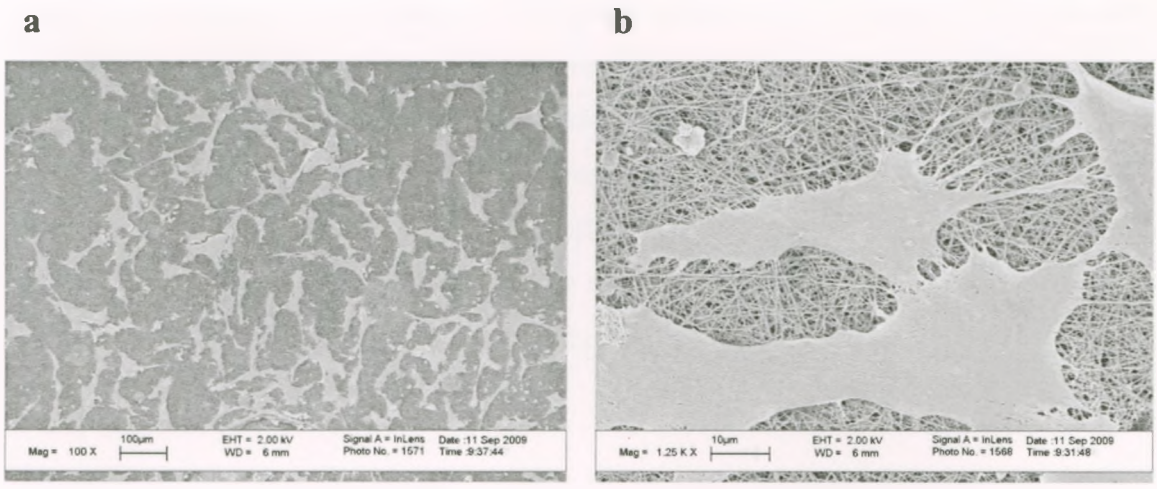

Figure 4.34. (a) Low and (b) high magnification SEM images of hsF on a sample N1 after 72 hours of culture.

Using non-reactive helium to modify the surface of the fibrous scaffold, the XPS data (Section 4.5.1) showed that the helium treatment modified the chemical structure of PVA similarly as the nitrogen treatment, but without introducing any amine and amide functional groups. Figure 4.35a shows the result of the hsF on a sample He3 after 72 hours of culture. The hsF appeared to be spreading out randomly and attaching to the fibers individually. In Figure 4.35b, a high magnification SEM image of a single hsF showed that the lamellipodia and filopodia were extending in all directions. A higher magnification SEM image (Figure 4.35c) captures the lower part of the hsF shown in Figure 4.35b. It shows that the filopodia extended outward and are entangled with the fiber network (these were also observed on all nitrogen treated samples). The results of the hsF adhesion and morphology on the sample He3 are therefore very similar to the results obtained for nitrogen treated samples. These results again confirm our previous observations on the hsF as a function of N^+ dosage that the nitrogen-containing (amine and amide) functional groups formed during the nitrogen treatment did not provide any additional advantage for hsF adhesion, morphology and spreading. Proliferation assay on three different incubation times is reported in a later section to quantify the difference between the nitrogen and the helium treatment.

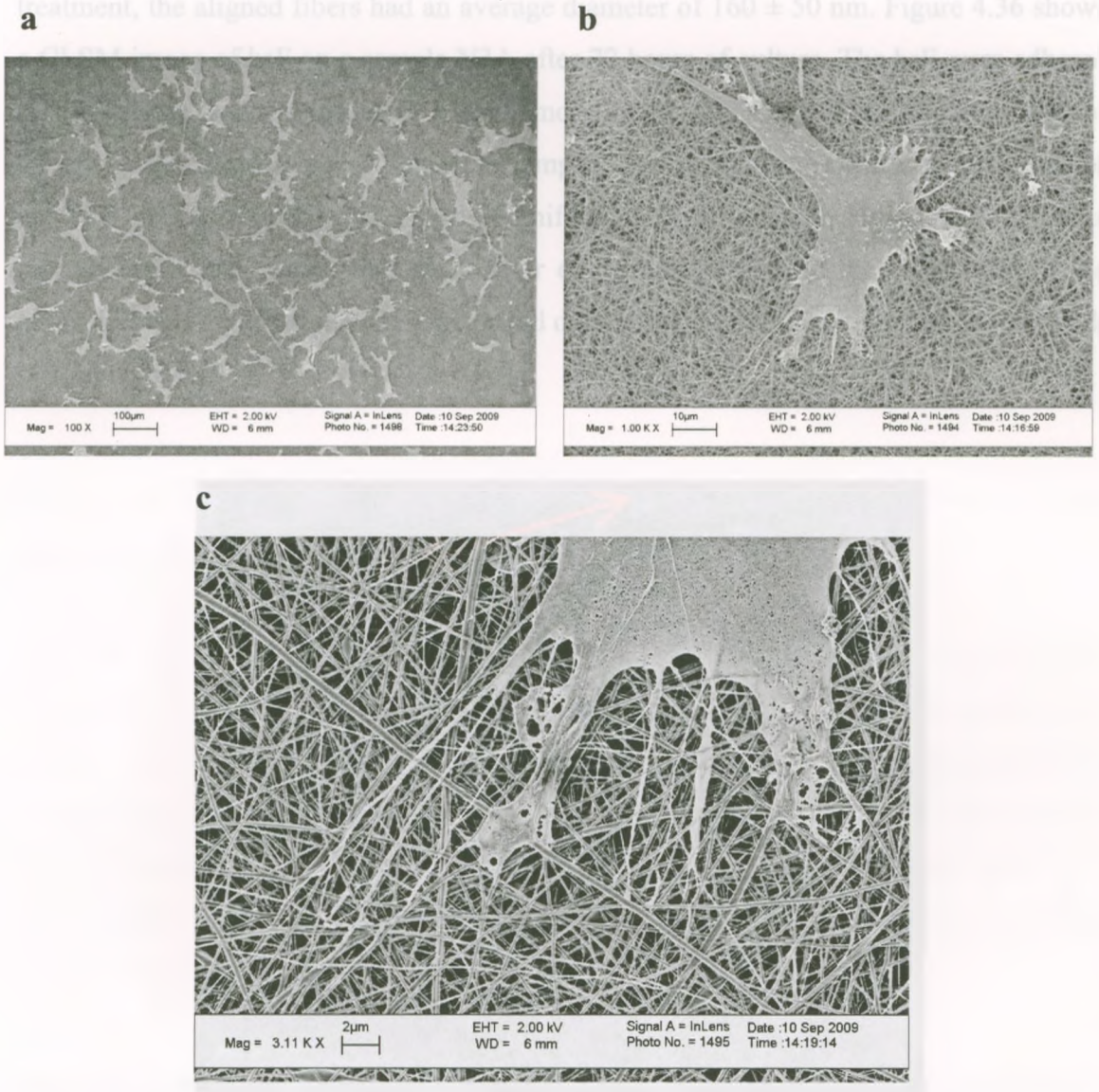

Figure 4.35. (a) Low and (b) high magnification SEM images of hsF on a sample He3 after 72 hours of culture. (c) High resolution SEM image of the extended filopodia in the lower part of the hsF shown in (b).

4.5.4 Effect of Fiber Orientation on Cell Morphology

The role of the surface morphology (topography) on the interaction of hsF with the fibrous scaffold was investigated. The morphological analysis of hsF adhesion, morphology and spreading was conducted on a scaffold that consisted of aligned fibers, as Figure 4.25b shows. After the thermal annealing and the 4×10^{15} ions/cm^2 of N^+

treatment, the aligned fibers had an average diameter of 160 ± 50 nm. Figure 4.36 shows a CLSM image of hsF on a sample N3A after 72 hours of culture. The hsF were adhered to the surface and elongated in bipolar morphology along the same direction. Figure 4.37a shows a SEM image of the same sample. The image further confirms that most of hsF had bipolar morphology. A high magnification SEM image in Figure 4.37b shows a representative hsF, which had the bipolar elongation parallel to the orientation of the aligned fibers. The filopodia were extended outward and entangled with the fiber network in all directions.

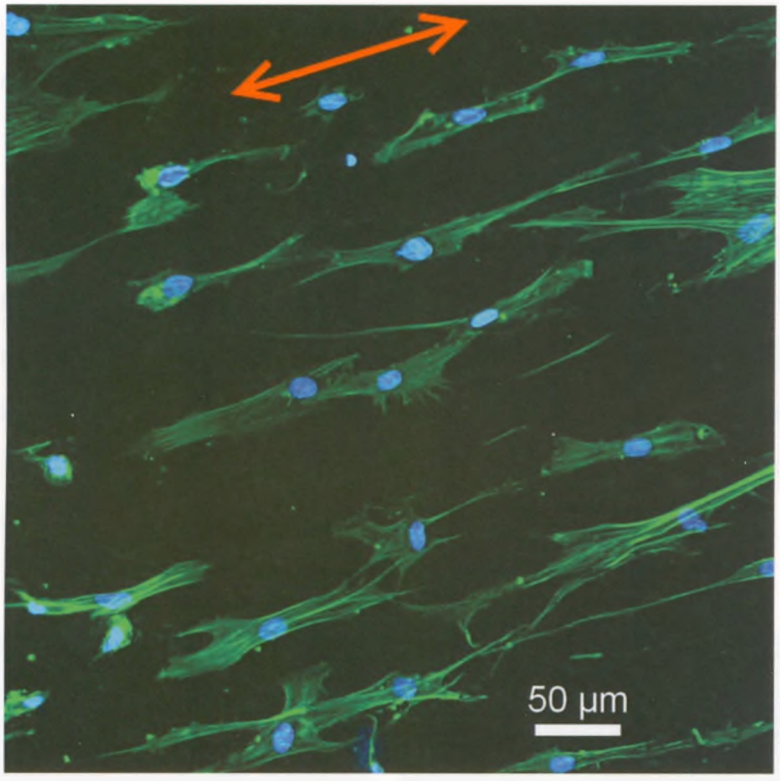

Figure 4.36. CLSM image of hsF on a sample N3A after 72 hours of culture. (The arrow indicates the oriented direction of the fibers)

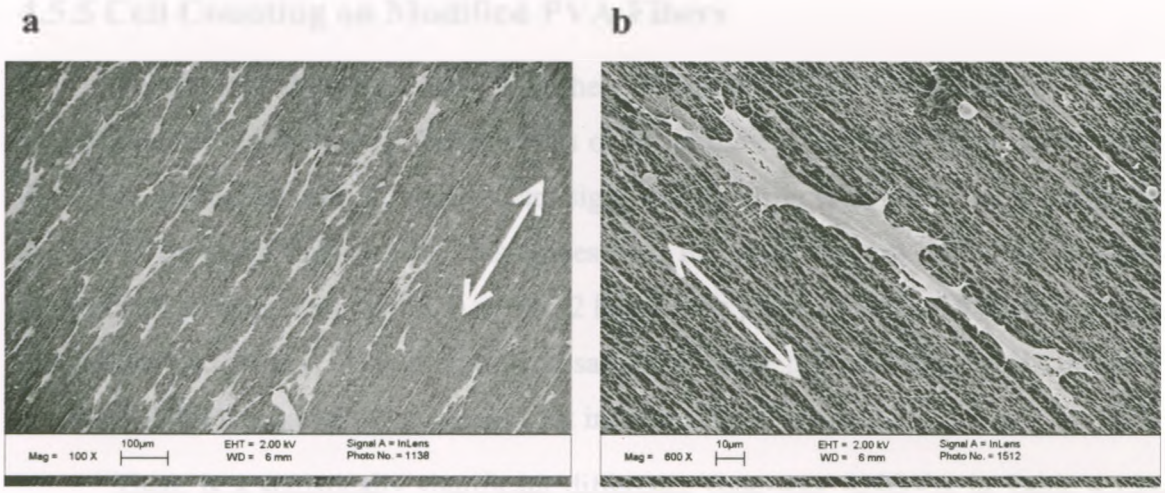

Figure 4.37. (a) Low and (b) high magnification SEM images of hsF on a sample N3A after 72 hours of culture.

On the same sample, several hsF infiltrated underneath the surface layer of the sample N3A, as the SEM image in Figure 4.38a shows. The morphology of the hsF was similar to the hsF attached to the surface layer. A high magnification SEM image (Figure 4.38b) clearly shows that there was a layer of fibers lying on top of the infiltrated hsF. The fiber network on top of the hsF was still intact with the fibers lying next to the hsF. This suggests that the hsF migrated into the scaffold through the small holes along the fiber network during the 72 hours of culture.

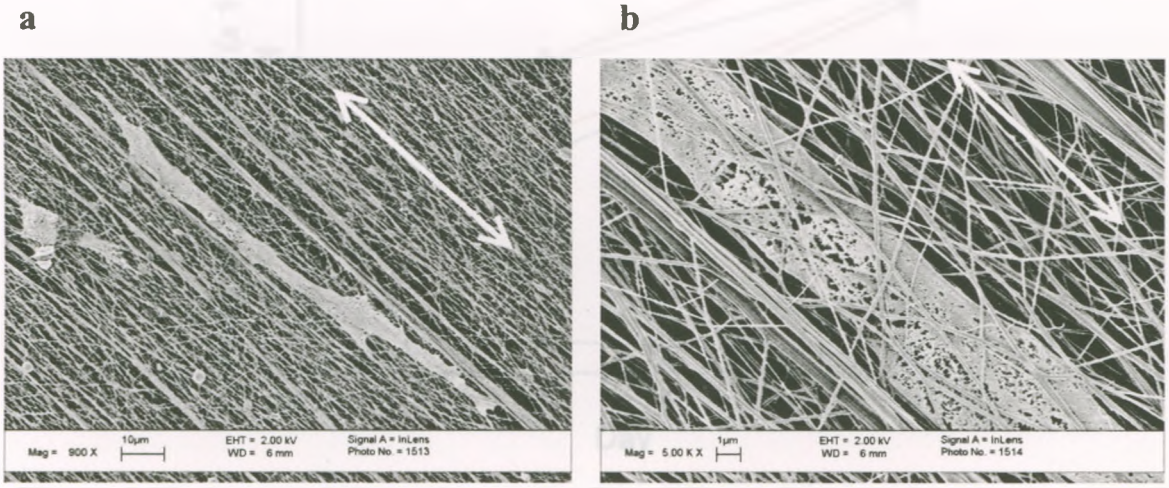

Figure 4.38. (a) Low and (b) high magnification SEM images of a hsF migrated and attached to the second layer of fibers on a sample N3A.

4.5.5 Cell Counting on Modified PVA Fibers

Figure 4.39 shows the results of the cell count on the control samples and the samples treated by the four different doses of N^+ at three time points for a period of 10 days. The number of hsF on sample C are significantly lower than the N^+ treated samples at each of the three time points. This agrees with the observation we obtained from the microscopic images (section 4.5.2) at the 72 hours time point. Over the 10 days of culture, the hsF showed no sign of proliferation on sample C as the hsF numbers did not increase, while all N^+ treated samples had significant increase in hsF numbers.

There is a statistically significant difference (one-way ANOVA in Table 4.15a) between the samples N1/N4 and N2/N3 after 1 day of culturing, but the numbers are relatively closed for all four samples. Figure 4.40 shows the SEM images of the samples N1 to N4 at all three time points. Cell densities on the samples after day 1 were low and the hsF were distributed randomly on the scaffold. The culture time of 1 day may not be long enough for the hsF to begin the proliferation. Most of the hsF were elongated in bipolar morphology, and indistinguishable among all four samples.

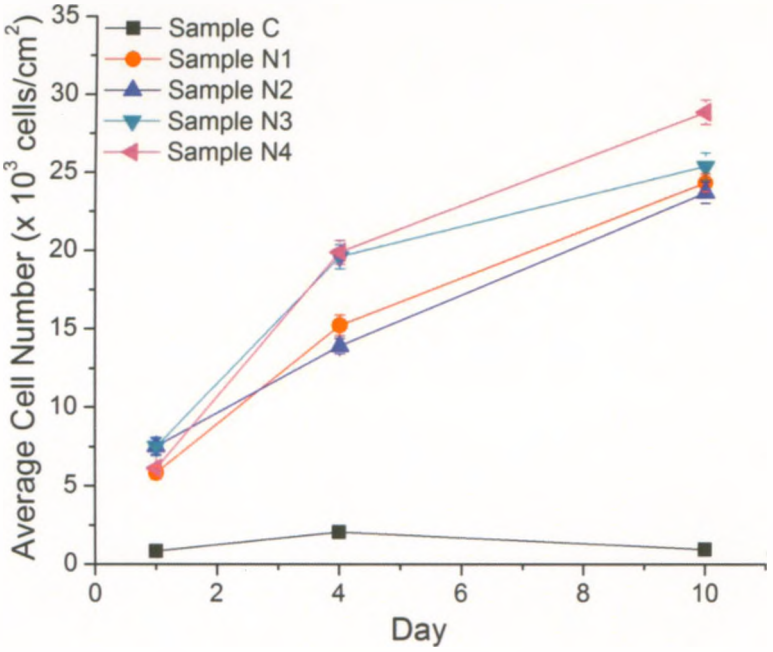

Figure 4.39. Average hsF number on the four different N^+ treated randomly oriented fibrous scaffolds after the 3 stages of culture.

At the next time point (day 4), the hsF started to proliferate and the cell numbers on the surface increased (Figure 4.39). The higher cell densities and the hsF were spreading and stretching out in all directions, leading to a larger coverage than at day 1. There is a significantly large difference (one-way ANOVA test in Table 4.15b) in cell number between samples N1 and N4. There are a 25% more hsF on the sample N4 than that of the sample N1 at day 4. When the culture time reached day 10, the sample N4 continued to maintain 16% more hsF than the sample N1 (one-way ANOVA test in Table 4.15c). A higher N^+ dose in the ion beam treatment resulted in a higher hsF proliferation rate.

As the numbers of hsF continued to increase after day 4, the area on the surface of the scaffold available for hsF to attach to was decreasing. The hsF began to form random confluence. The confluence consisted of small independent groups orientated at random with respect to other groups and were separated from the neighbors by narrow packing interstices [313].

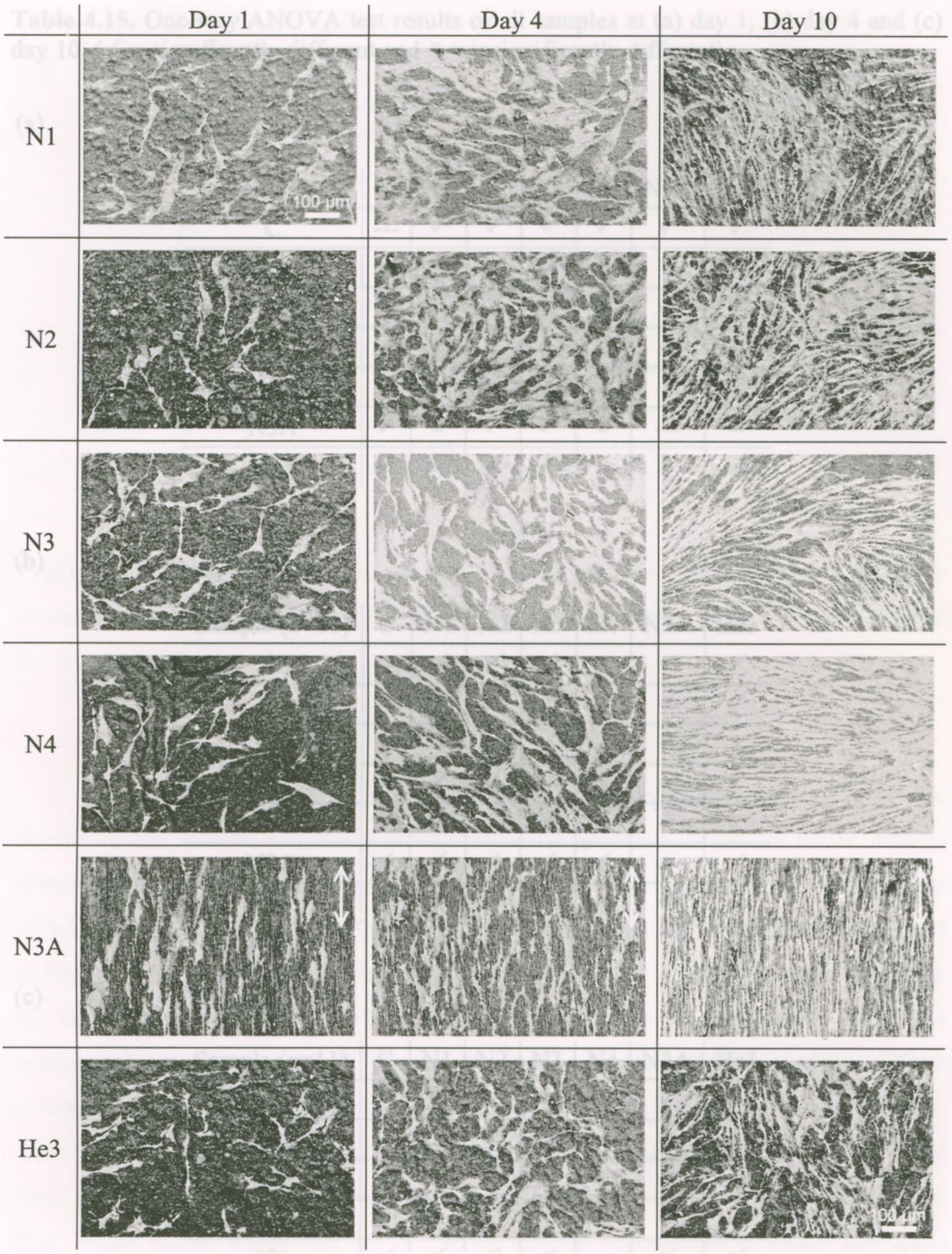

Figure 4.40. SEM image of all ion beam treated PVA fibrous scaffolds after 1, 4 and days of hsF culture. (All have the scale bar of 100 µm)

Table 4.15. One-way ANOVA test results of all samples at (a) day 1, (b) day 4 and (c) day 10. (✓ = significantly different and × = insignificantly different)

(a) Day 1

Sample (n=11)	C	N1	N2	N3	N4	N3A	He3
C	---	✓	✓	✓	✓	✓	✓
N1	✓	---	✓	✓	×	×	×
N2	✓	✓	---	×	✓	✓	✓
N3	✓	✓	×	---	✓	✓	✓
N4	✓	×	✓	✓	---	×	×
N3A	✓	×	✓	✓	×	---	×
He3	✓	×	✓	✓	×	×	---

(b) Day 4

Sample (n=11)	C	N1	N2	N3	N4	N3A	He3
C	---	✓	✓	✓	✓	✓	✓
N1	✓	---	×	✓	✓	✓	✓
N2	✓	×	---	✓	✓	✓	×
N3	✓	✓	✓	---	×	✓	✓
N4	✓	✓	✓	×	---	✓	✓
N3A	✓	✓	✓	✓	✓	---	✓
He3	✓	✓	×	✓	✓	✓	---

(c) Day 10

Sample (n=11)	C	N1	N2	N3	N4	N3A	He3
C	---	✓	✓	✓	✓	✓	✓
N1	✓	---	×	×	✓	✓	✓
N2	✓	×	---	×	✓	✓	✓
N3	✓	×	×	---	✓	✓	✓
N4	✓	✓	✓	✓	---	✓	✓
N3A	✓	✓	✓	✓	✓	---	✓
He3	✓	✓	✓	✓	✓	✓	---

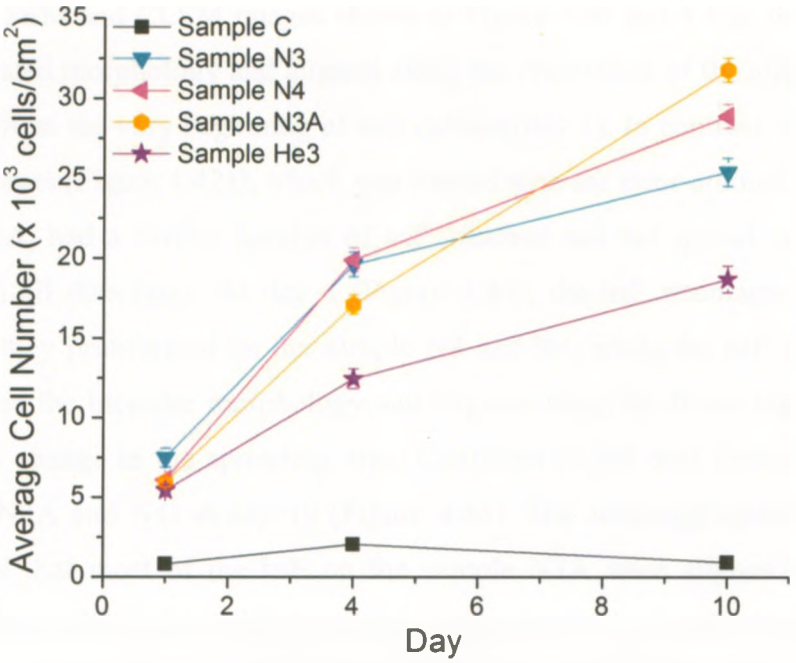

Figure 4.41 Average hsF number on the N^+ treated aligned and He^+ treated randomly oriented fibrous scaffolds after the 3 stages of culture. (Sample C, N3 and N4 are showed for comparison)

Over the 10 days of culture, Figure 4.40 shows that the sample He3 had the similar results in term of the hsF morphology and spreading as that of the N^+ treated samples. These agree with the results observed in the previous section 4.5.3. The number of hsF and the corresponding proliferation rate on the sample He3 over 10 days is plotted in Figure 4.41. Although the carboxyl introduced by He^+ treatment had a positive effect on the cell compatibility of PVA, the hsF growth rate on the sample He3 was significantly lower than all N^+ treated randomly oriented fibrous scaffolds. When compared with the results obtained from the sample N1, in which has 16 times less ion dose than that of the sample He3, the least amount of amide groups in the sample N1 still have a predominant effect to promote a higher hsF growth rate than that of the sample He3. These results shows that the N^+ doping and the introduction of amide functional groups on the surface of the PVA scaffolds has a more positive effect than carboxyl on the hsF proliferation, but the two have the similar effect on the hsF initial attachment, morphology and spreading.

As the SEM and CLSM images shown in Figure 4.40 and 4.42c, the hsF had the biopolar elongated morphology and aligned along the orientation of the aligned fibers on the sample N3A at the very beginning of cell culture (day 1). In contrast, the sample N3 with random fibers (Figure 4.42a), which was treated with the same amount of N^+ dose as the sample N3A, had a similar number of hsF attached and but spread out with stellar morphology in all directions. At day 4 (Figure 4.43), the hsF maintained the random orientation as they proliferated on the sample N3 and N4, while the hsF on the sample N3A maintained the biopolar morphology and aligned along the fibers together without any significant change in the spreading area. Confluent of hsF was formed on all three samples (N3, N3A and N4) at day 10 (Figure 4.44). The actin-aggregated stress fibers clearly showed that most of the hsF on the sample N3A were aligned in one single direction. Because the hsF morphology was maintained in a such compact, bipolar elongated form on the aligned fibers, there were more space available for the cell-matrix interactions to promote a higher cell proliferation [314, 315]. As the result shown in Figure 4.41, the final cell number of hsF on the sample N3A was even higher than that of the sample N4 treated with 2 times more of N^+ dose.

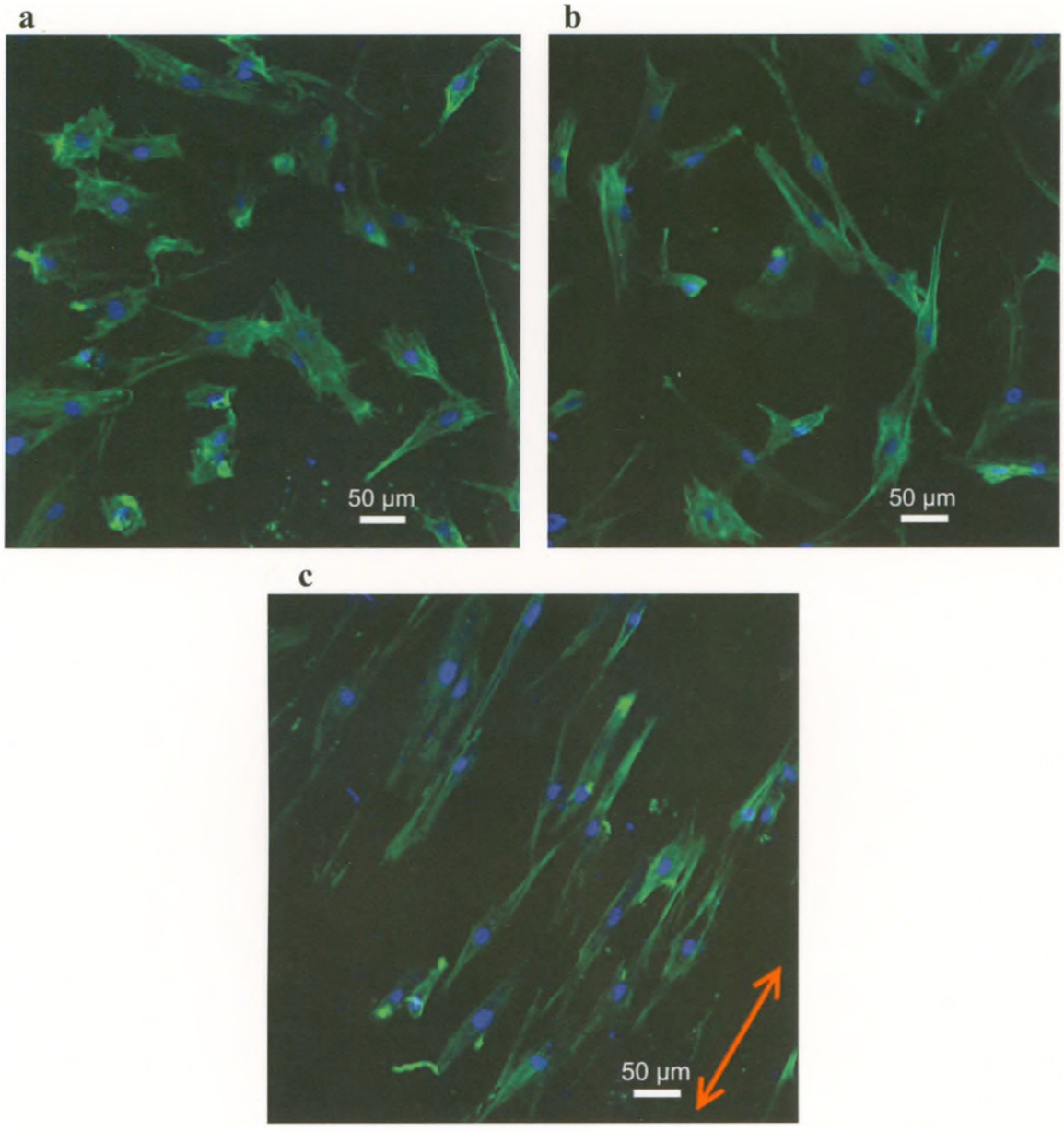

Figure 4.42. CLSM images of sample (a) N3, (b) N4 and (c) N3A after 1 day of culture.

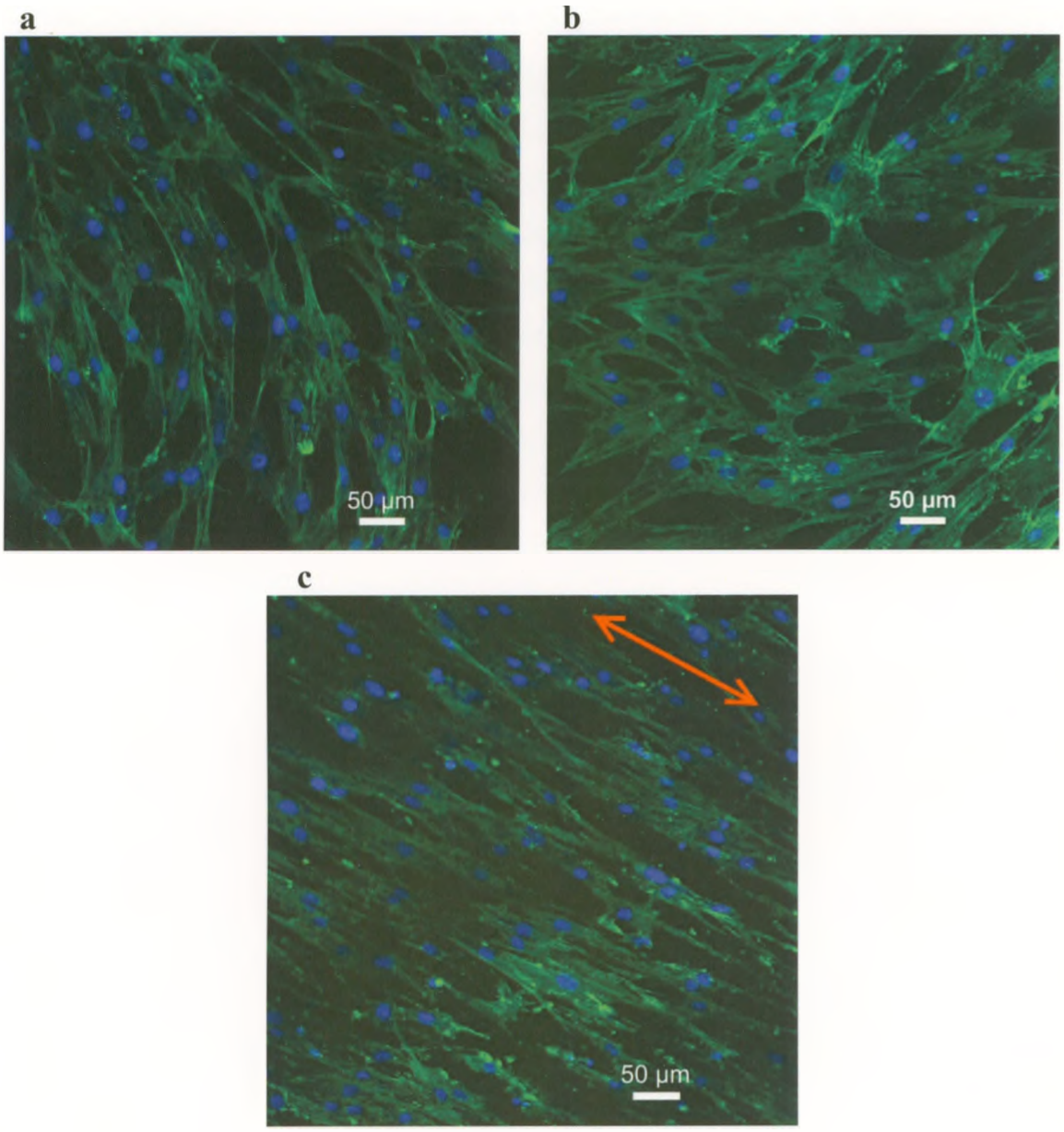

Figure 4.43. CLSM images of sample (a) N3, (b) N4 and (c) N3A after 4 days of culture.

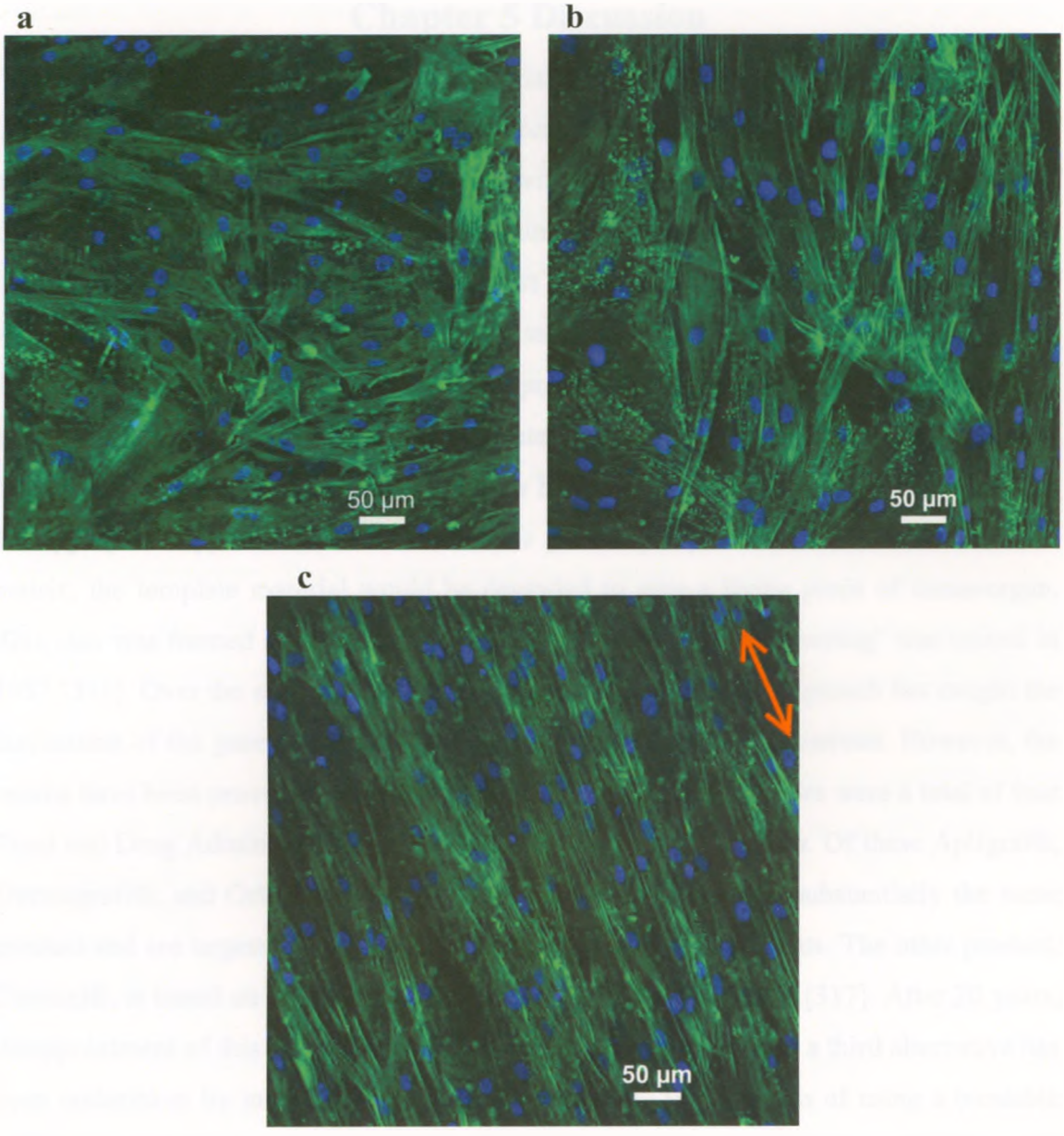

Figure 4.44. CLSM images of sample (a) N3, (b) N4 and (c) N3A after 10 day of culture.

Chapter 5 Discussion

In terms of the choice of materials, there are several approaches to the development of implantable medical devices. The traditional approach is the use of synthetic biomaterials and its combination with allograft or xenograft materials. Most of the currently used implants are fabricated using this approach. Examples range from total hip and knee replacements to artificial heart valves and large diameter vascular grafts. Although most of these implants perform satisfactorily, they are invariably imperfect. The currently most intensely researched approach is the tissue engineering/regeneration approach. This approach attempts to create living implants to replace the diseased tissue/organ by making use of biodegradable biomaterial as template and populate it with the appropriate types of cells. As these cells gradually lay down their own extracellular matrix, the template material would be degraded to give a living piece of tissue/organ. This idea was formed in the early 1980s and the term "tissue engineering" was coined in 1987 [316]. Over the ensuing 20 years, this seemingly "obvious" approach has caught the fascination of the general public and attracted "hugh" investment interests. However, the results have been proven to be rather disappointing. Up to 2006, there were a total of four Food and Drug Administration approved tissue engineered products. Of these Apligraf®, Dermagraft®, and OrCel® are living-skin equivalents which are substantially the same product and are targeted for diabetic, venous ulcers and burn patients. The other product, Carticel®, is based on autologous chondrocytes for cartilage repair [317]. After 20 years, disappointment of this approach is quite apparent and the search for a third alternative has been undertaken by increasing number of researchers. This consists of using a biostable synthetic biomaterial that is custom designed in terms of structure, geometry and properties to closely match that of the diseased tissue/organ. A "living" interface is then created between the body tissue and the implant surface to enhance compatibility and its long term performance. This approach, also known as the "tissue – biomaterial hybrid" approach, attempts to take advantage of the wealth of knowledge in synthetic stable biomaterials and combined it with knowledge in cell biology and biochemistry to address the problems of the traditional implants materials by incorporating a custom designed "living" interface. An attractive approach to fabricate the biomaterial part of a tissue –

biomaterial hybrid is in the form of nanofibers. In this thesis we choose to use the electrospinning technique for their generation.

Electrospun fibrous scaffold can provide the correct structure, geometry and mechanical properties which mimic that of the ECM of most soft tissues [36]. PVA is a good biostable [3] and biocompatible material, but it lacks of cell compatibility [5]. Although its lack of biodegradability has limited its use in tissue regeneration applications [27], there have been continuing efforts to instate cell compatibility [2, 5-20] to it to create a biomaterial-tissue hybrid based medical devices for cartilage [1, 31, 32], cornea [33, 34], and vascular grafts [14].

To develop a cell compatible PVA-based biomaterial – tissue hybrid (e.g. tympanic membrane), we used the electrospinning technique to fabricate 3D PVA scaffold based on nanofibers in either random or aligned orientation. The as-fabricated, PVA fibrous scaffold was not stable in aqueous environment; thermal annealing was applied to improve its aqueous stability. After the fibrous scaffold gained stability in aqueous environments including cell culture media, N^+ and He^+ ion beam implantations were used to modify its surface chemical properties to improve its cell compatibility. Cell compatibility of the modified PVA scaffold was evaluated *in-vitro* using primary human skin fibroblasts in term of cell attachment and proliferation.

5.1 Preparation of PVA Fibers by Electrospinning

Nanofibrous scaffolds, which consist of nanometer (< 500 nm) sized fibers, are particularly suitable for tissue engineering/regeneration and tissue – biomaterial hybrids fabrication than microfibrous and microporous scaffolds due to their high surface area to volume ratio and interconnected porous network [36]. In addition, fibrous scaffolds can be fabricated with controlled alignment [47, 48] to closely mimic the organized structure of the extracellular cellular matrix (ECM) of tissues such as blood vessels [45], vascular graft [143]. There are several commonly used polymer fiber spinning techniques including wet spinning [318-320], melt spinning [321-323], gel spinning [324, 325] and dry spinning [326, 327]. To make nanometer sized polymer fiber, electrospinning [38] is a widely adopted process capable of producing nanofibers to form 3D non-woven fibrous scaffolds [328] which is the method adopted for the work described in this thesis.

There is a wide range of parameters (Table 4.1) in the electrospinning process that can affect the formation, final diameters and morphology of the fiber produced. Tan et al. [300] investigated a wide range of the governing parameters including the applied voltage, the polymer solution flow rate, the polymer solution concentration, the molecular weight of the polymer, the tip-to-collector distance and the solvent system. They concluded that the polymer solution concentration and its molecular weight are the more dominant parameters compared to the applied voltage and tip-to-collector distance for controlling fiber diameter. Supaphol et al. [329] drew similar conclusions on three parameters: polymer solution concentration, applied voltage and tip-to-collector distance, for electrospinning of PVA fibers. In this thesis, a procedure adapted from Supaphol et al. [19] was developed and was found to produce PVA fibers of consistently good quality with fiber diameter in the range of 100 to 500 nm (Figure 4.1). This is important as Bashur et al. [127] and Kumbar et al. [128] have demonstrated that the spreading area, cell attachment and proliferation as well as collagen type III gene expression of fibroblasts are all dependent on the diameter of poly(lactic acid-*co*-glycolic acid) fibers.

The results (Figure 4.2) showed that the average PVA fiber diameter increased from 280 to 490 nm as the PVA concentration increased from 8.5 to 10.5 wt%, respectively. The FWHM of the best-fit normal distribution showed that an increase in PVA concentration broadened the distribution of the fiber diameter from 190 to 230 nm.

PVA solutions at concentrations below 8.5% and above 10.5 wt% are either not electrospinnable or produce fibers with beads indicating a strong effect of polymer solution viscosity on fiber quality. If the viscosity and surface tension of the polymer solution is too low, the electrospinning process forms droplets (electrospraying) [330] instead of a continuous liquid jet. On the other hand, if the viscosity is too high, the polymer solution prohibits the formation of the Taylor cone and consequently the fibers.

The average fiber diameter and the FWHM of the fiber diameter distribution increase as the applied voltage increases from 20 to 26 kV (Figure 4.3a). The increase in fiber diameter is caused by more material being drawn out to form the polymer jet when the applied voltage increases the electrostatic stress inside the Taylor cone. In the case of 26 kV, very broad fiber diameter distributions suggest that the voltage is too high and

over-charging the Taylor cone. The resulting polymer jet splits into multiple jets [300] and forms fibers with a broad diameter distribution [331].

Under a constant applied voltage, the fibers were smaller in diameter and have a lower FWHM value in the best-fit normal distribution as the distance between the needle and the collector electrode increases up to 20 cm (Figure 4.3b). The tip-to-collector distance provides the essential flight time to allow the polymer jet to be stretched under the electric field and the solvent to evaporate. At a constant applied voltage, the electric field gradient decreases as the distance increases. The resulting electric current and charge density inside the polymer solution will decrease [332] and limit the amount of material to be discharged from the Taylor's cone to undergo the whipping process [85, 333, 334].

The electrospinning setup used in this study was located inside a fume hood without an environmental control chamber. The impact of ambient temperature, humidity and air pressure can affect the evaporation rate of the DI water/ethanol solvent system [332] as well as the equilibrium humidity in the polymer jets. In Figure 4.17, two sample sets prepared for the ion beam treatment showed a significant 21% difference in the fiber diameter despite the fact that the samples were obtained using a solution with the same PVA concentration and the same electrospinning operating parameters. These sets were produced on two separate days (D_{avg} = 120 nm on Nov 2005 and D_{avg} = 95 nm on Apr 2006) which means that the differences are attributable to the uncontrolled environmental parameters. Since PVA is a very hydrophilic material, it is expected that the ambient relative humidity would have a significant effect on the equilibrium water content of the polymer jet during the whipping process as well as the fiber on the collector. In a low humidity environment, the lower equilibrium water content in the PVA matrix prohibits the electric field to stretch the jet into a small diameter. On the other hand, a high humidity can increase the plasticizing effect of water on PVA to extend the stretching process and produce smaller fibers. As our observations show, the differences of the fiber diameters due to the variation of humidity is similar to the results based on another hydrophilic polymer, poly(ethylene oxide), as reported by Tripatanasuwan et al. [335]. For the rest of the samples prepared in this study, these issues were generally addressed by adjusting the polymer solution concentration, voltage and tip-to-collector distance to

offset the effect of the ambient parameters to obtain smooth fibers with a relatively narrow diameter range.

Beside the polymer solution concentration, applied voltage and tip-to-collector distance, there are other important parameters, such as solution temperature [133, 336], polymer molecular weight [300, 337], ionic effect (e.g. adding salt) [133, 338] and solvent system [133], that can alter the fiber morphology and diameter in electrospinning. The response surface methodology (RSM) [297, 298, 339, 340] has been developed to model the effect of various electrospinning parameters on fiber formation. The model has been applied [298, 341, 342] to study and optimize the processing parameters on the fiber morphology and average fiber diameter. However, since the electrospinning process is not the main focus in this study; we did not attempt to apply the RSM for PVA fiber electrospinning process optimization.

While random PVA fibers (Figure 4.25a) were collected using a static plate electrode, a rotating mandrel similar to that shown in Figure 3.2b was used to collect aligned fibers (Figure 4.25b) that closely mimic the organized structure of the extracellular cellular matrix (ECM) of most tissue. Lee et al. [276] showed that fibroblasts were sensitive, in term of alignment, elongated direction and collagen synthesis, to polyurethane fibers alignment and mechanical strain. These similar fiber alignment effects were also observed in human smooth muscle cells on poly(*L*-lactid-*co*-ε-caprolactone) [45] or polystyrene fibers [129] and human Schwann cells on poly(ε -caprolactone) [281] or poly(ε-caprolactone)/collagen blends fibers [153]. Our approach of using a rotating mandrel can produce fibers that are aligned only in one direction. The degree of uniaxial alignment is a function of how well the rotating speed of the mandrel matches that of the fiber spinning rate [87, 343]. Ayres et al. [344] used fast Fourier Transform technique to analyze fiber alignment at different rotating speed with respect to polymer solution concentration. They found that the increase in the rotating speed does not always increase the uniformity of fiber alignment. They also demonstrated that the rotating speed to obtain the highest degree of fiber alignment is a function of polymer solution concentration. We did not systemically vary the rotating speed of our collector to study its effect on fiber orientation. All aligned fiber scaffold were collected with the mandrel spinning at a speed of 6.4 m/s. Fiber alignment degrades after a certain thickness

of the fibers is deposited on the mandrel because the charged polymer jet cannot be grounded effectively on the relatively low conductivity polymer fibers [89]. An increasing fraction of the resulting fibers will be misaligned as collect time increases (Figure 4.25b). Although for most applications, alignment in one direction is sufficient, there are tissues such as the tympanic membrane, which has fibrous structure consisting of collagen fibers arranged in multiple orientations (which are in radial, parabolic, circular and oblique) [345] which necessitates the creation of geometry with fibers that are aligned in multiple orientations. This multiply oriented fiber collection has been demonstrated by Li et al. [47] using multiple parallel electrodes.

5.2 Mechanical Properties of PVA Fibers

The overall mechanical properties of a fibrous scaffold are a function of the mechanical properties of the individual fiber, fiber density, connectivity between fibers as well as fiber orientation. A knowledge of the stiffness of individual fiber would allow the prediction of scaffold mechanical properties as a function of fiber orientation, connectivity between fibers and fiber density. It would also provide fundamental information for optimization of scaffold design for a particular application [170, 171]. Stylianopoulos et al. [161] demonstrated that the elastic modulus of electrospun polyurethane fiber mesh systematically varied from 0.56 to 3.0 MPa depending on the degree of fiber alignment and fiber diameter in a range of 500 to 900 nm. The degree of fiber alignment was determined in term of angular standard deviation by assuming all fibers are straight. This assumption is only valid when the fiber collecting speed of a rotating mandrel is perfectly matched that of the fiber spinning rate [87, 343]. The other parameter, fiber density, is usually determined based on the mass of fiber mesh and the overall porosity [161]. Alternatively, the fiber density can also be determined using cross-sectional SEM images of the fiber mesh as demonstrated by Peresin et al. [346]. A multi-scale structural model [164, 165] based on the combination of representative volume element (RVE) and finite element (FE) has been developed to simulate the mechanical properties as well as permeability [347] of a fibrous scaffold. Wei et al. [163] developed a model to predict the mechanical properties of a randomly oriented electrospun fiber

network with the fiber-to-fiber connectivity and van der Waals interaction. Their results predict that the strength of the fiber network increases as the number of connection (fusion) points between fibers increases. Jung et al. [162] showed that by increasing the number of fusion points between electrospun PVA fibers using cationic surfactant, the tensile strength of the fiber mat improved. Major parameters that are taken into consideration include fiber orientation, stiffness of individual fiber, fiber density and connectivity (and fusion) between fibers. Stylianopoulos et al. [161] employed this model to simulate the results obtained from the polyurethane fiber mesh; they used an arbitrary value of 18 MPa, which is six time higher than the modulus measured from a polyurethane solution-cast film, for the elastic modulus of single fiber in order to have a good match between the model predictions and the experimental data. For tissue regeneration and medical device applications involving cell scaffold interface, mechanical properties of the scaffold must be taken into account because on the macroscopic scale, it is necessary to mimic the mechanical properties of the tissue it is replacing and, on the microscopic scale, different cell types response differently to the stiffness of the scaffold [348].

A conventional uni-axial tensile testing system is the most frequently used technique to characterize the mechanical properties of fibrous scaffolds [94, 130, 166-169]. However, most of the results reported in the literature did not take into account the fiber density, connectivity between fibers and fiber orientation of the fibrous mat used in these experiments. These results are almost impossible to reproduce. In our study, we chose to determine stiffness of single electrospun PVA fibers. We choose to take a bottom-up approach starting with the determination of the mechanical properties of individual PVA fiber [1, 2]. By taking into account the fiber orientation, connectivity between fibers and fiber density, overall mechanical properties of the scaffold can be determined in a reproducible way.

For mechanical properties of single nanofiber determination, several methods have been reported in the literature. They were summarized in Chapter 3, Section 2.2. Some of these methods use rather complex micro-devices such as a nano-stressing stage [180, 181] or a micro-electromechanical system [182] that were developed specifically

for single nanofiber tensile testing. Despite the difficulty in manipulating individual nanofiber and the sensitivity limitations of these instruments, a full stress-strain curve (including elastic region, plastic region and ultimate tensile strength) of the nanofiber can be obtained. We choose to use a much simpler approach. Making use of the nanoNewton force detection sensitivity of the AFM, we developed a relatively simple multi-point bending technique (elastic region only) for fiber stiffness determination. This approach allows us to repeat the mechanical measurement on the single fibers to effectively determine the effect of the heat treatment or the ion beam treatment. It has been proven to be highly suitable for use in nanoscale fibrous materials including CNT [220], bacterial cellulose fiber [205] and composite fibers [95].

To measure the elastic modulus of a fiber, it was deposited on a standard TEM grid with the fiber spanning the opening of the grid. A bending test was performed using a normal force applied by the AFM cantilever onto the fiber. In its simplest form, a three-point bending test [134, 203] with only one AFM force measurement was performed at a location as close to the mid-point of the suspended portion of the fiber as possible. Additional measurements were made at two points on the supported portions (for force calibration purposes) of the fiber resting on the TEM grid surface. The determination of elastic modulus depends critically on the boundary conditions through an assumed mechanics model and, this approach cannot distinguish between alternate models, such as clamped beam or the supported beam configuration. It is also difficult to verify the exact position (midpoint) along the fiber where the force is applied. Any additional terms, such as deflection due to shear, would be very difficult to interpret from a single data point. These drawbacks can be overcome by using a multi-point approach [205] which measures the bending (displacement) of the fiber at several points along the suspended portion of the fiber and determines the elastic modulus using the clamped beam model. The advantage over the three-point measurement is that it can provide validation through the agreement between the experimental data and the model prediction as illustrated below.

In Figure 5.1, two SEM images of a suspended PVA fiber (a) before and (b) after the AFM measurement are shown. The dotted straight lines indicate that the fiber has

been permanently deformed and/or dislocate after the measurement. Data collected would therefore not satisfy the boundary conditions of the clamped beam model. Figure 5.2 shows a plot of fiber deflection versus fiber position along the suspended portion of the same fiber shown in Figure 5.1. This result can be compared to the well behaved results shown in Figure 3.15 in Chapter 3 indicating that the assumed boundary conditions for the model is not met. A single point bending test would not have detected any permanent deformation of the fiber. The advantage of using the multi-point approach for fiber elastic modulus determination is self evident.

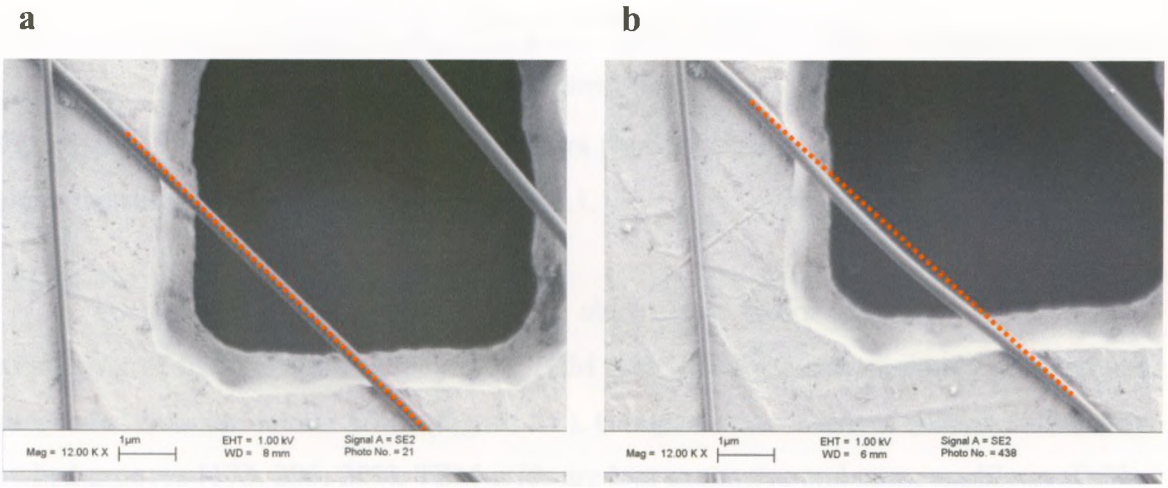

Figure 5.1. SEM images of a fiber (a) before and (b) after the AFM imaging. The red dotted lines indicated the fiber becomes loosen after the AFM measurement.

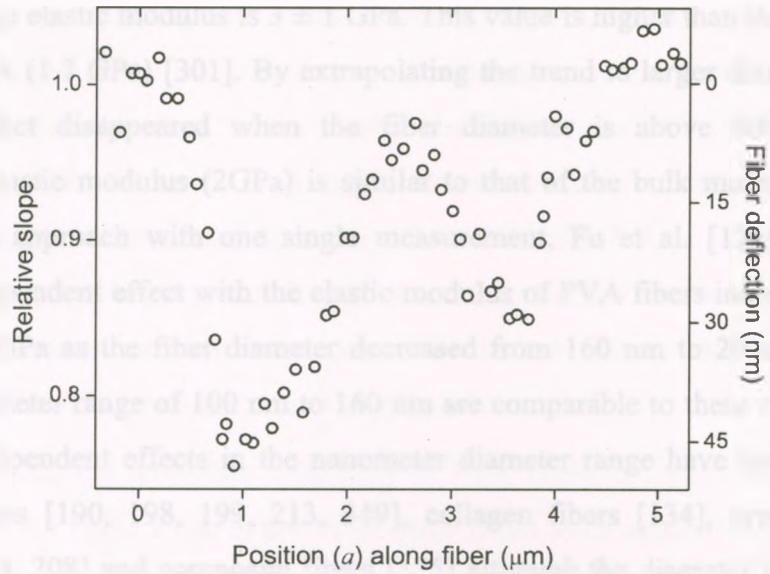

Figure 5.2. Plot of the slopes of force spectra (hollow circles) as a function of position *a* along the suspended fiber shown in Figure 5.1.

To perform a bending test on the electrospun fibers using the AFM, a sub-monolayer of fibers are deposited onto a TEM grid. The fibers are randomly oriented and suspended over the square holes (Figure 5.1). Compared to the use of silicon wafers with etched grooves [173, 205, 207], TEM grids are less expensive and more readily available. Figure 4.5 shows that it allows the bending test to be performed on PVA fibers in the diameter range of 100 to 400 nm without major change of AFM operating parameters and the type of cantilevers.

It is also possible to make repeat measurements on the same fiber. Figure 3.8 shows that the TEM grid allows every single fiber to be mapped and its positions identified for repeated measurements. For example, the position of a suspended fiber can be located using high-resolution SEM before and after AFM force-volume measurements. Using this approach, the effect of ion beam and annealing on PVA fiber mechanical properties were evaluated by comparing the values of elastic moduli and diameter of the same fibers before and after treatment.

As shown in Figure 4.5, the elastic moduli of individual electrospun PVA fibers determined using the multi-point bending approach exhibit a strong size-dependence in the diameter range of 100 nm to 375 nm. When the fiber diameter is between 300 – 375

nm, the average elastic modulus is 3 ± 1 GPa. This value is higher than the reported bulk moduli of PVA (1.7 GPa) [301]. By extrapolating the trend to larger diameter, the size-dependent effect disappeared when the fiber diameter is above 600 nm and the extrapolated elastic modulus (2GPa) is similar to that of the bulk modulus. Using a 3 point bending approach with one single measurement, Fu et al. [176] determined a similar size-dependent effect with the elastic modulus of PVA fibers increased from ~40 GPa to ~550 GPa as the fiber diameter decreased from 160 nm to 20 nm. Our results within the diameter range of 100 nm to 160 nm are comparable to these reported values. Similar size-dependent effects in the nanometer diameter range have been observed in metal nanowires [190, 198, 199, 213, 349], collagen fibers [134], synthetic polymer fibers [172-174, 208] and composite fibers [175] although the diameter for the onset of this size-dependent effect is material dependent.

For polymer fiber, Shin et al. [173] attributed the size-dependent effect to the orientation of polymer molecules insider the fibers. Specifically, they found that the strain rate of the electrospun polymer jets is usually very high; the electrospinning process can align the polymer chains inside the resulting polymer fiber along the fiber axis [350-352]. As the fiber diameter decreases, there will be fewer defects in polymer chain orientation and the resulting polymer fiber thus leading to a higher elastic modulus. Arinstein et al. [174] extended the concept of polymer chain orientation to a higher level of microstructure called supramolecular structure consisting of an oriented amorphous phase of the polymer chains. They proposed that this supramolecular structure, but not the crystallinity of the polymer matrix, has a major effect on the increase of the elastic modulus of the fiber as its diameter decreased toward the nanometer scale. However, there has yet been no experimental confirmation on the existence of the supramolecular structure.

Since PVA is a hydrophilic polymer, the equilibrium humidity is expected to have an effect on the mechanical properties of the electrospun PVA fiber. In Table 4.5, the mechanical measurement results show that the elastic modulus of electrospun PVA fibers experiences a 40 % reduction when the relative humidity in the fiber environment increases from 9 % to 32 %. PVA, being a hydrophilic polymer, is capable of absorbing water from its environment. At high relative humidity, the absorbed water leads to fiber

swelling which weakens the inter-chain interactions [302] and consequently induces a plasticization effect in the polymer matrix. The increase in the plasticization effect is responsible for the reduction in the elastic modulus of the PVA fibers. The elastic modulus of the PVA fibers is expected to further decrease as the relative humidity increases. We have demonstrated the relative humidity effect but, to systematically study the effect at a higher RH, a proper humidity control chamber similar to Stukalov et al. [353] is necessary to provide better humidity control and to isolate the electrical components of the AFM unit from water condensation.

The mechanical properties sensitivity of PVA fibers towards changing humidity shown in Table 4.5 implies that exposure of these fibers to an aqueous environment such as body fluid or cell culture media would lead to a significant decrease in their stiffness. This has important implications in both *in vivo* and *in vitro* tissue regeneration applications as the scaffold should have the mechanical properties matching that of the tissue it is replacing in a body. Wan et al. [354] showed that a fibrous scaffold made of electrospun poly(chitosan-g-DL-lactic acid) fibers had a significantly different elastic modulus when it was hydrated with fluid. For the dry scaffold, the measured elastic modulus has a value of 144 MPa. After the scaffold was immersed in a PBS buffer for 2 hours, the elastic modulus was reduced by 10 fold to 14 MPa. Similar reduction in elastic modulus due to hydration have also been observed in electrospun chitosan fibrous scaffold [354] and collagen/poly(D,L-lactide-co-glycolide) blend fibrous scaffold [355]. It should be pointed out that these mechanical measurements were made on fibrous scaffolds and not on individual fibers and represents stiffness of the fiber mesh. These values are a function of fiber diameter, density, porosity, orientation as well as the elastic modulus of the individual fiber which has not been taken into account in these studies. The PVA fibers we prepared for cell culture study fall within the diameter range of 100 to 200 nm with average elastic moduli of 24 ± 7 GPa as prepared. Depending on the amount of water uptake after fiber stabilization, this value may not be of direct relevance to cell culture study. Stiffness of the stabilized PVA fibers in the hydrated state would be more valid in a cell culture environment.

The role of mechanical properties of the scaffold in regulating cell behavior has been studied extensively and has been shown to be an important factor regulating cell behavior on the substrate. There are several reports [72, 348, 356-359] that summarized the different approaches used to study cell response as a function of varying stiffness of the substrate. Pelham et al. [71] used polymer gels of different degrees of crosslinking (and therefore stiffness) to study cell locomotion and focal adhesion of Swiss 3T3 fibroblasts. Their results showed that when cells were cultured on a less rigid substrate (smaller elastic modulus), the spreading was reduced and the rates of motility and lamellipodial activities were increased. Engler et al. [268] used the same approach to study smooth muscle cells and they found that the effective spreading area of the cells increased as the elastic modulus of the substrate increased. Nemir et al. [348] reported that the behavior of fibroblast including spreading, actin fiber formation, cytoskeletal organization, cell stiffness, focal adhesion size, cell growth and cell apoptosis can be different on the substrate with its rigidity ranged from 100 Pa to 100 kPa. Hadjipanayi et al. [360] showed that when fibroblasts were seeded on a matrix of collagen gel with different elastic modulus from two ends, they migrated preferentially towards the stiffer part (from 1050 kPa to 2300 kPa) after 3 and 6 days of culture. For neural stem cells, the responsive rigidity range is even broader (100 Pa – 600 kPa) [361]. Lemmon et al. [362] measured the traction stress exerted by the fibronectin matrix of NIH3T3 fibroblasts on the substrate to have a maximum value of 40 kPa, which is comparable with the substrate rigidity ranged that fibroblast is observed to response differently [348]. Since we have not quantified the mechanical properties of the PVA fibrous scaffolds used in our cell culture studies in the media, we would not be able to quantify cell behavior in terms of fiber stiffness. Instead, the focus will be on the effect of fiber surface modification using ion beam as detailed in the next section of this chapter.

Although mechanical properties of the substrate influence many aspects of cell behavior, it is no report of its effect on cell alignment. Instead, cell alignment can be induced by mechanical strain and has been demonstrated using endothelial cell [363, 364] and substrate topography on cardiomyoctes [365]. Since we have the ability to electrospun both random and oriented PVA fibers, in the cell culture studies on PVA

fibers as part of this thesis, we will also be investigating the effect of the fiber orientation on cell behavior.

5.3 Stability of Electrospun PVA Fibers in Aqueous Media

PVA is a hydrophilic polymer that readily dissolves in water. The as-spun PVA fibrous scaffold can be completely disintegrated upon contact with water (Figure 4.6). For biomedical applications that require the PVA fiber to be exposed to an aqueous environment such as cell culture media, the nanofiber geometry and the porosity of the scaffold has to be conserved.

Both physical and chemical crosslinking methods have been applied for the stabilization of bulk PVA. Among these, the most popular method is perhaps the use of the chemical crosslinking agent glutaraldehyde. For biomedical applications of the resultant PVA, this approach is less than desirable as glutaraldehyde is well known to be cytotoxic. For electrospun PVA fibers, the use of glutaraldehyde vapor [15, 16] and methanol [55, 56, 251] have been reported. In addition to the fact that both these chemical agents are highly toxic, the crosslinked fibers also exhibit high degree of swelling in water and the fiber morphology is altered.

We investigated a non-chemical approach of annealing towards stabilization of the electrospun PVA fibers. This annealing approach was investigated via a systematic variation of two experimental parameters, namely annealing temperature and annealing time on fiber stability. Our results (Figure 4.7 – 4.10 and 4.12) confirmed that fiber stability in an aqueous environment was a function of annealing temperature and time. Our results also showed that a minimum annealing temperature of 135 °C and an annealing time of 1 hour were required to impart stability to the fibers. To provide a safety margin, a treatment time of 4 hours at 135 °C was determined to be the condition for PVA fiber aqueous stability. Figure 4.9 showed that using this annealing condition, dimensional stability of the PVA fibers in water could be maintained for up to 30 days.

In addition to the use of glutaraldehyde vapor [15, 16], and methanol [55, 56, 251] to crosslink PVA fibers, to preserve the fiber morphology, Tang et al. [366] added glutaraldehyde into the PVA solution to in situ crosslink the PVA before electrospinning. Although the resulting fibers had the same morphology as the uncrosslinked PVA fibers, the aqueous stability of the fibers was not as good as what was achieved by annealing as shown in Figure 4.9. Moreover, since this is a non-chemical based technique, there is no concern of cytotoxicity as compare to the case when crosslinking reagent such as glutaraldehyde was used [367].

PVA solution can be converted into a solid hydrogel by physical crosslinking using a low temperature thermal cycling process [58]. Stability and mechanical properties control of the resultant hydrogel have been attributed to an increase in the polymer crystallinity [59]. In addition, for macroscopic PVA samples, thermal annealing has been reported to increase the degree of crystallinity without changing its chemical structure [61, 368]. Following a similar line of reasoning, the effect of thermal annealing on PVA fiber crystallinity was investigated. Using the XRD and FTIR techniques, the degree of crystallinity of PVA fibers as a function of annealing conditions was determined. The results, summarized in Table 4.8, showed that there was a systematic increase in fiber crystallinity with increasing treatment temperature up to 185 °C. The progressive improvement of the fiber in the aqueous stability could be correlated to the increase in the fiber crystallinity. A minimum temperature of 135 °C was required to activate the polymer chain mobility within the fiber, which is a prerequisite for the creation of sufficient crystallinity. On the other hand, once this temperature is reached, the time required to achieve stability is only a function of the polymer chain mobility. A minimum treatment of 1 hour at 135 °C was found to be sufficient to achieve aqueous stability for PVA fibers. At a longer treatment time of 4 hours at this temperature corresponding to a degree of crystallinity of 74 % is preferred to ensure fiber stability.

An alternative method to determine changing crystallinity as a function of annealing conditions was also investigated. This FTIR based technique was only able to give the relative change in crystallinity of the fibers since this is not an absolute method and standards of know degrees of crystallinity are not available. Using the ratio of

intensities of two well established infrared bands at 1141 cm^{-1} and 1425 cm^{-1}, the changing crystallinity as a function of annealing condition parallel to that of the XRD technique was determined and the results are also collected in Table 4.8. A criterion for aqueous stability of electrospun PVA fibers by annealing can be defined in terms of the intensity *a*/*b* ratio in the bands at 1141 cm^{-1} and 1425 cm^{-1} in the FTIR spectra. From Table 4.8, it can be seen that a value of *a*/*b* of 2.5 defines the boundary of fiber stability. With the *a*/*b* ratio $\geq$ 2.5, the fibers become stable. This can be regarded as an alternative criterion to that determined by XRD [293-295] or DSC [288, 369].

The annealing process not only resulted in the establishment of fiber stability in water, there is also an associated increase in their mechanical properties as measured by the elastic modulus of the individual fiber. Using an annealing condition of 135 °C for 4 hours, the elastic modulus of individual PVA fiber before and after the annealing process was determined. The results are displayed in Table 4.6. The average modulus for 16 fibers was increased by about 80 % from 4.4 ± 1.4 GPa to 7.6 ± 2.3 GPa. This significant increase in the elastic moduli of the fibers can be attributed to the increase in their crystallinity [249]. A physically crosslinked bulk PVA hydrogel system that showed increase in elastic modulus as a function of thermal cycling has attributed this increase to an increase in the volume fraction of the crystallites in the hydrogel as determined by small angle neutron scattering [59]. Corresponding to an increase in fiber stiffness by annealing, there is an average decrease of about 10 % in fiber diameter from 210 ± 30 nm to 190 ± 30 nm. This shrinkage in size corresponds to an increase in density, and is expected to depend on the annealing parameters in a similar fashion to the observations by Kenney et al. [289] on PVA hydrogel.

The results described in this section will be applied to the stabilized electrospun PVA fibers before they are modified by ion beam treatment for cell compatibility as described in the next section of this Chapter.

5.4 Ion Beam Modification of Electrospun PVA Fibers for Cell Compatibility

5.4.1 Ion Beam Modification

A material with a high hydrophilic surface, such as hydrogel, inhibits cell adhesion [5, 370, 371]. PVA is a very hydrophilic material and its surface has also been shown to inhibit cell adhesion, viability and growth [5]. To create biomaterial-tissue hybrid based medical devices based on PVA scaffold for tissue regeneration applications such as skin [22], ear drum [23], vascular [14], bladder [24] and nerve [25], cell compatibility is required.

Several approaches have been demonstrated to achieve cell adhesion, viability and growth on PVA. These include blend PVA with chitosan [8, 12-14], lipase enzyme [15], gelatin [16, 17], starch [18] and carboxymethyl chitin [19], surface functionalization using fibronectin [5, 7] and peptide [11], surface phosphorylation [6], surface coating using hydroxyapatite [21] and heparinized PVA–small intestinal submucosa composite [20].

Alternatively, post-processing surface chemical modification using ion beam treatment is an attractive approach to impart cell compatibility on polymer surfaces [243]. The cell compatible properties of the treated polymer has been shown to be a function of ion species, ion energy and ion dose. Pignataro et al [242] showed a strong improvement on adhesion, spreading and proliferation of astrocytic cells on the surface of polyurethane, poly(ether sulfones) after 35 keV of Ar^+ treatment. Meanwhile, Satriano et al. [240] also showed that 5 keV of Ar^+ treatment significantly increased fibroblast attachment and proliferation on poly(hydroxymethyl siloxane) surface. Using 150 keV of He^+ and Ne^+ treatment, Kusakabe et al. [74] found that the adhesion and spreading of endothelial cell on polypropylene and expanded polytetrafluoroethylene were improved. Similarly, Wertheimer et al. [75, 76] using plasma based ion beam treatment to deposit nitrogen compounds on the surface of polyethylene and polypropylene to improve human U937 macrophages and chondrocytes cell adhesion. Ion beam treatment is therefore a very simple, clean single-step process for improving cell compatibility of polymer surfaces. There is no other simpler method that can match its high controllability, versatility as

well as flexibility to modify many different types of polymer thus motivating us to investigate its use on the electrospun PVA fibers.

Prior to the ion beam treatment, a thermal annealing step at 135°C for four hours was applied to PVA fibrous scaffolds to stabilize the fibrous morphology and structure in preparation for subsequent cell culture study when they have to be exposed to cell culture media. This thermal treatment provides the necessary aqueous stability for the scaffold to stay intact and stick to the bottom surface of the cell culture plates since an anchored versus an unanchored scaffold can affect cellular morphology, signaling and proliferation [259-261].

After thermal treatment (Chapter 4, Section 4.3), the surface of the scaffolds was modified using various doses of broad-energy N^+ or He^+ implantation. As the ion-polymer interaction induces an irreversible chain scission and cross-linking in the polymer matrix, new functional groups are created as free radicals temporarily increase the chemical reactivity [62]. The amounts of amine and amide functional groups introduced by the N^+ treatment are a function of the ion dose (Figure 4.29). On the other hand, the He^+ treatment introduced carbonyl (or carboxyl) along the implantation path. These carbonyl (C=O) based functional groups are formed in both N^+ and He^+ treated PVA samples (Figure 4.28 & 4.29). Cell adhesion, viability and growth on the surface of polymeric materials have been demonstrated to improve with the introduction of biological adhesive molecules [372, 373], such as amide [73, 75, 374-380] and carboxyl [381-383] groups for cells to interact through integrin [384]. Successful incorporation of similar chemical functionalities via ion beam treatment is a good indication that the treated PVA scaffold may have improved cell compatibility.

It is very important to preserve the fiber morphology of the fibrous scaffold during any modification in order to maintain the structural similarity of the native ECM [36]. As shown in Figure 4.18 to 4.20, the PVA fibers exposed to the ion beam treatment have a small diameter range from 100 to 160 nm; this size range can minimize the variation in the ion implantation profiles that would occur for fibers at other diameters [65]. The energy deposited by the ion beam induced irreversible effects on the structural properties of the polymer fibers. Thus, the implantation profile must be carefully planned.

A 1μm thick Ta metal foil was placed in front of the sample to lower and broaden the energy of the mono-energetic 1.7 Mev N^+ or 520 keV He^+ beam such that the implantation depth ranges from the surface to about 900 nm (based on the SRIM simulation result shown in Figure 3.5). In turn, ion beam treatment introduced chemical modifications without causing any damage to the surface morphology of the PVA fibers as shown in the SEM images in Figure 4.18 to 4.20. Contrast to our results, the use of a mono-energetic oxygen ion beam [65] resulted in a modification that was mostly destructive for micrometer sized polyurethane fibers. The highly localized energy deposition from a monochromatic low energy ion beam can induce significant carbonization [62, 66] and melting [65] at the surface of polymeric materials. Similar irreversible surface morphological damages are also expected from using plasma-based ion implantation systems. Although plasma-based ion implantation is frequently used to modify the surface of a sample for particular applications, such as cell culture applications [75, 385] and filtering membranes [386], its high rate of destructive surface sputtering (surface erosion) [176] does not permit treatment of polymeric materials with valuable nano-sized physical features near the surface.

There is a significant shrinkage in fiber diameter as a result of ion beam treatment concurrent to the surface chemical modification. Figure 4.17 show that the diameter of the fibers decreased by 27% on average after exposure to 1.2×10^{16} N^+/cm^2. In comparison, the fiber diameter did not significantly change after exposure to 1.2×10^{16} He^+/cm^2, with the He^+ beam three times less energetic than the N^+ beam. In Figure 4.21, another set of fibers were treated with N^+ at the same energy but with a lower dose of 8×10^{15} N^+/cm^2, the diameter shrinkage was reduced 11%. A lower dose in ion implantation at a constant beam current means a shorter treatment time as well as less energy deposited into the polymer matrix. By comparing the two N^+ treatments using different doses as well as the results from the He^+ treatment, the shrinkage in fiber diameter is depended on the ion dose or the total energy deposited by the ion beam. This is the first time that the effect of ion beam treatment on the diameter of electrospun fibers has been observed. As the effect on fiber diameter can be controlled by the combination of ion beam treatment parameters, such as ion species and dose, it can be used to control the surface porosity of a scaffold required for specific applications.

The results shown in Figure 4.21 indicate that N^+ treatment increased the overall stiffness of the PVA fibers as a function of ion dose. The increase in the stiffness is attributed to the creation of three-dimensional cross-linked polymer chain networks (solubility results shown in Figure 4.24) via ion-polymer interaction and the ion-induced annealing effect. Similar improvements as a function of ion dose on mechanical properties of bulk polymer materials using ion beam treatment [69] have been demonstrated, these include, polyethylene by 1 keV Ar^+ [70], polycarbonate by 30 keV N^+ [387, 388]and Polyimide by 2 MeV Si^+ [389]. In addition, the decrease in fiber diameter with a concurrent increase in density (fiber diameter results shown in Figure 4.18) can then be the combined factors that led to the observed stiffness increase of the N^+ treated PVA fibers. The results shown in Figure 4.21 also indicate that for a dose higher than 1.6×10^{16} N^+/cm^2, the elastic moduli of the treated fibers began to decrease. This observation is attributed to the combination of the saturation of cross-linkable sites in the polymer matrix and the excessive amount of polymer chain scission [62]. On the other hand, the He^+ beam is less effective to create three-dimensional cross-linked polymer chain networks due to the lower energy and being chemically inert [68, 390]. In turn, the He^+ treatment did not introduce any elastic modulus improvement like N^+ (Figure 4.22). This ion beam effect on the stiffness of the fibers can be used to fine-tune the mechanical properties of the scaffold to match the tissue it is replacing.

Our approach of using ion beam treatment required a Ta foil to be an energy diffuser to convert a high-energy mono-energetic ion beam and generate a low poly-energetic beam from a conventional ion implanter. The energy of the beam is reduced and broadened through the collision/straggling process with the Ta atoms before a portion of it is transmitted through the foil, providing a wide implantation zone [305] in a single process, which in our case covers a range from the surface to 900 nm depth (theoretical SRIM value) of a PVA fibrous scaffold. Using a mono-energetic beam, there would be a need of multiple-energy implantation steps to achieve a similar range. Furthermore, the ion energy deposition profile has also been extended into a wider range, minimizing energy-related damage, particularly near the surface.

The high atomic mass of Ta can reduce, but not completely eliminate, the probability of recoil and/or sputtering of foil atoms onto the sample. Indeed, the XPS data

(Figure 5.3) show that the surface of N^+ treated PVA fibrous scaffold contained a small amount (~1%) of Ta atoms, which cannot be ignored if the treatment is for biomaterials application. However, Ta has long been considered a biocompatible metallic material [391, 392]. It shows cell-compatibility [393, 394] and no systemic toxicity inside body fluids [395]. It is used as a contrast agent in X-ray imaging and a material in orthopedic implants [396-399]. The presence of Ta is not expected to diminish the potential of applying this surface treatment technique to any suitable material for biomedical applications.

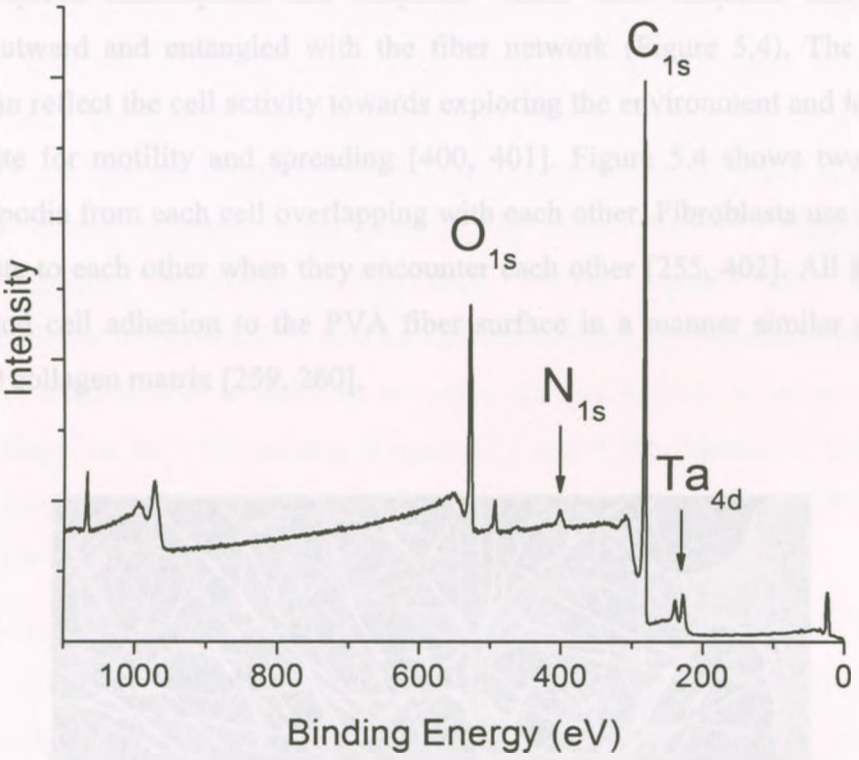

Figure 5.3. XPS survey spectra of 2.4×10^{16} ions/cm² N^+ treated PVA fibrous scaffold.

5.4.2 Cell Compatibility of Ion Beam Modified Electrospun PVA Fibers

The cell compatibility of the modified PVA scaffolds was first assessed using primary human skin fibroblasts (hsF) based on cell adhesion, morphology and spreading after 72 hours. Figure 4.31 showed that the control samples (annealed PVA fiber

scaffolds) had very few hsF attached and they were all in a rounded morphology with the network of extensions retracted. For the hsF that rested on the fiber surface, they appeared to adhere to each other to form clusters rather on the hydrophilic PVA fibers. This is an indication of poor cell adhesion to the surface that is expected of highly hydrophilic surfaces such as the PVA hydrogel [5]. In comparison, for all N^+ and He^+ treated scaffolds (Figure 4.32 – 4.35), the numbers of hsF attached to the surfaces had significantly increased due to the incorporation of amide and carboxyl functional groups (Figure 4.28 to 4.30). The hsF were flattened in either a stellate or a bipolar morphology with well spread lamellipodia and filopodia. There were filopodia that were well extended outward and entangled with the fiber network (Figure 5.4). The number of filopodia can reflect the cell activity towards exploring the environment and forming new adhesion site for motility and spreading [400, 401]. Figure 5.4 shows two hsFs with several filopodia from each cell overlapping with each other. Fibroblasts use filopodia to communicate to each other when they encounter each other [255, 402]. All these results indicate good cell adhesion to the PVA fiber surface in a manner similar to that of a stressed 3D collagen matrix [259, 260].

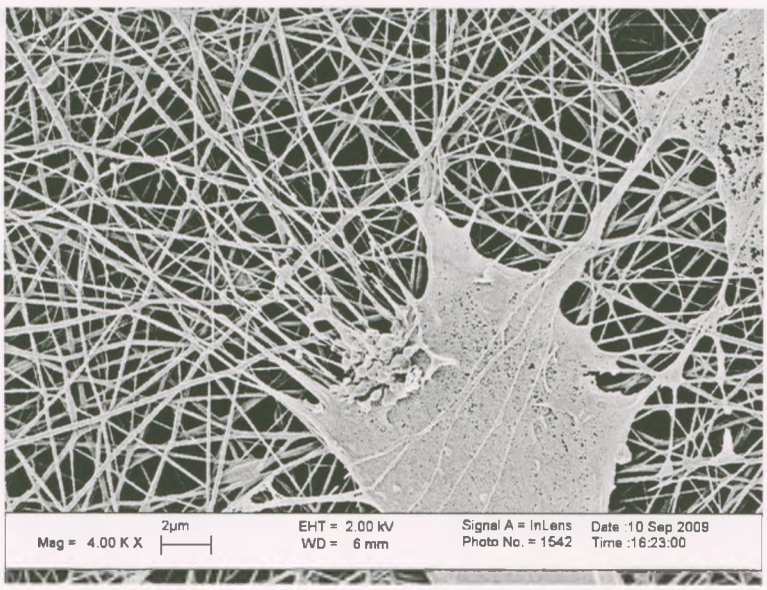

Figure 5.4. SEM image of hsF on a sample N4 after 72 hours of culture. It shows the well extended filopodia toward the fibers and the other hsF.

When the hsF were cultured on the N^+ treated scaffolds with aligned PVA fibers (N3A), (Figure 4.32 – 4.35) the hsF adopted a bipolar elongated morphology and aligned along the fiber axis with well spread lamellipodia and filopodia similar when they were on a surface of oriented native collagen fibers [254] and other cell compatible electrospun aligned fibers including polyurethane [276], poly(methyl methacrylate) and poly(D,L-lactic-*co*-glycolic acid) [127]. In some cases, such as cardiomyoctes, cell orientation and organization on a scaffold are the important factors to maintain the native electrophysiological and mechanical characteristics in the tissue regeneration process [365]. And because of the scaffold being three dimensional, there were few hsF infiltrated within the surface layer of the sample N3A (Figure 4.37). Cell infiltrations within a 3D scaffold are important toward 3D tissue formation [403] and have been reported in fibronectin-based matrix produced by mouse NIH-3T3 fibroblasts [257], electrospun random poly(DL-lactide-glycolid) fibrous scaffold [22] as well as electrospun aligned poly(L-lactide) fibrous scaffold. Overall, the amount of amide groups introduced as a function of N^+ dose did not affect the attached hsF in terms of spreading and morphology on the PVA surface (Figure 4.33 and 4.34). Moreover, similar results were also observed as no significant difference on the hsF spreading and morphology between the N^+ and He^+ treated scaffolds (Figure 4.33 and 4.35).

After the hsF are attached and spread on the modified PVA scaffolds, they start to grow and proliferate. As hsF grow to confluence, they can also grow on top of each other to form multilayer at the early stage of proliferation [404] (day 3) as shown on Figure 5.5.

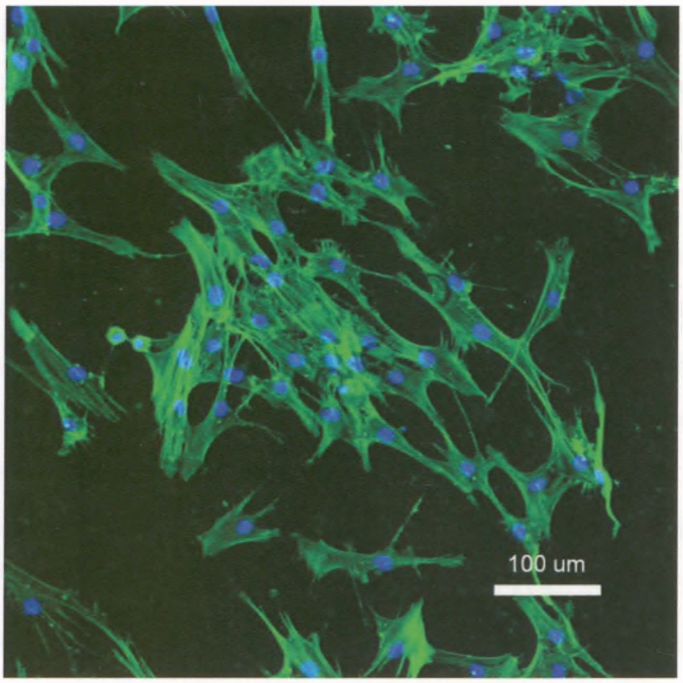

Figure 5.5. CLSM image of hsF on a sample N4 after 72 hours of culture. It shows multiple hsF grew on top of each other and form multiple layers.

At day 10, the hsF had expanded on the N^+ treated random fibrous scaffolds to form confluence. (Figure 4.40 and 4.44a & b); the confluence consists of small independent groups orientated at random with respect to other groups and are separated from the neighbors by narrow packing interstices [313]. Similar cell orientation as a confluent layer has also been observed on culture dish [405], microspherical poly(lactide-co-glycolide) scaffold [406], electrospun gelatin/poly(ε-caprolactone) scaffold [407] and electrospun poly(DL-lactide-glycolide) scaffold [22]. In contrast, the hsF maintained the aligned orientation and formed coherent confluences on sample N3A (Figure 4.39 and 4.45c).

In addition to having a beneficial effect on hsF adhesion and spreading, ion implantation also has a significant effect on their proliferation on PVA fibers. The proliferation results showed that on day 1 (Figure 4.39 & 4.41), the average cell density of all ion beam treated samples were in the range of 5,000 – 7,500 cells/cm^2 while the control samples had ~800 cells/cm^2. From here on, the cell density increased continuously for both the N+ and He+ treated samples for up to 10 days while the control

remains unchanged. Among the N+ treated samples using different ion dosages, there is not a clear cut trend of the cell proliferation rate as a function of N^+ dosage. Among the four randomly oriented PVA fiber samples, the nitrogen dose increased from 2.5×10^{14} ions/cm² (N1) and 8.0×10^{15} ions/cm² (N4), this 32 fold increase in ion dosage resulted in a significant increase in cell count of 15,000 versus 20,000 cells/cm^2 (day 4) and 24,000 versus 29,000 cells/cm^2 (day 10). There is no clear trend for the intermediate ion dosages (N2 and N3). The differences in the nitrogen dose between sample N1 and N2 or N3 and N4 are not large enough to allow a significant difference in the cell number to be observed. Although this ion dose dependent effect has been reported in different polymer systems with different ion species [74, 238, 239], our results suggest that a wider range of ion dose (e.g. 10^{13} to 10^{16} ions/cm²) should be applied [74, 242] in order to obtain a clearer and broader trend of cell adhesion and proliferation as a function of ion dose on PVA fibers. This N+ dose dependent cell growth is a reflection of increasing density of nitrogen functionalities such as amide and amine on the PVA fiber surface. These are binding sites for hsF to adhere to. A higher nitrogen density on the PVA fiber surface provides an increase in the number of sites for the hsF to adhere to thus stimulating an increase in proliferation rate.

The N^+ treated aligned fibrous scaffolds (N3A) gave the highest cell number at day 10 (32,000 cells/cm^2) including the randomly oriented scaffold (N4) which was treated with two times more N^+ dose at the end of day 10 (Figure 4.41). Several groups have demonstrated that the aligned surface topology can promote a cell number due to cell-cell interaction and cell-matrix interactions, such as bone marrow stromal cells on aligned silk fibroin electrospun fibers [314] and coronary artery smooth muscle cells on aligned poly(L-lactid-co-ε-caprolactone) electrospun fibers [45]. Our result is the first demonstration of this effect on the hydrophilic PVA fibers.

The He+ treated PVA fiber mat (He3) also showed satisfactory cell adhesion and proliferation properties. However, the cell number (5,500 (day 1) to 12,000 (day 4) to 19,000 (day 10) cells/cm^2) is much lower than the N^+ treated sample N3 (7,500 to 20,000 to 25,000 cells/mm^2) with the same ion dose (Figure 4.41). Since He^+ treatment only lead to the introduction of carboxyl groups to the PVA fiber surface, this indicates the

preference of hsF for interaction with amide and amine groups which are present in proteins and peptides [73].

All these results indicate that it is possible to create a PVA scaffold consisted of electrospun nanofibers with aqueous stability and cell compatibility, through a two steps of carefully developed post-processing treatments: thermal annealing and ion beam implantation. It is providing a first step towards an alternative for the realization of skin and tympanic membrane regeneration.

Chapter 6 Conclusions & Future Work

6.1 Conclusions

PVA is a widely used biocompatible material with poor cell compatibility. In our quest for the creation of biomaterial-tissue hybrid to improve the medical device – tissue interface of the next generation medical implants, we investigated the possibility of using PVA in the nanofiber form for PVA-tissue hybrid development. This involves the spinning of PVA nanofibers in the form of random and oriented fiber mats, the stabilization of these mats in aqueous solutions and modification of the fiber surface for cell compatibility.

The electrospinning technique was used to produce fibers and nonwoven fibrous scaffolds consisting of nanometer (< 500 nm) sized fibers from PVA. Scaffolds with aligned fibers were also collected using a rotating mandrel. Fibrous scaffolds are considered to be more suitable for tissue regeneration applications because they mimic the fibrous structure of the native ECM and provide a highly interconnected porous structure with high surface area to volume ratio. A wide range of parameters in electrospinning can affect the formation, final diameters and morphology of fibers produced. To obtain consistent bead-free fibers in the diameter range of 100 to 500 nm, three parameters were investigated: polymer solution concentration, applied voltage and tip-to-collector distance. Fiber diameters were found to increase as the polymer concentration and applied voltage increased, while an opposite trend in fiber diameter was observed as the tip-to-collector distance increased.

A high temperature annealing process was developed to improve the aqueous stability of the PVA fibrous scaffold. Annealing for 4 hours at 135 °C was found to impart long term (30 days) aqueous stability to the PVA fibers. Using the FTIR techniques, it was determined that annealing increased the crystallinity which resulted in inrcreased aqueous stability of the fiber. Aqueous stability can be defined by the ratio a/b of the FTIR band intensity at 1141 cm^{-1} and 1425 cm^{-1}. A value of $a/b \geq 2.5$ defined fiber stability in water. This level of crystallinity can be achieved by annealing at 135 °C for 4

hours. This thermal treatment method is simple and is particularly useful when these fibers are being considered for application in an aqueous environment such as membrane filter or tissue scaffold.

To impart cell compatibility properties to the thermally annealed PVA fibers, a second post-processing treatment was applied using ion implantation with a broad energy range ion beam. Nitrogen and helium ions were implanted onto the surface of the PVA scaffold under controlled conditions; key chemical modifications were achieved with the introduction of amide and carboxyl functional groups using N^+ beam without alteration of the fiber morphology. A reduction of fiber diameter as a function of ion dose was also observed. Treatment with the less energetic and chemically inert He^+ beam resulted in chemical rearrangement leading to the formation of carboxyl groups without altering the fiber diameter. A side benefit of ion beam treatment was an increase in fiber stability in water.

Elastic modulus of individual PVA fiber was determined using a multi-point bending method by AFM. Elastic moduli of as-spun fibers exhibited size dependence. There was a significant increase from the PVA bulk modulus at fiber diameters of less than 300 nm. This effect will play an important role in the engineering of the mechanical properties of a scaffold. Significant changes in the elastic modulus of the annealed and ion beam modified PVA fibers were also observed. Thermal treatment for 4 hours at 135°C resulted in an average of 80 % increase in the elastic modulus of the fibers. Also, N+ treatment at an ion dose of 8.0×10^{15} ions/cm² led to an average of 30 % increase in the fiber elastic modulus. The effect of N^+ treatments on elastic modulus is dosage dependent while treatment with He^+ at 8.0×10^{15} ions/cm² dose showed an opposite trend of 63 % decrease in the elastic modulus.

In vitro cell compatibility assessment of the stabilized and ion beam modified electrospun PVA fibrous scaffold was carried out using hsF and the as spun but stabilized PVA fiber mats as control. The introduction of amide/amine and carboxyl groups which are also present in proteins and peptides in many of the ECM proteins using the N^+ beam, good adhesion, spreading and proliferation of the hsFs have been demonstrated. The

proliferation rate was found to be a function of the N^+ dose. Increasing N^+ does resulted in higher proliferation rate. Aligned PVA fibers treated with N^+ beam induced the hsF into a bipolar morphology with the cells aligned along the axis of the fiber. A higher proliferation rate was also observed. The hsF not only populated the surface of the scaffold, they also infiltrated into the 3D aligned structure of the scaffold. He^+ treatment only introduced carboxyl groups into the PVA fibers. While this treatment approach also promoted hsF adhesion, spreading and proliferation, the effect was significantly less than that of the N^+ treatment.

The results reported in this study demonstrated that it is possible to produce nice, uniform PVA fiber of < 500 nm in diameter by electrospinning. Using a combination of two post-processing treatments of thermal annealing and ion implantation, cell-compatible PVA fibrous scaffold can be created. The results of this thesis represent a significant step towards the design and creation of PVA fiber based biomaterial-tissue hybrid for the next generation of implantable medical devices and for tissue regeneration applications.

6.2 Future Work

For polymer fiber production by electrospinning, it is important to obtain a comprehensive understanding of the effect of every spinning parameter on fiber morphology and fiber diameter. In the future, it will be necessary to extend the study to other electrospinning parameters such as solution temperature, polymer molecular weight and ionic strength. The response surface methodology [297, 298, 339, 340] can be employed to study and optimize the effect of processing parameters on fiber morphology and fiber diameter.

Since tissue possesses highly organized structure, it is necessary to have the structure of the PVA fibrous scaffold closely parallel that of the tissue it is replacing. For most tissues, such as the tympanic membrane, the fibrous structure of the ECM consisted of collagen fibers arranged in multiple, organized orientations (radial, parabolic, circular

and oblique) [345]. Therefore, a simple rotating mandrel can no longer satisfy the multiple orientations requirement. A new collector electrode that is capable of collecting aligned fibers in multiple orientations will be needed and should be designed and built for tissue regeneration applications.

A major hurdle toward potential commercialization of electrospun fibrous scaffold is the lack of a large scale production technique. Most of the works on electrospun fibers are performed using a conventional experimental set-up that can produce one fiber at a time using a single nozzle process. A multiple-nozzle approach should be investigated to significantly increase the production rate.

In this study, the elastic modulus of the PVA fibers was found to exhibit a size-dependent effect. This effect has also been reported for other polymer systems although the onset of size dependence varies among polymers [172-174, 208]. The suparmolecular structure model proposed [174] consisted of oriented amorphous phases of the polymer chains to account for the size-dependent effect. Small angle neutron or X-ray scattering experiments should be used to validate the structure in the fibers.

PVA shows a plasticization effect from the absorbed water and the elastic modulus of PVA fibers is a function of humidity. For both *in vivo* or *in vitro* studies, it is necessary to obtain the stiffness of the stabilized PVA fibers in fluid (PBS or cell culture media) so that the substrate mechanical properties on cell behavior may be quantified.

References

1. Kobayashi, M.; Chang, Y.-S., et al., A two year in vivo study of polyvinyl alcohol-hydrogel (PVA-H) artificial meniscus. Biomaterials, 2005; 26(16): 3243-3248.
2. DeMerlis, C. C.; Schoneker, D. R., Review of the oral toxicity of polyvinyl alcohol (PVA). Food and Chemical Toxicology, 2003; 41(3): 319-326.
3. Jiang, H.; Campbell, G., et al., Design and manufacture of a polyvinyl alcohol (PVA) cryogel tri-leaflet heart valve prosthesis. Medical Engineering & Physics, 2004; 26(4): 269-277.
4. Bodugoz-Senturk, H.; Macias, C. E., et al., Poly(vinyl alcohol)-acrylamide hydrogels as load-bearing cartilage substitute. Biomaterials, 2009; 30(4): 589-596.
5. Charles, R. N.; Derek, J. M., et al., Attachment of fibronectin to poly(vinyl alcohol) hydrogels promotes NIH3T3 cell adhesion, proliferation, and migration. Journal of Biomedical Materials Research, 2001; 57(2): 217-223.
6. Sailaja, G. S.; Sreenivasan, K., et al., Bioinspired mineralization and cell adhesion on surface functionalized poly(vinyl alcohol) films. Acta Biomaterialia, 2009; 5(5): 1647-1655.
7. Zajaczkowski, M. B.; Cukierman, E., et al., Cell-Matrix Adhesions on Poly(vinyl alcohol) Hydrogels. Tissue Engineering, 2003; 9(3): 525-533.
8. Tomoe, K.; Norihiko, M., et al., Attachment and growth of cultured fibroblast cells on PVA/chitosan-blended hydrogels. Journal of Biomedical Materials Research, 1998; 39(3): 486-490.
9. Lei Li; Hsieh, Y.-L., Chitosan bicomponent nanofibers and nanoporous fibers. Carbohydrate Research, 2006; 341(3): 374-381.
10. Takashi, S.; Takehisa, M., Photochemical surface derivatization of a peptide containing Arg-Gly-Asp (RGD). Journal of Biomedical Materials Research, 1995; 29(9): 1047-1052.
11. Schmedlen, R. H.; Masters, K. S., et al., Photocrosslinkable polyvinyl alcohol hydrogels that can be modified with cell adhesion peptides for use in tissue engineering. Biomaterials, 2002; 23(22): 4325-4332.
12. de Souza Costa-Júnior, E.; Pereira, M., et al., Properties and biocompatibility of chitosan films modified by blending with PVA and chemically crosslinked. Journal of Materials Science: Materials in Medicine, 2009; 20(2): 553-561.
13. Mansur, H. S.; de S. Costa Jr, E., et al., Cytocompatibility evaluation in cell-culture systems of chemically crosslinked chitosan/PVA hydrogels. Materials Science and Engineering: C, 2009; 29(5): 1574-1583.
14. Mathews, D. T.; Birney, Y. A., et al., Vascular cell viability on polyvinyl alcohol hydrogels modified with water-soluble and -insoluble chitosan. Journal of Biomedical Materials Research Part B: Applied Biomaterials, 2008; 84B(2): 531-540.
15. Wang, Y.; Hsieh, Y. L., Immobilization of lipase enzyme in polyvinyl alcohol (PVA) nanofibrous membranes. Journal of Membrane Science, 2008; 309(1-2): 73-81.

16. Yang, D.; Li, Y., et al., Preparation of gelatin/PVA nanofibers and their potential application in controlled release of drugs. Carbohydrate Polymers, 2007; 69(3): 538-543.
17. Liu, Y.; Geever, L. M., et al., Thermal behavior and mechanical properties of physically crosslinked PVA/Gelatin hydrogels. Journal of the Mechanical Behavior of Biomedical Materials, 2010; 3(2): 203-209.
18. Rui, S.; Aichen, Z., et al., In vitro degradation of starch/PVA films and biocompatibility evaluation. Journal of Applied Polymer Science, 2010; 115(1): 346-357.
19. Shalumon, K. T.; Binulal, N. S., et al., Electrospinning of carboxymethyl chitin/poly(vinyl alcohol) nanofibrous scaffolds for tissue engineering applications. Carbohydrate Polymers, 2009; 77(4): 863-869.
20. Jiang, T.; Wang, G., et al., Heparinized poly(vinyl alcohol)–small intestinal submucosa composite membrane for coronary covered stents. Biomedical Materials, 2009; 4(2): 025012.
21. Hayami, T.; Matsumura, K., et al., Imparting cell adhesion to poly(vinyl alcohol) hydrogel by coating with hydroxyapatite thin film. Materials Letters, 2007; 61(13): 2667-2670.
22. Zhu, X.; Cui, W., et al., Electrospun Fibrous Mats with High Porosity as Potential Scaffolds for Skin Tissue Engineering. Biomacromolecules, 2008; 9(7): 1795-1801.
23. Ghassemifar, R.; Redmond, S., et al., Advancing Towards a Tissue-Engineered Tympanic Membrane: Silk Fibroin as a Substratum for Growing Human Eardrum Keratinocytes. J Biomater Appl, 2009: 0885328209104289.
24. McManus, M.; Boland, E., et al., Electrospun nanofibre fibrinogen for urinary tract tissue reconstruction. Biomedical Materials, 2007; 2(4): 257-262.
25. Prabhakaran, M. P.; Venugopal, J., et al., Electrospun Biocomposite Nanofibrous Scaffolds for Neural Tissue Engineering. Tissue Engineering Part A, 2008; 14(11).
26. Dolder, J.; Jansen, J., Titanium Fiber Mesh: A Nondegradable Scaffold Material. In Engineering of Functional Skeletal Tissues, 2007; pp 69-80.
27. Seal, B. L.; Otero, T. C., et al., Polymeric biomaterials for tissue and organ regeneration. Materials Science and Engineering: R: Reports, 2001; 34(4-5): 147-230.
28. Nuttelman, C. R.; Henry, S. M., et al., Synthesis and characterization of photocrosslinkable, degradable poly(vinyl alcohol)-based tissue engineering scaffolds. Biomaterials, 2002; 23(17): 3617-3626.
29. Cahn, F.; Kyriakides, T. R., Generation of an artificial skin construct containing a non-degradable fiber mesh: a potential transcutaneous interface. Biomedical Materials, 2008; 3(3): 034110.
30. Cascone, M. G.; Laus, M., et al., Evaluation of poly(vinyl alcohol) hydrogels as a component of hybrid artificial tissues. Journal of Materials Science: Materials in Medicine, 1995; 6(2): 71-75.
31. Colin, G.; Pete, T., et al., Poly(vinyl alcohol) Hydrogel as a Biocompatible Viscoelastic Mimetic for Articular Cartilage. Biotechnology Progress, 2006; 22(5): 1400-1406.

32. Yudong Zheng; Hexiang Lv, et al., Performance of novel bioactive hybrid hydrogels in vitro and in vivo used for artificial cartilage. Biomedical Materials, 2009; 4(1): 1-7.
33. Yuichi, U.; Shigeto, S., et al., Amniotic membrane immobilized poly(vinyl alcohol) hybrid polymer as an artificial cornea scaffold that supports a stratified and differentiated corneal epithelium. Journal of Biomedical Materials Research Part B: Applied Biomaterials, 2007; 81B(1): 201-206.
34. Hideyuki, M.; Shigeto, S., et al., Collagen-immobilized poly (vinyl alcohol) as an artificial cornea scaffold that supports a stratified corneal epithelium. Journal of Biomedical Materials Research Part B: Applied Biomaterials, 2006; 76B(1): 56-63.
35. Ramakrishna, S.; Fujihara, K., et al., Electrospun nanofibers: solving global issues. Materials Today, 2006; 9(3): 40-50.
36. Stevens, M. M.; George, J. H., Exploring and Engineering the Cell Surface Interface Science, 2005; 310: 1135 - 1138.
37. Allan, I. U.; Shevchenko, R. V., et al., The use of Confocal Laser Scanning Microscopy to Assess the Potential Suitability of 3D Scaffolds for Tissue Regeneration, by Monitoring Extra-Cellular Matrix Deposition and by Quantifing Cellular Infiltration and Proliferation. Soft Materials, 2009; 7(4): 319 - 341.
38. Formhals, A., US Patent 2187306, 1940.
39. Li, D.; Xia, Y., Electrospinning of Nanofibers: Reinventing the Wheel?. Advanced Materials 2004; 16(14): 1151 - 1170.
40. Li, M.; Mondrinos, M. J., et al., Electrospun protein fibers as matrices for tissue engineering Biomaterials, 2005; 26(39): 5999-6008
41. Adam, D., A fine set of threads. Nature, 2001; 411: 236.
42. Gopal, R.; Kaur, S., et al., Electrospun nanofibrous filtration membrane. Journal of Membrane Science 2006; 281(1-2): 581-586.
43. Khil, M.-S.; Cha, D.-I., et al., Electrospun nanofibrous polyurethane membrane as wound dressing Journal of Biomedical Materials Research 2003; 67B(2): 675 - 679
44. Taepaiboon, P.; Rungsardthong, U., et al., Drug-loaded electrospun mats of poly(vinyl alcohol) fibres and their release characteristics of four model drugs. Nanotechnology, 2006; 17(9): 2317-2329.
45. Xu, C. Y.; Inai, R., et al., Aligned biodegradable nanofibrous structure: a potential scaffold for blood vessel engineering Biomaterials 2004; 25(5): 877-886
46. Li, W.-J.; Laurencin, C. T., et al., Electrospun nanofibrous structure: A novel scaffold for tissue engineering Journal of Biomedical Materials Research, 2002; 60(4): 613 - 621
47. Li, D.; Wang, Y., et al., Electrospinning Nanofibers as Uniaxially Aligned Arrays and Layer-by-Layer Stacked Films Advanced Materials 2004; 16(4): 361 - 366
48. Zhang, D.; Chang, J., Electrospinning of Three-Dimensional Nanofibrous Tubes with Controllable Architectures. Nano Lett., 2008; 8(10): 3283-3287.
49. Praptowidodo, V. S., Influence of swelling on water transport through PVA-based membrane. Journal of Molecular Structure, 2005; 739(1-3): 207-212.

50. Carvalho, L. B.; Araujo, A. M., et al., The use of polyvinyl alcohol glutaraldehyde antigen coated discs for laser induced fluorescence detection of plague. Sensors and Actuators B: Chemical, 1996; 36(1-3): 427-430.
51. Rosiak, J. M.; Ulanski, P., Synthesis of hydrogels by irradiation of polymers in aqueous solution. Radiation Physics and Chemistry, 1999; 55(2): 139-151.
52. Rosiak, J. M., Radiation formation of hydrogels for drug delivery. Journal of Controlled Release, 1994; 31(1): 9-19.
53. Hassan, C. M.; Peppas, N. A., Structure and applications of poly(vinyl alcohol) hydrogels produced by conventional crosslinking or by freezing/thawing methods. In Biopolymers/Pva Hydrogels/Anionic Polymerisation Nanocomposites, Springer-Verlag Berlin: Berlin, 2000; Vol. 153, pp 37-65.
54. Zhou, Y.; Yang, D., et al., Electrospun Water-Soluble Carboxyethyl Chitosan/Poly(vinyl alcohol) Nanofibrous Membrane as Potential Wound Dressing for Skin Regeneration. Biomacromolecules, 2008; 9(1): 349-354.
55. Yao, L.; Haas, T. W., et al., Electrospinning and Stabilization of Fully Hydrolyzed Poly(Vinyl Alcohol) Fibers. Chemistry of Materials, 2003; 15(9): 1860-1864.
56. Naebe, M.; Lin, T., et al., Effects of MWNT nanofillers on structures and properties of PVA electrospun nanofibres. Nanotechnology, 2007; 18(22): 225605.
57. Millon, L. E.; Mohammadi, H., et al., Anisotropic polyvinyl alcohol hydrogel for cardiovascular applications. Journal of Biomedical Materials Research Part B: Applied Biomaterials, 2006; 79B(2): 305-311.
58. Wan, W. K.; Campbell, G., et al., Optimizing the tensile properties of polyvinyl alcohol hydrogel for the construction of a bioprosthetic heart valve stent. Journal of Biomedical Materials Research, 2002; 63(6): 854-861.
59. Millon, L. E.; Nieh, M. P., et al., SANS Characterization of an Anisotropic Poly(vinyl alcohol) Hydrogel with Vascular Applications. Macromolecules, 2007; 40(10): 3655-3662.
60. Kenney J. F.; W., W. G., Structure-Property relationships of poly(vinyl alcohol). III. Relationships between stereo-regularity, crystallinity, and water resistance in poly(vinyl alcohol). Journal of Polymer Science Part A-1: Polymer Chemistry, 1966; 4(3): 679-698.
61. Peppas, N. A., Infrared spectroscopy of semicrystalline poly(vinyl alcohol) networks. Die Makromolekulare Chemie, 1977; 178(2): 595-601.
62. H. Dong; Bell, T., State-of-the-art overview: ion beam surface modification of polymers towards improving tribological properties Surface and Coatings Technology 1999; 111(1): 29-40
63. M. Guenther; K. Sahre, et al., Influence of ion-beam induced chemical and structural modification in polymers on moisture uptake Surface and Coatings Technology 2001 142-144: 482-488.
64. Andrzej Turos; Jacek Jagielski, et al., Ion beam modification of surface properties of polyethylene Vacuum 2003; 70(2-3): 201-206
65. Wong, K. H.; Zinke-Allmang, M., et al., Low energy oxygen ion beam modification of the surface morphology and chemical structure of polyurethane fibers Nuclear Inst. and Methods in Physics Research, B 2006; 243(1): 63-74

66. L.Calcagno, Ion-chains interaction in polymers Nuclear Instruments and Methods in Physics Research Section B: Beam Interactions with Materials and Atoms 1995; 105(1-4): 63-70
67. Wong, K. K. H.; Zinke-Allmang, M., et al., N+ surface doping on nanoscale polymer fabrics via ion implantation. Nuclear Instruments and Methods in Physics Research Section B: Beam Interactions with Materials and Atoms 2006; 249(1-2): 362-365
68. R.J. Rodríguez; J.A. García, et al., Modification of surface mechanical properties of polycarbonate by ion implantation Surface and Coatings Technology 2002; 158-159: 636-642.
69. J.C.Pivin, Contribution of ionizations and atomic displacements to the hardening of ion-irradiated polymers. Thin Solid Films 1995; 263(2): 185-193
70. Rhee, K. Y.; Oh, T. Y., et al., Tensile behavior of polyethylene fiber composites with polyethylene fiber surface-modified using ion irradiation. Journal of Materials Science, 2004; 39(5): 1809-1811.
71. Pelham, R. J., Jr.; Wang, Y.-l., Cell locomotion and focal adhesions are regulated by substrate flexibility. Proceedings of the National Academy of Sciences, 1997; 94(25): 13661-13665.
72. Dennis E. Discher; Paul Janmey, et al., Tissue Cells Feel and Respond to the Stiffness of Their Substrate Science, 2005; 310: 1139 - 1143.
73. de Mel, A.; Jell, G., et al., Biofunctionalization of Biomaterials for Accelerated in Situ Endothelialization: A Review. Biomacromolecules, 2008; 9(11): 2969-2979.
74. Kusakabe, M.; Suzuki, Y., et al., Control of endothelial cell adhesion to polymer surface by ion implantation Polymers for Advanced Technologies 2001; 12(8): 453 - 460
75. Nial A. Bullett; Diane P. Bullett, et al., Polymer surface micropatterning by plasma and VUV-photochemical modification for controlled cell culture Applied Surface Science 2004; 235(4): 395-405
76. Pierre-Luc Girard-Lauriault; Fackson Mwale, et al., Atmospheric Pressure Deposition of Micropatterned Nitrogen-Rich Plasma-Polymer Films for Tissue Engineering Plasma Processes and Polymers 2005; 2(3): 263 - 270
77. Formhals, A., US Patent 2160962, 1939.
78. Formhals, A., US Patent 1975504, 1934.
79. Thandavamoorthy Subbiah; G. S. Bhat, et al., Electrospinning of nanofibers. Journal of Applied Polymer Science, 2004; 96(2): 557 - 569.
80. Xinying Geng; Oh-Hyeong Kwon, et al., Electrospinning of chitosan dissolved in concentrated acetic acid solution. Biomaterials, 2005; 26(27): 5427-5432.
81. Lee, K. Y.; Jeong, L., et al., Electrospinning of polysaccharides for regenerative medicine. Advanced Drug Delivery Reviews, 2009; 61(12): 1020-1032.
82. Hyun Woo Lee; Mohammad Rezaul Karim, et al., Electrospinning and Characterisation of Poly(Vinyl Alcohol) Blend Submicron Fibres in Aqueous Solutions. Polymers and Polymer Composites, 2009; 17(1): 47-54.
83. Doshi, J.; Reneker, D. H., Electrospinning process and applications of electrospun fibers. Journal of Electrostatics, 1995; 35(2-3): 151-160.
84. Taylor, G., Electrically Driven Jets. Proceedings of the Royal Society of London. A. Mathematical and Physical Sciences, 1969; 313(1515): 453-475.

85. Y.M. Shin; M.M. Hohman, et al., Experimental characterization of electrospinning: the electrically forced jet and instabilities Polymer, 2001; 42(25): 09955-09967
86. Huan Pan; Luming Li, et al., Continuous aligned polymer fibers produced by a modified electrospinning method. Polymer, 2006; 47(14): 4901-4904.
87. Sian F. Fennessey; Farris, R. J., Fabrication of aligned and molecularly oriented electrospun polyacrylonitrile nanofibers and the mechanical behavior of their twisted yarns. Polymer, 2004; 45(12): 4217-4225.
88. A. Theron; E. Zussman, et al., Electrostatic field-assisted alignment of electrospun nanofibres. Nanotechnology, 2001; 12: 384-390.
89. Katta, P.; Alessandro, M., et al., Continuous Electrospinning of Aligned Polymer Nanofibers onto a Wire Drum Collector. Nano Letters, 2004; 4(11): 2215-2218.
90. Wang, X.; Zhang, K., et al., Continuous polymer nanofiber yarns prepared by self-bundling electrospinning method. Polymer, 2008; 49(11): 2755-2761.
91. Won-Il Park; Minsung Kang, et al., Electrospinning of Poly(ethylene oxide) with Bacterial Cellulose Whiskers. Macromolecular Symposia, 2007; 249-250(1): 289 - 294.
92. Abarrategi, A.; Gutiérrez, M. C., et al., Multiwall carbon nanotube scaffolds for tissue engineering purposes. Biomaterials, 2008; 29(1): 94-102.
93. Naebe, M.; Lin, T., et al., Electrospun single-walled carbon nanotube/polyvinyl alcohol composite nanofibers: structure–property relationships. Nanotechnology, 2008; 19(30): 305702.
94. Jeong, J. S.; Moon, J. S., et al., Mechanical properties of electrospun PVA/MWNTs composite nanofibers. Thin Solid Films, 2007; 515(12): 5136-5141.
95. Wong, K. K. H.; Zinke-Allmang, M., et al., The effect of carbon nanotube aspect ratio and loading on the elastic modulus of electrospun poly(vinyl alcohol)-carbon nanotube hybrid fibers. Carbon, 2009; 47(11): 2571-2578.
96. Ojha, S. S.; Stevens, D. R., et al., Characterization of Electrical and Mechanical Properties for Coaxial Nanofibers with Poly(ethylene oxide) (PEO) Core and Multiwalled Carbon Nanotube/PEO Sheath. Macromolecules, 2008; 41(7): 2509-2513.
97. Gao, J.; Itkis, M. E., et al., Continuous Spinning of a Single-Walled Carbon Nanotube-Nylon Composite Fiber. J. Am. Chem. Soc., 2005; 127(11): 3847-3854.
98. Ayutsede, J.; Gandhi, M., et al., Carbon Nanotube Reinforced Bombyx mori Silk Nanofibers by the Electrospinning Process. Biomacromolecules, 2006; 7(1): 208-214.
99. Rujitanaroj, P.-o.; Pimpha, N., et al., Wound-dressing materials with antibacterial activity from electrospun gelatin fiber mats containing silver nanoparticles. Polymer, 2008; 49(21): 4723-4732.
100. Wang, Y.; Yang, Q., et al., Preparation of silver nanoparticles dispersed in polyacrylonitrile nanofiber film spun by electrospinning. Materials Letters, 2005; 59(24-25): 3046-3049.
101. Bai, J.; Li, Y., et al., A simple and effective route for the preparation of poly(vinyl alcohol) (PVA) nanofibers containing gold nanoparticles by electrospinning method. Solid State Communications, 2007; 141(5): 292-295.

102. Hamlett, C. A. E.; Jayasinghe, S. N., et al., Electrospinning nanosuspensions loaded with passivated Au nanoparticles. Tetrahedron, 2008; 64(36): 8476-8483.
103. McCann, J. T.; Marquez, M., et al., Highly Porous Fibers by Electrospinning into a Cryogenic Liquid. Journal of the American Chemical Society, 2006; 128(5): 1436-1437.
104. You, Y.; Youk, J. H., et al., Preparation of porous ultrafine PGA fibers via selective dissolution of electrospun PGA / PLA blend fibers. Materials Letters, 2006; 60(6): 757-760.
105. Z. Sun; E. Zussman, et al., Compound Core–Shell Polymer Nanofibers by Co-Electrospinning. Advanced Materials, 2003; 15(22): 1929 - 1932.
106. J. H. Yu; S. V. Fridrikh, et al., Production of Submicrometer Diameter Fibers by Two-Fluid Electrospinning. Advanced Materials, 2004; 16(17): 1562 - 1566.
107. Bazilevsky, A. V.; Yarin, A. L., et al., Co-electrospinning of Core-Shell Fibers Using a Single-Nozzle Technique. Langmuir, 2007; 23(5): 2311-2314.
108. Li, X. H.; Shao, C. L., et al., A Simple Method for Controllable Preparation of Polymer Nanotubes via a Single Capillary Electrospinning. Langmuir, 2007; 23(22): 10920-10923.
109. Loscertales, I. G.; Barrero, A., et al., Electrically Forced Coaxial Nanojets for One-Step Hollow Nanofiber Design. Journal of the American Chemical Society, 2004; 126(17): 5376-5377.
110. Yang, Y.; Li, X., et al., Release pattern and structural integrity of lysozyme encapsulated in core-sheath structured poly(dl-lactide) ultrafine fibers prepared by emulsion electrospinning. European Journal of Pharmaceutics and Biopharmaceutics, 2008; 69(1): 106-116.
111. Hongliang Jiang; Yingqian Hu, et al., A facile technique to prepare biodegradable coaxial electrospun nanofibers for controlled release of bioactive agents. Journal of Controlled Release, 2005; 108(2-3): 237-243.
112. Liao, I. C.; Chen, S., et al., Sustained viral gene delivery through core-shell fibers. Journal of Controlled Release, 2009; 139(1): 48-55.
113. Thakur, R. A.; Florek, C. A., et al., Electrospun nanofibrous polymeric scaffold with targeted drug release profiles for potential application as wound dressing. International Journal of Pharmaceutics, 2008; 364(1): 87-93.
114. Townsend-Nicholson, A.; Jayasinghe, S. N., Cell Electrospinning: a Unique Biotechnique for Encapsulating Living Organisms for Generating Active Biological Microthreads/Scaffolds. Biomacromolecules, 2006; 7(12): 3364-3369.
115. Arumuganathar, S.; Irvine, S., et al., Pressure-assisted cell spinning: a direct protocol for spinning biologically viable cell-bearing fibres and scaffolds. Biomedical Materials, 2007; 2(4): 211-219.
116. Kong, C.-S.; Lee, T.-H., et al., Interference between the Charged Jets in Electrospinning of Polyvinyl Alcohol. Journal of Macromolecular Science, Part B: Physics, 2009; 48(1): 77-91.
117. Bocanegra, R.; Galán, D., et al., Multiple electrosprays emitted from an array of holes. Journal of Aerosol Science, 2005; 36(12): 1387-1399.
118. Varesano, A.; Carletto, R. A., et al., Experimental investigations on the multi-jet electrospinning process. Journal of Materials Processing Technology, 2009; 209(11): 5178-5185.

119. Kim, G.; Cho, Y.-S., et al., Stability analysis for multi-jets electrospinning process modified with a cylindrical electrode. European Polymer Journal, 2006; 42(9): 2031-2038.
120. Theron, S. A.; Yarin, A. L., et al., Multiple jets in electrospinning: experiment and modeling. Polymer, 2005; 46(9): 2889-2899.
121. Xin, W.; Haitao, N., et al., Needleless electrospinning of nanofibers with a conical wire coil. Polymer Engineering & Science, 2009; 49(8): 1582-1586.
122. Liu, Y.; He, J.-H., Bubble Electrospinning for Mass Production of Nanofibers. International Journal of Nonlinear Sciences and Numerical Simulation, 2007; 8(3): 393-396.
123. Dosunmu, O. O.; Chase, G. G., et al., Electrospinning of polymer nanofibres from multiple jets on a porous tubular surface. Nanotechnology, 2006; 17(4): 1123-1127.
124. Varabhas, J. S.; Chase, G. G., et al., Electrospun nanofibers from a porous hollow tube. Polymer, 2008; 49(19): 4226-4229.
125. Lukas, D.; Sarkar, A., et al., Self-organization of jets in electrospinning from free liquid surface: A generalized approach. Journal of Applied Physics, 2008; 103(8): 084309-7.
126. Qi, Z.; Yu, H., et al., Highly porous fibers prepared by electrospinning a ternary system of nonsolvent/solvent/poly(l-lactic acid). Materials Letters, 2009; 63(3-4): 415-418.
127. Bashur, C. A.; Dahlgren, L. A., et al., Effect of fiber diameter and orientation on fibroblast morphology and proliferation on electrospun poly(d,l-lactic-co-glycolic acid) meshes. Biomaterials, 2006; 27(33): 5681-5688.
128. Kumbar, S. G.; Nukavarapu, S. P., et al., Electrospun poly(lactic acid-co-glycolic acid) scaffolds for skin tissue engineering. Biomaterials, 2008; 29(30): 4100-4107.
129. Baker, S. C.; Atkin, N., et al., Characterisation of electrospun polystyrene scaffolds for three-dimensional in vitro biological studies. Biomaterials, 2006; 27(16): 3136-3146.
130. Angelo Pedicini; Farris, R. J., Mechanical behavior of electrospun polyurethane. Polymer, 2003; 44(22): 6857-6862.
131. M.M. Demir; I. Yilgor, et al., Electrospinning of polyurethane fibers Polymer, 2002; 43(11): 3303-3309
132. Pitt Supaphol; Chidchanok Mit-Uppatham, et al., Ultrafine electrospun polyamide-6 fibers: Effect of emitting electrode polarity on morphology and average fiber diameter Journal of Polymer Science Part B: Polymer Physics 2005; 43(24): 3699 - 3712
133. Chidchanok Mit-uppatham; Manit Nithitanakul, et al., Ultrafine Electrospun Polyamide-6 Fibers: Effect of Solution Conditions on Morphology and Average Fiber Diameter Macromolecular Chemistry and Physics 2004; 205(17): 2327 - 2338
134. Yang, L.; Fitié, C. F. C., et al., Mechanical properties of single electrospun collagen type I fibers. Biomaterials, 2008; 29(8): 955-962.
135. Jamil A. Matthews; Gary E. Wnek, et al., Electrospinning of Collagen Nanofibers Biomacromolecules, 2002; 3(2): 232 -238.

136. Ohkawa, K.; Minato, K. I., et al., Chitosan Nanofiber. Biomacromolecules, 2006; 7(11): 3291-3294.
137. Homayoni, H.; Ravandi, S. A. H., et al., Electrospinning of chitosan nanofibers: Processing optimization. Carbohydrate Polymers, 2009; 77(3): 656-661.
138. Xu, S.; Li, J., et al., Chemical crosslinking and biophysical properties of electrospun hyaluronic acid based ultra-thin fibrous membranes. Polymer, 2009; 50(15): 3762-3769.
139. Ji, Y.; Ghosh, K., et al., Electrospun three-dimensional hyaluronic acid nanofibrous scaffolds. Biomaterials, 2006; 27(20): 3782-3792.
140. Sikareepaisan, P.; Suksamrarn, A., et al., Electrospun gelatin fiber mats containing a herbal-Centella asiatia-extract and release characteristic of asiaticoside. Nanotechnology, 2008; 19(1): 015102.
141. Zarkoob, S.; Eby, R. K., et al., Structure and morphology of electrospun silk nanofibers. Polymer, 2004; 45(11): 3973-3977.
142. Min, B.-M.; Lee, G., et al., Electrospinning of silk fibroin nanofibers and its effect on the adhesion and spreading of normal human keratinocytes and fibroblasts in vitro. Biomaterials, 2004; 25(7-8): 1289-1297.
143. SOFFER, L.; WANG, X., et al., Silk-based electrospun tubular scaffolds for tissue-engineered vascular grafts. Journal of Biomaterials Science, Polymer Edition 2008; 19(5): 653.
144. Sukigara, S.; Gandhi, M., et al., Regeneration of Bombyx mori silk by electrospinning--part 1: processing parameters and geometric properties. Polymer, 2003; 44(19): 5721-5727.
145. Di, J.; Chen, H., et al., Fabrication of Zeolite Hollow Fibers by Coaxial Electrospinning. Chemistry of Materials, 2008; 20(11): 3543-3545.
146. Zhan, S.; Chen, D., et al., Co-electrospun SiO2 hollow nanostructured fibers with hierarchical walls. Journal of Colloid and Interface Science, 2008; 318(2): 331-336.
147. D. D. Lin, H. W. W. P., Photoswitches and Memories Assembled by Electrospinning Aluminum-Doped Zinc Oxide Single Nanowires. Advanced Materials, 2007; 19(22): 3968-3972.
148. Hota, G.; Kumar, B., et al., Fabrication and characterization of a boehmite nanoparticle impregnated electrospun fiber membrane for removal of metal ions. Journal of Materials Science, 2008; 43(1): 212-217.
149. Chandrasekar, R.; Zhang, L., et al., Fabrication and characterization of electrospun titania nanofibers. Journal of Materials Science, 2009; 44(5): 1198-1205.
150. Feng Yi; Zhao-Xia Guo, et al., Mimetics of Eggshell Membrane Protein Fibers by Electrospinning Macromolecular Rapid Communications 2004; 25(10): 1038-1043.
151. Kowalczyk, T.; Nowicka, A., et al., Electrospinning of Bovine Serum Albumin. Optimization and the Use for Production of Biosensors. Biomacromolecules, 2008; 9(7): 2087-2090.
152. Choi, J. S.; Lee, S. J., et al., The influence of electrospun aligned poly(e-caprolactone)/collagen nanofiber meshes on the formation of self-aligned skeletal muscle myotubes. Biomaterials, 2008; 29(19): 2899-2906.

153. Schnell, E.; Klinkhammer, K., et al., Guidance of glial cell migration and axonal growth on electrospun nanofibers of poly-[epsilon]-caprolactone and a collagen/poly-[epsilon]-caprolactone blend. Biomaterials, 2007; 28(19): 3012-3025.
154. Vega-Lugo, A.-C.; Lim, L.-T., Controlled release of allyl isothiocyanate using soy protein and poly(lactic acid) electrospun fibers. Food Research International, 2009; 42(8): 933-940.
155. Catledge, S. A.; Clem, W. C., et al., An electrospun triphasic nanofibrous scaffold for bone tissue engineering. Biomedical Materials, 2007; 2(2): 142-150.
156. Chen, Z.; Mo, X., et al., Electrospinning of collagen-chitosan complex. Materials Letters, 2007; 61(16): 3490-3494.
157. Chen, Z.; Wei, B., et al., Mechanical properties of electrospun collagen-chitosan complex single fibers and membrane. Materials Science and Engineering: C, 2009; 29(8): 2428-2435.
158. Khan, U.; Ryan, K., et al., The effect of solvent choice on the mechanical properties of carbon nanotube-polymer composites. Composites Science and Technology, 2007; 67(15-16): 3158-3167.
159. Kobayashi, M.; Toguchida, J., et al., Preliminary study of polyvinyl alcohol-hydrogel (PVA-H) artificial meniscus. Biomaterials, 2003; 24(4): 639-647.
160. Bodugoz-Senturk, H.; Choi, J., et al., The effect of polyethylene glycol on the stability of pores in polyvinyl alcohol hydrogels during annealing. Biomaterials, 2008; 29(2): 141-149.
161. Stylianopoulos, T.; Bashur, C. A., et al., Computational predictions of the tensile properties of electrospun fibre meshes: Effect of fibre diameter and fibre orientation. Journal of the Mechanical Behavior of Biomedical Materials, 2008; 1(4): 326-335.
162. Jung YH; Kim HY, et al., Characterization of PVOH Nonwoven Mats Prepared from Surfactant-Polymer System via Electrospinning. Macromolecular Research, 2005; 13(5): 385-390.
163. Xiaofan Wei; Zhenhai Xia, et al., Modelling of mechanical properties of electrospun nanofibre network. International Journal of Experimental and Computational Biomechanics, 2009; 1(1): 45 - 57.
164. Stylianopoulos, T.; Barocas, V. H., Volume-averaging theory for the study of the mechanics of collagen networks. Computer Methods in Applied Mechanics and Engineering, 2007; 196(31-32): 2981-2990.
165. Balaji, A.; Victor, H. B., Coupled Macroscopic and Microscopic Scale Modeling of Fibrillar Tissues and Tissue Equivalents. Journal of Biomechanical Engineering, 2001; 123(4): 362-369.
166. R. Inai; M. Kotaki, et al., Deformation behavior of electrospun poly(L-lactide-co-e-caprolactone) nonwoven membranes under uniaxial tensile loading. Journal of Polymer Science Part B: Polymer Physics, 2005; 43(12): 3205 - 3212.
167. Jonathan Ayutsede; Milind Gandhi, et al., Regeneration of Bombyx mori silk by electrospinning. Part 3: characterization of electrospun nonwoven mat. Polymer, 2005; 46(5): 1625-1634.

168. Thomas, V.; Zhang, X., et al., Functionally graded electrospun scaffolds with tunable mechanical properties for vascular tissue regeneration. Biomedical Materials, 2007; 2(4): 224-232.
169. Zhou, Z.; Lai, C., et al., Development of carbon nanofibers from aligned electrospun polyacrylonitrile nanofiber bundles and characterization of their microstructural, electrical, and mechanical properties. Polymer, 2009; 50(13): 2999-3006.
170. Wang, C. W.; Sastry, A. M., Structure, Mechanics and Failure of Stochastic Fibrous Networks: Part II---Network Simulations and Application. Journal of Engineering Materials and Technology, 2000; 122(4): 460-468.
171. Wang, C. W.; Berhan, L., et al., Structure, Mechanics and Failure of Stochastic Fibrous Networks: Part I---Microscale Considerations. Journal of Engineering Materials and Technology, 2000; 122(4): 450-459.
172. E. Zussman; X. Chen, et al., Mechanical and structural characterization of electrospun PAN-derived carbon nanofibers. Carbon, 2005; 43(10): 2175-2185.
173. Min Kyoon Shin; Sun I. Kim, et al., Size-dependent elastic modulus of single electroactive polymer nanofibers. Applied Physics Letters, 2006; 89: 231929.
174. Arkadii Arinstein; Michael Burman, et al., Effect of supramolecular structure on polymer nanofibre elasticity. Nature Nanotechnology, 2007; 2: 59 - 62
175. Ding, Y.; Zhang, P., et al., Mechanical properties of nylon-6/SiO2 nanofibers prepared by electrospinning. Materials Letters, 2009; 63(1): 34-36.
176. Qiang, F.; Yu, J., et al., Size-dependent mechanical properties of PVA nanofibers reduced via air plasma treatment. Nanotechnology, 2010; (9): 095703.
177. Yu, M.-F.; Files, B. S., et al., Tensile Loading of Ropes of Single Wall Carbon Nanotubes and their Mechanical Properties. Physical Review Letters, 2000; 84(24): 5552.
178. Tan, E. P. S.; Lim, C. T., Novel approach to tensile testing of micro- and nanoscale fibers. Review of Scientific Instruments, 2004; 75(8): 2581-2585.
179. Tan, E. P. S.; Goh, C. N., et al., Tensile test of a single nanofiber using an atomic force microscope tip. Applied Physics Letters, 2005; 86(7): 073115-3.
180. Yu, M.-F.; Lourie, O., et al., Strength and Breaking Mechanism of Multiwalled Carbon Nanotubes Under Tensile Load. Science, 2000; 287(5453): 637-640.
181. MinFeng Yu; Mark J Dyer, et al., Three-dimensional manipulation of carbon nanotubes under a scanning electron microscope. Nanotechnology, 1999; 10(3): 244-25.
182. Mohammad, N.; Ioannis, C., et al., Novel method for mechanical characterization of polymeric nanofibers. Review of Scientific Instruments, 2007; 78(8): 085108.
183. Weiqiang Ding; Lorenzo Calabri, et al., Mechanics of crystalline boron nanowires Composites Science and Technology 2006; 66(9): 1112-1124
184. Joost A. J. van der Rijt; Kees O. van der Werf, et al., Micromechanical Testing of Individual Collagen Fibrils. Macromolecular Bioscience, 2006; 6(9): 697-702.
185. Wong, K. K. H.; Hutter, J. L., et al., Physical properties of ion beam treated electrospun poly(vinyl alcohol) nanofibers. European Polymer Journal, 2009; 45(5): 1349-1358.

186. E. Zussman; M. Burman, et al., Tensile deformation of electrospun nylon-6,6 nanofibers. Journal of Polymer Science Part B: Polymer Physics, 2006; 44(10): 1482 - 1489.
187. Bozec, L.; Horton, M., Topography and Mechanical Properties of Single Molecules of Type I Collagen Using Atomic Force Microscopy. Biophys. J., 2005; 88(6): 4223-4231.
188. Espinosa, H. D.; Yong, Z., et al., Design and Operation of a MEMS-Based Material Testing System for Nanomechanical Characterization. Microelectromechanical Systems, Journal of, 2007; 16(5): 1219-1231.
189. Brown, J. J.; Suk, J. W., et al., Microsystem for nanofiber electromechanical measurements. Sensors and Actuators A: Physical, 2009; 155(1): 1-7.
190. Agrawal, R.; Peng, B., et al., Elasticity Size Effects in ZnO Nanowires-A Combined Experimental-Computational Approach. Nano Letters, 2008; 8(11): 3668-3674.
191. Demczyk, B. G.; Wang, Y. M., et al., Direct mechanical measurement of the tensile strength and elastic modulus of multiwalled carbon nanotubes. Materials Science and Engineering A, 2002; 334(1-2): 173-178.
192. Tan, E. P. S.; Lim, C. T., Nanoindentation study of nanofibers. Applied Physics Letters, 2005; 87(12): 123106.
193. Jae-Young Rho; Marcel E. Roy II, et al., Elastic properties of microstructural components of human bone tissue as measured by nanoindentation. Journal of Biomedical Materials Research, 1999; 45(1): 48-54.
194. Li, X.; Gao, H., et al., Nanoindentation of Silver Nanowires. Nano Letters, 2003; 3(11): 1495-1498.
195. F. Ko; Y. Gogotsi, et al., Electrospinning of Continuous Carbon Nanotube-Filled Nanofiber Yarns. Advanced Materials, 2003; 15(14): 1161-1165.
196. Mao Wang; Hyoung-Joon Jin, et al., Mechanical Properties of Electrospun Silk Fibers Macromolecules 2004 37(18): 6856-6864
197. Stephane, C.; Christian, F., et al., Measurement of elastic modulus of nanotubes by resonant contact atomic force microscopy. Journal of Applied Physics, 2003; 93(9): 5650-5655.
198. Stéphane Cuenot; Christian Frétigny, et al., Surface tension effect on the mechanical properties of nanomaterials measured by atomic force microscopy. Physical Review B, 2004; 69(16): 165410
199. C. Q. Chen; Y. Shi, et al., Size Dependence of Young's Modulus in ZnO Nanowires. Physical Review Letter, 2006; 96(075505).
200. Yang, N.; Wong, K. K. H., et al., Frequency-dependent viscoelasticity measurement by atomic force microscopy. Measurement Science and Technology, 2009; 20(2): 025703.
201. Boussaad, S.; Tao, N. J., Polymer Wire Chemical Sensor Using a Microfabricated Tuning Fork. Nano Letters, 2003; 3(8): 1173-1176.
202. Philippe Poncharal; Z. L. Wang, et al., Electrostatic Deflections and Electromechanical Resonances of Carbon Nanotubes. Science, 1999; 283(5407): 1513 - 1516.
203. Salvetat, J.-P.; Briggs, G. A. D., et al., Elastic and Shear Moduli of Single-Walled Carbon Nanotube Ropes. Physical Review Letters, 1999; 82(5): 944.

204. Bauchau, O. A.; Craig, J. I., Euler-Bernoulli beam theory. In Structural Analysis, 2009; pp 173-221.
205. Guhados, G.; Wan, W., et al., Measurement of the elastic modulus of single bacterial cellulose fiber using atomic force microscopy. Langmuir, 2005; 21(14): 6642-6646.
206. Sung-Hwan Lee; Cagri Tekmen, et al., Three-point bending of electrospun TiO2 nanofibers Materials Science & Engineering A 2005; 398(1-2): 77-81
207. E. P. S. Tan; Lim, C. T., Physical properties of a single polymeric nanofiber. Applied Physics Letters 2004; 84(9): 1603-1605
208. Stéphane Cuenot; Sophie Demoustier-Champagne, et al., Elastic Modulus of Polypyrrole Nanotubes Physical Review Letter, 2000; 85(8): 1690 - 1693.
209. Sriram Sundararajan; Bhushan, B., Development of AFM-based techniques to measure mechanical properties of nanoscale structures. Sensors and Actuators A: Physical, 2002; 101(3): 338-351.
210. Sundararajan, S.; Bhushan, B., et al., Mechanical property measurements of nanoscale structures using an atomic force microscope. Ultramicroscopy, 2002; 91(1-4): 111-118.
211. Namazu, T.; Isono, Y., et al., Plastic deformation of nanometric single crystal silicon wire in AFM bending test at intermediate temperatures. Journal of Microelectromechanical Systems, 2002; 11(2): 125-135.
212. Namazu Takahiro; Yoshitada, I., Quasi-static bending test of nano-scale SiO2 wire at intermediate temperatures using AFM-based technique. Sensors and Actuators A: Physical, 2003; 104(1): 78-85.
213. E. P. S. Tan; Y. Zhu, et al., Crystallinity and surface effects on Young's modulus of CuO nanowires. Applied Physics Letters, 2007; 90(163112): 16 April 2007.
214. Wu, B.; Heidelberg, A., et al., Mechanical properties of ultrahigh-strength gold nanowires. Nat Mater, 2005; 4(7): 525-529.
215. Cheng, Q.; Wang, S., et al., Effects of process and source on elastic modulus of single cellulose fibrils evaluated by atomic force microscopy. Composites Part A: Applied Science and Manufacturing, 2009; 40(5): 583-588.
216. Iwamoto, S.; Kai, W., et al., Elastic Modulus of Single Cellulose Microfibrils from Tunicate Measured by Atomic Force Microscopy. Biomacromolecules, 2009; 10(9): 2571-2576.
217. Cheng, Q.; Wang, S., A method for testing the elastic modulus of single cellulose fibrils via atomic force microscopy. Composites Part A: Applied Science and Manufacturing, 2008; 39(12): 1838-1843.
218. Gyu-Tae, K.; Gang, G., et al., Simple method to prepare individual suspended nanofibers. Applied Physics Letters, 2002; 80(10): 1815-1817.
219. Duvail, J. L.; Rétho, P., et al., Physical properties of conducting polymer nanofibers. Synthetic Metals, 2003; 135-136: 329-330.
220. Ganesh Guhados; Wankei Wan, et al., Simultaneous measurement of Young's and shear moduli of multiwalled carbon nanotubes using atomic force microscopy. Journal of Applied Physics, 2007; 101: 033514.
221. Shu-Ying Gu; Qi-Lin Wu, et al., Mechanical Properties of a Single Electrospun Fiber and Its Structures Macromolecular Rapid Communications 2005; 26(9): 716 - 720

222. Wong, E. W.; Sheehan, P. E., et al., Nanobeam Mechanics: Elasticity, Strength, and Toughness of Nanorods and Nanotubes. Science, 1997; 277(5334): 1971-1975.
223. Kaplan-Ashiri I. ; Cohen S.R. , et al., Mechanical behavior of individual WS2 nanotubes. Journal of Materials Research, 2004; 19(2): 454-459.
224. MacDonald, D. E.; Rapuano, B. E., et al., Thermal and chemical modification of titanium-aluminum-vanadium implant materials: effects on surface properties, glycoprotein adsorption, and MG63 cell attachment. Biomaterials, 2004; 25(16): 3135-3146.
225. Geetha, M.; Singh, A. K., et al., Ti based biomaterials, the ultimate choice for orthopaedic implants - A review. Progress in Materials Science, 2009; 54(3): 397-425.
226. Staiger, M. P.; Pietak, A. M., et al., Magnesium and its alloys as orthopedic biomaterials: A review. Biomaterials, 2006; 27(9): 1728-1734.
227. Giavaresi, G.; Ambrosio, L., et al., Histomorphometric, ultrastructural and microhardness evaluation of the osseointegration of a nanostructured titanium oxide coating by metal-organic chemical vapour deposition: an in vivo study. Biomaterials, 2004; 25(25): 5583-5591.
228. Rupp, F.; Scheideler, L., et al., Roughness induced dynamic changes of wettability of acid etched titanium implant modifications. Biomaterials, 2004; 25(7-8): 1429-1438.
229. Braceras, I.; Alava, J. I., et al., Interaction of engineered surfaces with the living world: Ion implantation vs. osseointegration. Surface and Coatings Technology, 2007; 201(19-20): 8091-8098.
230. Chu, P. K., Enhancement of surface properties of biomaterials using plasma-based technologies. Surface and Coatings Technology, 2007; 201(19-20): 8076-8082.
231. Chapiro, A., Radiation chemistry of polymeric systems. New York, Interscience Publishers, 1962.
232. J.F. Ziegler; J.P. Biersack, et al., The Stopping and Range of Ions in Solids. Pergamon, New York, 1985.
233. W. H. Bragg; Kleeman, R., Bragg's rule. Philosophical Magazine, 1905; 10: 318.
234. Both, G.; Krotz, R., et al., Density dependence of stopping cross sections measured in liquid ethane. Physical Review A, 1983; 28(6): 3212.
235. A. J.Wagner; D. H. Fairbrother, et al., A Comparison of PE Surfaces Modified by Plasma Generated Neutral Nitrogen Species and Nitrogen Ions Plasmas and Polymers 2003; 8(2): 119-134.
236. N. Sprang; D. Theirich, et al., Plasma and ion beam surface treatment of polyethylene Surface and Coatings Technology 1995; 74-75 Part 2: 689-695
237. J.S. Chen; S.P. Lau, et al., Structural and mechanical properties of nitrogen ion implanted ultra high molecular weight polyethylene Surface and Coatings Technology 2001; 138(1): 33-38
238. D.J. Li; F.Z. Cui, et al., F^+ ion implantation induced cell attachment on intraocular lens Biomaterials, 1999; 20(20): 1889-1896
239. K. Kurotobi; Y. Suzuki, et al., Platelet adhesion and plasma protein adsorption control of collagen surfaces by He^+ ion implantation Nuclear Instruments and

Methods in Physics Research Section B: Beam Interactions with Materials and Atoms, 2003; 206: 532-537

240. Satriano, C.; Marletta, G., et al., Cell adhesion on low-energy ion beam-irradiated polysiloxane surfaces. Nuclear Instruments and Methods in Physics Research Section B: Beam Interactions with Materials and Atoms, 1999; 148(1-4): 1079-1084.
241. Suzuki, Y., Ion beam modification of polymers for the application of medical devices. Nuclear Instruments and Methods in Physics Research Section B: Beam Interactions with Materials and Atoms, 2003; 206: 501-506.
242. Pignataro, B.; Conte, E., et al., Improved cell adhesion to ion beam-irradiated polymer surfaces. Biomaterials, 1997; 18(22): 1461-1470.
243. J. Jagielski; A. Piatkowska, et al., Ion implantation for surface modification of biomaterials. Surface and Coatings Technology, 2006; 200(22-23): 6355-6361.
244. Zuweia Ma; M. Kotaki, et al., Surface modified nonwoven polysulphone (PSU) fiber mesh by electrospinning: A novel affinity membrane. Journal of Membrane Science, 2006; 272(1-2): 179-187.
245. Tan, E. P. S.; Lim, C. T., Effects of annealing on the structural and mechanical properties of electrospun polymeric nanofibres. Nanotechnology, 2006; 17(10): 2649-2654.
246. Lee, S. J.; Oh, S. H., et al., The use of thermal treatments to enhance the mechanical properties of electrospun poly(ε-caprolactone) scaffolds. Biomaterials, 2008; 29(10): 1422-1430.
247. Newton, D.; Mahajan, R., et al., Regulation of material properties in electrospun scaffolds: Role of cross-linking and fiber tertiary structure. Acta Biomaterialia, 2009; 5(1): 518-529.
248. Y.Z. Zhang; J. Venugopal, et al., Crosslinking of the electrospun gelatin nanofibers. Polymer, 2006; 47(8): 2911-2917.
249. Peppas, N. A.; Merrill, E. W., Poly(vinyl alcohol) hydrogels: Reinforcement of radiation-crosslinked networks by crystallization. Journal of Polymer Science: Polymer Chemistry Edition, 1976; 14(2): 441-457.
250. Taepaiboon, P.; Rungsardthong, U., et al., Effect of cross-linking on properties and release characteristics of sodium salicylate-loaded electrospun poly(vinyl alcohol) fibre mats. Nanotechnology, 2007; 18(17): 175102.
251. Kenawy, E.-R.; Abdel-Hay, F. I., et al., Controlled release of ketoprofen from electrospun poly(vinyl alcohol) nanofibers. Materials Science and Engineering: A, 2007; 459(1-2): 390-396.
252. Buddy D. Ratner; Bryant, S. J., Biomaterials: Where We Have Been and Where We are Going. Annual Review of Biomedical Engineering, 2004; 6: 41-75
253. Anderson, J. M., Biological Responses to Materials. Annual Review of Materials Research, 2001; 31(1): 81-110.
254. Hay, E. D., The mesenchymal cell, its role in the embryo, and the remarkable signaling mechanisms that create it. Developmental Dynamics 2005; 233 (3): 706-720
255. Doljanski, F., The Sculpturing Role of Fibroblast-Like Cells in Morphogenesis. Perspectives in Biology and Medicine., 2004; 47(3): 18.
256. Alan Stevens; Lowe, J. S., Human Histology, 3rd Edition. Elservier Limited, 2005.

257. Cukierman, E.; Pankov, R., et al., Cell interactions with three-dimensional matrices. Current Opinion in Cell Biology, 2002; 14(5): 633-640.
258. Lauffenburger, D. A.; Horwitz, A. F., Cell Migration: A Physically Integrated Molecular Process. Cell, 1996; 84(3): 359-369.
259. Grinnell, F., Fibroblast biology in three-dimensional collagen matrices. Trends in Cell Biology, 2003; 13(5): 264-269.
260. Grinnell, F.; Ho, C.-H., et al., Dendritic Fibroblasts in Three-dimensional Collagen Matrices. Mol. Biol. Cell, 2003; 14(2): 384-395.
261. Cukierman, E.; Pankov, R., et al., Taking Cell-Matrix Adhesions to the Third Dimension. Science, 2001; 294(5547): 1708-1712.
262. Anselme, K.; Bigerelle, M., Topography effects of pure titanium substrates on human osteoblast long-term adhesion. Acta Biomaterialia, 2005; 1(2): 211-222.
263. Wan, Y.; Wang, Y., et al., Adhesion and proliferation of OCT-1 osteoblast-like cells on micro- and nano-scale topography structured poly(l-lactide). Biomaterials, 2005; 26(21): 4453-4459.
264. Jäger, M.; Zilkens, C., et al., Significance of Nano- and Microtopography for Cell-Surface Interactions in Orthopaedic Implants. Journal of Biomedicine and Biotechnology, 2007; 2007: 69036.
265. Teixeira, A. I.; Abrams, G. A., et al., Epithelial contact guidance on well-defined micro- and nanostructured substrates. J Cell Sci, 2003; 116(10): 1881-1892.
266. J. Glass-Brudzinski, D. P. D. M. B., Effects of substratum surface topography on the organization of cells and collagen fibers in collagen gel cultures. Journal of Biomedical Materials Research, 2002; 61(4): 608-618.
267. Chun-Min Lo; Hong-Bei Wang, et al., Cell Movement Is Guided by the Rigidity of the Substrate Biophysical Journal, 2000; 79(1): 144-152.
268. Adam J. Engler; Ludovic Richert, et al., Surface probe measurements of the elasticity of sectioned tissue, thin gels and polyelectrolyte multilayer films: Correlations between substrate stiffness and cell adhesion Surface Science 2004; 570(1-2): 142-154
269. Hong-Bei Wang; Micah Dembo, et al., Substrate flexibility regulates growth and apoptosis of normal but not transformed cells Am J Physiol Cell Physiol 2000; 279(5): C1345-C1350.
270. Fringer, J.; Grinnell, F., Fibroblast Quiescence in Floating or Released Collagen Matrices. Journal of Biological Chemistry, 2001; 276(33): 31047-31052.
271. Tamariz, E.; Grinnell, F., Modulation of Fibroblast Morphology and Adhesion during Collagen Matrix Remodeling. Mol. Biol. Cell, 2002; 13(11): 3915-3929.
272. Rhee, S.; Grinnell, F., Fibroblast mechanics in 3D collagen matrices. Advanced Drug Delivery Reviews, 2007; 59(13): 1299-1305.
273. Jiang, H.; Grinnell, F., Cell-Matrix Entanglement and Mechanical Anchorage of Fibroblasts in Three-dimensional Collagen Matrices. Mol. Biol. Cell, 2005; 16(11): 5070-5076.
274. Croce, M. A.; Silvestri, C., et al., Adhesion and Proliferation of Human Dermal Fibroblasts on Collagen Matrix. J Biomater Appl, 2004; 18(3): 209-222.
275. Wang, J. H. C.; Jia, F., et al., Cell orientation determines the alignment of cell-produced collagenous matrix. Journal of Biomechanics, 2003; 36(1): 97-102.

276. Chang Hun Lee; Ho Joon Shin, et al., Nanofiber alignment and direction of mechanical strain affect the ECM production of human ACL fibroblast Biomaterials 2005; 26(11): 1261-1270
277. H. Yoshimoto; Y.M. Shin, et al., A biodegradable nanofiber scaffold by electrospinning and its potential for bone tissue engineering Biomaterials, 2003; 24(12): 2077-2082
278. Chunmei Li; Charu Vepari , et al., Electrospun silk-BMP-2 scaffolds for bone tissue engineering Biomaterials 2006; 27(16): 3115-3124
279. Fujihara, K.; Kotaki, M., et al., Guided bone regeneration membrane made of polycaprolactone/calcium carbonate composite nano-fibers. Biomaterials, 2005; 26(19): 4139-4147.
280. Santos, M. I.; Tuzlakoglu, K., et al., Endothelial cell colonization and angiogenic potential of combined nano- and micro-fibrous scaffolds for bone tissue engineering. Biomaterials, 2008; 29(32): 4306-4313.
281. Chew, S. Y.; Mi, R., et al., The effect of the alignment of electrospun fibrous scaffolds on Schwann cell maturation. Biomaterials, 2008; 29(6): 653-661.
282. The University of Western Ontario. http://www.uwo.ca/isw/facilities/Tandetron/index.htm (2010).
283. Howard, J. C.; Varallo, V. M., et al., Wound healing-associated proteins Hsp47 and fibronectin are elevated in Dupuytren's contracture. Journal of Surgical Research, 2004; 117(2): 232-238.
284. http://www.cellgro.com/shop/customer/pages.php?pageid=29, Counting Cells -- Hemacytometer. 29th Sept 2009.
285. S. Timoshenko; Gere, J. M., Mechanics of Materials, 4th ed. PWS Publishing Co.: Boston, MA,, 1996.
286. W. H. Press; S. A. Teukosky, et al., Numerical Recpies in Fortran77. Cambridge University Press: Cambridge, U.K., 1986.
287. Hutter, J. L.; Bechhoefer, J., Calibration of atomic-force microscope tips. Review of Scientific Instruments 1993; 64(7): 1868-1873
288. Nikolaos, A. P.; Edward, W. M., Differential scanning calorimetry of crystallized PVA hydrogels. Journal of Applied Polymer Science, 1976; 20(6): 1457-1465.
289. Kenney, J. F.; Willcockson, G. W., Structure-Property relationships of poly(vinyl alcohol). III. Relationships between stereo-regularity, crystallinity, and water resistance in poly(vinyl alcohol). Journal of Polymer Science Part A-1: Polymer Chemistry, 1966; 4(3): 679-698.
290. W. H. Press; Teukolsky, S. A., Numerical Recipes in C: the art of scientific computing. Cambridge University Press, Cambridge, U.K., 1992.
291. Howard, S. A.; Preston, K. D., Profile fitting of powder diffraction patterns. Reviews in Mineralogy and Geochemistry, 1989; 20(1): 217-275.
292. Fava, R., Methods of experimental physics polymer Part B: Crystal structure and morphology 16th edn. Academic Press, New York, 1980.
293. Hermans, P. H.; Weidinger, A., On the determination of the crystalline fraction of polyethylenes from X-ray diffraction. Die Makromolekulare Chemie, 1961; 44(1): 24-36.

294. Benedetti, A.; Cocco, G., et al., X-ray diffraction methods to determine crystallinity and preferred orientation of lithium disilicate in Li-Zn-silicate glass-ceramic fibres. Journal of Materials Science, 1983; 18(4): 1039-1048.
295. Bhajantri, R. F.; Ravindrachary, V., et al., Microstructural studies on BaCl2 doped poly(vinyl alcohol). Polymer, 2006; 47(10): 3591-3598.
296. Klug, H. P.; Alexander, L. E., X-Ray Diffraction Procedures: For Polycrystalline and Amorphous Materials, 2nd Edition. John Wiley, New York 1974.
297. Tsimpliaraki, A.; Svinterikos, S., et al., Nanofibrous Structure of Nonwoven Mats of Electrospun Biodegradable Polymer Nanocompositesî—¸A Design of Experiments (DoE) Study. Industrial & Engineering Chemistry Research, 2009; 48(9): 4365-4374.
298. Sukigara, S.; Gandhi, M., et al., Regeneration of Bombyx mori silk by electrospinning. Part 2. Process optimization and empirical modeling using response surface methodology. Polymer, 2004; 45(11): 3701-3708.
299. Wenguo, C.; Xiaohong, L., et al., Investigation on process parameters of electrospinning system through orthogonal experimental design. Journal of Applied Polymer Science, 2007; 103(5): 3105-3112.
300. S-H. Tan; R. Inai, et al., Systematic parameter study for ultra-fine fiber fabrication via electrospinning process Polymer, 2005; 46(16).
301. Paul Podsiadlo; Amit K. Kaushik, et al., Ultrastrong and Stiff Layered Polymer Nanocomposites. Science, 2007; 318(5847): 80 - 83.
302. Bicerano, J., Prediction of polymer properties. Marcel Dekker (New York) 1993: 280–284.
303. Robert, K. T., Melting point and heat of fusion of poly(vinyl alcohol). Journal of Polymer Science Part A: General Papers, 1965; 3(12): 4181-4189.
304. Tanaka, N., Two equilibrium melting temperatures and physical meaning of DSC melting peaks in poly(ethylene terephthalate). Polymer, 2008; 49(24): 5353-5356.
305. Y.C. Yu; J.Y. Hsu, et al., Energy loss straggling of energetic 3He and 6Li ions into polymer foils. Nuclear Inst. and Methods in Physics Research, B, 2006; 249(1-2): 47-50.
306. de Souza, J. P.; Suprun-Belevich, Y., et al., Mechanical strain and damage in Si implanted with O and N ions at elevated temperatures: Evidence of ion beam induced annealing. Journal of Applied Physics, 2001; 89(1): 42-46.
307. Orvek, K. J.; Huffman, C., Carbonized layer formation in ion implanted photoresist masks. Nuclear Instruments and Methods in Physics Research Section B: Beam Interactions with Materials and Atoms, 1985; 7-8(Part 2): 501-506.
308. Jongok, W.; Myung Ho, K., et al., Surface modification of polyimide and polysulfone membranes by ion beam for gas separation. Journal of Applied Polymer Science, 2000; 75(12): 1554-1560.
309. G. Beamson; Briggs, D., High Resolution XPS of Organic Polymers. John Wiley & Son Ltd., 1992.
310. Stuart, B., Infrared Spectroscopy: Fundamentals and Applications. John Wiley and Sons Ltd, Kent, UK, 2004.
311. Senkevich, S.; Druzhinina, T., et al., Thermal transformations of polyvinyl alcohol as a source for the preparation of carbon materials. Solid Fuel Chemistry, 2007; 41(1): 45-51.

312. Hyder, M. N.; Huang, R. Y. M., et al., Correlation of physicochemical characteristics with pervaporation performance of poly(vinyl alcohol) membranes. Journal of Membrane Science, 2006; 283(1-2): 281-290.
313. Elsdale, T.; Foley, R., Morphogenetic Aspects of Multilayering in Petri Dish Cultures of Human Fetal Lung Fibroblasts. J. Cell Biol., 1969; 41(1): 298-311.
314. Teh, T. K. H.; Goh, J. C. H., et al., Characterization of Electrospun Substrates for Ligament Regeneration using Bone Marrow Stromal Cells. In 13th International Conference on Biomedical Engineering, 2009; pp 1488-1491.
315. Yim, E. K. F.; Leong, K. W., Significance of synthetic nanostructures in dictating cellular response. Nanomedicine: Nanotechnology, Biology and Medicine, 2005; 1(1): 10-21.
316. Langer, R.; Vacanti, J. P., Tissue engineering. Science, 1993; 260(5110): 920-926.
317. Shin, M.; Vacanti, J., Tissue Engineering. In Emerging Technologies in Surgery, 2007; pp 133-151.
318. Torrestiana-Sanchez, B.; Ortiz-Basurto, R. I., et al., Effect of nonsolvents on properties of spinning solutions and polyethersulfone hollow fiber ultrafiltration membranes. Journal of Membrane Science, 1999; 152(1): 19-28.
319. Foroughi, J.; Spinks, G. M., et al., Production of polypyrrole fibres by wet spinning. Synthetic Metals, 2008; 158(3-4): 104-107.
320. Bulters, M. J. H.; Meijer, H. E. H., Analogy between the modelling of pullout in solution spinning and the prediction of the vortex size in contraction flows. Journal of Non-Newtonian Fluid Mechanics, 1990; 38(1): 43-80.
321. Fambri, L.; Pegoretti, A., et al., Biodegradable fibres of poly(L-lactic acid) produced by melt spinning. Polymer, 1997; 38(1): 79-85.
322. Doufas, A. K.; McHugh, A. J., et al., Simulation of melt spinning including flow-induced crystallization: Part II. Quantitative comparisons with industrial spinline data. Journal of Non-Newtonian Fluid Mechanics, 2000; 92(1): 81-103.
323. Doufas, A. K.; McHugh, A. J., et al., Simulation of melt spinning including flow-induced crystallization: Part I. Model development and predictions. Journal of Non-Newtonian Fluid Mechanics, 2000; 92(1): 27-66.
324. Zhang, X.; Liu, T., et al., Gel spinning of PVA/SWNT composite fiber. Polymer, 2004; 45(26): 8801-8807.
325. Lovett, M. L.; Cannizzaro, C. M., et al., Gel spinning of silk tubes for tissue engineering. Biomaterials, 2008; 29(35): 4650-4657.
326. Notin, L.; Viton, C., et al., Pseudo-dry-spinning of chitosan. Acta Biomaterialia, 2006; 2(3): 297-311.
327. Gou, Z.; McHugh, A. J., Two-dimensional modeling of dry spinning of polymer fibers. Journal of Non-Newtonian Fluid Mechanics, 2004; 118(2-3): 121-136.
328. Dzenis, Y., Material Science: Spinning Continuous Fibers for Nanotechnology. Science, 2004; 304(5679): 1917-1919.
329. Pitt Supaphol, S. C., On the electrospinning of poly(vinyl alcohol) nanofiber mats: A revisit. Journal of Applied Polymer Science, 2008; 108(2): 969-978.
330. Berkland, C.; Pack, D. W., et al., Controlling surface nano-structure using flow-limited field-injection electrostatic spraying (FFESS) of poly(D,L-lactide-co-glycolide). Biomaterials, 2004; 25(25): 5649-5658.

331. J.M. Deitzel; J. Kleinmeyer, et al., The effect of processing variables on the morphology of electrospun nanofibers and textiles Polymer, 2001; 42(1): 261-272
332. S.A. Theron; E. Zussman, et al., Experimental investigation of the governing parameters in the electrospinning of polymer solutions Polymer, 2004; 45(6): 2017-2030
333. Moses M. Hohman; Michael Shin, et al., Electrospinning and electrically forced jets. I. Stability theory. Physics of Fluids, 2001; 13(8): 2201-2220
334. Shin, Y. M.; Hohman, M. M., et al., Electrospinning: A whipping fluid jet generates submicron polymer fibers. Applied Physics Letters, 2001; 78(8): 1149-1151.
335. Tripatanasuwan, S.; Zhong, Z., et al., Effect of evaporation and solidification of the charged jet in electrospinning of poly(ethylene oxide) aqueous solution. Polymer, 2007; 48(19): 5742-5746.
336. Wang, C.; Chien, H.-S., et al., Electrospinning of Polyacrylonitrile Solutions at Elevated Temperatures. Macromolecules, 2007; 40(22): 7973-7983.
337. A. Koski; K. Yim, et al., Effect of molecular weight on fibrous PVA produced by electrospinning Materials Letters, 2004; 58(3-4): 493-497
338. Lin, T.; Wang, H., et al., The charge effect of cationic surfactants on the elimination of fibre beads in the electrospinning of polystyrene. Nanotechnology, 2004; 15(9): 1375-1381.
339. Montgomery, D. C., Design and Analysis of Experiments. John Wiley Sons, 2002.
340. Montgomery, D. C.; Myers, R. H., Response Surface Methodology: Process and Product Optimization Using Designed Experiments. NewYork: Wiley-Interscience, 1995.
341. Yördem, O. S.; Papila, M., et al., Effects of electrospinning parameters on polyacrylonitrile nanofiber diameter: An investigation by response surface methodology. Materials & Design, 2008; 29(1): 34-44.
342. Shu-Ying, G.; Jie, R., Process Optimization and Empirical Modeling for Electrospun Poly(D,L-lactide) Fibers using Response Surface Methodology. Macromolecular Materials and Engineering, 2005; 290(11): 1097-1105.
343. Li, W.-J.; Mauck, R. L., et al., Engineering controllable anisotropy in electrospun biodegradable nanofibrous scaffolds for musculoskeletal tissue engineering. Journal of Biomechanics, 2007; 40(8): 1686-1693.
344. Ayres, C.; Bowlin, G. L., et al., Modulation of anisotropy in electrospun tissue-engineering scaffolds: Analysis of fiber alignment by the fast Fourier transform. Biomaterials, 2006; 27(32): 5524-5534.
345. Kawabata, I.; Ishii, H., Fiber Arrangement in the Tympanic Membrane: Scanning Electron Microscope Observations. Acta Oto-Laryngologica, 1971; 72(1): 243 - 254.
346. Peresin, M. S.; Habibi, Y., et al., Nanofiber Composites of Polyvinyl Alcohol and Cellulose Nanocrystals: Manufacture and Characterization. Biomacromolecules, 2010.
347. Triantafyllos, S.; Andrew, Y., et al., Permeability calculations in three-dimensional isotropic and oriented fiber networks. Physics of Fluids, 2008; 20(12): 123601.

348. Nemir, S.; West, J., Synthetic Materials in the Study of Cell Response to Substrate Rigidity. Annals of Biomedical Engineering, 2010; 38(1): 2-20.
349. Haiyi, L.; Moneesh, U., et al., Size-dependent elasticity of nanowires: Nonlinear effects. Physical Review B (Condensed Matter and Materials Physics), 2005; 71(24): 241403.
350. Jaeger, R.; Schonherr, H., et al., Chain Packing in Electro-Spun Poly(ethylene oxide) Visualized by Atomic Force Microscopy. Macromolecules, 1996; 29(23): 7634-7636.
351. Stephens, J. S.; Chase, D. B., et al., Effect of the Electrospinning Process on Polymer Crystallization Chain Conformation in Nylon-6 and Nylon-12. Macromolecules, 2004; 37(3): 877-881.
352. Chen, Z.; Foster, M. D., et al., Structure of Poly(ferrocenyldimethylsilane) in Electrospun Nanofibers. Macromolecules, 2001; 34(18): 6156-6158.
353. Oleg Stukalov; Chris A. Murray, et al., Relative humidity control for atomic force microscopes. Review of Scientific Instruments, 2006; 77(033704).
354. Wan, Y.; Cao, X., et al., Fibrous poly(chitosan-g-dl-lactic acid) scaffolds prepared via electro-wet-spinning. Acta Biomaterialia, 2008; 4(4): 876-886.
355. In Jeong, S.; Kim, S. Y., et al., Tissue-engineered vascular grafts composed of marine collagen and PLGA fibers using pulsatile perfusion bioreactors. Biomaterials, 2007; 28(6): 1115-1122.
356. Ross, A. M.; Jason, A. B., Controlling Stem Cell Fate with Material Design. Advanced Materials, 2009; 22(2): 175-189.
357. Georges, P. C.; Janmey, P. A., Cell type-specific response to growth on soft materials. J Appl Physiol, 2005; 98(4): 1547-1553.
358. Engler, A. J.; Sen, S., et al., Matrix Elasticity Directs Stem Cell Lineage Specification. Cell, 2006; 126(4): 677-689.
359. Rebecca, G. W., The role of matrix stiffness in regulating cell behavior. Hepatology, 2008; 47(4): 1394-1400.
360. Ektoras, H.; Vivek, M., et al., Guiding cell migration in 3D: A collagen matrix with graded directional stiffness. Cell Motility and the Cytoskeleton, 2009; 66(3): 121-128.
361. Solon, J.; Levental, I., et al., Fibroblast Adaptation and Stiffness Matching to Soft Elastic Substrates. Biophysical Journal, 2007; 93(12): 4453-4461.
362. Lemmon, C. A.; Chen, C. S., et al., Cell Traction Forces Direct Fibronectin Matrix Assembly. Biophysical Journal, 2009; 96(2): 729-738.
363. Matsumoto, T.; Yung, Y. C., et al., Mechanical Strain Regulates Endothelial Cell Patterning In Vitro. Tissue Engineering, 2007; 13(1): 207-217.
364. Ives, C.; Eskin, S., et al., Mechanical effects on endothelial cell morphology: In vitro assessment. In Vitro Cellular & Developmental Biology - Plant, 1986; 22(9): 500-507.
365. Kim, D.-H.; Lipke, E. A., et al., Nanoscale cues regulate the structure and function of macroscopic cardiac tissue constructs. Proceedings of the National Academy of Sciences, 2010; 107(2): 565-570.
366. Tang, C.; Saquing, C. D., et al., In Situ Cross-Linking of Electrospun Poly(vinyl alcohol) Nanofibers. Macromolecules, 2009; 43(2): 630-637.

367. Lynn, L. H. H.; Hsing-Wen, S., et al., Biocompatibility study of a biological tissue fixed with a naturally occurring crosslinking reagent. Journal of Biomedical Materials Research, 1998; 42(4): 568-576.
368. Huang, H.; Gu, L., et al., Non-isothermal crystallization and thermal transitions of a biodegradable, partially hydrolyzed poly(vinyl alcohol). Polymer, 2006; 47(11): 3935-3945.
369. Gyeong-Man, K.; et al., Electrospun PVA/HAp nanocomposite nanofibers: biomimetics of mineralized hard tissues at a lower level of complexity. Bioinspiration & Biomimetics, 2008; 3(4): 046003.
370. Chunming, W.; Jing, B., et al., Enhancing cell affinity of nonadhesive hydrogel substrate: The role of silica hybridization. Biotechnology Progress, 2008; 24(5): 1142-1146.
371. Luo, Y.; Shoichet, M. S., A photolabile hydrogel for guided three-dimensional cell growth and migration. Nat Mater, 2004; 3(4): 249-253.
372. Faucheux, N.; Schweiss, R., et al., Self-assembled monolayers with different terminating groups as model substrates for cell adhesion studies. Biomaterials, 2004; 25(14): 2721-2730.
373. Lan, M. A.; Gersbach, C. A., et al., Myoblast proliferation and differentiation on fibronectin-coated self assembled monolayers presenting different surface chemistries. Biomaterials, 2005; 26(22): 4523-4531.
374. T. Yokota; T. Terai, et al., Cell adhesion to nitrogen-doped DLCS fabricated by plasma-based ion implantation and deposition method Nuclear Inst. and Methods in Physics Research, B 2006; 242(1-2): 48-50
375. Graz, I.; Ebner, A., et al., Micropatterned atmospheric pressure discharge surface modification of fluorinated polymer films for mammalian cell adhesion and protein binding. Applied Physics A: Materials Science & Processing, 2008; 92(3): 547-555.
376. Mwale, F.; Wang, H. T., et al., The effect of glow discharge plasma surface modification of polymers on the osteogenic differentiation of committed human mesenchymal stem cells. Biomaterials, 2006; 27(10): 2258-2264.
377. Mwale, F.; Girard-Lauriault, P.-L., et al., Suppression of Genes Related to Hypertrophy and Osteogenesis in Committed Human Mesenchymal Stem Cells Cultured on Novel Nitrogen-Rich Plasma Polymer Coatings. Tissue Engineering, 2006; 12(9): 2639-2647.
378. Lerouge, S.; Major, A., et al., Nitrogen-rich coatings for promoting healing around stent-grafts after endovascular aneurysm repair. Biomaterials, 2007; 28(6): 1209-1217.
379. Sipehia, R.; Martucci, G., et al., Enhanced Attachment and Growth of Human Endothelial Cells Derived from Umbilical Veins on Ammonia Plasma Modified Surfaces of Ptfe and EPTFE Synthetic Vascular Graft Biomaterials. Artificial Cells, Blood Substitutes and Biotechnology, 1993; 21(4): 455-468.
380. Xue, X.; Wang, J., et al., Biocompatibility of pure titanium modified by human endothelial cell-derived extracellular matrix. Applied Surface Science, 2010; 256(12): 3866-3873.
381. De, S.; Sharma, R., et al. In Enhancement of blood compatibility of implants by helium plasma treatment, Industry Applications Conference, 2004. 39th IAS

Annual Meeting. Conference Record of the 2004 IEEE, 2004; 2004; pp 932-936 vol.2.
382. De, S.; Sharma, R., et al., Plasma treatment of polyurethane coating for improving endothelial cell growth and adhesion. Journal of Biomaterials Science, Polymer Edition, 2005; 16: 973-989.
383. Ratner, B. D.; Hoffman, A. S., et al., Biomaterials Science: An Introduction to Materials in Medicine Academic Press, NY (2nd edition), 2004.
384. Schwartz, M. A.; Ginsberg, M. H., Networks and crosstalk: integrin signalling spreads. Nat Cell Biol, 2002; 4(4): E65-E68.
385. A. Ohl; Schröder, K., Plasma-induced chemical micropatterning for cell culturing applications: a brief review Surface and Coatings Technology, 1999; 116-119: 820-830
386. D.J. Upadhyay; Bhat, N. V., Pervaporation studies of gaseous plasma treated PVA membrane. Journal of Membrane Science, 2004; 239(2): 255-263.
387. L. Guzman; A. Miotelloa, et al., Hard coating adhesion on ion implanted polymer surfaces. Thin Solid Films 2000; 377-378: 760-765
388. Guzman, L.; Celva, R., et al., Polymer surface modification by ion implantation and reactive deposition of transparent films. Surface and Coatings Technology, 1998; 103-104: 375-379.
389. Chen, T.; Yao, S., et al., The modification of mechanical properties by 2 MeV Si ions irradiating polyimide. Nuclear Instruments and Methods in Physics Research Section B: Beam Interactions with Materials and Atoms, 2008; 266(12-13): 3091-3094.
390. Rodríguez, R. J.; Medrano, A., et al., Improvement of surface mechanical properties of polymers by helium ion implantation. Surface and Coatings Technology, 2007; 201(19-20): 8146-8149.
391. Maccauro, G.; Iommetti, P. R., et al., An overview about biomedical applications of micron and nano size tantalum. Recent Patents on Biotechnology, 2009; 3(3): 157-165.
392. Black, J., Biologic performance of tantalum. Clinical Materials, 1994; 16(3): 167-173.
393. David M. Findlay; Katie Welldon, et al., The proliferation and phenotypic expression of human osteoblasts on tantalum metal Biomaterials, 2004; 25(12): 2215-2227
394. Maik, S.; Martin, L., et al., Morphology, proliferation, and osteogenic differentiation of mesenchymal stem cells cultured on titanium, tantalum, and chromium surfaces. Journal of Biomedical Materials Research Part A, 2008; 86A(2): 448-458.
395. Yu, S. B.; Watson, A. D., Metal-Based X-ray Contrast Media. Chem. Rev., 1999; 99(9): 2353-2378.
396. Bobyn, J. D.; Poggie, R. A., et al., Clinical Validation of a Structural Porous Tantalum Biomaterial for Adult Reconstruction. J Bone Joint Surg Am, 2004; 86(suppl_2): 123-129.
397. Brett Russell Levine; Scott Sporer, et al., Experimental and clinical performance of porous tantalum in orthopedic surgery Biomaterials, 2006; 27(27): 4671-4681

398. Frigg, A.; Dougall, H., et al., Can Porous Tantalum Be Used to Achieve Ankle and Subtalar Arthrodesis?: A Pilot Study. Clinical Orthopaedics and Related Research®, 2010; 468(1): 209-216.
399. Eike, H. M.; Jan, C. S., et al., Porous tantalum and poly-ϵ-caprolactone biocomposites for osteochondral defect repair: Preliminary studies in rabbits. Journal of Orthopaedic Research, 2010; 28(2): 141-148.
400. Johnston, S.; Bramble, J., et al., Arp2/3 complex activity in filopodia of spreading cells. BMC Cell Biology, 2008; 9(1): 65.
401. Suk-Won Lee; Kim, S.-Y., et al., Influence of microgroove dimension on cell behavior of human gingival fibroblasts cultured on titanium substrata. Clinical Oral Implants Research, 2009; 20(1): 56-66.
402. Sherer, N. M.; Lehmann, M. J., et al., Retroviruses can establish filopodial bridges for efficient cell-to-cell transmission. Nat Cell Biol, 2007; 9(3): 310-315.
403. Yang, X.; Shah, J. D., et al., Nanofiber Enabled Layer-by-Layer Approach Toward Three-Dimensional Tissue Formation. Tissue Engineering Part A, 2009; 15(4): 945-956.
404. Sangsanoh, P.; Suwantong, O., et al., In vitro biocompatibility of electrospun and solvent-cast chitosan substrata towards Schwann, osteoblast, keratinocyte and fibroblast cells. European Polymer Journal, 2010; 46(3): 428-440.
405. Lambert, F. L.; Pelletier, G., et al., Specific properties of smooth muscle cells from different layers of rabbit myometrium. Am J Physiol Cell Physiol, 1990; 258(5): C794-802.
406. Sang-Soo, K.; So-Jung, G., et al., Skin regeneration using keratinocytes and dermal fibroblasts cultured on biodegradable microspherical polymer scaffolds. Journal of Biomedical Materials Research Part B: Applied Biomaterials, 2005; 75B(2): 369-377.
407. Heydarkhan-Hagvall, S.; Schenke-Layland, K., et al., Three-dimensional electrospun ECM-based hybrid scaffolds for cardiovascular tissue engineering. Biomaterials, 2008; 29(19): 2907-2914.

Appendix A

Derivation of Equations – Clamped Beam Model

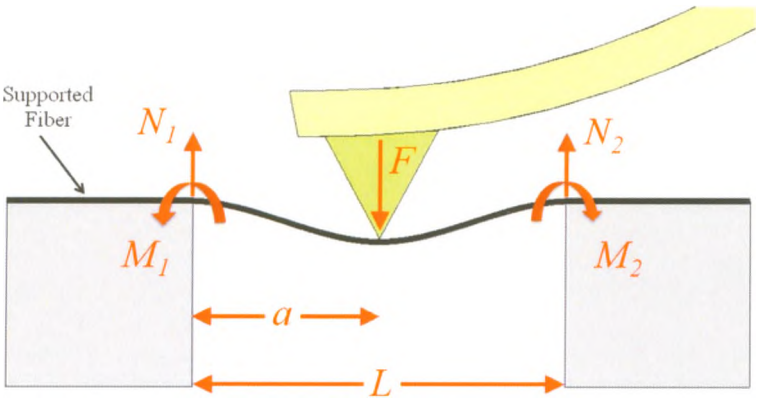

Initial State (1)

$$F = N_1 + N_2$$

Initial State (2)

$$\Sigma \tau_y = M_1 - aF + N_2 L - M_2 = 0$$

Definition:

$$y = \delta \ = Deflection$$

$$y' = Slope$$

$$y'' = \frac{M}{EI} = Curvature, \text{ where as } M = Torque$$

$$y''' = \frac{M'}{EI} = \frac{V}{EI}, \text{ where as } V = Shear\ Force$$

$$y'''' = \frac{P}{EI}, \text{ where as } P = Distributed\ Load$$

The area of moment of inertia (I) for fiber with circular cross-section:

$$I = 2\int_{-r}^{r} z^2 \sqrt{r^2 - z^2}\, dz$$

where $z = r\sin\theta$ and $dz = r\cos\theta d\theta$

$$I = 2\int_{-\pi/2}^{\pi/2} r^2 \sin^2\theta \sqrt{r^2 - r^2\sin^2\theta}\; r\cos\theta d\theta$$

$$I = 2r^4 \int_{-\pi/2}^{\pi/2} \sin^2\theta \cos^2\theta d\theta$$

$$I = \frac{r^4}{2}\int_{-\pi/2}^{\pi/2} \sin^2 2\theta d\theta$$

where $\phi = 2\theta$ and $d\phi = 2d\theta$

$$I = \frac{r^4}{4}\int_{-\pi}^{\pi} \sin^2\phi d\phi$$

$$I = \frac{\pi r^4}{4}$$

Therefore:

$$I = \frac{\pi d^4}{64}$$

For x<a,

$$y_1(x) = a_1x^3 + b_1x^2 + c_1x + d_1$$

Boundary Condition:

$$y(0) = 0 \rightarrow d_1 = 0$$

$$y'(0) = 0 \rightarrow c_1 = 0$$

Therefore

$$y_1(x) = a_1x^3 + b_1x^2$$

For x>a,

$$y_2(x) = a_2x^3 + b_2x^2 + c_2x + d_2$$

For x=L,

$$y(L) = a_2L^3 + b_2L^2 + c_2L + d_2 = 0$$

$$y'(L) = 3a_2L^2 + 2b_2L + c_2 = 0$$

For x=a,

$$y_1(a) = y_2(a)$$

$$a_1a^3 + b_1a^2 - a_2a^3 - b_2a^2 - c_2a - d_2 = 0$$

and

$$y_1'(a) = y_2'(a)$$

$$3a_1a^2 + 2b_1a - 3a_2a^2 - 2b_2a - c_2 = 0$$

The curvature at x=0:

$$y_1''(0) = \frac{M_1}{EI} = 2b_1$$

at x=L:

$$y_2''(L) = \frac{M_2}{EI} = 6a_2L + 2b_2$$

at x=a:

$$y_1''(a) = y_2''(a) \rightarrow 6a_1a + 2b_1 - 6a_2a - b_2 = 0$$

For general case:

$$y_1(x) = a_1x^3 + b_1x^2$$

$$y_2(x) = a_2x^3 + b_2x^2 + c_2x + d_2$$

Conditions:

(1) $y_2(L) = 0$

$$a_2L^3 + b_2L^2 + c_2L + d_2 = 0$$

(2) $y_2'(L) = 0$

$$3a_2L^2 + 2b_2L + c_2 = 0$$

(3) $y_1(a) = y_2(a)$

$$a_1a^3 + b_1a^2 - a_2a^3 - b_2a^2 - c_2a - d_2 = 0$$

(4) $y_1'(a) = y_2'(a)$

$$3a_1a^2 + 2b_1a - 3a_2a^2 - 2b_2a - c_2 = 0$$

(5) $\tau_{a-} = 0$

$$-aN_1 - EIy''(0) + EIy''(a) = 0$$

$$-N_1+EI(6a_1) = 0$$

(6) $\tau_{a+} = 0$

$$(L-a)N_2+EIy''(L)-EIy''(a) = 0$$

$$N_2+EI(6a_2) = 0$$

(7) $\tau_a = 0$

$$(L-a)N_2-aN_1+EI\left[y''(L)-y''(a)\right] = 0$$

$$(L-a)N_2-aN_1+EI(6a_2L+2b_2-2b_1) = 0$$

(8)

$$N_1+N_2 = F$$

Using matrix (solve it using Maple)

$$\begin{bmatrix} 0 & 0 & L^3 & L^2 & L & 1 & 0 & 0 \\ 0 & 0 & 3L^2 & 2L & 1 & 0 & 0 & 0 \\ a^3 & a^2 & -a^3 & -a^2 & -a & -1 & 0 & 0 \\ 3a^2 & 2a & -3a^2 & -2a & -1 & 0 & 0 & 0 \\ 6EI & 0 & 0 & 0 & 0 & 0 & -1 & 0 \\ 0 & 0 & 6EI & 0 & 0 & 0 & 0 & 1 \\ 0 & -2EI & 6EIL & 2EI & 0 & 0 & -a & L-a \\ 0 & 0 & 0 & 0 & 0 & 0 & 1 & 1 \end{bmatrix} \begin{bmatrix} a_1 \\ b_1 \\ a_2 \\ b_2 \\ c_2 \\ d_2 \\ N_1 \\ N_2 \end{bmatrix} = \begin{bmatrix} 0 \\ 0 \\ 0 \\ 0 \\ 0 \\ 0 \\ 0 \\ F \end{bmatrix}$$

$$\begin{bmatrix} a_1 \\ b_1 \\ a_2 \\ b_2 \\ c_2 \\ d_2 \\ N_1 \\ N_2 \end{bmatrix} = \begin{bmatrix} \frac{1}{6}\frac{F}{EIL^3}(2a^3 - 3La^2 + L^3) \\ -\frac{1}{2}\frac{aF}{EIL^2}(a^2 - 2aL + L^2) \\ \frac{1}{6}\frac{a^2F}{EIL^3}(2a - 3L) \\ -\frac{1}{2}\frac{a^2F}{EIL^2}(a - 2L) \\ -\frac{1}{2}\frac{a^2F}{EI} \\ \frac{1}{6}\frac{a^3F}{EI} \\ \frac{F}{L^3}(2a^3 - 3a^2L + L^3) \\ -\frac{a^2F}{L^3}(2a - 3L^2) \end{bmatrix}$$

Therefore:

$$y_1(x) = \left[\frac{1}{6}\frac{F}{EIL^3}(2a^3 - 3La^2 + L^3)\right]x^3 + \left[-\frac{1}{2}\frac{aF}{EIL^2}(a^2 - 2aL + L^2)\right]x^2$$

$$y_1(x) = \frac{F(L-a)}{2EIL^2}\left[\frac{(L^2 + aL - 2a^2)}{3L}x^3 - a(L-a)x^2\right]$$

$$y_1(a) = \frac{F(L-a)}{2EIL^2}\left[\frac{a^3}{3L}(L^2 + aL - 2a^2) - a^3(L-a)\right]$$

$$y_1(a) = \frac{F(L-a)a^3}{6EIL^3}\left[L^2 + aL - 2a^2) - 3L(L-a)\right]$$

$$y_1(a) = \frac{F(L-a)a^3}{6EIL^3}(-2L^2 + 4aL - 2a^2)$$

$$y_1(a) = \delta(a) = -\frac{F}{3EI}\left[\frac{a(L-a)}{L}\right]^3$$

For a=L/2 (at the centre of the fiber):

$$y_1(\frac{L}{2}) = -\frac{F}{3EI}\left[\frac{\frac{L}{2}(L-\frac{L}{2})}{L}\right]^3$$

$$y_1(\frac{L}{2}) = -\frac{F}{3EI}\left(\frac{L^3}{64}\right)$$

$$y_1(\frac{L}{2}) = -\frac{FL^3}{192EI}$$

Relate to the AFM force curve measurement:

$$(z - z_0) = (y - y_0) - \delta(a)$$

$$(z - z_0) = (y - y_0) + \frac{k(y - y_0)}{3EI}\left[\frac{a(L-a)}{L}\right]^3$$

$$(y - y_0) = \frac{(z - z_0)}{1 + \frac{k}{3EI}\left[\frac{a(L-a)}{L}\right]^3}$$

Slope of the force curve:

$$\frac{dy}{dz} = \frac{1}{1 + \frac{k}{3EI}\left[\frac{a(L-a)}{L}\right]^3}$$

Appendix B

Copyright Waivers

SPRINGER LICENSE
TERMS AND CONDITIONS

Mar 15, 2010

This is a License Agreement between Kenneth Wong ("You") and Springer ("Springer") provided by Copyright Clearance Center ("CCC"). The license consists of your order details, the terms and conditions provided by Springer, and the payment terms and conditions.

All payments must be made in full to CCC. For payment instructions, please see information listed at the bottom of this form.

License Number	2381070242170
License date	Mar 02, 2010
Licensed content publisher	Springer
Licensed content publication	Journal of Materials Science (full set)
Licensed content title	Effect of annealing on aqueous stability and elastic modulus of electrospun poly(vinyl alcohol) fibers
Licensed content author	Kenneth Kar Ho Wong
Licensed content date	Jan 1, 2010
Type of Use	Thesis/Dissertation
Portion	Full text
Number of copies	8
Author of this Springer article	Yes and you are the sole author of the new work
Order reference number	
Title of your thesis / dissertation	Cell Compatible Electrospun Poly(vinyl alcohol) Fibers for Tissue Regeneration
Expected completion date	Mar 2010
Estimated size(pages)	150
Total	0.00 USD
Terms and Conditions	

ELSEVIER LICENSE
TERMS AND CONDITIONS

Mar 15, 2010

This is a License Agreement between Kenneth Wong ("You") and Elsevier ("Elsevier") provided by Copyright Clearance Center ("CCC"). The license consists of your order details, the terms and conditions provided by Elsevier, and the payment terms and conditions.

All payments must be made in full to CCC. For payment instructions, please see information listed at the bottom of this form.

Supplier	Elsevier Limited The Boulevard,Langford Lane Kidlington,Oxford,OX5 1GB,UK
Registered Company Number	1982084
Customer name	Kenneth Wong
Customer address	Department of Physics and Astronomy London, ON N6A3K7
License Number	2381080132192
License date	Mar 02, 2010
Licensed content publisher	Elsevier
Licensed content publication	European Polymer Journal
Licensed content title	Physical properties of ion beam treated electrospun poly(vinyl alcohol) nanofibers
Licensed content author	Kenneth Kar Ho Wong, Jeffrey L. Hutter, Martin Zinke-Allmang, Wankei Wan
Licensed content date	May 2009
Volume number	45
Issue number	5
Pages	10
Type of Use	Thesis / Dissertation
Portion	Full article
Format	Both print and electronic
You are an author of the Elsevier article	Yes
Are you translating?	No
Order Reference Number	
Expected publication date	Mar 2010
Elsevier VAT number	GB 494 6272 12
Permissions price	0.00 USD
Value added tax 0.0%	0.00 USD
Total	0.00 USD